

UNIVERSITAT POLITÈCNICA DE VALÈNCIA  
DEPARTAMENT DE COMUNICACIONS

**Integrated Microwave Photonic  
Processors using Waveguide Mesh  
Cores**



UNIVERSITAT  
POLITÈCNICA  
DE VALÈNCIA

Ph.D THESIS

Daniel Pérez López

Supervisors:

José Capmany Francoy

Ivana Gasulla Mestre



*A mi tío Nica...*



*If you want to go fast, go alone.*

*If you want to go far, go together.*

*Si quieres llegar rápido, camina solo.*

*Si quieres llegar lejos, ve acompañado*

**African proverb.**









# Agradecimientos

---

Este trabajo representa muchas cosas, y ninguna de ellas hubiera sido posible sin vosotros.

En primer lugar, quiero dirigirme a mis dos directores de Tesis: Ivana y José, José e Ivana. Vosotros me habéis acompañado, desde la obtención de mi proyecto final de carrera y trabajo fin de master hasta la consecución de esta Tesis doctoral, y os habéis preocupado de orientarme e inculcarme los mejores hábitos. Habéis, además, traspasado la línea de la educación estrictamente académica, aportando nuevos matices a mi forma de ser y de pensar, por los que os estaré siempre agradecido. Soy consciente de que encaminar mis pasos durante este tiempo ha podido resultar algo duro, tropezando cientos de veces con exactamente las mismas piedras, pero me alegra pensar que sabéis que mi esfuerzo en todo momento ha sido el máximo. Vuestra pasión por la ciencia no ha hecho más que alimentar mi motivación, curiosidad y espíritu crítico, llevándome a pensar, imaginar y soñar con poder seguir vuestros pasos algún día. La clave: esfuerzo y perseverancia. Juntos habéis construido un gran equipo, como diría uno que yo me sé...*the A Team!* Estos agradecimientos bien podrían ocupar un capítulo de Tesis, o un extenso apéndice, pero, todo el mundo sabe que rodeando una mesa y sosteniendo alguna pinta estas palabras se asimilarían mucho mejor.

También quiero aprovechar la oportunidad para agradecer al resto de mis compañeros y a todos los que forman Photonics Research Labs por su labor y dedicación diaria: Pascual, gracias por incluirme en tu grupo de trabajo más cercano y permitirme discutir y aprender con vosotros cada semana; David (y por extensión VLC photonics crew), es siempre un placer poder conversar contigo de nuevos avances para, además de disfrutar, terminar dándome cuenta de la gran cantidad de trabajo que queda por hacer y de conceptos que me quedan por asimilar. He de reconocer que he aprendido gran cantidad de cosas gracias a ti.

Señores *barriers*, ustedes merecen un punto a parte. Gracias a vuestra inherente capacidad para desconfiar del buen trascurso de las cosas, de alejarme de lo estrictamente positivo y de estampar el vaso medio lleno contra el suelo, me habéis enseñado nada. Como excepción, podríamos salvar que con humor y buenas compañías se puede conseguir cualquier meta; o al menos que el camino hasta un

inevitable final se haga agradable y divertido. Tenéis el humor más ácido que he conocido en mi vida. Solo os puedo decir una cosa: cuando necesitéis cualquier cosa, ya sabéis dónde estoy. “...oigo agradecer, pero no oigo escribir tesis...”

Quisiera agradecer, por duplicado, a Rocío. Con una pequeña porción de tus enormes conocimientos en el laboratorio he conseguido llevar en tiempo record a buen puerto las demostraciones de este trabajo. Sin tu ayuda nada de esto hubiera sido posible.

Gracias a la estancia realizada en el Optoelectronics Research Centre (University of Southampton), pudimos fabricar el chip fotónico clave para la demostración de este trabajo. El trabajo fue liderado por el Prof. Goran Mashanovich y Dr David Thomson, quienes siempre estuvieron abiertos a colaborar con nuestra propuesta. Además, tuve el placer de conocer a Zhibo (Will) Qu, Wei Cao, Callum Littlejohns, Milos Nedeljković, Scott Reynolds, Milan Milošević, Thalia Dominguez-Bucio, Nathan Soper, Lorenzo Mastronardi and Jordi Soler.

Me gustaría agradecer, de manera simbólica, a todas las personas que luchan y apuestan por la ciencia en general, particularmente a los que trabajan en el mundo de la fotónica. Quiero daros las gracias por todos y cada uno de vuestros esfuerzos y vuestros avances, sin los cuales este trabajo, ni ninguno, hubiera podido ser realizado. Agradecimiento especial a R. A. Soref, por sus discusiones, dedicación y colaboración.

Agradezco también al programa FPI de la Universitat Politècnica de València, por hacer posible la realización de este trabajo.

Por último, pero no menos importante, quiero agradecer a mi círculo de personas más cercano que me ha acompañado hasta aquí por todo su apoyo: A toda la familia y amigos.

Mamá y Papá, ya dije en su momento que en tiempos de niebla y tempestad, sois el mejor remo y la mejor dirección. Solo tengo palabras de agradecimiento eterno y orgullo para vosotros. Mis queridos hermanos, gracias por vuestro afecto incondicional, por todo lo que hemos compartido, y por lo que nos queda por compartir. María, tu cariño, apoyo e inexorable fe ciega en mi representan el mejor motivo para no rendirme jamás.

Desde lo más profundo de mí, gracias a todos.





# Abstract

---

Integrated microwave photonics changes the scaling laws of information and communication systems offering architectural choices that combine photonics with electronics to optimize performance, power, footprint and cost. Application Specific Photonic Integrated Circuits, where particular circuits/chips are designed to optimally perform particular functionalities, require a considerable number of design and fabrication iterations leading to long-development times and costly implementations.

A different approach inspired by electronic Field Programmable Gate Arrays is the programmable Microwave Photonic processor, where a common hardware implemented by the combination of microwave, photonic and electronic subsystems, realizes different functionalities through programming. Here, we propose the first-ever generic-purpose Microwave Photonic processor concept and architecture. This versatile processor requires a powerful end-to-end field-based analytical model to optimally configure all their subsystems as well as to evaluate their performance in terms of the radiofrequency gain, noise and dynamic range. Therefore, we develop a generic model for integrated Microwave Photonics systems. The key element of the processor is the reconfigurable optical core. It requires high flexibility and versatility to enable reconfigurable interconnections between subsystems as well as the synthesis of photonic integrated circuits. For this element, we focus on a 2-dimensional photonic waveguide mesh based on the interconnection of tunable couplers. Within the framework of this Thesis, we have proposed two novel interconnection schemes, aiming for a mesh design with a high level of versatility. Focusing on the hexagonal waveguide mesh, we explore the synthesis of a high variety of photonic integrated circuits and particular Microwave Photonics applications that can potentially be performed on a single hardware. In addition, we report the first-ever demonstration of such reconfigurable waveguide mesh in silicon. We demonstrate a world-record number of functionalities on a single photonic integrated circuit enabling over 30 different functionalities from the 100 that could be potentially obtained with a simple seven hexagonal cell structure. The resulting device can be applied to different fields including communications, chemical and biomedical sensing, signal processing, multiprocessor networks as well as quantum information systems. Our work is an important step towards this paradigm and sets the base for a new era of generic-purpose photonic integrated systems.



# Resumen

---

Los dispositivos integrados de fotónica de microondas ofrecen soluciones optimizadas para los sistemas de información y comunicación. Generalmente, están compuestos por diferentes arquitecturas en las que subsistemas ópticos y electrónicos se integran para optimizar las prestaciones, el consumo, el tamaño y el coste del dispositivo final. Hasta ahora, los circuitos/chips de propósito específico se han diseñado para proporcionar una funcionalidad concreta, requiriendo así un número considerable de iteraciones entre las etapas de diseño, fabricación y medida, que origina tiempos de desarrollo largos y costes demasiado elevados.

Una alternativa, inspirada por las FPGA (del inglés Field Programmable Gate Array), es el procesador fotónico programable. Este dispositivo combina la integración de subsistemas de microondas, ópticos y electrónicos para realizar, mediante la programación de los mismos y sus interconexiones, diferentes funcionalidades. En este trabajo, proponemos por primera vez el concepto del procesador de propósito general, así como su arquitectura. Además, con el fin de diseñar, optimizar y evaluar las prestaciones básicas del dispositivo, hemos desarrollado un modelo analítico extremo a extremo basado en las componentes del campo electromagnético. El modelo desarrollado proporciona como resultado la ganancia, el ruido y el rango dinámico global para distintas configuraciones de modulación y detección, en función de los subsistemas y su configuración. El elemento principal del procesador es su núcleo óptico reconfigurable. Éste requiere un alto grado de flexibilidad y versatilidad para reconfigurar las interconexiones entre los distintos subsistemas y para sintetizar los circuitos para el procesado óptico. Para este subsistema, proponemos el diseño de guías de onda reconfigurables para la creación de mallados bidimensionales. En el marco de esta tesis, hemos propuesto dos nuevos nodos de interconexión óptica para mallas reconfigurables, con el objetivo de obtener un mayor grado de versatilidad. Una vez escogida la malla hexagonal para el núcleo del procesador, hemos analizado la configuración de un gran número de circuitos fotónicos integrados y de funcionalidades de fotónica de microondas. El trabajo se ha completado con la demostración de la primera malla reconfigurable integrada en un chip de silicio, demostrando además la síntesis de 30 de las 100 funcionalidades que potencialmente se pueden obtener con la malla diseñada compuesta de 7 celdas hexagonales. Este hecho supone un record frente a los sistemas de propósito específico. El sistema puede aplicarse en diferentes campos como las comunicaciones, los sensores químicos y biomédicos, el procesado de señales, la gestión y procesamiento de redes y los sistemas de información cuánticos. El conjunto del trabajo realizado representa un paso importante en la evolución de este paradigma, y sienta las bases para una nueva era de dispositivos fotónicos de propósito general.





# Resum

---

Els dispositius integrats de Fotònica de Microones oferixen solucions optimitzades per als sistemes d'informació i comunicació. Generalment, estan compostos per diferents arquitectures en què subsistemes òptics i electrònics s'integren per a optimitzar les prestacions, el consum, la grandària i el cost del dispositiu final. Fins ara, els circuits/xips de propòsit específic s'han dissenyat per a proporcionar una funcionalitat concreta, requerint així un nombre considerable d'iteracions entre les etapes de disseny, fabricació i mesura, que origina temps de desenrotllament llargs i costos massa elevats.

Una alternativa, inspirada per les FPGA (de l'anglès Field Programmable Gate Array), és el processador fotònic programable. Este dispositiu combina la integració de subsistemes de microones, òptics i electrònics per a realitzar, per mitjà de la programació dels mateixos i les seues interconnexions, diferents funcionalitats. En este treball proposem per primera vegada el concepte del processador de propòsit general, així com la seua arquitectura. A més, a fi de dissenyar, optimitzar i avaluar les prestacions bàsiques del dispositiu, hem desenrotllat un model analític extrem a extrem basat en els components del camp electromagnètic. El model desenrotllat proporciona com resultat el guany, el soroll i el rang dinàmic global per a distintes configuracions de modulació i detecció, en funció dels subsistemes i la seua configuració. L'element principal del processador és el seu nucli òptic reconfigurable. Este requerix un alt grau de flexibilitat i versatilitat per a reconfigurar les interconnexions entre els distints subsistemes i per a sintetitzar els circuits per al processat òptic. Per a este subsistema, proposem el disseny de guies d'onda reconfigurables per a la creació de mallats bidimensionals. En el marc d'esta tesi, hem proposat dos nous nodes d'interconnexió òptica per a malles reconfigurables, amb l'objectiu d'obtindre un major grau de versatilitat. Una vegada triada la malla hexagonal per al nucli del processador, hem analitzat la configuració d'un gran nombre de circuits fotònics integrats i de funcionalitats de fotònica de microones. El treball s'ha completat amb la demostració de la primera malla reconfigurable integrada en un xip de silici, demostrant a més la síntesi de 30 de les 100 funcionalitats que potencialment es poden obtindre amb la malla dissenyada composta de 7 cèl·lules hexagonals. Este fet suposa un rècord enfront dels sistemes de propòsit específic. El sistema pot aplicarse en diferents camps com les

comunicacions, els sensors químics i biomèdics, el processat de senyals, la gestió i processament de xarxes i els sistemes d'informació quàntics. El conjunt del treball realitzat representa un pas important en l'evolució d'este paradigma, i assenta les bases per a una nova era de dispositius fotònics de propòsit general.

*Thesis Reviewers:*

Prof. Wim Bogaerts

Prof. Andrea Melloni

Dr. Maurizio Burla

*Thesis Committee*

Prof. Javier Fraile

Prof. Wim Bogaerts

Dr. David Marpaung



# Contents

Contents	xxi
List of Figures	xxv
List of Tables	xxxvii
List of Acronyms	xxxix
Chapter 1 Introduction and Thesis objectives	1
1.1 Application specific vs Application agnostic integrated circuits .....	3
1.2 A Paradigm shift: Greatest challenges .....	6
1.3 Objective and Thesis Structure.....	8
1.3.1 Original contributions of this Thesis:.....	9
Chapter 2 Integrated Microwave Photonics	11
2.1 Introduction .....	11
2.1.1 The fundamentals of Microwave Photonics.....	12
2.2 Historical evolution .....	17
2.3 Technology review .....	18
2.3.1 Technology platforms .....	19
<i>Silicon nitride</i> .....	20
<i>III-V semiconductor compounds</i> .....	21
<i>Summary and Comparison</i> .....	21
2.3.2 State of the Art for integrated Microwave photonics .....	24
Chapter 3 Theoretical aspects of generic MWP Processors	25
3.1 Introduction .....	25
3.2 Generic architecture .....	26
3.3 Analytical modelling .....	29

3.3.1	<i>Direct Detection MWP links/systems</i> .....	30
3.3.2	<i>Self-Beating coherent processors</i> .....	37
3.3.3	<i>End-to-end model</i> .....	50
3.4	Linearization.....	53
3.4.1	<i>Direct Detection end-to end linearization</i> .....	53
3.4.2	<i>Linearization of Self-Beating schemes at the MWP stage employing a Dual Parallel Mach-Zehnder Modulator</i> .....	60
3.5	Implementation of different modes of operation.....	67
3.6	Discussion .....	69
Chapter 4	Optical Core Design for RF-Photonic Processors	71
4.1	Introduction .....	71
4.2	Waveguide mesh design and comparative analysis.....	74
4.3	The hexagonal waveguide mesh optical core.....	91
4.3.1	Finite Impulse Response (FIR) filters .....	91
4.3.2	Infinite Impulse Response (IIR) filters.....	93
4.3.3	Complex multistage filters .....	94
4.3.4	Universal linear optics transformers.....	96
4.3.5	Functional designs for MWP applications .....	101
4.4	The software layer.....	118
Chapter 5	Design, fabrication and demonstrations	121
5.1	Introduction .....	121
5.2	Chip design.....	121
5.2.1	Photonic layer.....	123
5.2.2	Electrical layer .....	128
5.2.3	Thermal isolation layer.....	130
5.3	Chip Fabrication.....	131
5.4	Chip experimental characterization.....	132
5.5	Measurement results.....	136
5.5.1	Finite Impulse Response (FIR) filters .....	138
5.5.2	Infinite Impulse Response (IIR) filters.....	142
5.5.3	Complex tunable and reconfigurable filters .....	145

5.5.4	Multiple input multiple output linear optic transformation devices:	148
5.5.5	Optical Delay Lines:.....	156
5.6	Discussion .....	160
Chapter 6	Summary, Conclusions and Future Work	165
6.1	Summary and Conclusions.....	165
6.1	Future work .....	166
Appendix A	Analytical model of a MWP system/link	171
Appendix B	Reconfigurable optical core algorithms	187
Appendix C	Non-ideal effects in mesh-based circuits	205
	Author's Publication List	210
	References	214





## List of Figures

Figure 1.1 Future communications scenario with embedded RF-photonics systems. The Integrated Microwave Photonic system is labelled as (IMWP). .....	2
Figure 1.2 Programmable signal processors classification: DSP (Digital Signal Processors), FPGA (Field-programmable gate arrays), Reconfigurable waveguide meshes in photonic integrated circuits (PICs), and Few-purpose PICs.....	3
Figure 1.3 Price per chip estimation for an electronic ASIC and FPGA assuming the following figures of Non-Recurring Engineering cost (NRE) and Production Die Cost (PDC). NRE Higher: 1.7 M€, NRE Lower: 0.8 M€; PDC Higher: 6 €, PDC Lower: 2 €; FPGA Higher: 15 €, FPGA Lower: 6 €.....	5
Figure 2.1 Generic microwave photonics system scheme. E/O: Electro-optic conversion, O/E: Optoelectronic conversion.....	12
Figure 2.2 Typical microwave photonics system scheme with the signal frequency characteristics. ....	13
Figure 2.3 Possible Instantaneous Frequency Measurement System (IFM) microwave photonics system scheme with the signal frequency characteristics.....	14
Figure 2.4 Basic MWP link/system and illustration of electrical losses, noise and non-linearities. ....	15
Figure 2.5 Classification of sub-octave and multi-octave MWP systems and links given the highest and lowest frequency (bandwidth). ....	16
Figure 2.6 Proposed layouts for multi-purpose photonic integrated circuits for IMWP operations. ....	18
Figure 2.7 Examples of different cross sections for each technology and typical sizes. ....	19
Figure 3.1 Microwave Photonic Transistor architecture, from [12]. ....	27
Figure 3.2 Generic architecture of a software-defined reconfigurable MWP signal processor. E/O: Electro-optic converter, O/E: Opto-Electronic converter. ....	28
Figure 3.3 Generic architecture of a software-defined reconfigurable MWP signal processor offering signal flow modification.....	29

Figure 3.4 Schematic of a filtered MWP link or MWP system applying Intensity or Phase modulation (inset) with balanced detection scheme, [40].	30
Figure 3.5 (a) Spectral response of a two-tones-test when the input power is increased and (b) typical fundamental and third order intermodulation power levels vs input power for the determination of the $SFDR_3$ .	35
Figure 3.6 Schematic of a Self-beating filtered MWP link or MWP system applying Intensity ODSB or OSSB modulation (inset) with balanced detection scheme, [81].	39
Figure 3.7 (Upper) Schematic diagram of a ring-loaded Mach-Zehnder Interferometer considered as an example. (Lower) Chebyshev Type-II filter implemented by the ring-loaded MZI (filter details in text).	43
Figure 3.8 RF frequency response of the RF Front end obtained by self-beating and single detection.	44
Figure 3.9 Contour plots vs the value of $K_1$ and $K_2$ for the RF Gain (Upper left), Noise Figure (Upper right), $SFDR_2$ (Lower left) and $SFDR_3$ (Lower right) for the tunable RF-front end obtained by self-beating and single detection. System parameters are given in the text with $\alpha_L = 3$ dB and $\alpha_U = 6$ dB.	45
Figure 3.10 RF Gain (upper left), Noise Figure (upper right), Second-order Spurious free dynamic range (lower left) and Third-order Spurious free dynamic range (lower right) vs the value of the couplers $K_1 = K_2 = K$ , taking $\alpha_U$ as a parameter for the tunable RF-front end obtained by self-beating and single detection. System parameters are given in the text.	46
Figure 3.11 RF frequency response of the RF Front end obtained by self-beating and optimum balanced detection ( $K_2 = 0.5$ ).	47
Figure 3.12 Contour plots vs the value of $K_1$ and $K_2$ for the RF Gain (Top left), Noise Figure (Top right), $SFDR_2$ (lower left) and $SFDR_3$ (Bottom right) for the tunable RF-front end obtained by self-beating and balanced detection. System parameters are given in the text with $\alpha_L = 3$ dB and $\alpha_U = 6$ dB.	48
Figure 3.13 RF Gain (upper left), Noise Figure (Upper right), $SFDR_2$ (Bottom left) and $SFDR_3$ (Bottom right) vs the value of the input coupler $K_1$ and taking $\alpha_U$ as a parameter for the tunable RF front end obtained by self-beating and balanced detection ( $K_2 = 0.5$ ).	49
Figure 3.14 Generic concept of a software-defined reconfigurable MWP signal processor.	50
Figure 3.15 Impact of the three terms in Eq. (3.35) on the overall third-order SFDR of the processor.	54
Figure 3.16 Circuit layouts of the three optical filtering subsystems considered: a) FM-DD, b) BPF and c) MZI.	55

Figure 3.17 Transfer function of the three optical filtering subsystems considered as a function of the microwave frequency $f$ : a) FM-DD (up), b) BPF (lower left) and c) MZI (lower right). .....	56
Figure 3.18– SFDR variation as a function of $NF_{RF}$ (left) and as a function of $ H_{eN}(\eta\Omega_1 - \Omega_2) $ , $\eta = \{1,2\}$ , (right), for all the optical filtering subsystems considered: FM-DD, BPF and MZI. ....	58
Figure 3.19 (Upper) Second- and (lower) third-order SFDR variation as a function of $b/a$ for the FM-DD. ....	60
Figure 3.20 Schematic of a Self-beating filtered MWP link or MWP system applying Intensity modulation with a Dual Parallel MZM (inset) with balanced detection scheme. ....	61
Figure 3.21 Photodetected spectrum without (Left) and with the applied linearization (Right). ....	63
Figure 3.22 Case 1. (Upper) Optical penalties vs Electrical Penalties, (Lower) Coupler coefficient vs Electrical Penalty for Case 1 (left) and Case 2 (right). ....	65
Figure 3.23 Generic purpose MWP processor architecture in Electrical/Electrical operation mode. (Left) Processor settings and signal flow, (right) targeted operation scheme. ....	68
Figure 3.24 Generic purpose MWP processor architecture in Electrical/Optical operation mode. (Left) Processor settings and signal flow, (right) targeted operation scheme. ....	68
Figure 3.25 Generic purpose MWP processor architecture in Optical/Electrical operation mode. (Left) Processor settings and signal flow, (right) targeted operation scheme. ....	68
Figure 3.26 Generic purpose MWP processor architecture in Optical/Optical operation mode. (Left) Processor settings and signal flow, (right) targeted operation scheme. ....	69
Figure 4.1 Demonstrated photonic filters allowing pole and zero reconfigurability/tunability. (a) 4-cell based reconfigurable filter [42], (b) 2- and 1-cell reconfigurable filter [82, 19] and (c) 1-cell reconfigurable filter [43]. ....	71
Figure 4.2 Reconfigurable Optical Core implementation based on component switching. ....	72
Figure 4.3 (a) Reck/Miller Triangular arrangement [26, 27], (b) Clements Rectangular arrangement, [88], (c) Square Mesh topology, [51], (d) Hexagonal Mesh Topology [52], (e) Triangular Mesh Topology, [52]. ....	73
Figure 4.4 Reconfigurable Mesh designs (upper): (a) Hexagonal type, (b) triangular type, (c) square type [51], and their associated interconnections points (bottom). .	75
Figure 4.5 (a) (Upper) Labelled schematic of a general tunable coupler acting as the basic building block of the mesh. The Basic Unit Length (BUL) is illustrated as the	

sum of the tunable coupler length and the arc length of the access waveguides. (Lower) Particular case of an integrated balanced MZI-based tunable coupler. (b) Signal flow for the different TBU configuration states..... 75

Figure 4.6 Optical Ring Resonator (left) and Mach-Zehnder Interferometer (right) configurations over a hexagonal mesh (up) and corresponding light paths (bottom). ..... 78

Figure 4.7 Optical Ring Resonator (left) and Mach-Zehnder Interferometer (right) configurations over a triangular mesh (up) and corresponding light paths (bottom). ..... 78

Figure 4.8 (Left) Reconfiguration performance vs available maximum value of  $N$  expressed as an integer number  $n$  of the  $BUL$  for the square, triangular and hexagonal meshes. ORR (upper) and MZI (lower) designs. (Right) Maximum Interferometric length limitation due to accumulated losses (topology-independent and more restricting) and area constrains for each alternative topology..... 80

Figure 4.9 Different mesh types configured to synthesise cascaded ORRs of fixed FSR in different geometries. (Up/left) Hexagonal waveguide mesh programming three cascaded ORRs of 10-BUL cavity length, (Up/Right) triangular waveguide mesh programming two OORs of 6-BUL cavity length and (lower) square waveguide mesh programming five ORRs of 8-BUL cavity length..... 83

Figure 4.10 Access length and angle definition for each mesh: (a) square, (b) hexagonal, (c) triangular. .... 84

Figure 4.11 Relation between the  $BUL$  of a given mesh design to that of the square mesh as a function of the ratio between the access waveguides and the tunable coupler length..... 85

Figure 4.12 Optical Ring Resonator filters with different cavity lengths that can be implemented in a  $5 \times 5$   $BUL^2$  area using the hexagonal, triangular and square mesh designs. ORR  $N$  means an optical ring resonator filter with cavity length of  $N$  BULs. .... 87

Figure 4.13 Spectra of the different ORRs available for each mesh design option. In all the cases, the cavity coupler is adjusted to attain critical coupling. Larger and shorter FSR are highlighted with dashed and dotted lines, respectively, for each mesh. .... 88

Figure 4.14 Mach-Zehnder Interferometer filters with different path length mismatch that can be implemented in a  $5 \times 5$   $BUL^2$  area using the hexagonal, triangular and square mesh designs. MZI  $Z$  means a Mach-Zehnder Interferometer filter with path length mismatch of  $Z$  BULs. .... 89

Figure 4.15 Spectra of the different MZIs available for each mesh design option. In all the cases, the output coupler is 50:50 and the input coupler is adjusted to attain maximal rejection (loss balancing)..... 90

Figure 4.16 FIR filter implementations. (Left) hexagonal mesh setting for (Right) three different targeted UMZI Filters..... 92

Figure 4.17 Cascaded FIR filter implementations: (left) hexagonal mesh setting for (right) two different targeted lattice UMZI Filters of 6<sup>th</sup> and 5<sup>th</sup> order..... 92

Figure 4.18 Single-cavity IIR Filter implementations. (Left) hexagonal mesh setting for (right) three different targeted ORR filters. .... 94

Figure 4.19 (Left) Settings for CROW & SCISSOR filter implementations in the hexagonal mesh core for (right) (a) 10<sup>th</sup>-order CROW, (b) 9<sup>th</sup>-order Single channel SCISSOR, (c) 5<sup>th</sup>-order Double channel SCISSOR, and (e) twisted double channel SCISSOR..... 95

Figure 4.20 Ring-Loaded MZIs: (Left) Hexagonal mesh settings and (right) targeted single-loaded fourth order and double-loaded eighth order filter, respectively. .... 96

Figure 4.21 Universal interferometers: (a) Classical triangular arrangement and (b) hexagonal mesh based implementation of a 4 x4 interferometer. (c) Beamsplitter for the classical approach and (d) corresponding beamsplitter implementation with 3 TBUs for the hexagonal waveguide Mesh. .... 97

Figure 4.22 Universal interferometer: TBU settings of the hexagonal mesh for the Triangular arrangement implementation programming a Hadamard 4x4 linear transformation. ID: TBU identification Label,  $K$ : coupling constant,  $\phi$ : additional phase shift,  $P$ : coupling constant when both phase shifters are unbiased. Green-colour edges for TBUs acting as a tunable coupler and Black-colour for the cross state... 98

Figure 4.23 Universal interferometer: TBU settings of the hexagonal mesh for the rectangular arrangement implementation programming a Hadamard 4x4 linear transformation. ID: TBU identification Label,  $K$ : coupling constant,  $\phi$ : additional phase shift,  $P$ : coupling constant when both phase shifters are unbiased. Green-colour edges for TBUs acting as a tunable coupler, black colour for the cross state and orange colour for the bar state..... 99

Figure 4.24 Universal interferometer: Rectangular arrangement TBU settings on hexagonal mesh based programming a Hadamard 4x4 linear transformation. .... 100

Figure 4.25 Waveguide mesh settings for channel management application: (up) Add-drop configurations for channels 1-4. Channel 5 bypasses the device. (Lower) fully reconfigurable channel management station that allows channel broadcasting, add/drops, channel combinations and demultiplexing. M: Signal monitoring points. .... 101

Figure 4.26 General-purpose photonic integrated processor architecture and candidate fabrication platforms for each subsystem. .... 102

Figure 4.27 True Time delay line implementation for two different techniques: (top) Overlapping group delays of 7 cascaded ORRs, (bottom) SCT technique. The left part depicts the processor configuration and the right part shows the targeted scheme. .... 105

Figure 4.28 General-purpose signal processor configuration for RF filtering implementation (left) based on a self-homodyne modulation/detection scheme (right). The optical filter is composed of six cascaded ORRs defined by a cavity length of 6 BULs. .... 108

Figure 4.29 Linewidth vs maximum frequency of the different demonstrated techniques for optical generation of microwave and millimetre-wave signals, [79]. ..... 109

Figure 4.30 General-purpose signal processor configuration for microwave and mm-wave tone generation based on (upper) External modulator approach, (bottom) Optoelectronic oscillation approach. The right figures illustrate the targeted configuration schemes. .... 111

Figure 4.31 General-purpose signal processor configuration for RF-mixing scheme example (left) for a targeted configuration scheme composed of 2 electrooptic modulators and an optical filter implemented by four cascaded MZIs (right). .... 112

Figure 4.32 General-purpose photonic processor settings for the implementation of Arbitrary waveform generation (left) and targeted system scheme composed of an spectral shaper and a dispersive subsystem (right). .... 113

Figure 4.33 General-purpose photonic processor settings (left) for the implementation of beamforming networks based on discrete optical delay lines with a differential length of  $\Delta L$  (right). .... 115

Figure 4.34 Beamforming networks based on discrete delay line implementation for broadband operation. A differential of  $0.04 \text{ rads}/\pi$  on the y-axis has been applied to improve readability. For this example, we consider a distance between radiating elements  $d = 1 \text{ cm}$ . .... 115

Figure 4.35 Bandwidth vs Error (%) for partially integrated IFM systems demonstrated in the literature. .... 116

Figure 4.36 General-purpose photonic processor settings for the implementation of instantaneous frequency measurement based on ACP function mapping (left) and targeted system scheme (right). .... 117

Figure 4.37 Processor workflow including optional dynamic operation. .... 119

Figure 4.38 Software-definition levels depending on the capabilities of the signal processor to perform configuration and evaluation tasks. .... 120

Figure 5.1 Different layout candidates for the hexagonal mesh-based optical reconfigurable core. .... 122

Figure 5.2 Silicon platform cross-section. Waveguide, thermal tuner, thermal isolation trench. .... 124

Figure 5.3 Photonic layer: (a) Tunable Basic Unit Design: Schematic and (b) GDS layout. .... 125

Figure 5.4 Photonic layer: Fibre-to-chip grating coupler (a) schematic and (b,c) GDS layout..... 126

Figure 5.5 Photonic layer: Test structures schematic for optical properties characterisation. (a) Propagation losses, (b) bend losses, (c) MMI insertion losses, and (d) MMI coupling and insertion losses..... 127

Figure 5.6 Reconfigurable optical core photonic layer: Complete optical layer labelled layout..... 127

Figure 5.7 Reconfigurable optical core electrical layer layout: (a) Internal TBU, (b) external TBU and (c) complete electrical layout..... 129

Figure 5.8 Reconfigurable optical core isolation trenches layout (red-coloured), and metal layer layout (gold-coloured). (Left) Inner TBU distribution, (right) Inner Cell distribution..... 131

Figure 5.9 Fabricated hexagonal waveguide mesh chip. a, Fabricated SOI chip. b, zoomed vision of the 7-cell hexagonal waveguide mesh. c, zoomed image of a single hexagonal cell showing the MZI, tuning heaters and star-type thermal isolation trenches. d, zoomed image of an optical interconnection node of 3 TBUs. e, wire bonded PIC. e, f, Printed circuit board with the waveguide mesh chip mounted and wired bonded..... 132

Figure 5.10 Characterization and measurement setup: (a) Scheme and (b) Lab picture..... 133

Figure 5.11 (Left) Operational window for each test structure and (right) Linear fitting for the passive properties characterisation of specific dies (a) Measured propagation losses, (b) Measured bend losses, (c) Measured cascaded MMIs, (d) Measured distributed MMIs..... 134

Figure 5.12 Characterisation output of a tunable basic unit. Up/Left, Normalised losses versus electrical power applied for each heater. Up/Right, Normalised losses vs electrical current. Bottom/Left, Resistance vs electrical current. Bottom/Right, Coupling Factor vs electrical current..... 136

Figure 5.13 Experimental results for tunable UMZIs of  $\Delta L = 2$  BULs. (a) Waveguide mesh connection diagram, (b) circuit layout indicating the normalized waveguide length in BULs and measured modulus and phase transfer function for (c) different values of the coupling constants  $K_1$  and  $K_2$ , and (d) for fixed coupling factors and active phase shifter tuning..... 139

Figure 5.14 Experimental results for tunable UMZIs of  $\Delta L = 4$  BULs. (a) Waveguide mesh connection diagram, (b) circuit layout indicating the normalized waveguide length in BUL units and measured modulus and phase transfer function for (c) different values of the coupling constants  $K_1$  and  $K_2$ , and (d) for fixed coupling factors and active phase shifter tuning..... 140

Figure 5.15 Experimental results for tunable UMZIs of  $\Delta L = 8$  BULs. (a) Waveguide mesh connection diagram, (b) circuit layout indicating the normalized waveguide

length in BUL units, and measured modulus and phase transfer function for (c) different values of the coupling constants  $K_1$  and  $K_2$ . ..... 141

Figure 5.16 Experimental results for cascaded tunable UMZIs and FIR Filters. Waveguide mesh connection diagram, circuit layout and measured modulus for different values of the coupling constants  $K_1$  and  $K_2$ ,  $K_3$  (and  $K_4$ ) in the case of **a**, two cascaded 2-BUL lattice UMZI filters, including full-FSR tunability (inset); **b**, a 4-BUL UMZI transversal filter. C: Optical Carrier wavelength..... 141

Figure 5.17 Experimental results for 6 BUL ring resonator IIR and FIR+IIR filters. (a) Waveguide mesh connection diagram, (b) circuit layout and measured modulus and phase transfer function for a, (c) IIR filter for different values of the coupling constants  $K_1$  and  $K_2$ , (d), FIR+IIR filter for different values of the coupling constants  $K_1$  and  $K_2$ , (e) IIR filter along a full spectral period for different values of the optical ring resonator round-trip phase shift. .... 143

Figure 5.18 Experimental results for 12 BUL ring resonator IIR filters. (a) Waveguide mesh connection diagram, (b) circuit layout and (c) measured modulus and phase transfer function for different values of the coupling constants  $K_1$  and  $K_2$ . ..... 144

Figure 5.19 Experimental results for 18 BUL ring resonator IIR filters. (a) Waveguide mesh connection diagram, (b) circuit layout and (c) measured modulus and phase transfer function for different values of the coupling constants  $K_1$  and  $K_2$ . ..... 144

Figure 5.20 Experimental results for complex double ring-loaded 6-BUL optical ring resonator filters. Waveguide mesh connection diagram, circuit layout and measured modulus and phase transfer function for a, a 6-BUL double ORR SCISSOR filter and different values of the coupling constants  $k_1$  and  $k_2$ ; b, a 6-BUL double ORR CROW filter and different values of the coupling constants  $k_1$  and  $k_2$ ; c, a 6-BUL double ORR ring-loaded MZI. .... 145

Figure 5.21 Layout of fabricated 7-cell hexagonal mesh and TBU settings (left) for the implementation of 2 cascaded 6 ORRs (up), for the implementation of 2 coupled 6 ORRs (middle) and 3 coupled 6 ORRs (bottom) and its respective Normalized Optical Response (right). The 3-dB bandwidth is indicated for each example. All FSR corresponds to 12.26 GHz. Note that a direct optical-to-radiofrequency conversion has been applied to the frequency axis. SLL: Side Lobe Level. C: Optical Carrier ..... 147

Figure 5.22 Experimental (solid-line) and theoretical (dashed-line) results for 6-BUL ring resonator IIR filter. 2 cascaded 6 ORRs transmission response and associated group delay..... 147

Figure 5.23 Experimental results for the hexagonal waveguide mesh configuration of a 3 x 3 interferometer based on a triangular arrangement. (a) Hexagonal core settings for 1-3 input mode swapping unitary transformation (CS = TBU in cross state, BS = TBU in bar state, TC = TBU in tunable coupler state, AV = TBU not employed), (b): circuit layout of the implemented interferometer, (c) spectral measurement of all



input/output port connections, (d) normalized bar diagram of the resulting measured unitary matrix for  $\lambda = 1571$  nm. .... 149

Figure 5.24 Experimental results for the hexagonal waveguide mesh configuration of a 3 x 3 interferometer based on a triangular arrangement. (a) Hexagonal core settings for 1-2, 2-3 and 3-1 input mode swapping unitary transformation. (CS = TBU in cross state, BS = TBU in bar state, TC = MZI in tunable coupler state, AV = TBU not employed), (b): circuit layout of the implemented interferometer, (c): Spectral measurement of all input/output port connections. (d) Normalized Bar diagram of the resulting measured unitary matrix for  $\lambda = 1571$  nm. .... 150

Figure 5.25 Pauli-Z 2 x 2 transformation experimental results involving complex-valued matrix coefficients using the hexagonal waveguide mesh, (a): 7-cell configuration (CS = MZI in cross state, BS = MZI in bar state, TC = MZI in tunable coupler state, AV = MZI not employed, PS = Phase shifter), (b) circuit layout of the implemented interferometer, (c) spectral measurement of all input/output port connections, (d) normalized bar diagram of the resulting measured unitary matrix for  $\lambda = 1571$  nm..... 151

Figure 5.26 Pauli X and Pauli Y 2 x 2 transformations experimental results involving complex-valued matrix coefficients using the hexagonal waveguide mesh, (a) 7-cell configuration (CS = TBU in cross state, BS = TBU in bar state, TC = TBU in tunable coupler state, AV = TBU not employed, PS = Phase shifter), (b): circuit layout of the implemented interferometer, (c): spectral measurement of all input/output port connections, (d) normalized bar diagram of the resulting measured unitary matrix for  $\lambda = 1571$  nm..... 152

Figure 5.27 Hadamard 2 x 2 transformation involving complex-valued matrix coefficients using the hexagonal waveguide mesh. (a) 7-cell configuration (CS = MZI in cross state, BS = TBU in bar state, TC = TBU in tunable coupler state, AV = TBU not employed, PS = Phase shifter), (b) circuit layout of the implemented interferometer, (c) spectral measurement of all input/output port connections, (d) normalized bar diagram of the resulting measured unitary matrix for  $\lambda = 1571$ nm. .... 153

Figure 5.28 Identity transformation configuration of a 4 x 4 interferometer based on a rectangular arrangement. (a) 7-cell configuration (CS = TBU in cross state, BS = MZI in bar state, TC = TBU in tunable coupler state, AV = TBU not employed), (b) circuit layout of the implemented interferometer, (c) spectral measurement of all input/output port connections, (d) normalized bar diagram of the resulting unitary matrix for  $\lambda = 1571$  nm..... 154

Figure 5.29 C-NOT transformation configuration of a 4 x 4 interferometer based on a rectangular arrangement. (a) 7-cell configuration (CS = TBU in cross state, BS = MZI in bar state, TC = TBU in tunable coupler state, AV = TBU not employed), (b) circuit layout of the implemented interferometer, (c) spectral measurement of all input/output port connections, (d) normalized bar diagram of the resulting unitary matrix for  $\lambda = 1571$  nm..... 155

Figure 5.30	SWAP transformation configuration of a 4 x 4 interferometer based on a rectangular arrangement. (a) 7-cell configuration (CS = TBU in cross state, BS = MZI in bar state, TC = TBU in tunable coupler state, AV = TBU not employed), (b) circuit layout of the implemented interferometer, (c) spectral measurement of all input/output port connections, (d) normalized bar diagram of the resulting unitary matrix for $\lambda = 1571$ nm.....	156
Figure 5.31	Measured time response of an ORR corresponding to 6 BULs. Each figure corresponds to a different coupling factor. The inset shows the corresponding spectral response. (Top/left) the tunable coupler is in bar state so no signals travel through the cavity, (Top/right) the tunable coupler sets a coupling ratio below the critical coupling of the cavity, (Bottom/left) the tunable coupler sets the critical coupling condition in the cavity, (Bottom right) the tunable coupler sets an over-coupling condition in the cavity. ....	157
Figure 5.32	Measured time response of a MZI corresponding to 4 BULs. Each figure corresponds to a different input coupling factor and a fixed value of 50:50 for the output coupler division factor. The inset shows the corresponding spectral response. (Top left) The input tunable coupler introduces more power in the shortest path to obtain a difference of 20-dB at the MZI output, (Top right) the input tunable coupler introduces more power the shortest path to obtain a 5-dB difference at the MZI output, (Bottom left) The input tunable coupler sets the critical coupling condition in the MZI to obtain equal power contributions at the output, (Bottom right) the tunable coupler introduces more power to the long path. ....	158
Figure 5.33	Discrete optical delay lines. (Left) 7-cell layout and settings for two different time delays. (Right) Measured delays up to 12 BULs. ....	159
Figure 5.34	Measured optical beamformer network: (a) 2-BUL delay, (b) 3-BUL delay. ....	160
Figure 5.35	Electrical ports vs number of cells for 2 different ground configurations. (Up), Single-Point Ground. (Bottom), Common Ground.....	162
Figure 5.36	Synthesized waveguide losses impact due to: (a), MMI Insertion Losses for propagation losses of 2.5 dB/cm. (b), propagation losses for a fixed MMI IL of 0.15 dB. (c), discretization due to Basic Unit Length variation and relative path losses. ....	163
Figure 6.1	5.5 x 11 mm <sup>2</sup> optical layout of a hexagonal waveguide mesh to be integrated in Si <sub>3</sub> N <sub>4</sub> at VLC Photonics – CNM Platform. (Black) optical layer, (copper-coloured) metal layer, (red) thermal isolation layer.....	168
Figure 6.2	Optical core power consumption estimation vs average TBU power for the synthesis of circuits involving 50, 100 and 200 TBUs assuming a $P_{\pi}$ of: (left) 10 mW and (right) 1 mW. A green area between 40-60 % of the average TBU power represents typical feeding values depending on the synthesised circuit.....	168





## List of Tables

Table 1.1. Number of different devices that can be configured for each mesh design .....	5
Table 2.1. Qualitative comparison and availability of different basic building blocks for each integration platform. WG: Waveguide, PD: Photodetector, MOD: Modulator.....	22
Table 2.2. Comparison and availability of different phase modulators for each integration platform. AV/CMP: Availability/Compactness, (-) No, ~ on-going research. TBD: To Be Determined.....	23
Table 3.1 – Overall FOM computed values for the three optical filtering subsystems considered .....	58
Table 4.1 – Values for the possible cavity lengths (ORR) and arm length mismatch (MZI) in BUL units for the different mesh designs, $n \in \mathbb{N} \{0,1,2,\dots\}$ for MZIs and $n \in \mathbb{N} \{1,2,3,\dots\}$ for ORRs. ....	79
Table 4.2. Number of different devices that can be configured for each mesh design .....	82
Table 4.3. Summary of values for the figures of merit of the different mesh designs .....	86
Table 4.4. Frequency grid associated to 4 different BULs. The interferometric structure available for the hexagonal core is also indicated. ....	103
Table 5.1. Main characterization figures.....	135
Table 5.2. Frequency grid associated to the fabricated BULs. The interferometric structure available for the hexagonal core is also indicated. ....	137



## **List of Acronyms**

ACF: Amplitude Comparison Function

ASPIC: Application Specific Photonic Integrated Circuit

BD: Balanced Detection

BUL: Basic Unit Length

CROW: Coupled-Resonator Optical Waveguides

DD: Direct Detection

DFB: Distributed feedback laser

DSP: Digital Signal Processor

E/O: Electrooptic

FIR: Finite Impulse Response

FPGA: Field Programmable Gate Array

GFM: Generic Foundry Model

GIM: Generic Integration Model

IFM: Instantaneous Frequency Measurement

IIR: Infinite Impulse Response

IM: Intensity Modulation

IMWP: Integrated Microwave Photonics

InP: Indium Phosphide

MMI: Multimode Interferometer

---

MWP: Microwave Photonics

NF: Noise Figure

MZI: Mach-Zehnder Interferometer

ODL: Optical Delay Line

O/E: Optoelectronic

OIP: Optical Interception Point

ORR: Optical Ring Resonator

ORSE: Optical routing and switching elements subsystems

PIC: Photonic Integrated Circuit

PM: Phase Modulation

RF: Radiofrequency

SCISSOR: Side-Coupled Integrated Spaced Sequence of Resonators

SCT: Separate Carrier Tuning

SOI: Silicon on Insulator

SFDR: Spurious Free Dynamic Range

SWaP: Space, Weight and Power consumption

TBU: Tunable Basic Unit



# Chapter 1

## Introduction and Thesis objectives

It has been only seventy years since the invention of the first solid-state transistor, but it is already hard to think about our contemporary world without electronics. Deeply embedded, a myriad of transistors are nowadays grouped together into a single electronic integrated circuit enabling signal processing and computing operations. This sets a perfect example of how a technological invention has the powerful ability to change our lifestyle. These electronic small processors are the basic building block of bigger systems and subsystems covering countless research areas such as the telecommunications and information science, computing, biotechnology, biomedicine and astrophysics.

However, for certain applications, electronics by itself might be near its operational limits as regards to scalability and speed, [1]. In the case of communications, the Internet core relies on photonic systems to match the continuously growing demand for bandwidth and capacity. These photonic systems have been relentlessly incorporated to cover nearly the end-to-end architecture of the communications network. Whereas electronics and radiofrequency (RF) applications depend on the *fermion* properties of electrons, the *boson* character of photons unleashes unprecedented capabilities in terms of low propagation losses for extremely larger bandwidths and distances, electromagnetic-immune systems and improved performance.

Within the particular context of communication applications, the emergence of new paradigms, such as 5G wireless systems [2, 3, 4], smart cities [5, 6], the Internet of Things [7], and advanced civil radar systems [8], will call for a new approach in the design of radio access networks. In particular, future wireless networks will need to satisfy two fundamental requirements. First, the need to accommodate unprecedented data bit rates per end user (for instance, 5G targets up to 10 Gb/s per user). Second, they will need to cope with an ever-increasing number of simultaneous wireless connections, for instance man–man, man–machine and machine–machine

communications, smoothly interfacing them with the core optical fibre transport network. Addressing these challenges requires the use of radiofrequency carriers with higher frequencies and smaller coverage cells (that is, pico and femto-cells) serviced by base stations with smaller antennas. It will also require the extension of the photonic segment of the network (that is, the optical fibre) into wireless base stations. A key to success will be the realization of a smooth, broadband and upgradable interface between the radio and the photonic parts of the access network. Microwave photonics (MWP) is the natural option for this interface, [3, 9, 10, 11, 12, 13, 14, 15]. It enables the generation, processing and distribution of microwave and millimetre-wave signals by optical means, benefiting from the unique aforementioned advantages inherent to photonics. Figure 1.1 depicts a possible future communication scenario where the MWP systems are embedded.

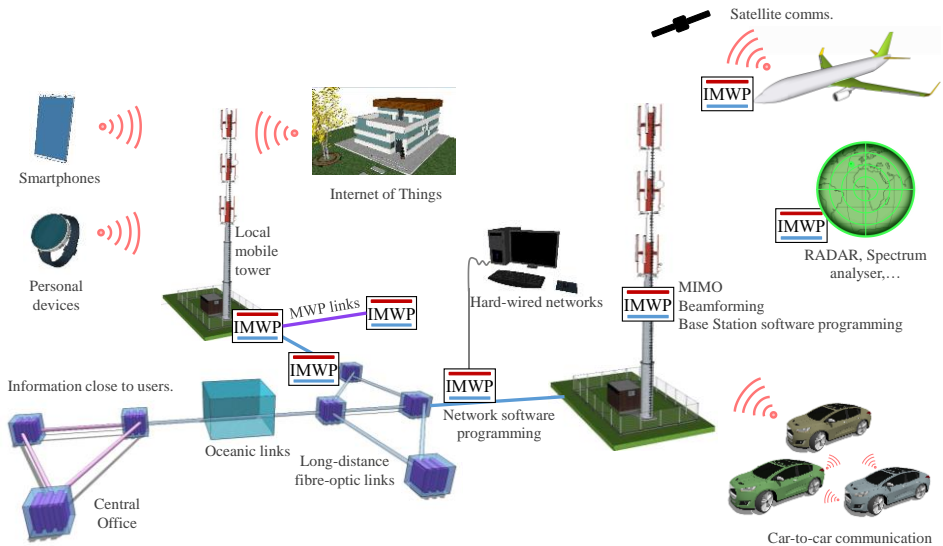


Figure 1.1 Future communications scenario with embedded RF-photonics systems. The Integrated Microwave Photonic system is labelled as (IMWP).

Until recently, the applicability of MWP has been limited by the high cost, bulky size and power-hungry nature of the constituent systems. The emergence of integrated microwave photonics (IMWP) is changing this situation by integrating MWP components and/or subsystems in miniature monolithic or hybrid photonic circuits, [13, 16, 17, 18, 19, 20]. IMWP has the potential to change the power scaling laws of high-bandwidth systems through architectures that combine photonics with electronics to optimize performance, power, footprint and cost. IMWP has focused so far on the so-called application specific photonic integrated circuits (ASPICs),

where a particular circuit is designed to perform a specific MWP function, [16, 18, 21, 22, 23]. This trend is leading to fragmentation, where the number of technological solutions almost equals the number of required applications.

A radically different approach is to design a generic-purpose MWP signal processor that can be integrated on a chip and programmed to perform a variety of functions. This concept is inspired by field-programmable gate arrays (FPGAs) in the world of electronics, where a common hardware platform, or processor, is reconfigured by software to perform a multitude of tasks, [24, 25]. Such a processor should bring greater flexibility and reductions in space, weight, power and cost compared with existing ASPICs. Figure 1.2 classifies several types of programmable processors depending on the nature of the components present within them.

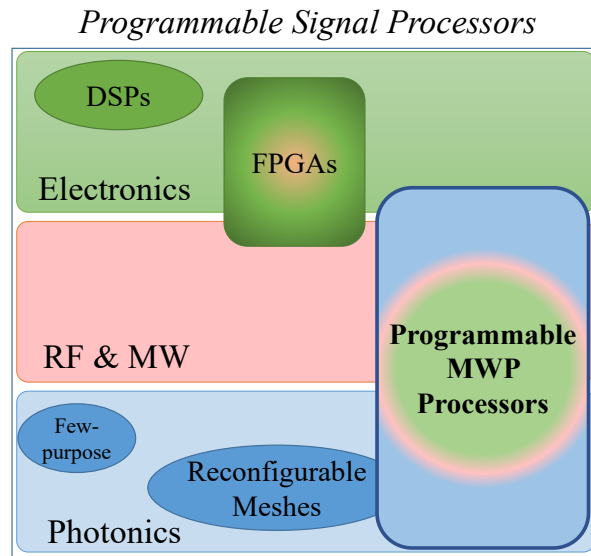


Figure 1.2 Programmable signal processors classification: DSP (Digital Signal Processors), FPGA (Field-programmable gate arrays), Reconfigurable waveguide meshes in photonic integrated circuits (PICs), and Few-purpose PICs.

### 1.1 Application specific vs Application agnostic integrated circuits

The advantages of designing application agnostic photonic chips that can be programmed for a wide variety of functionalities after fabrication can be anticipated by comparison with its electronic counterpart.

In electronic custom designs where an optimum process is developed to meet a set of specific requirements, the time to market is mainly limited by an extensive manufacturing effort, taking several months (typically 9-12 months). These designs are associated to a high non-recurring engineering (NRE) cost, which refers to the one-time cost devoted to research, design, development and testing of an specific new product. Depending on the required customisation degree and circuit complexity, this overhead cost typically ranges from 200,000 to 2,500,000 €. Since the final price depends on the design performance and complexity, it is not possible to give a narrow price range for comparison purposes. This complexity depends on the chip requirements in size, temperature range, additional grades (military medical, high-reliability, radiation hardening), the application area, the pin counts, the clock speed, the operating voltage, the RAM size, the Electrically Erasable Programmable Read-Only Memory (EEPROM) size, the circuitry complexity, the analogue circuitry content complexity, the number and rates of Analogue-to-Digital Converters and Digital-to-Analogue Converters, as well as the packaging. The final unit cost will include the production die cost of each chip (about 1-10 €) and the NRE cost divided by the number of manufactured units.

In contrast, non-specific programmable electronic circuits, in general, and FPGAs in particular, are circuits that present a final logic structure that can be configured by the end user to meet the application requirements after fabrication. These programmable devices enable reaching the market with new products in the shortest possible time, which is essential for a new product to be competitive. In this way, they provide instant development with negligible NRE cost, providing a more competitive final unit cost at low and medium volumes than ASICs. Missing the market window actually translates into a cost. System reconfigurability has an impact on cost, since it enables the extension of this market window. Considering the total cost of FPGAs, as in ASICs, depends on the particular FPGA type along with its performance characteristics and capabilities. In this sense, the unit costs (only FPGA die) ranges from 2 up to 10 € for flash-based and SRAM-based FPGA solutions. Additional support circuitry increases the total cost depending on the type, the requirements (analogue, digital, both), and the chip area.

As an approximation to a quantitative example, we analyse in Figure 1.3 the impact of NRE cost on the final price per chip, for the following NRE and Production Die Cost (PDC) prices: NRE Higher: 1.7 M€, NRE Lower: 0.8 M€; PDC Higher: 6 €, PDC Lower: 2 €; FPGA Higher: 15 €, FPGA Lower: 6 €. Although these prices are design-variable, the comparative study is useful to understand the order of magnitude of the number of fabricated units and the final chip price relation. Figure 1.3, illustrates that for a low manufacturing volume (< 70,000 Units), the FPGA results in a more cost-effective solution. The crossover volume is expected to move even higher for each technology advance.

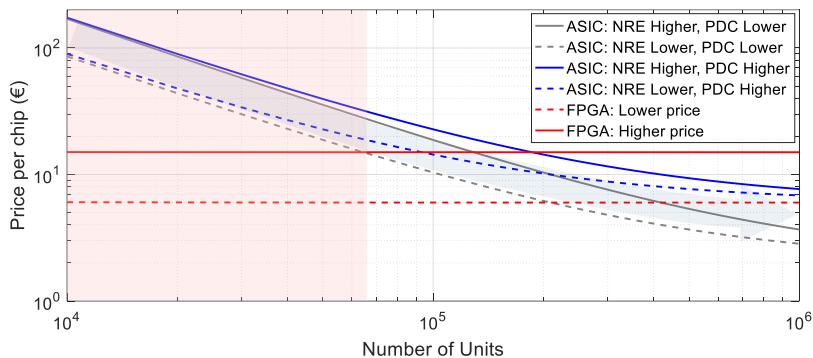


Figure 1.3 Price per chip estimation for an electronic ASIC and FPGA assuming the following figures of Non-Recurring Engineering cost (NRE) and Production Die Cost (PDC). NRE Higher: 1.7 M€, NRE Lower: 0.8 M€; PDC Higher: 6 €, PDC Lower: 2 €; FPGA Higher: 15 €, FPGA Lower: 6 €.

Although, as mentioned before, the chip complexity and final requirements will have an impact on the time to market, the cost and the performance, these basic figures can be qualitatively summarised in Table 1.1.

Table 1.1. Number of different devices that can be configured for each mesh design

	<b>ASIC</b>	<b>FPGA</b>
Time to Market	Slow	Fast
Non-Recurring Engineering	Very High	Low
Unit Cost	Low	Medium
Design Flow	Complex	Simple
Performance	High	Medium
Application Flexibility/Versatility	Very low	High
Power consumption	Low	High
Size	Low	Medium

The previous analysis can be translated to the field of photonic integrated circuits to envision the characteristics of application-specific devices versus programmable devices. Like in the electronic field, ASPICs are the most efficient solution in terms of power consumption, footprint and optical power transmission for a certain single application or functionality. As illustrated for the electronics custom-design case, the overhead cost given by the design and the long-time development that includes many

costly fabrication iterations are the main drawbacks of the manufacturing process. This fact is even more pronounced in the photonic field, where less mature technologies and design processes, as well as the lack of full-standard procedures and a wide offer of complex building blocks lead to a more expensive NRE cost.

Once fabricated, custom designs only perform one single (two or three in the best cases) functionality(ies), limiting the number of fabricated units and resulting in a solution far from being cost-effective for most applications.

A promising solution is the fabrication of a programmable photonic integrated circuit, where a common hardware is configured by the user during application time by means of a software layer configuration. Inspired by the FPGAs, DSPs and electronic microcontrollers, the photonic programmable device is envisioned to reduce the final cost per chip compared to an ASPIC solution, while offering invaluable flexibility and versatility required for the future photonic systems.

In addition, these photonic systems would bring unprecedented capabilities to photonics like instant prototyping, ready-to-use chips, upgradable and updatable photonic circuits that could be remotely controlled/reconfigured and even self-healing photonics circuits.

## **1.2 A Paradigm shift: Greatest challenges**

The surge of programmable photonics does not imply the extinction of ASPICs in the same way as ASPICs have not been extinct by programmable electronics. The mass production of software-defined PICs with non-specific functionalities is envisioned to enable the spread of photonics, offering cost-effective photonic-based solutions with unprecedented capabilities.

However, these results previously require the problem-solving associated to several questions inherent to photonic integrated circuits that are even exacerbated when designing programmable integrated photonic devices, and the apparition of new ones:

*Lack of a versatile/programmable high-level design:* As mentioned, the photonic IC community has focused on application specific circuits. Back to the starting date of this work, no generic-purpose PIC architecture had been either proposed or demonstrated. Remarkable pure-photonics universal devices for unitary [26] and linear operations [27] have been proposed, and are a good example of programmable photonic circuits. A complete top-level design is required, in order to demonstrate versatility and performance for the typical RF-photonics and pure-photonic applications.

*Overall link losses:* One of the main drawbacks of photonic circuits applied to microwave photonic operations are the optical link losses that are mainly limited by the conversion losses at the modulation and photodetection stages. Typical values of microwave photonic links that range from 30 to -30 dB have been demonstrated over the last 20 years, [28, 29]. The fully integration of the typical components/subsystems in a MWP link/system in a monolithic or hybrid platform has not been achieved, and their performance is not yet as mature compared to the discrete and heterogeneous counterpart solutions, leading to losses between -20 and -40 dB. Moreover, designing a non-specific purpose structure comes at the expense of adding additional blocks and increasing insertion losses, since the circuit has not been optimised for a single application. Further research on developing more efficient integrated modulators and photodetectors is required, although integrated optical amplification stages can be employed for certain platforms like indium phosphide and its hybrid combination in silicon.

*Power consumption:* This figure is one of the most important in application specifications. The integration of microwave photonic systems offers by itself a reduction of the power consumption, since the thermal control unit is shared by all the subsystems inside the chip. In the same way as an FPGA, these devices are envisioned to consume more than their application-specific counterpart. For example, the addition of a more complex electronic IC to initialise, characterise and reconfigure the photonic IC will increment this figure. A figure below 3 W for all the microwave photonic system would be an excellent starting point.

*Photonics active and passive element integration:* This research area has gained attention from the scientific community and several companies in the field. Nowadays, there is not a perfect monolithic integration platform capable of providing optimum performance in passive integration and active integration. The weaknesses of each platform have move the community to hybrid designs in order to combine the strongest points of different integration materials.

*Lack of a software layer:* Since ASPICs can survive without the inclusion of a complex software layer design, very few efforts have been made on photonic reconfiguration algorithms, generic photonic systems modelling and subsystem management. However, several algorithms are currently available for the design and optimization of common structures like optical filters, [30, 31, 32] and universal couplers [33, 34, 27] that could be translated to a programmable photonic circuit. Once a generic-purpose architecture is proposed, the development of a group of algorithms for characterisation, reconfiguration and dynamic optimization is mandatory. In this sense, the final design might require monitoring points that will serve as the optimization algorithm input.

### 1.3 Objective and Thesis Structure

The research work presented within the framework of this Ph.D. Thesis has been developed in the Photonics Research Labs, a part of the iTEAM Research Institute at the Universitat Politècnica de València. The thesis activities are focused on the concept proposal, theoretical analysis and experimental demonstration of generic-purpose integrated programmable photonic processors. The achievement of the thesis objectives relies on a sequential order that attempts to follow the natural design process of a new technological development, from the first concept and architecture proposals in Chapter 3, to the final experimental validations in Chapter 5.

Chapter 2 includes a review of Integrated Microwave Photonics research. It covers the basics, the historical evolution, the analysis of the available material platforms and the current state-of-the-art, which is essential to understand the strengths and weaknesses of the available material platforms for photonic chip integration.

Chapter 3 deals with the definition and the proposal of an architecture for the first generic-purpose MWP processor. A field-based end-to-end modelling is fully developed for several modulation/detection schemes. This analytical model is a powerful design tool that computes figures of merit accounting for overall radiofrequency gain, noise figure and dynamic range and can be employed for both the processor design and for its future evaluation.

After reviewing some of the possible architecture implementations for the optical core of the photonic processor, Chapter 4 includes a deep analysis of the most flexible approach, which is based on tunable-coupler waveguide meshes. The mesh-based design is presented considering its historical aspects, definitions and topologic comparative analysis. The hexagonal topology, proposed in the framework of this Thesis, is chosen as the most versatile one and the settings for several photonic integrated circuits that can be programmed over this mesh are presented. This chapter ends with the complete processor configuration for the implementation of the main MWP functionalities.

In order to demonstrate experimentally the general-purpose photonic processor core, Chapter 5 covers the fabrication, testing and measurements of a hexagonal-mesh based architecture integrated in silicon-on-insulator. The presented device is the first integrated hexagonal-mesh-based generic-purpose photonic processor core and the most complex to date. It is composed of seven hexagonal cells and is potentially able to perform over 100 different flexible photonic integrated circuits configurations. These photonic integrated circuits were fabricated at the Optoelectronic Research Centre (ORC) of the University of Southampton.



---

Since software-defined photonic processors are envisioned to potentially spread the market of photonics, we address in Chapter 6 the necessary future work required to produce a fully integrated version of the general-purpose photonic processor, together with the summary and conclusions of this Thesis.

### 1.3.1 Original contributions of this Thesis:

- In this thesis, we propose the new concept of generic-purpose software-defined integrated MWP photonic processor. Being a radically different approach from ASPICs, this new PIC class enables the programmability of the main MWP functionalities on the same hardware platform.
- We present the photonic processor system architecture together with a full end-to-end model for the future evaluation of the main figures of merit: RF gain, noise figure and dynamic range. It allows the complete system evaluation and provides, at the same time, a powerful tool to properly design and programme the photonic processor. Some examples of operational modes are outlined for the processor configuration.
- The generic-purpose photonic processor relies on a powerful and versatile optical core to perform the reconfigurable optical interconnects and the photonic filtering tasks. Chapter 4 is focused on this key subsystem. We believe that reconfigurable waveguide lattice meshes [40, 41] are optimal candidates for the optical core of the photonic processor, since they provide the required versatility. In that chapter, we propose two alternative lattice topologies to the existing square mesh design: the hexagonal and triangular waveguide meshes. We present an extensive analysis of the three mesh topologies and define several figures of merit that account for photonic integration efficiency and versatility when programming PICs: flexibility, switching elements per area and reconfiguration performance. We obtain as a result that the hexagonal mesh topology outperforms both the square and triangular meshes. We illustrate the processor configuration, whose optical core is based on a hexagonal waveguide mesh, for several MWP functionalities like RF and optical filtering, instantaneous frequency measurement, optical beamforming, arbitrary signal generation and frequency mixing.
- In Chapter 5, we present the design, fabrication and testing process of the first integrated hexagonal waveguide lattice mesh. This 7-cell layout integrated on silicon achieves, to the best of our knowledge, several records beyond the current state of the art. First, it is the first integrated hexagonal mesh ever reported. Secondly, it is the mesh-based PIC with a higher cell count number: Whereas the previous one integrated 2 square cells (7 Tunable Basic Units), our design features 7 hexagonal cells (30 Tunable Basic Units). Finally, this higher cell count number allows the demonstration of a record

number of 30 different functionalities, which is only limited by the current sources available at the moment of measurement (18 current sources). With 12 additional current sources, we estimate that over 100 different functionalities can be programmed in our fabricated PIC. Moreover, our optical core enables for the first time the synthesis of filtering structures like Optical Ring Resonators (ORRs) and MZIs as well as the universal interferometers. The latter enable the synthesis of any operation defined by a linear unitary matrix of size limited by the number and distribution of the cells. Here, we are able to synthesize the two arrangements proposed for this linear operation: the triangular beamsplitter and, for the first time, the rectangular beamsplitter.

# Chapter 2

## Integrated Microwave Photonics

### 2.1 Introduction

Microwave photonics (MWP) is an area of research that leverages the unique properties of photonic devices and systems to generate, process and distribute RF, microwave and millimetre-wave signals with unprecedented performance. MWP systems benefit from specific properties of optical systems, including low loss (independent of frequency), high bandwidth, immunity to electromagnetic interference and multiple-input multiple-output parallel processing to enable the realization of key functionalities that are either complex, or even not directly possible, in the radiofrequency domain, such as filtering, arbitrary waveform generation, frequency up/down conversion and instantaneous measurement, [9]. These systems have been thoroughly studied for the last 50 years regarding both radio-over-fibre signal distribution and advanced signal processing in form of bulky fibre-based systems and, more recently, integrated on chips as introduced in Chapter 1, [16, 14].

MWP systems aim to interface the microwave and the photonic domains as depicted in Figure 2.1. They are typically at the heart of analogue signal processing engines that are placed in between the signal acquisition devices and the front-end digital signal processors (DSPs) to accommodate the signal formats to the constraints imposed by the DSP limited sampling rates.

These applications entail the realization of a wide variety of functionalities. Typical space, weight and power consumption (SWaP) figures for commercial MWP systems are around 0.04-0.2 m<sup>2</sup> in size, 1.5-10 kg in weight and 15-20 W in power consumption [35], making them unsuitable for the mass production and widespread use required by the next generation of emerging applications. Hence, despite the tremendous potential of MWP unveiled by future information and communication systems and networks, the widespread use and application of this technology is currently limited by the high-cost, bulky, complex and power consuming nature of its systems. The major challenge that MWP researchers have to overcome is therefore related to the reduction of SWaP figures. Solving this problem is a major challenge for the photonics research community with expected considerable scientific, technical and economic impacts.

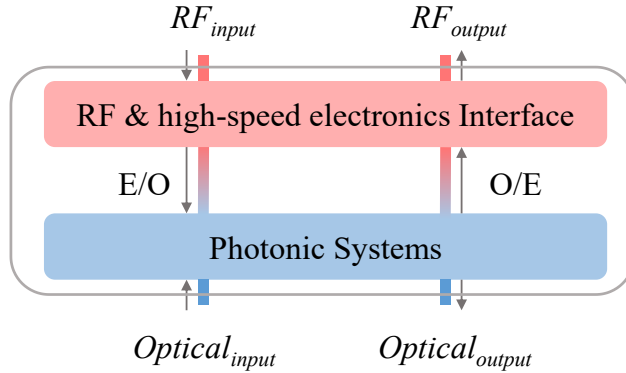


Figure 2.1 Generic microwave photonics system scheme. E/O: Electro-optic conversion, O/E: Optoelectronic conversion.

Integrated photonics has the potential to change the power scaling laws of high-bandwidth systems through proper architectural choices that combine photonics with electronics to optimize performance, power, footprint, and cost [36, 37]. In particular, analogue photonics has a qualitatively different behaviour compared to digital electronics since the energy per analogue task is dominated by the steady-state bias power and does not increase significantly as the bandwidth increases [36]. Furthermore, most photonic devices are currently highly temperature dependent and therefore, temperature regulation is required, which consumes the majority of bias power. As integrated photonics favours alternative means of temperature control that draw less power, the power consumed by the photonic devices can be reduced drastically. Integrated Microwave Photonics (IMWP) [16] aims at the incorporation of MWP components/subsystems in monolithic or hybrid photonic circuits and is instrumental to achieve the aforementioned evolution objectives.

### 2.1.1 The fundamentals of Microwave Photonics

Depending on the targeted functionality/application, different architectures can be employed for a photonic-assisted RF circuit. Typically, they employ an optical transmitter (composed of one or various optical sources driven by a common electro-optical modulator) and an optical receiver (composed of one or various photodetectors) acting as opto-electronic converters, as well as a photonic core circuit that performs the specific processing in the optical domain. Some of them require electronics and radiofrequency systems to drive the electro-optical modulators and/or signal amplification, either in the optical or in the radiofrequency stage, to overcome conversion losses.

As illustrated in Figure 2.2, the typical performance of a MWP link or system can be described in the following terms: first, the input RF signal modulates a continuous-wave optical carrier by an electro-optic modulator, so the input signal frequency is up-converted to optical frequencies around 194 THz. Next, an optical core performs the photonic signal processing. The architecture of the optical processing core is often developed by a specific photonic waveguide layout designed to perform the targeted operation. Finally, the processed optical signal is photo-detected and down-converted to the RF domain in the photodetector.

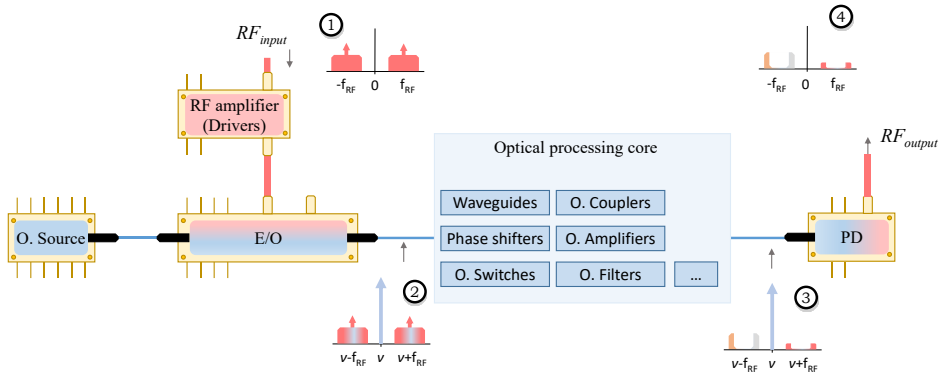


Figure 2.2 Typical microwave photonics system scheme with the signal frequency characteristics.

In order to illustrate the basics of a MWP system, we can introduce one of the main MWP applications: RF-photonics filtering. In this case, the input signal (Point 1, Figure 2.2) is the RF signal that will be filtered in the frequency domain. This signal is modulated by an external modulator translating the input signal to optical frequencies determined by the optical power source (Point 2, Figure 2.2). In this case, the optical processing core implements an optical frequency filter. For example, this building block can be developed by the interference produced by combining the signal propagating through different waveguide lengths or by combining a larger number of copies of the signal coming from resonant structures. The characteristics of the top-level layout and the technology platform will determine the optical filter specifications (insertion losses, shape, extinction ratio, free spectral range, etc.). The photodetector translates a copy of the filtered signal to the RF domain. Both frequency domain conversion losses introduce extra losses of around 20 - 40 dB that will limit the circuit operation. Most of demonstrated circuits employ external amplification with Erbium Doped Fiber Amplifiers (EDFAs) or integrated Semiconductor Optical Amplifiers (SOAs) that give up to 20-dB amplification. When

compared to pure electronic solutions, RF-photonics filters are able to work at higher frequencies and several designs allow reconfigurability and tunability.

Another MWP functionality is the Instantaneous Frequency Measurement (IFM). This application consists in determining the frequency from an unknown input RF tone. Although two approaches have been proposed for this purpose, relying on non-linear processing [38] and employing complementary optical filters [23, 39], here we illustrate in Figure 2.3 the latter. In this case, a Dual Side Band – Carrier Suppressed modulation (DSB-CS) carrying the tone information goes through a complementary optical filter. Both outputs are photodetected and combined to form the amplitude comparison function (ACF). This ACF function maps directly to the RF frequency tone independently from the RF input power. Depending on the filter characteristics a trade-off appears between frequency resolution and operational frequency range. Compared to the pure electronics counterpart, some features stand out: reduced measurement error (below 2%), increased frequency range and high-frequency performance.

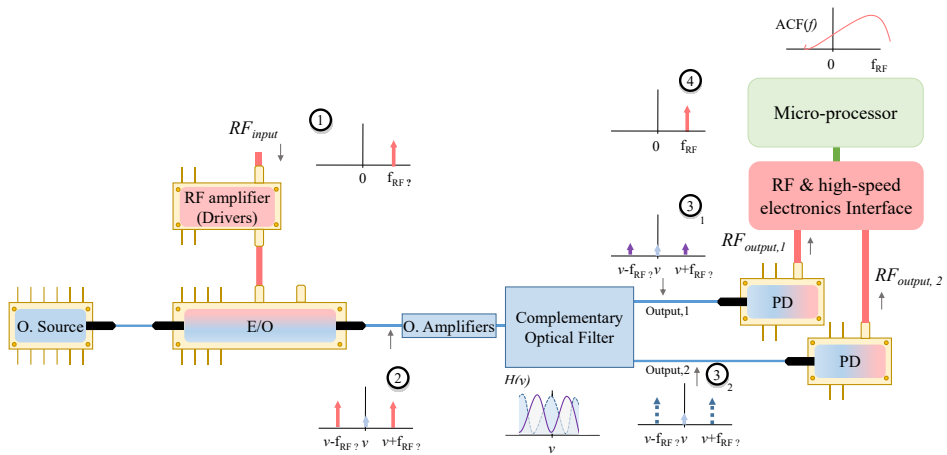


Figure 2.3 Possible Instantaneous Frequency Measurement System (IFM) microwave photonics system scheme with the signal frequency characteristics.

Despite the two previous examples, not all the functionalities deal with the processing of RF signals in the optical domain. In this sense, a consolidated number of application addresses the generation of RF and millimetre wave signals. In this case, the aim is to produce high-quality and high-frequency tones or arbitrary waveform signals.

The aforementioned MWP functionalities are explained in more detail in Chapter 4.

The typical specifications of a MWP system are application-variable. However, their performance is commonly evaluated in terms of a set of figures of merit (FOM) employed for pure microwave links/systems: the radiofrequency gain ( $G_{RF}$ ), the noise figure (NF) and the spurious free dynamic range (SFDR) [64]. In order to illustrate these basic concepts, Figure 2.4 depicts a basic MWP link/system with the typical spectral components. For single tone (or group of tones) present at the input of the system, at the output we find the processed tone(s) attenuated by the system losses. In addition, non-linear terms will appear at the output spectrum. In general, the component that causes most of the nonlinear distortion is the external modulator. Finally, the noise produced by each subsystem contributes to a noise floor at the output that does not depend on the RF signal power at the input. The previous Figures of Merit employ these processed, non-linear terms and noise terms and their related power to evaluate the system performance according to:

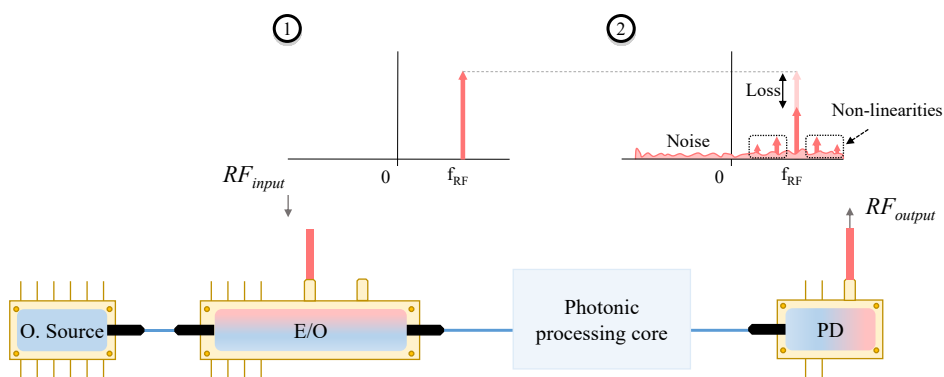


Figure 2.4 Basic MWP link/system and illustration of electrical losses, noise and non-linearities.

*Radiofrequency gain:* This figure computes the ratio between the RF signal power at the output and the input of the system. Limited by the conversion efficiencies in the modulator and the photodetector, and exacerbated by the quadratic relation between optical losses and RF loss, MWP systems often show negative link/system gain. However, a broad range of reported RF gains from -30 to 30 dB have been demonstrated over the last 20 years, [28, 29]. By pumping more optical power from the laser, an increment in the RF gain can be achieved.

*Dynamic Range:* The non-linear terms mainly generated by O/E and E/O conversions are known as intermodulation distortions. They are often evaluated by a two-tones-

test. Depending on the quadratic- or cubic- non-linear relation, second- and third-order distortions will appear. For sub-octave systems, where the maximum frequency is less than twice of the lowest frequency, the second-order intermodulation is typically far enough from the fundamental term to be filtered. However, third-order distortion terms will limit the system performance as they fall closest to the fundamental. This system classification is illustrated in Figure 2.5. Typical reported values of second-order SFDR are in the range of 70 to 90 dB Hz<sup>1/2</sup>, [40]. Moreover, linearization techniques can be employed to obtain a third-order SFDR in the range of 95 to 130 dB Hz<sup>2/3</sup> [16, 35, 40].

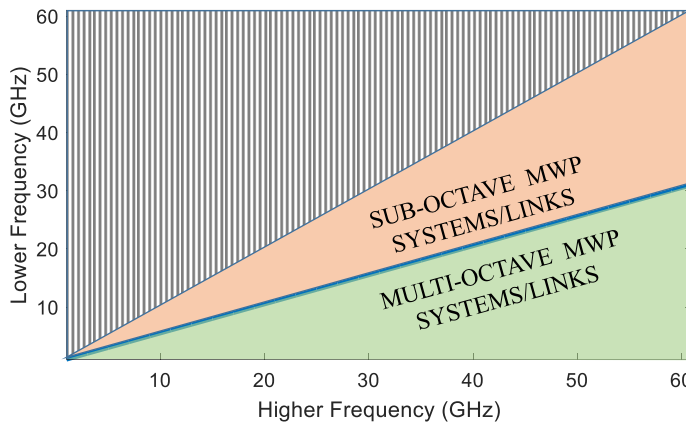


Figure 2.5 Classification of sub-octave and multi-octave MWP systems and links given the highest and lowest frequency (bandwidth).

*Noise Figure:* It relates the noise power at the output of the system to the noise at the input. The principal noise sources are the thermal noise, shot noise and relative intensity noise. The former is generated in resistors (Johnson). The second one is generated due to the random nature of photon counting in a given time interval. The last one is produced due to fluctuations of laser intensity caused by random spontaneous emissions. If the system contains an optical amplifier, the amplified spontaneous emission (ASE) noise often dominates over the aforementioned noise sources. A higher noise floor level might cover the processed signals, setting a minimum power where desired signals can be distinguished. Again, reported values from 1 to 30 dB depend on each subsystem performance present in the circuit, [28, 29].

Efficient lasers, modulators and photodetectors are required for optimum RF gain, Dynamic Range and NF. In addition, the insertion losses of the photonic processing core must be as low as possible.



---

## 2.2 Historical evolution

As in the electronics early stages, the activity in IMWP has been almost exclusively focused towards the so-called Application Specific Photonic Integrated Circuits (ASPICs), where a particular circuit and chip configuration is designed to optimally perform a single MWP functionality. In most of them, around a modest 20% of the components are integrated, [41]. Since the 90's, ASPICs have been developed in three main technologies: Indium Phosphide (InP) [42, 43, 20], Silicon photonics [17, 44, 45, 46, 47] and Silicon Nitride ( $\text{Si}_3\text{N}_4$ ) for a number of applications [18, 23]. These include: optical beamforming, fully programmable MWP filters using ring resonators structures, frequency discriminators, instantaneous frequency measurement, transmitters for THz applications, dual wavelength lasers for THz generation, pulse shapers, arbitrary waveform generators and monolithic-integrated optical phase-locked loops for coherent detection schemes, [16]. Only very recently, an ASPIC, with up to a full 100% integration was reported on InP [20].

Some of the aforementioned IMWP PICs have proven the possibility to perform more than one application. Although multi-purpose PICs represent a limited minority, Figure 2.6 illustrates the light increase trend that can be appreciated for the last 6 years. Some of them have demonstrated both arbitrary waveform generation and frequency filtering [48, 21], while others perform up to three functionalities among: Frequency discrimination, optical filtering, instantaneous frequency measurement, fractional Hilbert transform, phase shift, true time delay lines, integration and differentiation, [18, 39, 10]. In the best cases, only two or three applications can be completed. A new trend targeting generic-purpose PICs started in 2013. The so-called reconfigurable photonic processors are based on flexible layouts that interconnect waveguides and route the light by means of tunable couplers. Some of these layouts are built upon reconfigurable photonic filters based on the interconnection of optical cavities and interferometric structures with phase shifting capabilities, [49]. While they represent versatile optical architectures, they lack flexibility and scalability and have achieved a limited number of operations.

An alternative to ASPICs proposes to consider a generic-purpose processor architecture that can be integrated on a photonic chip, featuring single and/or multiple input/output operation and being capable of performing different RF and optical signal processing tasks by programming of its electronic control signals, as proposed as part of this Thesis, [50].

To support this concept, a versatile architecture that aims at programmable optical cores inspired by the photonic FPGA-like concept was recently proposed, [51]. The concept is to break down complex circuits in a large network of identical two-dimensional (2D) unit cells implemented by means of a Mach-Zehnder Interferometers (MZI) waveguide mesh or lattice. Through external electronic control signals, each MZI can be configured to operate as a directional coupler or

simply as an optical switch in a cross or bar state providing amplitude- and phase-controlled optical routing. In this way, the combination of different MZIs in the 2D square grid, -each individually configured as desired-, enables the synthesis of any kind of optical core circuit topology, including finite and infinite impulse response filters, on the condition that the targeted design fits in the discrete waveguide lattice. We recently proposed two different waveguide mesh-topologies that are described within the framework of this Thesis, and outperform the capabilities of the square lattice mesh, [52].

In this Thesis, we propose a more versatile device that comprises both RF and photonics subsystems and allows reconfigurable optical and RF interconnections via software. The reconfigurable optical core inside the processor can be implemented by means of programmable lattice meshes. The final device constitutes by itself the first proposal of an application-agnostic IMWP signal processor.

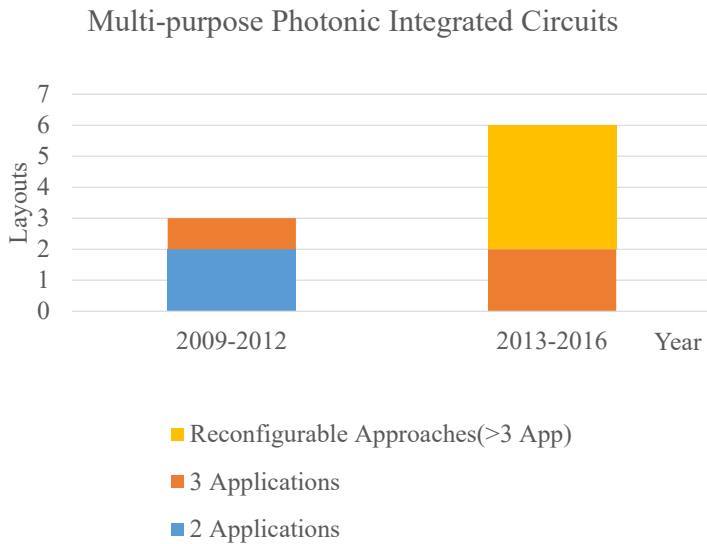


Figure 2.6 Proposed layouts for multi-purpose photonic integrated circuits for IMWP operations.

## 2.3 Technology review

ASPICs have been developed in three main technologies: Indium Phosphide (InP), Silicon photonics (Si-Ph) and Silicon Nitride ( $\text{Si}_3\text{N}_4$ ). These technologies have reached the required degree of maturity to be considered as viable options for the

implementation of complex photonic integrated circuits, either monolithic or hybrid, in general and the envisaged MWP universal processor in particular. Each technology platform operates mainly in the 1.3 and 1.55  $\mu\text{m}$  wavelength regions. An example of waveguide cross-section is illustrated in Figure 2.7. Note that for each integration platform and procedure, these geometries and values will vary.

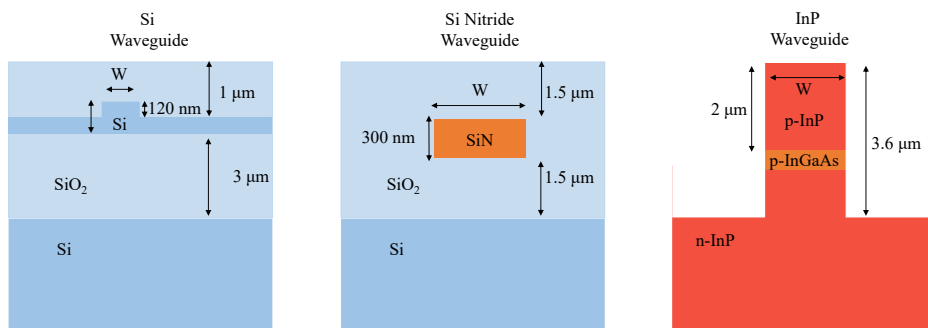


Figure 2.7 Examples of different cross sections for each technology and typical sizes.

### 2.3.1 Technology platforms

#### *Silicon Photonics*

Silicon Photonics (Si-Ph) [3, 16, 53, 54, 55, 56, 57, 58], is a semiconductor technology where components are etched/patterned/fabricated in a 180-220 nm Si layer placed on top of a 1-3  $\mu\text{m}$  insulator layer. Si passives are formed by initial few mask layers through partial and/or full Si etching steps after which multiple ion implantations are conducted for “active” devices such as Ge photodetectors and Si modulators. Coupling into and outside of the chip can be performed via edge/butt couplers (with typical losses of 1 dB/facet) or vertically, via Si surface vertical gratings (3.5-6 dB/coupler with 40-70 nm 3-dB bandwidth). The main advantage of Si-Ph technology resides in its compatibility with CMOS fabrication processes and the infrastructure used in microelectronics and, thus, in the potential for monolithic integration of the electronic and photonic parts of the chip. Refractive index contrast is typically in the 40-45% range but can be over 100% ( $n = 3.4$  for Si and  $n = 1.45$  for  $\text{SiO}_2$ ), leading to small footprint circuits. Two main types of waveguides are available: Ridge or shallow (1-8  $\mu\text{m}$  width), which exhibit relatively low losses down to 0.1-0.5 dB/cm, but are limited in bending radius to around 100  $\mu\text{m}$ , and Strip waveguides (500 nm width) that exhibit much higher losses (1-3 dB/cm) but support lower values for minimum bending radius (5-20  $\mu\text{m}$ ). Integration density on a chip is currently below 450 components [59], but the component count integration trend is

exceeding the rate given by Moore's law. Several basic photonic components are available in monolithic Si-Ph, including: passives, such as arrayed waveguide gratings and optical filters, Ge photodetectors, ring and travelling-wave electro-refractive modulators (up to 50 GHz). For example, Generic Foundry (GFM) and Generic Integration (GIM) Models are being developed in Europe by several foundries and packagers with granted access organized by the EURO PRACTICE platform [60], which also provides several Basic Building Blocks. Dedicated fabrication runs for complex chips are also accessible at a cost per PIC that, depending on the fabrication volume, oscillates between 1000 € for 100-1000 units and 10 € for more than one million chips per year. Si-Ph technology represents an optimum choice if the coexistence in a single chip of low-loss photonic components and driving/RF electronics through CMOS compatible processes is sought. Although it does not currently support optical sources and optical amplifiers, this limitation can be overcome by integrating III-V functionalities into the Si-Ph platform by means of heterogeneous or hybrid approaches. Heterogeneous approaches integrate more than one material system into a common process, an integration that can be accomplished by initially synthesizing materials on foreign substrates or bonding different materials together. Hybrid integration generally implies that separate chips are brought together in backend steps, such as die-attach, flip-chip, molecular [61] or adhesive [62] bonding to produce multichip modules. Hybrid approaches, have succeeded in incorporating distributed feedback lasers (DFB) and modelocked lasers, optical amplifiers, Electroabsorption (>70 GHz), and Mach-Zehnder (>25 GHz) modulators, photodetectors (>35 GHz) and polarization handling components into Si-Ph chips, [3, 16]. Several foundries in Europe are developing heterogeneous integration as well.

### Silicon nitride

This waveguide technology is based on a combination of stoichiometric silicon nitride ( $\text{Si}_3\text{N}_4$ ) as waveguide layers, filled by and encapsulated with silica ( $\text{SiO}_2$ ) as cladding layers grown on a silicon wafer [63, 64, 65, 66, 67, 68].  $\text{SiO}_2$  and  $\text{Si}_3\text{N}_4$  layers are fabricated with CMOS-compatible industrial equipment that enables cost-effective volume production. TriPleX™ technology [63], developed by the Dutch company LioniX, allows the fabrication of waveguides with minimized surface roughness, resulting in high refractive index contrast (20-30%) and low scattering losses. Three different waveguide cross-sectional geometries are standardized [64]. Their salient characteristics @1550 nm are: box-shaped ( $1 \times 1 \mu\text{m}^2$ )  $\leq 0.2$  dB/cm losses [64] and minimum bending radius around 150  $\mu\text{m}$ ; double-stripe ( $1 \mu\text{m} \times 1 \mu\text{m}$ , suited for sharp bends) 0.095-0.12 dB/cm losses and minimum bending radii in between 50-70  $\mu\text{m}$ ; and single-stripe with ultralow losses of 0.00045 dB/cm (current world record). In/out-coupling is achieved by means of adiabatically tapered spot-size converters with <1 dB coupling loss. Several fundamental building blocks for passive components are available and access to this platform is currently being offered as a multi-project wafer service run by JePPIX platform ([www.jepix.eu](http://www.jepix.eu)), [66]. The main

---

disadvantage is that too many key components present at IMWP systems, such as optical sources, detectors, amplifiers or modulators are not available, so their integration would require a complex hybrid approach to interface separately fabricated InP platform chips.

### III-V semiconductor compounds

InP is a semiconductor material capable of the monolithic integration of active and passive photonic components [3, 16, 69, 70, 71, 72]. A variety of techniques can be employed to integrate regions with different absorption/gain properties along a single waveguide. Waveguide types include shallow and deeply etched designs. Shallow waveguides have typical widths of 2  $\mu\text{m}$  and this figure is approximately 1.5  $\mu\text{m}$  for deeply etched designs. Typical losses are around 1.5 and 3 dB/cm for shallow and deeply etched waveguides, respectively. These high losses are one of the main disadvantages of this technology, requiring optical amplification if circuits with a minimum complexity are targeted. Another limitation of the InP platform is the difficulty of its integration with electronics into the same chip. Polarization rotation and mixing due to slight trapezoidal waveguide configuration is a serious limitation for MWP applications. Minimum bending radii are in between 10 and 500  $\mu\text{m}$  for deeply etched and shallow etched waveguides, respectively. InP provides a fairly complete list of passive (waveguides, couplers, etc.) and active (sources and amplifiers) components for integration [69]. GIM and GFM platforms have been developed with Europe and access generic processes is organized by the JePPIX platform ([www.jeppix.eu](http://www.jeppix.eu)), [66].

This platform has demonstrated the integration of active devices such as optical amplifiers, modulators, and optical sources together with passive devices. In fact, this platform has enabled the first fully monolithically integrated microwave photonic device in Indium Phosphide.

### Summary and Comparison

In the light of the previous review, it is possible to qualitatively summarise the availability and performance of the most typical basic building blocks for each integration technology platform, as covered by Table 2.1. Note that for a certain platform, quantitative results differ depending on the final cross section (geometry and materials) and the fabrication procedure.

Table 2.1. Qualitative comparison and availability of different basic building blocks for each integration platform. WG: Waveguide, PD: Photodetector, MOD: Modulator.

PLATFORM	OPTICAL PASSIVES		E/O & O/E		OPTICAL ACTIVES			OTHERS
	WG Losses	Confined Mode	PD	MOD	Thermo-optic Effect	Electro-optic Effects	O. Source / Amp.	Embedded Electronics
Si-Ph	✓✓	✓✓✓	✓✓	✓	✓✓✓	✓✓	-	✓✓
Si Nitride	✓✓✓	✓✓	-	-	✓	-	-	✓
InP	✓	✓	✓✓✓	✓✓	✓✓	✓	✓✓✓	-
Hybrid Solution Si + InP	✓✓	✓✓✓	✓✓✓	✓✓	✓✓✓	-	-	✓✓

From this table, it can be inferred that InP performs the greatest propagation losses, resulting in a medium-efficient solution for passives integration. In contrast, Si-Ph and Si-Nitride exhibit reduced propagation losses.

When the optical mode is more confined, as in Si-Ph, the radius of curvature of the waveguide can be reduced, allowing more compact devices and increasing the component integration density.

With respect to high-performance modulators and photodetectors, InP outstands medium-efficient Si-Ph solutions. While typical integrated values of InP photodetectors are around 0.7-1.14 A/W [20], Si-Ph are around 0.40-1.00 and require additional germanium compounds. Silicon Nitride do not allow neither of them. Hybrid Solutions InP + Si-Ph have demonstrated efficiencies around 0.7 A/W for a bandwidth of 67 GHz, [73].

The most important feature of InP platforms is that they provide light generation / amplification capabilities, that is mandatory for the integration of light sources and optical amplifiers.

The ability to modify the effective index after fabrication, allows a wide range of applications. This capability produces one of the most employed basic building block in PICs, the phase shifter. This building block is mandatory for any flexible design and also allows the implementation of tunable couplers by means of Mach Zehnder Interferometers. There is a great number of alternatives to develop a phase shifter. The typical approaches are summarised in Table 2.2 for each integration technology platform: thermo-optics, electro-optics and opto-mechanics. Here, we perform a comparison of the power consumption, associated tuning losses, availability and compactness. A typical Figure of Merit to classify the power consumption is the  $P_{\pi}$ . This figure specify what is the electrical power required to induce a 180° optical phase shift.

Thermo-optics devices rely on the temperature dependence of the waveguide materials. By heating up with a micro-heater a certain length of waveguide, it is possible to produce a change in the phase of the light traveling underneath. Since the micro-heaters are easily fabricated by a thin metal layer where electrical current goes through, they are widely employed in PICs for fabrication errors correction or for reconfigurable and tunable devices where the speed is limited by several microseconds.

Electro-optic effects based on the effective index change to the presence of electrical carriers [74], (carrier depletion [75], injection and accumulation) rely on the waveguide effective index change produced by the electronic charges traveling through the waveguide. They need larger devices and introduce additional propagation losses. However, the time constant is reduced to several ns, allowing several-GHz-bandwidth modulations.

Finally, opto-mechanical approaches try to modify the waveguide cross-section geometry by applying gradient electric forces, [76]. On-going research on this approach is being carried out in silicon and silicon nitride. For the former, devices shorter than 60  $\mu\text{m}$  are expected, allowing  $P_\pi$  lower than 50 mW and with reduced additional propagation losses for a time constant shorter than for thermo-optics. But to date, it is not as consolidated as its alternatives.

Table 2.2. Comparison and availability of different phase modulators for each integration platform. AV/CMP: Availability/Compactness, (-) No, ~ on-going research. TBD: To Be Determined.

PLATFORM	THERMO-OPTICS				ELECTRO-OPTICS				OPTO-MECHANICAL (MEMS)			
	$P_\pi$ (mW)	Associated Losses	Time Constant	AV /CMP	$P_\pi$ (mW)	Associated Losses	Time Constant	AV /CMP	$P_\pi$ (mW)	Associated Losses	Time Constant	AV /CMP
Si-Ph	1-30	-	Few $\mu\text{s}$	$\checkmark\checkmark$	< 1	$\times\times$	Few ns	$\checkmark$	< 30	$\times$	$\mu\text{s}$ -ns	$\sim$
Si Nitride	250-600	-	Few $\mu\text{s}$	$\checkmark\checkmark$	-	-	-	-	TBD	$\times$	TBD	$\sim$
InP	40-200	-	Few $\mu\text{s}$	$\checkmark\checkmark$	< 1	$\times\times$	Few ns	$\checkmark$	-	-	-	-
Hybrid Solution Si + InP	1-30	-	Few $\mu\text{s}$	$\checkmark\checkmark$	< 1	$\times\times$	Few ns	-	-	-	-	-

The precision required for each phase shifter and coupler varies from each application. Typically, tolerances of 2 - 5 % can be tolerated but degrade the systems' overall performance. For example, a simple filter made by means of an unbalanced MZI tuned by a phase shifter in one of its arms would experience a decrement in its extinction ratio (due to the coupling constant error) and a drift in the resonance position (due to the phase shift error). In this sense, thermo-optics take advantage from not including additional losses (if the metal layer is far enough from the optical mode). In contrast, electro-optic approaches introduce variable losses depending on

the targeted phase shift. In this case, if the MZI filter is tuned and the couplers are kept fixed, the extinction ratio will vary, since the losses in the arm that include the phase shifter vary.

### 2.3.2 State of the Art for integrated Microwave photonics

*InP* ASPICs have been developed for a number of applications (see particular performance in [3, 16, 70]), including: optical beamforming, fully programmable MWP filters using ring resonator structures, frequency discriminators, instantaneous frequency measurement, transmitters for THz applications, dual wavelength lasers for THz generation, pulse shapers, arbitrary waveform generators and monolithic-integrated optical phase-locked loops for coherent detection schemes. Most of the *Si-Ph* ASPICs for MWP have been demonstrated using the lower loss rib waveguides, since MWP systems entail strict requirements regarding losses to reach suitable values of dynamic range and purely passive platforms cannot make use of optical amplification.

*Si-Ph* monolithic configurations have been reported for (see performance in [3, 16]): arbitrary waveform generators [77], true time delay lines and beamforming networks with multi-GHz bandwidth [22], bandpass and notch reconfigurable filters based on Mach-Zehnder interferometer (MZI) tunable couplers and optical ring resonators (ORRs) fabricated in silicon-buried channel waveguides [78] and tunable phase shifters and true time delay lines based on etched *Si-Ph* gratings [17]. Monolithic *Si-Ph* ASPICs, based on stripe waveguides have been reported for optical delay lines, arbitrary waveform generation and ultrawideband signal generation. Hybrid *InP-Silicon* ASPICs have been reported for beamsteering, reconfigurable bandpass filtering using ORR loaded MZIs and for tunable phase shifters based on disk resonators [3, 16].

Finally, *Si<sub>3</sub>N<sub>4</sub>-SiO<sub>2</sub> TriPleX* ASPICs mainly based on the double-stripe waveguide configuration have been reported (performance in [3, 16, 64]) for: optical beamforming, microwave phase shifters, microwave filters, MWP links, ultrawideband signal generation, instantaneous frequency measurement, microwave polarization networks and fractional Hilbert transformers.

In most of them, around a modest 20% of the components are integrated, [41].



# Chapter 3

## Theoretical aspects of generic MWP Processors

### 3.1 Introduction

A careful analysis of the architectures of an extensive variety of MWP systems demonstrated in the literature shows that they share a high number of components independently of their final application [79]: As stated in the previous chapter, an optical transmitter (composed of one or various optical sources driven by a common electro-optical modulator) and an optical receiver (composed of one or various photodetectors) acting as opto-electronic converters, as well as a photonic core circuit that performs the specific processing in the optical domain. Some of them require electronics and radiofrequency systems to drive the electro-optical modulators and/or signal amplification to overcome conversion losses, either in the optical or in the radiofrequency stage to overcome conversion losses.

As stated in Chapter 2, the performance of MWP links and systems is commonly evaluated in terms of a set of figures of merit (FOM): the radiofrequency gain ( $G_{RF}$ ), the noise figure (NF) and the spurious free dynamic range (SFDR) [40]. These metrics have been obtained for a wide variety of MWP systems/links employing different modulation/detection configurations. Starting from the most basic intensity modulated-direct detection (IM-DD) links and systems, new optical devices, modulation and detection techniques have been also considered. Traditional, as well as more sophisticated MWP links and systems can be represented by a general model where either intensity or phase modulation can be applied. If we assume a generic transfer function including all the optical components placed between the electro-optic and opto-electronic stages, the analytical model for MWP links and systems developed in this chapter will work under very general conditions for the coherence properties of the optical source. However, every functionality of MWP requires one or several figures of merit that are specific to each application. For example, instantaneous frequency measurement systems define the *frequency measurement*

*error* and the *operational frequency range* as a figure to evaluate its explicit operation.

In this chapter, we present a proposal for the architecture of an integrated general-purpose software-defined MWP signal processor that is based on a reconfigurable optical core that interconnects the signal processor elements and performs the optical processing core tasks. All the elements inside the processor can be configured externally by suitably modifying their electrical control signals. Thus, we can alter the signal flow and enable as well as configure each subsystem for a required application.

Moreover, we present a generic end-to-end analytical model that computes the basic figures of merit of MWP filtered links and systems for several modulation and detection schemes. Due to its versatility, it can be directly applied to the general-purpose MWP processor. The model includes the commonly overlooked impact of the elements in the RF stage (RF filter and RF amplifier) as well. This tool can be used to anticipate performance as well as to design and configure properly each subsystem to fulfil the desired application specifications.

## 3.2 Generic architecture

The first attempt to develop an application agnostic architecture for MWP systems was the MWP transistor, [12]. The basic skeleton, illustrated in Figure 3.1, is composed of different subsystems, each of which is a collection of connected fixed and variable components. This architecture is derived from opening the feedback loop of a generalized optoelectronic oscillator.

This architecture is in principle capable of performing some of the required functionalities in MWP provided that its optical subsystems can be reconfigured by means of suitable control signals. Its main limitation is however that it does not support the reconfiguration of interconnections between its internal optical subsystems. This results in an intermediate performance between ASPIC and a programmable MWP processor. For example, if the reconfigurable optical filtering system in the transistor is designed as a lattice finite impulse response filter (FIR) for a MWP filtering application, then it cannot be reconfigured to implement a broadband dispersive delay line required for the generation of an arbitrary waveform (as then, a grating or a photonic crystal waveguide is needed). However, if both elements are present in the chip and the output from the modulator can be switched to any of them, then both functionalities can be implemented. According to [12], the synthesis of any given MWP functionality can be achieved using only three different types of optical filters: FIR, infinite impulse response (IIR) and dispersive delay lines (DDL). In the most usual case, only one type is required but, in certain applications, such as arbitrary waveform generation, a cascade of two types: FIR+DDL or IIR+DDL is

necessary [12]. Moreover, the scalability of this system is limited and a cascade of several transistors is required to enable more complex operations.

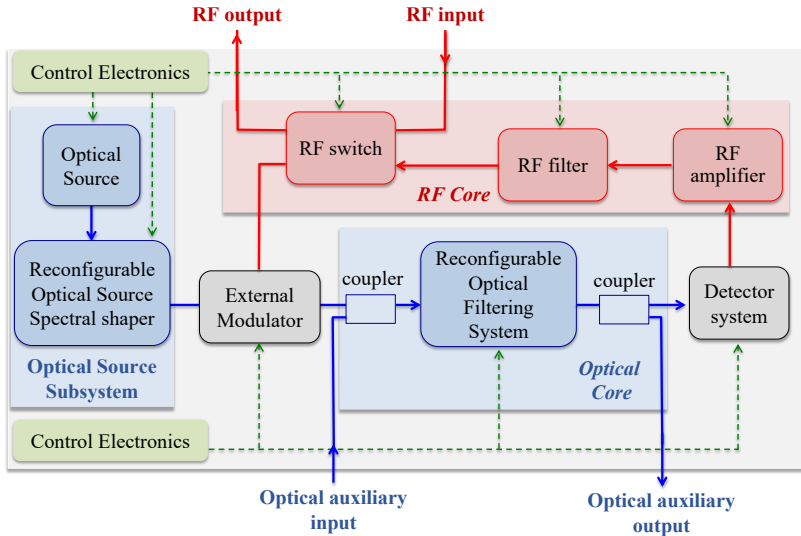


Figure 3.1 Microwave Photonic Transistor architecture, from [12].

To overcome the photonic transistor limitations related to reconfigurability, a more versatile optical core is required into the MWP transistor architecture to provide this missing full reconfiguration. By modifying the optical core to accommodate a more flexible layout, the system will allow the use of either an internal optical source or a previously modulated or continuous wave (CW) external source to up-convert the input RF signal. It will also allow the extraction of an auxiliary RF modulated optical signal outside the chip. Prior to detection, it will also enable the processed up-converted RF signal either to be directly detected or to exit the chip without being subject to optical detection and the injection of an optical input local oscillator to implement coherent detection of the processed up-converted RF signal. In Chapter 4, we analyse the different alternatives considered for the reconfigurable optical core subsystem.

A powerful approach providing more versatility calls for a re-design of the MWP transistor enabling software-defined reconfiguration to all the architecture. The final design must be fully integrated on a chip and must be capable of performing all the main functionalities by suitable programming of its control signals. This is inspired, in part, by the flexibility of software-radio [80] and digital signal processors, where a common hardware is shared by multiple functionalities through a software-defined approach (or programmability), leading to significant cost reduction in the hardware fabrication.

A generic layout of the software-defined MWP signal processor architecture is illustrated in Figure 3.2, where we show its operation over an arbitrary input RF signal. It comprises the RF interface and core system, the optical power source, the electrooptic (E/O) and optoelectronic (O/E) converters, the optical processing core as well as the electronics to perform the programmable control via software. The required RF, photonic and control electronic signal flows are also shown. To date, as outlined in Chapter 2, only three material platforms: Indium Phosphide (InP), Silicon on Insulator (SOI) either monolithic or hybrid, and Silicon Nitride ( $\text{Si}_3\text{N}_4\text{-SiO}_2$ ) have reached the required degree of maturity to be considered as viable options for the implementation of complex photonic integrated circuits in general and the envisaged MWP reconfigurable processor in particular. If we directly connect all the subsystems to the reconfigurable optical core, a much more versatile architecture is achieved, as illustrated in Figure 3.3.

The architecture displayed in Figure 3.3 represents, to the best of our knowledge, the first proposal for a generic-purpose software-defined MWP processor that incorporates the possibility of modifying the control signal flow to alter the subsystems connection diagram when required. It can perform electrical/electrical, electrical/optical, optical/electrical and optical/optical operations. For example, it can configure a frequency filter stage prior and after modulation.

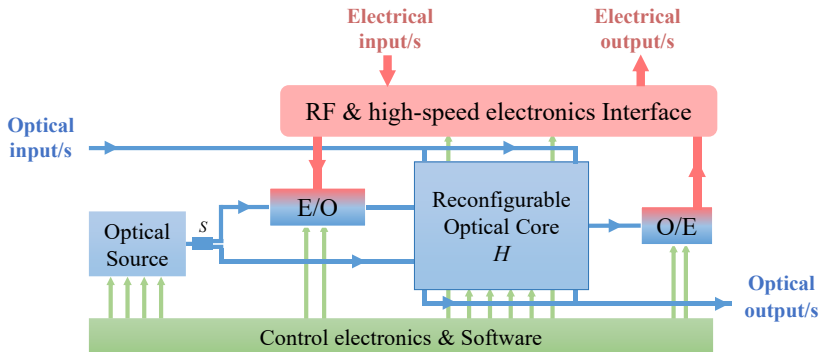


Figure 3.2 Generic architecture of a software-defined reconfigurable MWP signal processor.  
E/O: Electro-optic converter, O/E: Opto-Electronic converter.

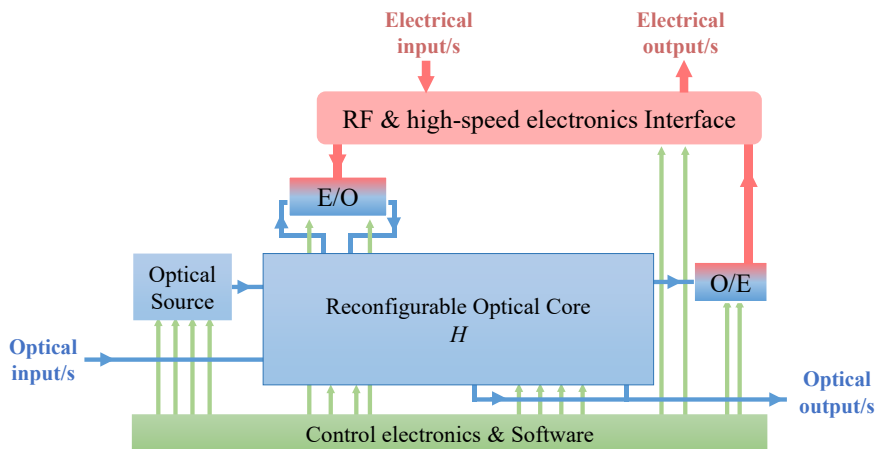


Figure 3.3 Generic architecture of a software-defined reconfigurable MWP signal processor offering signal flow modification.

The proposed software-defined reconfigurable signal processor must be capable, using the same hardware platform, of covering the main functionalities required in MWP, including: optical tunable and reconfigurable filtering, arbitrary waveform generation, optoelectronic oscillation, optically-assisted analogue-to-digital conversion, frequency up- and down-conversion, instantaneous frequency measurement, frequency multiplication, tunable phase shifters and true time delay lines for optical beamforming. Some of these functionalities have been demonstrated in the above-mentioned technology platforms with a variable degree of photonic component integration ranging from a modest 20% to up to a full 100% [41]. Regardless of the material platform employed, most of the reported ASPICs have been demonstrated for a single functionality and, to the best of our knowledge, no effort has been reported so far towards the development of a reconfigurable software-defined MWP signal processor in a similar way as, for example, a Field Programmable Gate Array operates in electronics or a Software Radio in wireless communications.

### 3.3 Analytical modelling

The majority of MWP systems and links can be represented by the generic schematic shown in Figure 3.4. It consists of an RF signal that modulates a continuous wave optical source in order to upconvert the signal frequency. Once in the optical domain, the optical core carries out the particular signal processing required for each functionality. Finally, the processed signal is photodetected. The modulation can be intensity modulation (IM) or (Phase modulation) and the optical-to-electronic

conversion can be done with a direct or a balanced photo-detection scheme. The effect of all intermediate optical components placed between E/O and the O/E conversion stages can be lumped into an optical transfer function  $H(\omega)$ , [40].

The design of the software-defined MWP signal processor requires a full end-to-end field-based model that provides, not only the description of the relevant linear and nonlinear signal terms, but also expressions for the evaluation of its overall figures of merit. The model of a generic MWP system provides a powerful tool to design, anticipate and evaluate the required values of the relevant performance parameters, which would then need to be programmed to run on multi-purpose chip architectures.

In the next sections, we first derive the model for the internal MWP processor stage (i. e. excluding all RF components) for several modulation and detection schemes and, finally, we extend it considering the impact of the external RF stage (RF amplifier and RF filter).

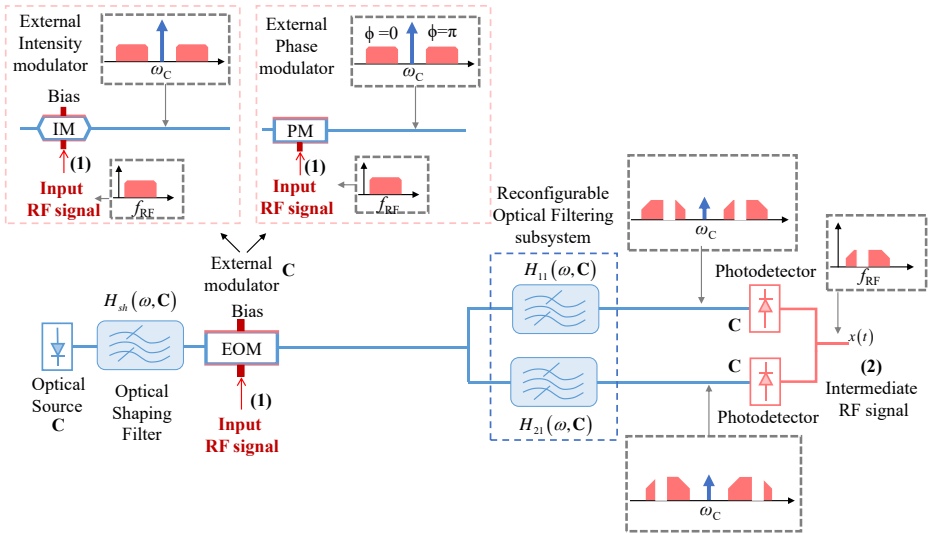


Figure 3.4 Schematic of a filtered MWP link or MWP system applying Intensity or Phase modulation (inset) with balanced detection scheme, [40].

### 3.3.1 Direct Detection MWP links/systems

Figure 3.4 shows a basic schematic diagram of the internal MWP part of the signal processor, where we can easily distinguish the aforementioned subsystems: the optical power source, the optical core as well as the E/O and O/E converters. A vector  $C$  represents the set of parameters that can be reconfigured by software. As we can

see, the MWP stage of the signal processor acts over an RF input signal (point (1) in Figure 3.4) and returns an output RF signal (point (2) in Figure 3.4). Within the processor, the RF input waveform is converted to the optical domain by modulating the signal produced by an optical source, which can be a fixed/tunable single wavelength laser, a comb/multiwavelength array or a broadband super-continuum source. In some cases, it may be convenient to shape the spectral characteristics of the emitter signal prior to modulation and this is done via an additional optical shaping filter that is represented by the optical transfer function  $H_{sh}(\omega, \mathbf{C})$ , being  $\omega$  the angular optical frequency. The optical source signal is modulated by the input RF signal in an external (amplitude or phase) electro-optic modulator, illustrated in the inset of Figure 3.4. After the modulator, the signal is fed to a generic reconfigurable optical filtering subsystem in order to be processed. In the case of MWP configurations where balanced detection (BD) is required, this optical subsystem can be represented as two different parallel optical filters that are characterized by the optical transfer functions  $H_{11}(\omega, \mathbf{C})$  and  $H_{21}(\omega, \mathbf{C})$ . It must be noted that this terminology also applies to single-detection configurations simply by making  $H_{11}(\omega, \mathbf{C}) = H(\omega, \mathbf{C})$  and  $H_{21}(\omega, \mathbf{C}) = 0$ . The output signal from the filtering subsystem is then directed towards the photodetection stage that closes the so-called internal MWP part of the signal processor and defines an intermediate RF signal point (point (2) in Figure 3.4).

The generic field-based analytical model representing this scheme was reported in [40] for filtered MWP links operating under direct detection (i.e. IM/SD, PM/SD and PM/BD). For the sake of completeness and further extension covering IM/BD and RF stage contributions, we reproduce here the salient results regarding the values of the relevant FOMs. Appendix A.1 covers the intermediate model steps including the photocurrent and power terms for the fundamental and intermodulation tones computation that are essential for the model extension.

#### *Radiofrequency Gain:*

The linear end-to-end RF gain (or loss) of a filtered MWP link/system, illustrated in Figure 3.4, is defined as the ratio of the RF power (at the modulating angular frequency  $\Omega$ ) delivered to a matched load ( $R_{out}$ ) at the photodetector output,  $P_{RF|out}$ , to the available RF power at the input at  $\Omega$ ,  $P_{RF|in}$ , delivered to the modulation device of input resistance  $R_{in}$ , as:

$$G_{RF}^{Mod}(\Omega) = \frac{P_{RF}(\Omega)|_{Out}}{P_{RF}(\Omega)|_{in}}, \quad (3.1)$$

where:

- *Mod*: It specifies the modulation type: intensity modulated (*I*) and phase modulated (*Φ*).

The RF gain is computed for each modulation scheme, obtaining:

$$G_{RF}^{Mod}(\Omega) = \varepsilon_{Mod} \left( \frac{I_{dc} \pi}{V_{\pi}} \right)^2 R_{in} R_{out} \left| \frac{A_{\Omega}^{Mod}}{2} \right|^2, \quad (3.2)$$

$$\varepsilon_{Mod} = \begin{cases} \varepsilon_I = \sin^2(\phi_{dc}), \\ \varepsilon_{\Phi} = 16, \end{cases}$$

where:

- $V_{\pi}$  is the modulator half-wave voltage. It is the applied voltage at which the phase of light shifts  $180^\circ$ . This figure depends on the material properties, the wavelength and the device geometry. It typically ranges from 1.5 to tens of volts.
- $V_{dc}$  is the modulator bias voltage. This figure sets the modulation bias point in intensity modulators. It ranges from  $-V_{\pi}$  to  $V_{\pi}$ .
- $\phi_{dc} = \pi V_{dc} / V_{\pi}$  is the intensity modulator bias point. The bias point will define the position of the optical carrier along the modulator transmission curve. For example, a 50% transmission point (Quadrature Bias point) is achieved when  $V_{dc}$  is equal to  $V_{\pi}/2$ .
- $A_{\Omega}^{Mod}$  is the spectral coefficient related to the fundamental tone position and the spectral response of the system  $H(\omega)$ . The definition of this coefficient is given in Eq. (3.12) followed by the definition of the spectral coefficients for each of the relevant intermodulation tones.
- $I_{dc}$  is the DC-current term obtained when the optical carrier is photodetected. Typical values ranges from 0.05 to 5 mA.

Incidentally, the DC-current term is defined as

$$I_{dc} = \alpha_{Mod} \Re \frac{P_0}{2}, \quad (3.3)$$

where:

- $\alpha_{Mod}$  is the modulator optical excess loss. Typical values ranges from 2 to 6 dB, which translates into 0.63 and 0.25.
- $\Re$  represents the photodetector responsivity in [A/W]. As stated in Chapter 2, typical values of photodetection efficiency ranges from 0.6 to 1.0 A/W.
- $P_0$  accounts for the optical power at the optical source output at the optical frequency  $\omega_0$ . Typical values are between -5 and 10 dBm, which translates into 0.31 to 10mW.

In the case of balanced detection, the photodetected total current is computed by subtracting the current obtained in the second detector from the corresponding to the first:  $I(t) = I_1(t) - I_2(t)$ .



### Noise Figure:

As stated in Chapter 2, the processed microwave signal will be affected by a variety of noise sources: input and output thermal noises, shot noise and laser noise contributions. The noise characterization can be defined by the noise figure parameter as the ratio between the noise present at the output with respect to the noise present at the input:

$$NF^{Mod} = \frac{N_{tot}}{G_{RF}^{Mod} N_{in}}, \quad (3.4)$$

where:

- $N_{in}$  is the input noise spectral density (noise power per unit of bandwidth).
- $N_{tot}$  is the total output noise spectral density.

The  $NF$  can be computed in terms of the total relative intensity noise parameter ( $RIN_{tot}$ ), which is the sum of all the noise contributions [40]. For MWP links/systems, the noise characterization can be summarized by the following expressions:

$$NF^{Mod} = \varepsilon_{Mod} \frac{RIN_{tot}^{Mod} V_{\pi}^2 |A_{DC}^{Mod}|^2}{\pi^2 R_m k_B T |A_{\Omega}^{Mod}|^2}, \quad (3.5)$$

$$\varepsilon_{Mod} = \begin{cases} \varepsilon_I = \frac{4[1 - \cos(\phi_{dc})]^2}{\sin^2(\phi_{dc})}, \\ \varepsilon_{\Phi} = 1, \end{cases}$$

being:

- $k_B$  the Boltzmann constant equal to  $1.38064852 \times 10^{-23} \text{ m}^2 \text{ kg s}^{-2} \text{ K}^{-1}$ .
- $T$  the temperature in Kelvins.
- $A_{DC}^{Mod}$  the spectral coefficient related to the DC component defined in Eq. (3.12) for each modulation format specified by  $Mod$ .

The noise contributions that contribute to the total  $RIN_{tot}$  are the *thermal noise at the input (i,th)*, the *thermal noise at the output (o,th)* and the *shot noise (shot)*:

$$RIN_{i,sh}^{Mod} = \varepsilon_{Mod} \frac{\pi^2 R_{in} k_B T |A_{\Omega}^{Mod}|^2}{V_{\pi}^2 |A_{DC}^{Mod}|^2}, \quad (3.6)$$

$$\varepsilon_{Mod} = \begin{cases} \varepsilon_I = \frac{\sin^2(\phi_{dc})}{4[1 - \cos(\phi_{dc})]^2}, \\ \varepsilon_{\Phi} = 1, \end{cases}$$

$$\begin{aligned}
 RIN_{o,sh}^{Mod} &= \varepsilon_{Mod} \frac{k_B T}{I_{dc}^2 R_{out} |A_{DC}^{Mod}|^2}, \\
 \varepsilon_{Mod} &= \begin{cases} \varepsilon_I = \frac{1}{[1 - \cos(\phi_{dc})]^2}, \\ \varepsilon_\Phi = \frac{1}{4}, \end{cases} \quad (3.7)
 \end{aligned}$$

$$\begin{aligned}
 RIN_{shot}^{Mod} &= \varepsilon_{Mod} \frac{e}{I_{dc} |A_{DC}^{Mod}|}, \\
 \varepsilon_{Mod} &= \begin{cases} \varepsilon_I = \frac{2}{[1 - \cos(\phi_{dc})]}, \\ \varepsilon_\Phi = 1, \end{cases} \quad (3.8)
 \end{aligned}$$

where:

- $e$  is the electron charge constant =  $1.6021766208(98) \times 10^{-19}$  coulombs.

*Dynamic Range:*

Finally, for the dynamic range evaluation, we use a commonly employed figure of merit, the spurious free dynamic range (SFDR). The SFDR is defined as the carrier-to-noise ratio when the noise floor in the signal bandwidth equals to the power of a given order intermodulation product. Figure 3.5 (a) illustrates the apparition of distortion terms when applying more RF input power. As depicted in Figure 3.5 (b), by sweeping the input power as well as measuring and interpolating the fundamental tone power and the corresponding distortion term, it is possible to measure the dynamic range. For this figure, we assume a modulating signal composed of two RF tones, characterised by the same amplitude at angular frequencies  $\Omega_1$  and  $\Omega_2$ . For each intermodulation order, the SFDR can be computed as, [40]:

$$\begin{aligned}
 SFDR_2^{Mod} &= \left( \frac{OIP_2^{Mod}}{N_{tot}} \right)^{1/2}, \\
 SFDR_3^{Mod} &= \left( \frac{OIP_3^{Mod}}{N_{tot}} \right)^{2/3}, \quad (3.9)
 \end{aligned}$$

where:

- $OIP_2$  and  $OIP_3$ , known as second and third-order optical interception points

respectively, are the linearly extrapolated input powers at which the fundamental tone and their respective intermodulation terms ( $IMD_2$  and  $IMD_3$ ) output powers are equal.

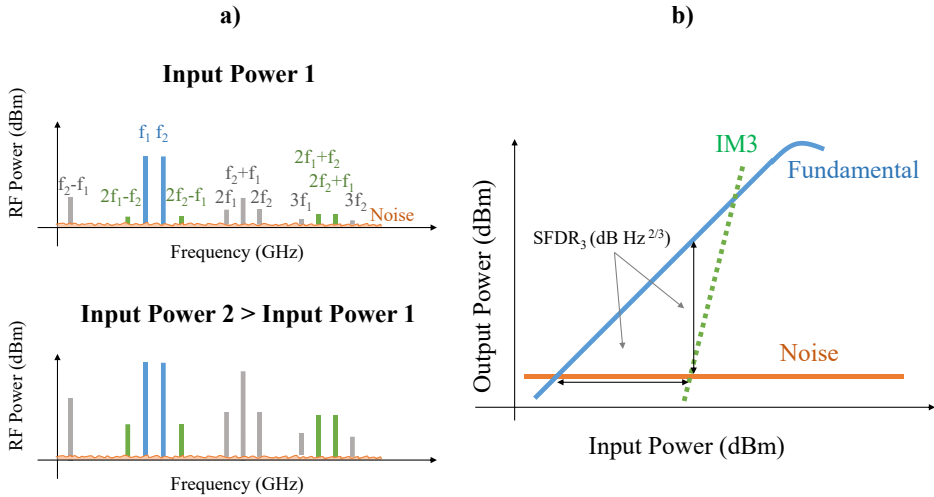


Figure 3.5 (a) Spectral response of a two-tones-test when the input power is increased and (b) typical fundamental and third order intermodulation power levels vs input power for the determination of the  $SFDR_3$ .

In practice, the tones related to the  $SFDR_3$  ( $2\Omega_1 - \Omega_2$ ) and ( $2\Omega_2 - \Omega_1$ ) will appear within the system bandwidth.  $SFDR_2$  terms ( $\Omega_1 \pm \Omega_2$  and  $\Omega_2 \pm \Omega_1$ ) fall outside the passband of a suboctave, hence they are only important for systems whose bandwidth extends over one octave, as stated in Chapter 2.

By computing and substituting the corresponding  $OIP$  points and total noise for each modulation scheme, we can express the  $SFDR$  in terms of the  $RIN_{tot}$  parameter as:

$$\begin{aligned}
SFDR_2^{Mod} &= \varepsilon_{Mod} \sqrt{\frac{2}{RIN_{\omega}^{Mod}} \frac{|A_{\Omega}^{Mod}|^2}{|A_{\Omega_1 \pm \Omega_2}^{Mod}| |A_{DC}^{Mod}|}}, \\
\varepsilon_{Mod} &= \begin{cases} \varepsilon_I = \frac{\sin^2(\phi_{dc})}{|1 - \cos(\phi_{dc})|}, \\ \varepsilon_{\Phi} = 1, \end{cases} \\
SFDR_3^{Mod} &= \left( \varepsilon_{Mod} \frac{2}{RIN_{\omega}^{Mod}} \frac{|A_{\Omega}^{Mod}|^3}{|A_{2\Omega_1 - \Omega_2}^{Mod}| |A_{DC}^{Mod}|^2} \right)^{2/3}, \\
\varepsilon_{Mod} &= \begin{cases} \varepsilon_I = \frac{\sin^2(\phi_{dc})}{|1 - \cos(\phi_{dc})|}, \\ \varepsilon_{\Phi} = 2, \end{cases}
\end{aligned} \tag{3.10}$$

with:

- $A_{\omega}^{Mod}$  being the spectral coefficient for the frequency tone defined by  $\omega$ .

The different optical spectral coefficients appearing in the previous equations are given, assuming a monochromatic optical source, by:

$$A_{DC}^{Mod} = |H_{11}(\omega_0)|^2 + |H_{21}(\omega_0)|^2, \tag{3.11}$$

$$A_{\Omega_{1,2}}^{Mod} = \sum_{n=\{0,1\}} \varepsilon_{Mod} \begin{bmatrix} H_{11}(\omega_0 + n\Omega_{1,2}) H_{11}^*(\omega_0 + (n-1)\Omega_{1,2}) \\ -H_{21}(\omega_0 + n\Omega_{1,2}) H_{21}^*(\omega_0 + (n-1)\Omega_{1,2}) \end{bmatrix}, \tag{3.12}$$

$$\varepsilon_{Mod} = \begin{cases} \varepsilon_I = 1 \\ \varepsilon_{\Phi} = (-1)^n \end{cases},$$

$$\begin{aligned}
A_{2\Omega_{1,2}}^{Mod} &= \sum_{n=\{0,1,2\}} \varepsilon_{Mod} \begin{bmatrix} H_{11}(\omega_0 + n\Omega_{1,2}) H_{11}^*(\omega_0 + (n-2)\Omega_{1,2}) \\ -H_{21}(\omega_0 + n\Omega_{1,2}) H_{21}^*(\omega_0 + (n-2)\Omega_{1,2}) \end{bmatrix}, \\
\varepsilon_{Mod} &= \begin{cases} \varepsilon_I = [(-1)^n - \cos \phi_{dc}] \left(\frac{1}{2}\right)^{|n-1|} \\ \varepsilon_{\Phi} = (-1)^n \left(\frac{1}{2}\right)^{|n-1|} \end{cases},
\end{aligned} \tag{3.13}$$

$$A_{\Omega_{1,2} \pm \Omega_{2,1}}^{Mod} = \pm \sum_{\substack{n=\{0,1\} \\ m=\{-1,0\}}} \mathcal{E}_{Mod} \begin{bmatrix} H_{11}(\omega_0 + n\Omega_{1,2} \mp m\Omega_{2,1})H_{11}^*(\omega_0 + (n-1)\Omega_{1,2} \mp (m+1)\Omega_{2,1}) \\ -H_{21}(\omega_0 + n\Omega_{1,2} \mp m\Omega_{2,1})H_{21}^*(\omega_0 + (n-1)\Omega_{1,2} \mp (m+1)\Omega_{2,1}) \end{bmatrix}, \quad (3.14)$$

$$\mathcal{E}_{Mod} = \begin{cases} \mathcal{E}_I = [(-1)^{n+m} - \cos(\phi_d)] \\ \mathcal{E}_\Phi = (-1)^{n+m} \end{cases},$$

$$A_{2\Omega_1 - \Omega_2}^{Mod} = \sum_{\substack{n=\{0,1,2\} \\ m=\{-1,0\}}} \mathcal{E}_{Mod} \begin{bmatrix} H_{11}(\omega_0 + n\Omega_1 + m\Omega_2)H_{11}^*(\omega_0 + (n-2)\Omega_1 + (m+1)\Omega_2) \\ -H_{21}(\omega_0 + n\Omega_1 + m\Omega_2)H_{21}^*(\omega_0 + (n-2)\Omega_1 + (m+1)\Omega_2) \end{bmatrix}, \quad (3.15)$$

$$\mathcal{E}_{Mod} = \begin{cases} \mathcal{E}_I = \left(\frac{1}{2}\right)^{|n-1|} \\ \mathcal{E}_\Phi = (-1)^{m+n} \left(\frac{1}{2}\right)^{|n-1|} \end{cases}.$$

A non-monochromatic source can be employed as well. In this case, only the spectral coefficients must be modified and are defined in [40]. Moreover, the spectral shape of the optical source can be modified by the filter  $H_{sh}(\omega, \mathbf{C})$ . The global character of the obtained photocurrent terms and, particularly, of the developed figures of merit, makes the model suitable for its application to the generic-purpose MWP processor provided that it employs direct detection and the impact of external RF components can be neglected. However, it does not account for the case of coherent detection and, most particularly, for the case where self-homodyne or self-beating detection is employed. Furthermore, the previous model does not account for the influence of the external RF components (RF amplifiers and filters), which are always required. To take into account these, the model must be extended, and this has been carried within the framework of this Thesis.

### 3.3.2 Self-Beating coherent processors

An emerging and important class of MWP systems operates in the so-called self-beating mode. In this modulation/detection scheme, shown in Figure 3.6, a continuous wave (CW) optical carrier is first split into two paths by an input coupler characterized by a coupling coefficient  $K_1$ . The CW carrier in one of the paths is intensity modulated (either single or double sideband) by an input RF signal in an external modulator, filtered to suppress the optical carrier leaving the single (or double) RF sideband(s), which is (are) then processed by an optical core represented by a field transfer function  $H(\omega)$ . The filter transfer function can be employed to suppress one of the sidebands as well. Through this arm, the signal experiences an overall loss characterized by a lumped optical power transmission factor  $\alpha_U$ . In the

other arm, the CW signal propagates subject to no modulation and experiences an overall loss characterized by a lumped optical power transmission factor  $\alpha_L$ . Both paths are finally combined by an output coupler characterized by a coupling coefficient  $K_2$  prior to enter to one (or two) photodetector(s), where the RF-modulated signal beats with the CW signal that operates as a self-local oscillator. The balanced configuration comprises two photodetectors placed at each output of the coupler  $K_2$ , where each one is characterized by a responsivity  $\mathfrak{R}$ . The photocurrents generated at each one of these photodetectors are electrically subtracted to produce an output photocurrent  $i_{RF,out}(t)$  flowing across an output impedance  $R_{out}$ . The single detection scheme comprises one single detector (photodetector 2 is disabled). The detailed derivation of  $i_{RF,out}(t)$  and the figures of merit is provided in the Appendix A.2.

In essence, this operation corresponds to a self-homodyne coherent system that is called to play a significant role in on-chip tunable MWP signal processors. In particular, this approach has been recently shown to bring improved flexibility in integrated MWP filters and beamforming networks [64]. As with any MWP system, the performance of self-beating configurations can be described in terms of the traditional figures of merit: RF Gain, Noise Figure (NF) and Spurious Free Dynamic Range (SFDR). However, to our knowledge, there was no reported model yielding expressions for these figures in this particular, but important case. The purpose of this section is to report such model, [81]. In fact, our original contribution is to derive the expression for the contribution from the signal-local oscillator beating term, which is not available in the case described in [40] and which will dominate the figures of merit in practice. We consider intensity modulation in two different system configurations: single and balanced detection respectively. Phase modulation is not developed here, but could be obtained following the same procedure, defined in Appendix A.2

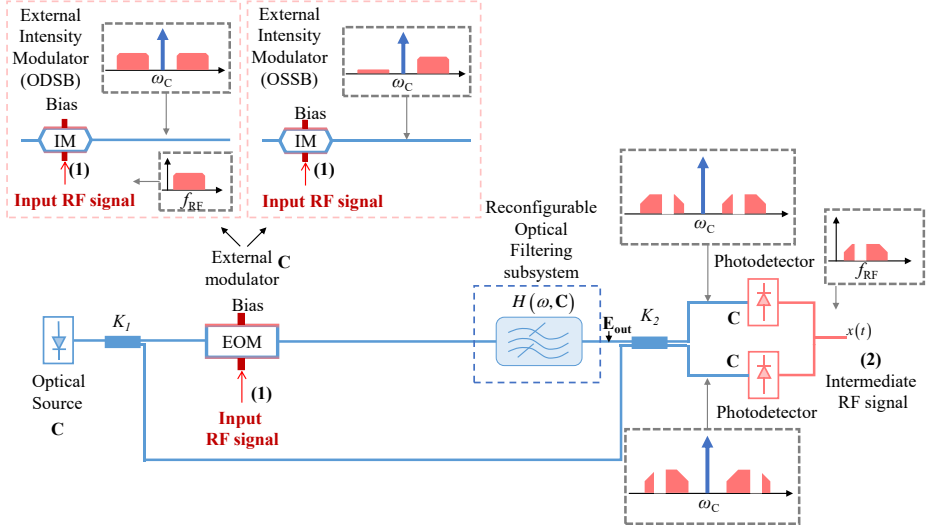


Figure 3.6 Schematic of a Self-beating filtered MWP link or MWP system applying Intensity ODSB or OSSB modulation (inset) with balanced detection scheme, [81].

Following a similar procedure as that reported in [10] we get the main figures of merit as:

$$G_{RF,RF}^I(\Omega_1) = \frac{P_{RF}^{out}(\Omega_1)}{P_{RF}^{in}(\Omega_1)} = \left[ \frac{I_{dc} \pi \sin(\phi_{DC}) D}{2V_{\pi}} \frac{D}{X} \right]^2 \left| jDA_{\Omega_1}^I + CA_{\Omega_1}^{I,SB} \right|^2 Z_{in} Z_{out}, \quad (3.16)$$

$$NF = \frac{RIN_{Total} I_{dc,Total} Z_{out}}{G_{RF}(\Omega_1) k_B T}, \quad (3.17)$$

$$\begin{aligned}
RIN_{Total} &= RIN_{thermal,input} + RIN_{thermal,output} + RIN_{shot} + RIN_{laser} = \\
&= \frac{k_B T \left[ \frac{\pi \sin(\phi_{DC})}{2V_\pi} \right]^2 \left| jDA_{\Omega_1}^I + CA_{\Omega_1}^{I,SB} \right|^2 Z_{in} + \frac{2k_B T}{\left( \frac{DI_{dc}}{X} \right)^2 Z_{out}}}{\left[ (-1)^p D |H(\omega_o)|^2 (1 - \cos \phi_{DC}) + Y + 4C \sin\left(\frac{\phi_{DC}}{2}\right) \cos \varphi \operatorname{Im}\{H(\omega_o)\} \right]^2} + \quad (3.18)
\end{aligned}$$

$$\begin{aligned}
&+ \frac{2e}{\left( \frac{DI_{dc}}{X} \right) \left[ (-1)^p D |H(\omega_o)|^2 (1 - \cos \phi_{DC}) + Y + 4C \sin\left(\frac{\phi_{DC}}{2}\right) \cos \varphi \operatorname{Im}\{H(\omega_o)\} \right]} + \\
&+ RIN_{laser},
\end{aligned}$$

$$OIP_2 = 2 \left( I_{dc} \sin^2(\phi_{DC}) \frac{D}{X} \right)^2 Z_{out} \frac{|jDA_{\Omega_1}^I + CA_{\Omega_1}^{I,SB}|^4}{|jDA_{\Omega_1-\Omega_2}^I + CA_{\Omega_1-\Omega_2}^{I,SB}|^2}, \quad (3.19)$$

$$OIP_3 = 2 \left( I_{dc} \sin(\phi_{DC}) \frac{D}{X} \right)^2 Z_{out} \frac{|jDA_{\Omega_1}^I + CA_{\Omega_1}^{I,SB}|^3}{|jDA_{2\Omega_1-\Omega_2}^I - CA_{2\Omega_1-\Omega_2}^{I,SB}|}, \quad (3.20)$$

$$SFDR_2 = \left[ \frac{OIP_2}{N_{Total}^{output}} \right]^{\frac{1}{2}}, \quad SFDR_3 = \left[ \frac{OIP_3}{N_{Total}^{output}} \right]^{\frac{2}{3}}, \quad (3.21)$$

where  $C$ ,  $D$ ,  $X$ ,  $Y$ , for each detection scheme (Single ( $SD$ ) and balanced ( $BD$ )), account for the splitting action of the input and output couplers as well as the optical losses of the upper and lower branches and can be defined as:

$$\begin{aligned}
C &= \sqrt{\alpha_l K_1 K_2} \Leftarrow (SD), \\
C &= 2\sqrt{\alpha_l K_1 K_2 (1 - K_2)} \Leftarrow (BD),
\end{aligned} \quad (3.22)$$

$$\begin{aligned}
D &= \sqrt{\alpha_u (1 - K_1)(1 - K_2)} \Leftarrow (SD), \\
D &= (1 - 2K_2) \sqrt{\alpha_u (1 - K_1)} \Leftarrow (BD),
\end{aligned} \quad (3.23)$$



$$\begin{aligned} X &= 1 \Leftarrow (SD), \\ X &= 1 - 2K_2 \Leftarrow (BD), \end{aligned} \quad (3.24)$$

$$\begin{aligned} Y &= 2C^2 / D \Leftarrow (SD), \\ Y &= \alpha_L K_1 X^2 / D \Leftarrow (BD). \end{aligned} \quad (3.25)$$

Finally, the spectral coefficients for the fundamental, second- and third-order intermodulation terms for the beating contribution present at Eqs. (3.16)-(3.21) are respectively:

$$A_{\Omega_1}^{I,SB} = \frac{[H(\omega_o + \Omega_1) - H^*(\omega_o - \Omega_1)]}{\sin(\phi_{dc}/2)} \cos \varphi, \quad (3.26)$$

$$\begin{aligned} A_{\Omega_1 - \Omega_2}^{I,SB} &= 2[H(\omega_o + \Omega_1 - \Omega_2) - H^*(\omega_o - \Omega_1 + \Omega_2)] \sin(\phi_{dc}/2) \cos \varphi, \\ A_{2\Omega_1 - \Omega_2}^{I,SB} &= \frac{[H(\omega_o + 2\Omega_1 - \Omega_2) - H^*(\omega_o - 2\Omega_1 + \Omega_2)]}{2\sin(\phi_{dc}/2)} \cos \varphi, \end{aligned} \quad (3.27)$$

where:

- $\cos \varphi$  represents the polarization mismatch between the beating optical signals from the upper and lower branches.

#### *Simplified expressions for self-beating term domination*

The previous equations provide the most general expressions for the computation of the figures of merit, taking into account most of the factors behind non-ideal operation (insertion losses, finite CW optical carrier suppression, non-ideal filtering effects, polarization mismatch, etc.). In practice, however, several simplifications can be made. The most important one is that the term from the beating of the CW carrier (lower branch) and the modulated signal (upper branch) should be the dominant one in the output photocurrent. We will also assume that the optical carrier is completely suppressed by the filter in the upper branch. Under these conditions, the general figures of merit simplify to:

$$G_{RF}(\Omega_1) = \left[ \frac{I_{dc} \pi \sin(\phi_{DC})}{2V_\pi} \frac{CD}{X} |A_{\Omega_1}^{I,B}| \right]^2 Z_{in} Z_{out}, \quad (3.28)$$

$$N_{\text{Total}}^{\text{output}} = 2^p k_B T + 2eI_{dc} Z_{\text{out}} \frac{DY}{X} + \left[ \frac{I_{dc} \pi \sin(\phi_{DC})}{2V_\pi} \frac{CD}{X} |A_{\Omega_1}^{I,B}| \right]^2 Z_{\text{in}} Z_{\text{out}} k_B T, \quad (3.29)$$

$$OIP_2 = 2 \left( I_{dc} \sin^2(\phi_{DC}) \frac{CD}{X} \right)^2 Z_{\text{out}} \frac{|A_{\Omega_1}^{I,B}|^4}{|A_{\Omega_1 - \Omega_2}^{I,B}|^2}, \quad (3.30)$$

$$OIP_3 = 2 \left( I_{dc} \sin(\phi_{DC}) \frac{CD}{X} \right)^2 Z_{\text{out}} \frac{|A_{\Omega_1}^{I,B}|^3}{|A_{2\Omega_1 - \Omega_2}^{I,B}|}. \quad (3.31)$$

The noise figure and the spurious free dynamic ranges are obtained substituting Eqs. (3.28)-(3.31) into (3.17) and (3.21) respectively. In the case of balanced detection, we consider in addition ideal operation, that is, the same responsivity in both photodetectors and  $K_2 = 1/2$  that results in  $DY/X = 0$  and  $CD/X = [\alpha_U \alpha_L K_1(1 - K_1)]^{1/2}$ .

#### *Application example: Self-beating MWP filter*

As an application example for the above model, we consider a MWP filter employing a tunable integrated filter composed of a ring-loaded Mach-Zehnder interferometer [13] illustrated in the upper part of Figure 3.7. This type of filter is made of a symmetric MZI, where both interferometer arms are coupled to a set of two ring resonators of the same perimeter. The coupling between the top/bottom MZI arms and the ring resonators is achieved by means of optical couplers with different coupling constants. These are schematically shown in upper part of Figure 3.7 as  $K_{b,i}$  and  $K_{t,i}$  (with  $i = 1, 2$ ), where 'K' stands for the power coupling constant (in linear units), and 'b' and 't' stand for 'bottom' and 'top', respectively. Together with the relative optical phases of the ring resonators ( $\phi_{b,i}$ ,  $\phi_{t,i}$ ) and the relative phases of the MZI arms ( $\phi_{t,a}$ ,  $\phi_{b,a}$ ), they completely define the transfer function of the filter, as described in [32].

Ring-loaded MZI filters can be mathematically described with the same formalism employed in digital signal processing filters [32], so identical techniques can be used for their design. Our structure implements a canonical, 4th-order Chebyshev Type-II filter with a low-pass response. It features a stopband rejection of 35 dB and a passband cut-off frequency of 9.44 GHz. The designed filter is shown in the lower part of Figure 3.7. The values of the different phase shifts and coupling constants required to achieve this transfer function are:  $K_{t,1} = K_{b,1} = 0.489$ ,  $K_{t,2} = K_{b,2} = 0.943$ ,  $\phi_{t,1} = -\phi_{b,1} = 86.1096^\circ$ ,  $\phi_{t,2} = -\phi_{b,2} = -98.7306^\circ$ , and  $\phi_{t,a} = -\phi_{b,a} = 54.5716^\circ$ . Also

note that the optical response of the filter is periodic in frequency. The spectral period is known as the Free Spectral Range (FSR), and in this case, is 20 GHz.

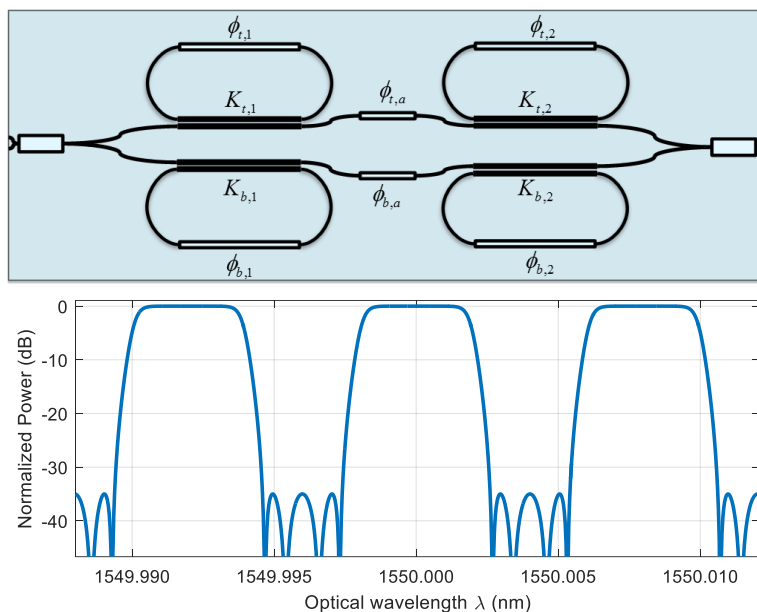


Figure 3.7 (Upper) Schematic diagram of a ring-loaded Mach-Zehnder Interferometer considered as an example. (Lower) Chebyshev Type-II filter implemented by the ring-loaded MZI (filter details in text).

The integrated filter was designed for implementation in an InP platform at a nominal wavelength of 1550 nm. The effective group index of the employed waveguides is 3.7056, which yields a ring perimeter of 4.0451 mm for a FSR of 20 GHz. Multimode interference couplers (MMIs) were employed to implement the input/output 3-dB couplers that split/recombine the signals in the MZI arms, as well as the couplers with different coupling constants that connect the arms with the ring resonators.

#### *Results for Self-beating intensity modulation-single detection systems/links*

We have applied the model derived in this section to a single-detector RF filter configuration using the double-loaded MZI optical filter of fourth order. We consider single-sideband modulation with a high degree of optical carrier suppression (around 35 dB achieved as compared to the selected RF bands) by applying a carrier frequency shifting of  $\Delta f_0 = 10$  GHz. For the evaluation of the figures of merit, we have employed the model, i.e. Eqs. (3.16)-(3.27), and the following values for the relevant parameters:  $\alpha_L = 10^{-3/10}$ ,  $\varphi = 0$ , (perfect state of polarization matching),  $\phi_{dc} =$

$\pi/2$  (MZM biased at the quadrature point),  $V_\pi = 6.9$  volt,  $I_{dc} = 5$  mA (which accounts for the modulation insertion losses, the responsivity of the photodetectors and the optical power at the carrier frequency),  $T = 298$  °K,  $k_B = 1.3810^{-23}$  J °K $^{-1}$ ,  $K_1 = K_2$ ,  $Z_{in} = Z_{out} = 50 \Omega$ . For the signal frequencies, we have chosen (referred to the value of the optical carrier frequency  $f_o = \omega_o/2\pi$ ),  $f_1 = 6.5$  GHz,  $f_2 = 6.6$  GHz,  $|f_1 - f_2| = 100$  MHz (for second-order intermodulation products) and  $|2f_1 - f_2| = 6.4$  GHz,  $|2f_2 - f_1| = 6.7$  GHz, (for third-order intermodulation products).

Figure 3.8 displays the RF link gain (RF filter response) for the optimum case  $\alpha_U = \alpha_L$  as a function of the frequency. The locations of the relevant RF tones are also displayed. As we can observe, the spectral characteristic of the optical filter in Figure 3.7 (Chebyshev Type-II) is translated or downconverted into the RF domain. In Figure 3.9, we represent the contour plots for the RF gain, the noise figure as well as the second- and third-order spurious free dynamic ranges as a function of  $K_1$  and  $K_2$  for a realistic case where  $\alpha_L = 3$  dB and  $\alpha_U = 6$  dB (note that, due to the presence of the optical filter in the upper branch, it is reasonable to assume that  $\alpha_L < \alpha_U$ ). As we can see, the  $K_1 = K_2$  direction defines a region for optimum operation for all these performance parameters. For this particular case, we represent in Figure 3.10 the values of the RF gain, Noise Figure,  $SFRD_2$  and  $SFDR_3$ , where the loss value of the upper branch  $\alpha_U$  is taken as a parameter.

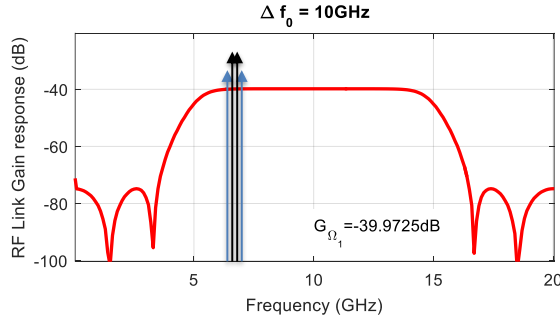


Figure 3.8 RF frequency response of the RF Front end obtained by self-beating and single detection.

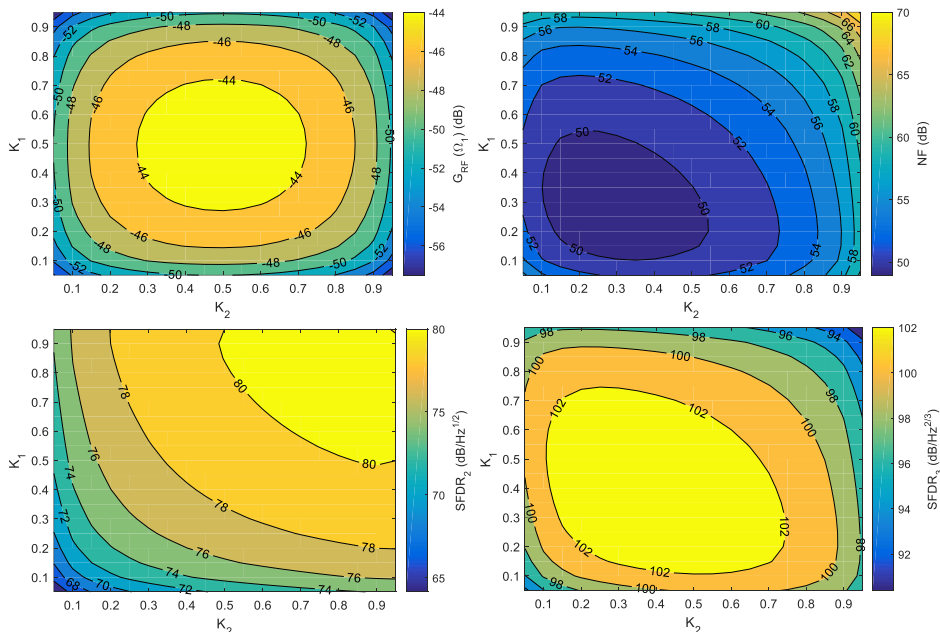


Figure 3.9 Contour plots vs the value of  $K_1$  and  $K_2$  for the RF Gain (Upper left), Noise Figure (Upper right), SFDR<sub>2</sub> (Lower left) and SFDR<sub>3</sub> (Lower right) for the tunable RF-front end obtained by self-beating and single detection. System parameters are given in the text with  $\alpha_L = 3$  dB and  $\alpha_U = 6$  dB.

The front-end performance is very sensitive to the loss in the two branches. As we can observe from Figure 3.10, it impacts three of the four figures of merit and the best values are obtained when  $\alpha_U = \alpha_L$ . However, as we have previously explained, it is realistic to assume that in practice  $\alpha_U > \alpha_L$ . Note that the best values for each figure of merit are obtained for different values of  $K = K_1 = K_2$ . In particular, the region around  $K = 0.5$  renders optimum values for the RF Gain and SFDR<sub>3</sub>, and almost optimum for SDFR<sub>2</sub> and NF. Since SDFR<sub>2</sub> is not relevant for suboctave frequency spanning systems and the NF value is only 1 dB above the minimum, we conclude that  $K = 0.5$  is the best operating point for this kind of configuration. Moreover, it is worth noticing that the MWP stage suffers from high-conversion losses assumed for the electro-optical and opto-electronic converters. Considering the quadratic relation between optical losses and RF loss, this can be mitigated using more efficient modulators and photodetectors, by increasing the optical power source or by integrating semiconductor optical amplifiers prior photodetection.

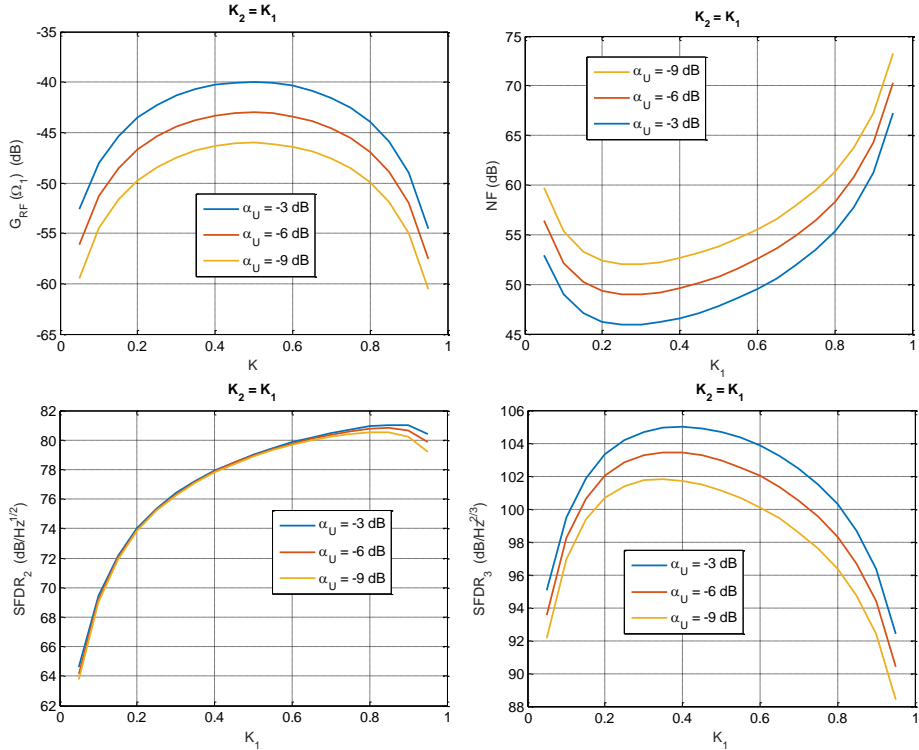


Figure 3.10 RF Gain (upper left), Noise Figure (upper right), Second-order Spurious free dynamic range (lower left) and Third-order Spurious free dynamic range (lower right) vs the value of the couplers  $K_1 = K_2 = K$ , taking  $\alpha_U$  as a parameter for the tunable RF-front end obtained by self-beating and single detection. System parameters are given in the text.

### *Results for self-beating intensity modulated balanced detection systems/links*

In this occasion, we combine the two photocurrents generated by the two outputs from the output coupler. We expect an improved performance in terms of optimum RF gain as well as in terms of noise figure due to the common mode noise rejection under balanced detection. We use the same values for the rest of the system parameters as in the single detection case.

Figure 3.11 displays the RF link gain (RF filter response) for the optimum case,  $K_2 = 0.5$ , and  $\alpha_U = \alpha_L$  as a function of the frequency. The locations of the relevant RF tones are also displayed and, again, for comparison single-sideband modulation with optical carrier suppression is considered. As in the single-detector case, the spectral characteristic of the optical filter (Chebyshev Type-II) has been translated or downconverted into the RF domain. Note that the optimum gain in this case is 6 dB

higher as the detected RF current is double as compared to the single-detector case (i.e. RF power is 4 times higher). In this case, the requirement for balanced detection directly implies that  $K_2$  should be as close as possible to 0.5. Nevertheless, and as in the previous example, we show in Figure 3.12 the contour plots for the RF gain, the noise figure and the second- and third-order spurious free dynamic ranges as a function of  $K_1$  and  $K_2$ . Again, we consider a realistic case where  $\alpha_L = 3$  dB and  $\alpha_U = 6$  dB.

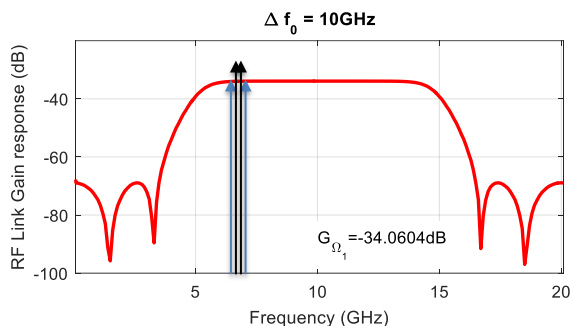


Figure 3.11 RF frequency response of the RF Front end obtained by self-beating and optimum balanced detection ( $K_2 = 0.5$ ).

In this case, we can observe that the  $K_2 = 0.5$  direction defines a region for optimum operation for most of the performance parameters. For this particular case, we represent in Figure 3.13 the values of the RF gain, Noise Figure, SFRD<sub>2</sub> and SFDR<sub>3</sub>. In this last figure, the loss value of the upper branch  $\alpha_U$  is taken as a parameter.

As in the single-detection case, the filter performance is very sensitive to the loss in the two branches. In this case, however, it impacts all the four figures of merit and the best values are obtained when  $\alpha_U = \alpha_L$ . However, as mentioned before, it is realistic to assume that in practice  $\alpha_U > \alpha_L$ . Another difference is the symmetric behaviour of all the figures of merit around the point  $K_1 = 0.5$ . We therefore conclude that  $K_1 = K_2 = 0.5$  is the best operating point for this kind of configuration.

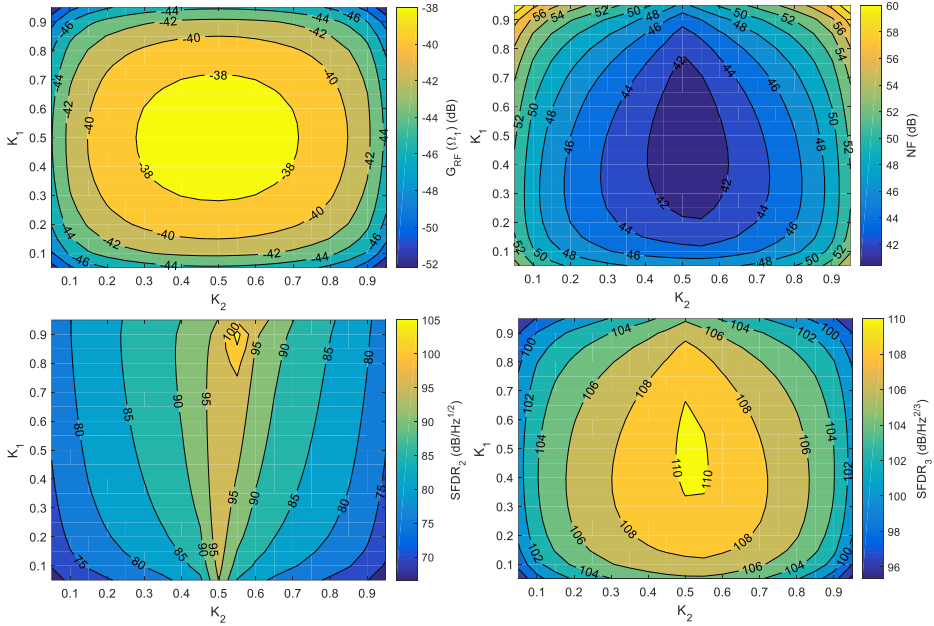


Figure 3.12 Contour plots vs the value of  $K_1$  and  $K_2$  for the RF Gain (Top left), Noise Figure (Top right), SFDR<sub>2</sub> (lower left) and SFDR<sub>3</sub> (Bottom right) for the tunable RF-front end obtained by self-beating and balanced detection. System parameters are given in the text with  $a_L = 3$  dB and  $a_U = 6$  dB.

### Discussion of the application example

The model developed for self-beating systems/links is very useful for two main reasons. In first place, it provides a means for the computation of the figures of merit in a novel class of MWP systems, which is called to play a significant role in integrated optic chips and, particularly, in programmable processors. Self-beating MWP configurations using OSSB modulation are ideal for small footprint subsystems, where a common laser source can be employed as both an optical source for modulation as well as a self-local oscillator, opening a completely new class of operation regime, where optical field spectral characteristics are directly translated into the RF region. In our case, the general model accounts for a considerable list of parameters that influence the overall performance.

A second added value of the model is that it can be employed as a tool for comparing different configurations of complex MWP systems designed to perform the same task and to choose the best option in terms of the standard performance metrics given by the figures of merit. In this context, in the example shown, the model provides relevant information to compare both detection approaches. For instance, it



provides the optimum operation conditions as far as the values of the coupling constants  $K_1$  and  $K_2$  are concerned. For both configurations, the ideal performance is achieved around the  $K_1 = K_2 = 0.5$  region, however the performance of each one is completely different. While the single-detector architecture shows a completely asymmetric performance around this point, the balanced-detector configuration results in a symmetric performance and is, therefore, more robust against drifts in the value of the coupling constants. For equal parameters, the balanced configuration renders a higher RF Gain (by 6 dB), higher  $\text{SFDR}_2$  (by 19 dB) and  $\text{SFDR}_3$  (by 7 dB) and lower NF (by 7 dB) compared to the single-detection case.

The model allows, as well, the analysis of the performance of a given configuration when one or several relevant parameters (losses, DC modulator biasing,  $V_\pi$ , etc.) are changed, providing an invaluable help in the design and performance prediction stages.

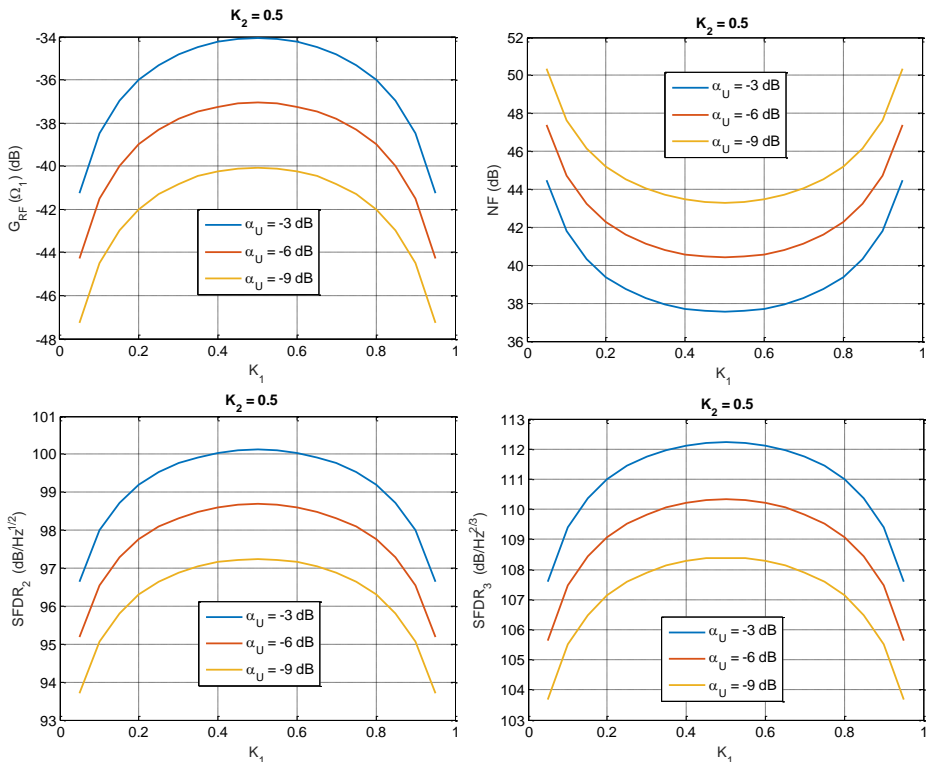


Figure 3.13 RF Gain (upper left), Noise Figure (Upper right),  $\text{SFDR}_2$  (Bottom left) and  $\text{SFDR}_3$  (Bottom right) vs the value of the input coupler  $K_1$  and taking  $\alpha_U$  as a parameter for the tunable RF front end obtained by self-beating and balanced detection ( $K_2 = 0.5$ ).

### 3.3.3 End-to-end model

In order to obtain the closed-form expressions for the overall FOMs as a function of the FOMs of both the MWP and RF parts, we will derive the linear and nonlinear RF terms in the transition point between these two segments (point (2) of Figure 3.14). From this point forward, the detected signal enters into the RF part of the signal processor where it is restored by an RF amplifier and filtered by an RF filter characterized by an electrical transfer function  $H_e(\Omega, \mathbf{C})$ , where  $\Omega$  is the angular electrical frequency, before exiting the processor.

In our treatment (and for simplicity) we will not show explicitly the dependence of the transfer functions and figures of merit with the configuration vector  $\mathbf{C}$  although this dependence must be understood to hold. We consider the following four possible operation regimes, [40]: Intensity modulation with single ( $I$ ) or balanced ( $I$ -BD) detection and phase modulation with single ( $\Phi$ ) or balanced ( $\Phi$ -BD) detection, self-beating intensity modulation ( $I, SB$ ) for both detection schemes.

For a modulating signal composed of two sinusoidal functions at different electrical angular frequencies  $\Omega_1$  and  $\Omega_2$  (point (1) of Figure 3.14), the photocurrent at the output of the MWP part considering up to the second-order and the most relevant third-order frequency contributions (point (2) of Figure 3.14) are included in Appendices A.1 and A.2 for each MWP modulation scheme, including direct and self-beating detection.

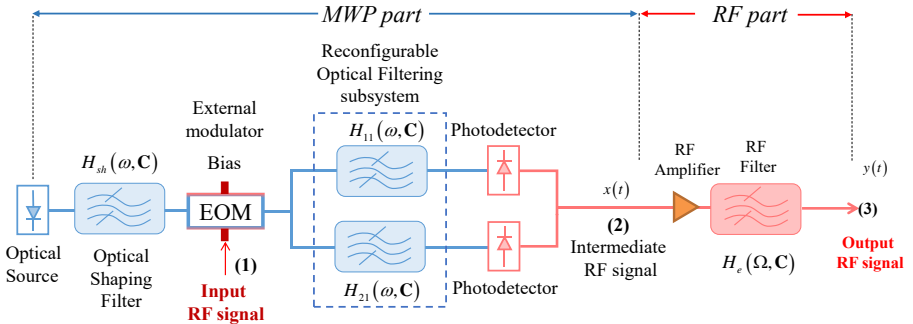


Figure 3.14 Generic concept of a software-defined reconfigurable MWP signal processor.

These input current terms to the RF part  $x(t)$  are subject to the action of the nonlinear RF amplifier modelled by a transfer curve  $y(t) = ax(t) + bx^2(t)$ , where  $a$  represents the amplifier gain and  $b$  its second-order nonlinear coefficient. The currents at the output of the RF filter for the signal, second- and significant third-order distortion terms are computed and specified in Appendix A.3 together with the power terms that get the FOM.

From these power values, one can get the overall processor FOMs as a function of the FOMs of the MWP part, the RF part gain  $G_{RF} = a^2 |H_e(\Omega)|^2$ , the RF Noise Figure  $NF_{RF}$  and the RF amplifier parameters. This way, the processor overall Gain is given by:

$$G^{Mod}(dB) = G_{RF}(dB) + G_{MWP}^{Mod}(dB). \quad (3.32)$$

The processor Noise Figure results in:

$$NF^{Mod}(dB) = NF_{RF}(dB) + NF_{MWP}^{Mod}(dB). \quad (3.33)$$

For the dynamic range, and the particular case of self-beating, we will assume the domination of the self-beating term. For each modulation, the processor second- and third-order  $SFDR$  are, respectively, given by:

$$\begin{aligned} SFDR_2^{Mod}(dB \cdot Hz^{1/2}) &= SFDR_{2,MWP}^{Mod}(dB \cdot Hz^{1/2}) - \left[ |H_{eN}(\Omega_1 - \Omega_2)| (dB) + \frac{1}{2} NF_{RF}(dB) \right] \\ &\quad - 5 \log(1 + T_2^{Mod}) \\ \text{for } T_2^{Mod} &= \varepsilon_{Mod} \left( \frac{b}{a} \right)^2 \frac{|A_{\Omega_1}^{Mod}|^2 |A_{\Omega_2}^{Mod}|^2}{|A_{\Omega_1 - \Omega_2}^{Mod}|^2} = \frac{P_{IMD_2,RF}}{P_{IMD_2,MWP}^{Mod}} \\ \text{and } \varepsilon_{Mod} &= \begin{cases} \varepsilon_I = 4I_{dc}^2 \sin^4(\phi_{dc}) \\ \varepsilon_\Phi = 16I_{dc}^2 \\ \varepsilon_{I,SB} = 4I_{dc}^2 \sin^4(\phi_{dc}) \alpha_U \alpha_L C^2 D^2 \end{cases}, \end{aligned} \quad (3.34)$$

$$\begin{aligned} SFDR_3^x(dB \cdot Hz^{2/3}) &= \\ SFDR_{3,MWP}^{Mod}(dB \cdot Hz^{2/3}) &- \frac{2}{3} \left[ |H_{eN}(2\Omega_1 - \Omega_2)| (dB) + NF_{RF}(dB) \right] - \frac{10}{3} \log(1 + T_3^{Mod}) \\ \text{for } T_3^{Mod} &= \varepsilon_{Mod} \left( \frac{b}{a} \right)^2 \frac{\left[ |A_{\Omega_1}^{Mod}|^2 |A_{\Omega_1 - \Omega_2}^{Mod}|^2 + |A_{\Omega_1}^{Mod}|^2 |A_{\Omega_2 - \Omega_1}^{Mod}|^2 + |A_{2\Omega_1}^{Mod}|^2 |A_{\Omega_2}^{Mod}|^2 \right]}{|A_{2\Omega_1 - \Omega_2}^{Mod}|^2} = \frac{P_{IMD_3,RF}}{P_{IMD_3,MWP}^{Mod}} \\ \text{and } \varepsilon_{Mod} &= \begin{cases} \varepsilon_I = 4I_{dc}^2 \\ \varepsilon_\Phi = 16I_{dc}^2 \\ \varepsilon_{I,SB} = 4I_{dc}^2 \alpha_U \alpha_L C^2 D^2 \end{cases}, \end{aligned} \quad (3.35)$$

where:

- $|H_{eN}(\eta\Omega_1 - \Omega_2)|$  (dB) =  $|H_e(\eta\Omega_1 - \Omega_2)|$  (dB) -  $|H_e(\Omega_1)|$  (dB), for  $\eta = \{1,2\}$ , is defined as the RF filter transfer function at each intermodulation term normalized to the fundamental.
- $T_2^{Mod}$  and  $T_3^{Mod}$  are coefficients that represent the quotient between the RF power of the intermodulation distortion terms caused by the RF part, respectively  $P_{IMD2,RF}$  and  $P_{IMD3,RF}$ , and the RF power of the intermodulation terms caused by the MWP part and subsequently amplified by the RF stage, respectively  $P_{IMD2,MWP}$  and  $P_{IMD3,MWP}$ .

This way, the greater the  $T_2^{Mod}$  or  $T_3^{Mod}$ , the more limiting the effect of the distortion introduced by the RF part is to the dynamic range of the processor. Note that, for the self-beating scheme, we have considered that the beating-term is dominant.

The behaviour of the overall processor gain and noise figure predicted by (3.32), (3.33) is quite straightforward to interpret. The gain  $G^{Mod}$  is actually the sum in logarithmic units of the MWP and RF individual gains hence the two parts can be designed independently to achieve an overall gain target. A similar behaviour is observed for the overall noise figure  $NF^{Mod}$  with respect to the noise figure values of the MWP and the RF parts. The situation is, however, different when we consider the dynamic range parameters since it is not possible, in principle, to decompose the contributions of the MWP and the RF parts as they are coupled by the  $T_2^{Mod}$  and  $T_3^{Mod}$  coefficients, (3.34), (3.35). As a consequence, it is important to focus our performance analysis on the evaluation of the system linearity.

The developed end-to-end model is extremely powerful and comprehensive. It provides analytical expressions for the evaluation of the main figures of merit characterizing the full end-to-end performance of the processor and taking into consideration the impact of both the photonic and the RF parts. Although these figures are expressed in terms of internal parameters and transfer functions that can be changed by means of suitable programming, the overall expressions are common for all the represented cases, regardless of the particular functionality for which the processor is programmed at a given instant of time.

From the previous examples can be inferred the low efficient conversions in passive MWP systems that results in low RF gain. Higher optical power, lower modulator biasing and higher photodetector responsivities directly impact on greater RF gains. In the literature, we can find that EDFAs and SOAs are employed to obtain even positive RF Gain solutions or to, at least, compensate loss. This is crucial due to the quadratic relation between optical losses and RF loss. Special attention must be paid in the maximum optical inputs admitted by modulators and photodetectors. When employing optical amplification, the ASE noise is often dominant over the rest. In addition, the RF amplifier and the electronic filter can be employed to optimize

this Figures of Merit, but wideband RF amplifiers with operational frequencies greater than 25 GHz are difficult to find.

Each application might require stronger or softer specifications. For example, commercial high-frequency MWP transceivers are in the order of 5-10 dB of RF gain, 7-10 dB of NF and 100-108 dB Hz<sup>2/3</sup>, [35]. In the case of IFMs, the RF gain is not the most limiting FoM, since a minimum RF input signal greater than the system sensitivity will estimate the input frequency.

Larger SFDRs imply that the difference between the maximum fundamental signal power and the distortion terms that will degrade the system's performance becomes larger. Several linearization techniques can be applied to optimize this FoM.

### 3.4 Linearization

#### 3.4.1 Direct Detection end-to end linearization

The end-to-end model provides a simple physical interpretation of the roles played by the photonic and the RF parts, even in the case of nonlinear operation. As mentioned, as far as gain and noise figures are concerned, the model predicts an uncoupled and additive behavior (in dB units) of the photonic and RF parts. Therefore, if the impact of nonlinearity is of no particular concern, the designs of both parts can be carried independently. However, the processor performance as far as dynamic range is concerned, shows a coupled behavior between the two stages. For instance, considering third-order nonlinearities (a similar analysis can be carried out with second-order nonlinearities), the overall SFDR in Eq. (3.35) is composed of three terms. The first one corresponds to the overall dynamic range related to the internal photonic stage ( $SFDR_{3,MWP}^{Mod}$ ) and is shown in Figure 3.15.

The second term is an uncoupled contribution arising exclusively from to the RF stage that can improve or degrade the dynamic range of the preceding photonic part. The first case happens when the undesired nonlinear term is sufficiently rejected by the RF filter so that  $|H_{eN}(2\Omega_1 - \Omega_2)|$  (dB) +  $NF_{RF}$  (dB) < 0. In the second case,  $|H_{eN}(2\Omega_1 - \Omega_2)|$  (dB) +  $NF_{RF}$  (dB) > 0, the dynamic range is degraded as it is shown in Figure 3.15. The third term represents the coupling between the photonic and the RF sections of the processor. This coupling depends on the parameter  $T_3^{Mod} = P_{IMD3,RF} / P_{IMD3,MWP}$  that relates the RF power of the nonlinear terms generated at the RF and the photonic parts of the processor. The coupling appears because part of the nonlinearities generated by the RF stage are due to the mixing of linear and nonlinear terms generated by the previous photonic stage. Its effect is the shifting of the system's IMD<sub>3</sub> curve as shown in Figure 3.15. In fact, if the nonlinear coefficient  $b$  of the RF part vanishes, then  $T_3^X = 0$  and the third term in Eq. (3.35) becomes zero

and therefore both the photonic and RF parts can be independently designed as far as RF gain, noise figure and dynamic range parameters are concerned.

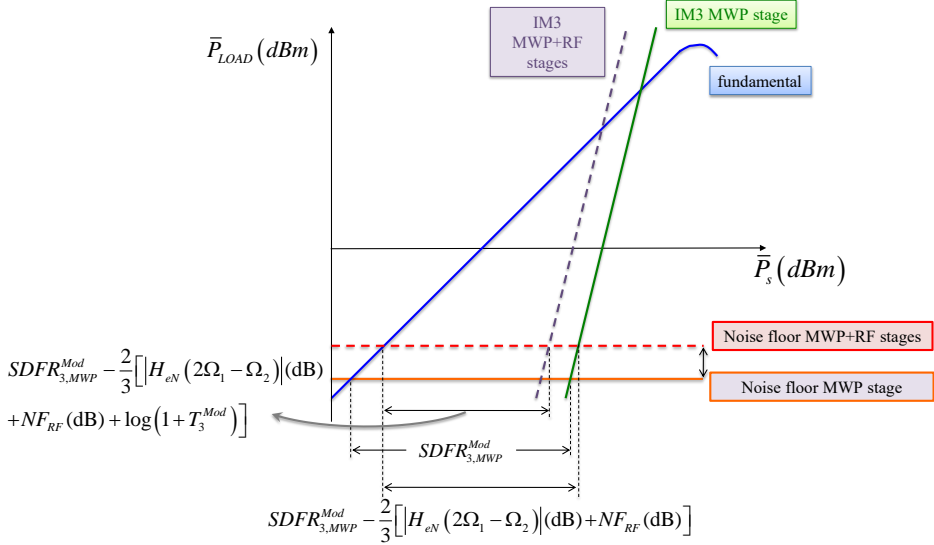


Figure 3.15 Impact of the three terms in Eq. (3.35) on the overall third-order SFDR of the processor.

It is expected that NF and SFDR tradeoff relationships when designing the general processor architecture will be substantially different than those of ASPICs. This is due to the fact that the former will most probably include generic optical amplifying stages that will increase the noise floor and switching loopbacks, which will increase losses. However, at the same time, the filtering stages will have the possibility of reconfiguration and thus provide a higher suppression of intermodulation terms. All in all, the processor architecture is expected to provide different programming alternatives towards obtaining more flexible NF and SFDR tradeoff relationships.

Depending on the required functionality, either an overall linear operation will be targeted (e.g. microwave filtering, beam-steering, etc.), whereas in other cases, it is the nonlinear performance that needs to be boosted (e.g. up- and down-conversion, frequency multiplication, etc.). The model presented here will provide a valuable tool for the design of both the photonic and RF stages and, if required, the necessary coupling between them to exacerbate an overall nonlinear behavior.

We can illustrate the model applicability, focusing on system linearity, with three examples already reported in the literature so that we cover different optical filtering subsystems and detection schemes. We consider in particular: (1) an integrated frequency discriminator for phase-modulated microwave photonics links with direct

balanced detection (FM-DD) [13]; (2) an integrated optical bandpass filter (BPF) with single detection [82]; and (3) an asymmetric MZI with balanced detection [40]. Figure 3.16 illustrates the schematic layout of the three optical filters.

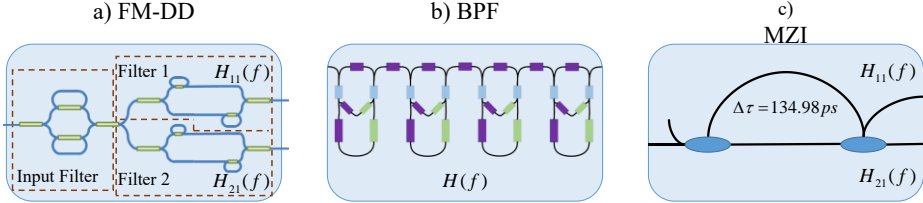


Figure 3.16 Circuit layouts of the three optical filtering subsystems considered: a) FM-DD, b) BPF and c) MZI.

The closed-form expressions for the global end-to-end FOMs derived in (3.32)-(3.35) require the knowledge of the two parallel optical transfer functions,  $H_{11}(\omega)$  and  $H_{21}(\omega)$ , that describe the reconfigurable optical filtering subsystem for a given state of the configuration vector  $\mathbf{C}$ . Figure 3.17 shows the transfer function of the three optical filter examples as a function of the microwave frequency  $f = \Omega/2\pi$ . We must note that the FM-DD operates in phase modulation, the BPF in intensity modulation, while we consider both intensity and phase modulation for the MZI. In all the scenarios, we assume a monochromatic optical source whose spectral density function is approximated by a delta function. The following parameters are kept fixed in all the computations: Mach-Zehnder intensity modulator biased at quadrature point  $\phi_{dc} = \pi/2$ ,  $I_{dc} = 5$  mA, input and output resistances  $R_{in} = R_{out} = 50 \Omega$  and 20-dB RF amplifier gain ( $a = 10$ ).

As it is shown in Figure 3.16 (a), the PIC implementing the FM-DD is composed of two branches that are labeled as Filter 1 and Filter 2 and characterized, respectively, by  $H_{11}(\omega)$  and  $H_{21}(\omega)$ . This photonic discriminator implements two functionalities: (1) the conversion of phase-modulated signals to intensity modulation and (2) the enhancement of the radio-over-fiber link performance by increasing the linearity and/or suppressing the noise. We consider two different frequency locations for the modulating tones: ( $f_1 = 7$  GHz and  $f_2 = f_1 + 1$  MHz) and ( $f_1 = 5$  GHz and  $f_2 = f_1 + 1$  MHz).

The integrated BPF is composed of four cascaded stages, each one implemented with ring resonators in an asymmetrical MZI structure with feedback [82], as depicted in Figure 3.16 (b). By designing each filter stage to provide a pole, we obtain a bandpass response with a free spectral range of 15.6 GHz. In this case, we place the microwave frequencies in the vicinity of the first resonance:  $f_1 = 16.5$  GHz and  $f_2 = 14.7$  GHz.

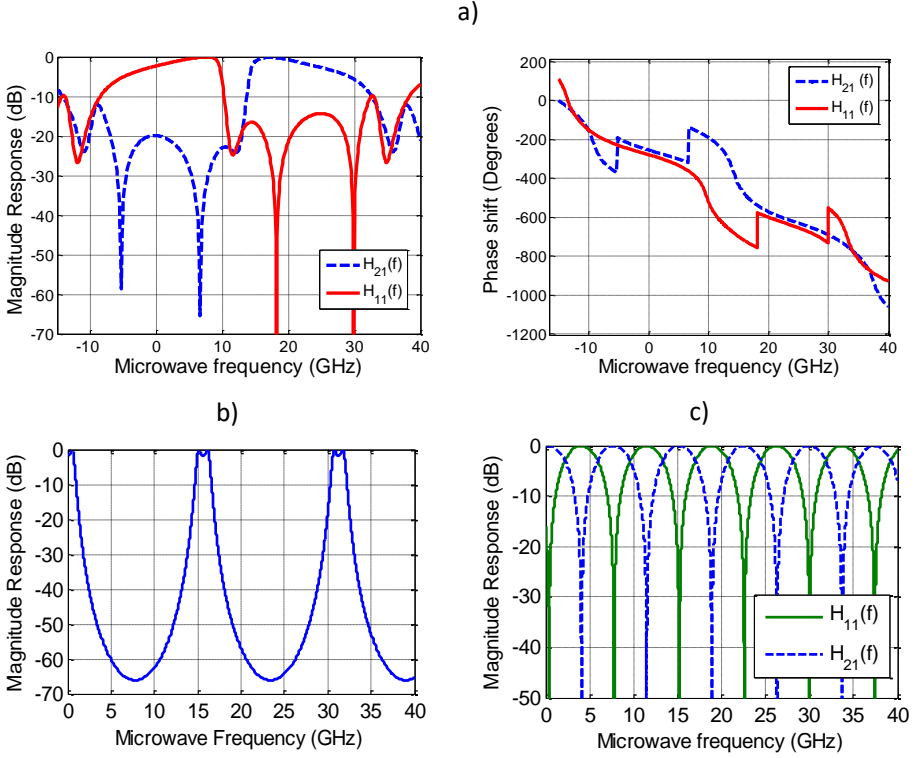


Figure 3.17 Transfer function of the three optical filtering subsystems considered as a function of the microwave frequency  $f$ : a) FM-DD (up), b) BPF (lower left) and c) MZI (lower right).

The asymmetric MZI filter is represented by two parallel optical filters with the following transfer functions:

$$H_{11}(\omega) = j\sqrt{\alpha_{MZI}}e^{j\omega\tau/2}\sin(\omega\tau/2) \quad \text{and} \quad H_{21}(\omega) = j\sqrt{\alpha_{MZI}}e^{j\omega\tau/2}\cos(\omega\tau/2) \quad (3.36)$$

where  $\alpha_{MZI} = 1$  is the MZI insertion loss and  $\tau = 134.98$  ps is the MZI differential time delay, [40]. We set the MZI to operate at quadrature, i.e. applying  $\omega_0\tau = \pi/2$ , and place the microwave tones at the frequencies  $f_1 = 17.3$  GHz and  $f_2 = 15.3$  GHz.

As we stated above, we cannot obtain the end-to-end processor dynamic range as the direct decomposition into its MWP and RF individual contributions for the dynamic range. As it can be concluded from (3.34), (3.35), the difference in the SFDR between the overall processor and the MWP stage, i.e.  $SFDR_{2}^{Mod} - SFDR_{2,MWP}^{Mod}$



and  $SFDR^{Mod}_3 - SFDR^{Mod}_{3,MWP}$ , depends on the  $NF_{RF}$ , the normalized electrical filter response and the coefficients  $T_2^{Mod}$  and  $T_3^{Mod}$ .

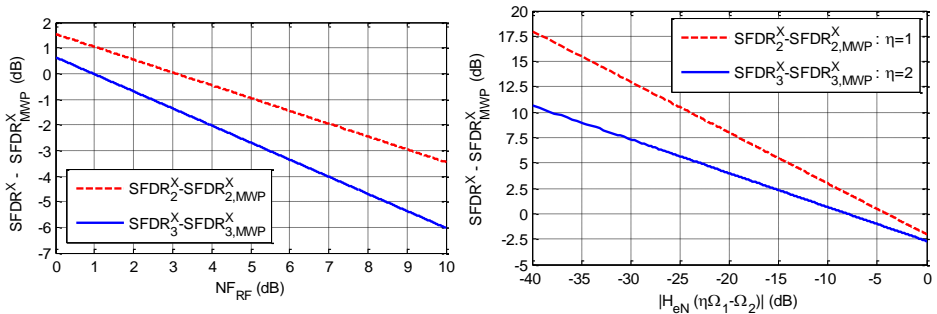
Table 3.1 gathers the overall values of the processor FOMs computed for each one of the MWP application examples described above for a given RF stage. In particular, we consider a quasi-linear RF amplifier given by  $b/a = 0.15$  and  $NF_{RF} = 4$  dB as well as an electrical filter characterized by  $|H_{eN}(\Omega_1)| = |H_{eN}(\Omega_2)| = 0$  dB,  $|H_{eN}(\Omega_1 - \Omega_2)| = -3$  dB and  $|H_{eN}(2\Omega_1 - \Omega_2)| = -2$  dB. For this set of typical RF parameters, we find that the coefficients  $T_2^{Mod}$  and  $T_3^{Mod}$  are both  $\ll 1$  since the quotient involving the spectral optical coefficients  $A^{Mod}_{\Omega_s}$  in (3.11)-(3.15) is not big enough as compared to the term  $\varepsilon_{Mod}(b/a)^2$ , (which is of the order of  $10^{-6}$  and  $10^{-5}$ , respectively for phase and intensity modulation). This means that for this particular design the impact of the MWP and the RF parts on the final dynamic range is decoupled, similarly to the behavior of the overall link gain and noise figure. Under this condition, if we keep using a linear or quasi-linear RF amplifier ( $b/a = 0.15$ ), the variation in the dynamic range,  $SFDR^{X_2} - SFDR^{X_{2,MWP}}$  and  $SFDR^{X_3}$ , will depend solely on the noise figure of the RF stage and the response of the electrical filter, (see (3.34), (3.35)). In a first set of simulations, we will analyze the impact of the RF part on the dynamic range when varying either  $NF_{RF}$  or the absolute value of  $H_{eN}(\eta\Omega_1 - \Omega_2)$ .

Figure 3.18 (left) shows both the second- and third-order distortion variations as a function of  $NF_{RF}$  for all the optical filtering subsystems considered. As described before, the results are identical for all the MWP stage cases evaluated since  $T_2^{Mod}$  and  $T_3^{Mod}$  are negligible. The difference in the slopes for the SFDR variation can be understood from (3.34), (3.35) since this variation has a slope of  $-1/2$  for second-order nonlinearities while  $-3/2$  for third-order nonlinearities. We can see that for a 3-dB degradation of the SFDR variation, this behavior results in a maximum  $NF_{RF}$  change of 6.2 and 4.5 dB, respectively. Figure 3.18 (right) illustrates the impact of the magnitude value of the RF filter at the frequencies of the intermodulation terms when keeping the rest of the simulation parameters fixed. Again, identical performance results were obtained for each one of the designs of the MWP stage. We can see how the SFDR variation increases as the absolute value of  $H_{eN}(\eta\Omega_1 - \Omega_2)$  decreases. The different slopes for the SFDR variation are also understood from (3.34), (3.35) since this variation has a logarithmic slope of  $-1$  and  $-2/3$ , respectively, for the second- and third-order nonlinearities. We can see that the dynamic range related to the MWP part can be improved (SFDR variation greater than 0 dB) if the undesired distortion term is sufficiently rejected by the RF filter. To be more precisely,  $SFDR^{X_{2,MWP}}$  and  $SFDR^{X_{3,MWP}}$  are unaltered (SFDR variation of 0 dB) respectively for a 4-dB and 8-dB rejection of the RF distorting term as compared to the RF signal tone. This information is actually very useful since it allows a proper design of the RF filtering stage in order to improve the dynamic range of the MWP subsystem.

Table 3.1 – Overall FOM computed values for the three optical filtering subsystems considered

Optical filter	Scheme <i>Mod/Det</i>	$SFDR_2^{Mod}$ (dB·Hz <sup>1/2</sup> )	$SFDR_3^X$ (dB·Hz <sup>2/3</sup> )	$G^{Mod}$ (dB)	$NF^{Mod}$ (dB)
FM-DD ( $f_1 = 7$ GHz)	$\Phi$ -BD	99.68	105.36	0.17	$NF_{MWP}^{Mod}$ (dB) + 4
FM-DD ( $f_1 = 5$ GHz)	$\Phi$ -BD	88.02	102.27	-3.60	$NF_{MWP}^{Mod}$ (dB) + 4
BPF	$I$	84.36	115.71	-7.87	$NF_{MWP}^{Mod}$ (dB) + 4
MZI	$I$ -BD	83.11	107.54	-5.20	$NF_{MWP}^{Mod}$ (dB) + 4
	$\Phi$ -BD	79.79	109.28	1.75	$NF_{MWP}^{Mod}$ (dB) + 4

However, the rejection of third-order distorting terms in the electrical domain is difficult to achieve efficiently since they are placed close or even within the signal bandwidth. As mentioned, the suppression of these terms before leaving the MWP stage is advisable. The processor architecture is expected to provide different programming alternatives to implement flexible filtering stages for distortion suppression and different modulation/detection schemes to enhance system linearity or to foster the non-linear terms as desired. Another possibility, is to suppress the intermodulation terms prior to the RF amplifier by means of another electrical filter.

Figure 3.18– SFDR variation as a function of  $NF_{RF}$  (left) and as a function of  $|H_{eN}(\eta\Omega_1 - \Omega_2)|$ ,  $\eta = \{1,2\}$ , (right), for all the optical filtering subsystems considered: FM-DD, BPF and MZI.

In a second set of simulations, we analyze the impact of the RF amplifier linearity on the SFDR variation as a function of the ratio  $b/a$  in the range from 0 to 10 while keeping fixed  $NF_{RF}$  and  $H_{eN}(\eta\Omega_1 - \Omega_2)$ . Note that  $b/a$  relationships for commercial

RF amplifiers are often in the range (0.1-2), but it is extended to 10 to incorporate the highly nonlinear cases. Under these conditions, the dynamic range variation behaves differently when we compare the different optical filtering subsystems. For the BPF and the MZI examples, the impact of the RF amplifier linearity is not significant and we obtain nearly constant values for both dynamic range variations:  $SFDR^X_2 - SFDR^X_{2,MWP} = -0.45$  dB and  $SFDR^X_3 - SFDR^X_{3,MWP} = -2.02$  dB. However, a different behavior is observed in the case of the optical frequency discriminator, depending on the location of the modulating tones. Figure 3.19 shows the SFDR variation as a function of the ratio  $b/a$  for the FM-DD for both modulating conditions and different values of the RF noise figure. On one hand, we see how the variation of the second-order SFDR for the microwave frequencies  $f_1 = 7$  GHz and  $f_2 = f_1 + 1$  MHz (solid lines) decreases substantially as the non-linearity of the RF amplifier increases. This is sustained by the fact that the impact of the MWP and the RF parts on the overall dynamic range is coupled by the spectral term  $T_2^{Mod}$ . The 3-dB degradation point at  $b/a = 2.65$  sets the boundary between the MWP-limited and the RF-limited second-order SFDR. On the other hand, the SFDR variation becomes nearly constant if the microwave tones are placed at the frequencies  $f_1 = 5$  GHz and  $f_2 = f_1 + 1$  MHz (dashed lines) since, in this case, the spectral coefficients reduce the  $T_2^{Mod}$  contribution. A similar condition is indeed shown for the third-order SFDR where the dynamic range variation remains constant with the ratio  $b/a$  for both modulating conditions.

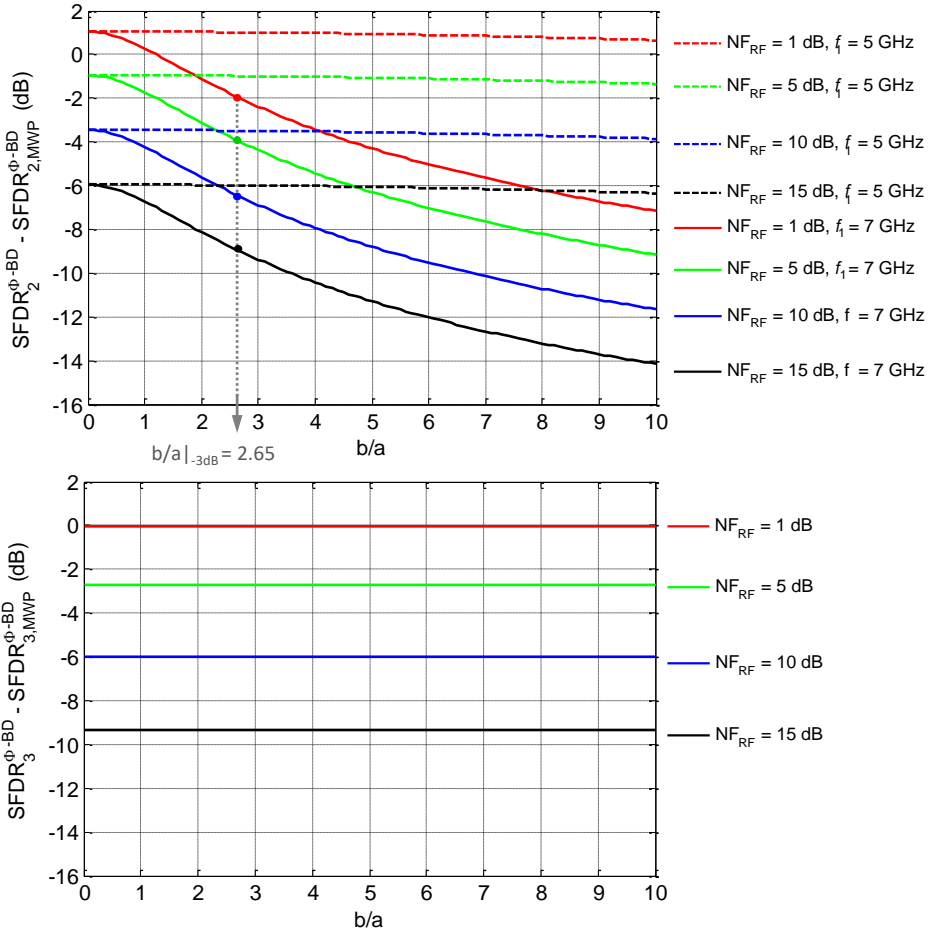


Figure 3.19 (Upper) Second- and (lower) third-order SFDR variation as a function of  $b/a$  for the FM-DD.

### 3.4.2 Linearization of Self-Beating schemes at the MWP stage employing a Dual Parallel Mach-Zehnder Modulator

As stated in the previous section, it is possible to design or configure the RF stage of a MWP system to enhance the system linearization. However, due to the proximity of the third-order distortion terms it is advisable to overcome the linearization task in the optical domain.

Some linearization techniques can be performed directly in the MWP part, prior to the pure RF part of the processor. The dual parallel MZM architecture has been employed for the mitigation of third-order harmonic and intermodulation distortions on IM/DD schemes, [83, 84]. We have developed a linearization model that can be applied to the self-beating modulation/detection scheme developed in the previous sections, when a dual parallel MZM is employed (DPMZM), [85].

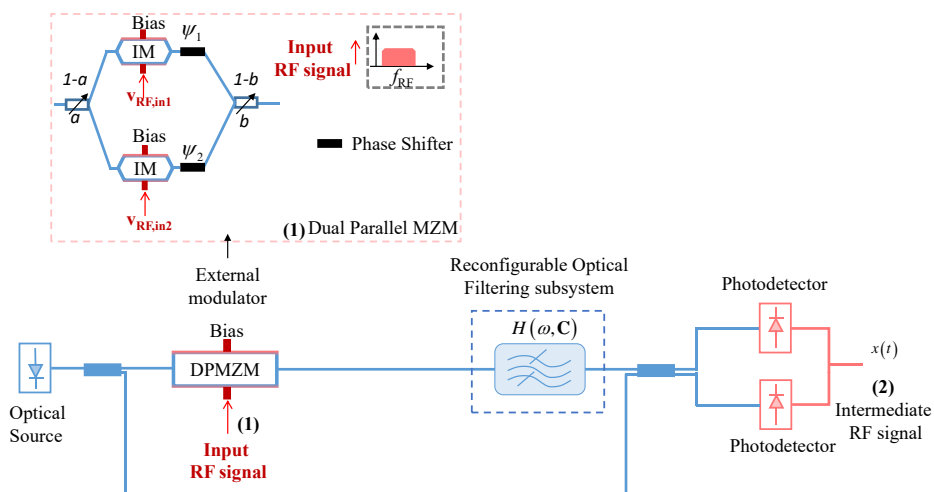


Figure 3.20 Schematic of a Self-beating filtered MWP link or MWP system applying Intensity modulation with a Dual Parallel MZM (inset) with balanced detection scheme.

Figure 3.20 shows the layout of a general self-beating filtered MWP system based in self-homodyne coherent detection with amplitude modulation described in [81], where, in this case, the modulation stage incorporates a DPMZM to perform the linearization process. Similarly to the technique developed in [83], for direct detection systems using two parallel MZMs, we have derived an analytical end-to-end model exploiting the same physical principle of achieving destructive interference in the detected photocurrent for a desired intermodulation order and maximizing the fundamental term relation. The linearization process is carried providing the optimum parameters of the modulator to suppress the  $IMD_3$ .

The linearized system design will have seven degrees of freedom: the two bias voltages of the MZMs defined by  $\phi_{dc,i} = \pi V_{dc,i}/V_{\pi}$ , the excess coupling ratio  $\gamma$  of the (same) RF signal supplied to one of the modulators with respect to the other, (where  $\phi_{rf,1} = \pi V_{rf}/V_{\pi}$  and  $\phi_{rf,2} = \gamma \phi_{rf,1}$ ), the optical in- and out- coupling ratios in the DPMZM ( $a$  and  $b$ , respectively) as well as the phase shifts for the upper and the lower arms ( $\psi_1$  and  $\psi_2$ ). The physical meaning of  $\gamma > 1$  is related to the increase in the RF amplitude voltage that has to be applied to one modulator with respect to the value

applied to the other and therefore, can be considered as an electrical power penalty  $EP = 20 \log(\gamma)$ .

By developing the same analytical procedure used in the self-beating intensity modulated system [81], but including the DPMZM, we can obtain the fundamental tone  $C$  at the frequency  $\Omega_1$  given by the photocurrent beating term  $I_b(\Omega_1)$ , and those associated to the intermodulation tones  $IMD_2$  and  $IMD_3$ . All of them are computed and included in the Appendix A.4.

The third-order linearization can be achieved by finding a value of  $\gamma$  that cancels the  $IMD_3$  photocurrent term and maximises at the same time the fundamental photocurrent term without increasing the second-order intermodulation  $IMD_2$  photocurrent. By forcing the  $IMD_3$  to zero and solving for  $\gamma$ , we obtain the optimum value as:

$$\gamma = \sqrt[3]{-\sqrt{\frac{(1-a)(1-b)}{ab}} \left[ \frac{H(\omega_0 + 2\Omega_1 - \Omega_2)e^{j\psi_1} - H^*(\omega_0 - 2\Omega_1 + \Omega_2)e^{-j\psi_1}}{H(\omega_0 + 2\Omega_1 - \Omega_2)e^{j\psi_2} - H^*(\omega_0 - 2\Omega_1 + \Omega_2)e^{-j\psi_2}} \right] \frac{\cos(\phi_{dc1}/2)}{\cos(\phi_{dc2}/2)}}. \quad (3.37)$$

In practice, we prefer a real value of  $\gamma$  since otherwise an extra RF phase shifter has to be inserted prior to the RF modulation input of one of the MZMs. A real value for  $\gamma$  is obtained if  $\psi_1 = \pi$  and  $\psi_2 = 0$ :

$$\gamma = \sqrt[3]{\sqrt{\frac{(1-a)(1-b)}{ab}} \frac{\cos(\phi_{dc1}/2)}{\cos(\phi_{dc2}/2)}}. \quad (3.38)$$

For comparison purposes, it is necessary to know how the linearization process affects the fundamental and the  $IMD_2$  terms. Ideally, the photocurrent associated to the linearized fundamental tone  $C_L$  should not decrease whereas the  $IMD_{2,L}$  should do. Figure 3.21 (a) shows the spectral components when one MZM is employed without linearization, i.e.  $a = b = 0$ ,  $\gamma = 0$ , while Figure 3.21 (b) shows the spectral components after the linearization process that employs the DPMZM. As a figure of merit to evaluate the change produced in the fundamental and the  $IMD_2$  contributions by the linearization process, we define the ratio between the linearized and un-linearized second order intermodulation terms  $IMD_{2,L}/IMD_2$  and the ratio between the linearized and un-linearized fundamental terms  $C_L/C$  as:

$$\frac{CIMD_{2,L}}{CIMD_2} = \frac{C_L/IMD_{2,L}}{C/IMD_2} = \frac{\hat{I}_{b,L}(\Omega_1)/\hat{I}_{b,L}(\Omega_1 - \Omega_2)}{\hat{I}_b(\Omega_1)/\hat{I}_b(\Omega_1 - \Omega_2)}. \quad (3.39)$$

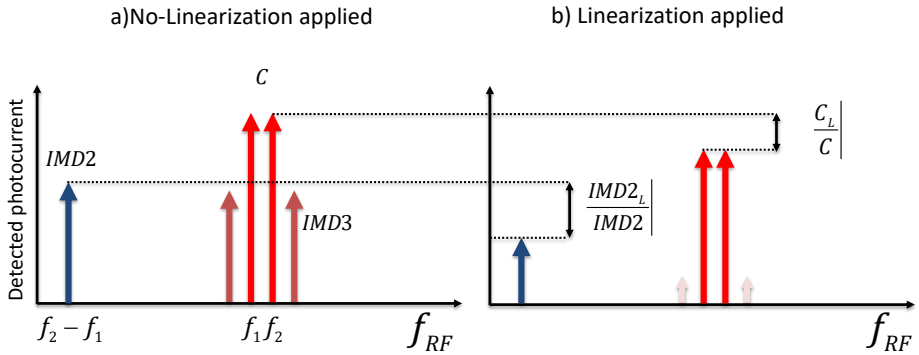


Figure 3.21 Photodetected spectrum without (Left) and with the applied linearization (Right).

We require values greater than 1 for this figure of merit to guarantee that the second-order distortion compared to the fundamental term is not increased as a result of the  $IMD_3$  suppression. We have identified two cases of practical interest due to their simplicity in terms of the required values for the bias points and phase shifters in the two arms of the DPMZM.

*Case 1:  $\psi_1 = \pi$  and  $\psi_2 = 0$ ,  $\varphi_{dc,1} = \varphi_{dc,2} = \pi/2$*

In this case, our degrees of freedom in the DPMZM are the coupling constants ( $a$  and  $b$ ) of its in- and out- Y junctions, which we can design, optimize and fix. Both upper- and lower- arm modulators are biased in quadrature and will modulate the same RF signal. However, as previously mentioned, the lower modulator will be feed with the same RF signal as the upper modulator but with a voltage amplitude excess given by  $\gamma = \phi_{RF2}/\phi_{RF1}$ . Finally, there is a static  $\pi$ -phase shift between the upper and lower arms of the DPMZM to produce destructive interference between the parallel outputs. By substituting the parameters values, we can directly obtain from Eq. (3.38) the necessary value of  $\gamma$  to suppress the  $IMD_3$ :

$$\sqrt{(1-a)(1-b)} - \gamma^3 \sqrt{ab} = 0. \quad (3.40)$$

The ratio between linearized and unlinearized ( $a = b = 0$ ) fundamental tone currents  $C_L/C$  is obtained the fundamental term equation as:

$$\frac{C_L}{C} = \sqrt{(1-a)(1-b)} - \gamma \sqrt{ab}, \quad (3.41)$$

and must be maximized subject to the condition given by Eq. (3.40). This is done by means of a Lagrange multipliers method, which is described in detail in the Appendix A.4. The outcome of this optimization renders the following values for  $a$  and  $b$ :

$$a = b = \frac{1}{1 + \gamma^3}. \quad (3.42)$$

Under this condition, the ratios between the linearized photocurrents and the unlinearized terms are obtained as:

$$\frac{C_L}{C}_{MAX} = \frac{\gamma(\gamma^2 - 1)}{1 + \gamma^3}; \quad (3.43)$$

$$\frac{IMD_{2,L}}{IMD_2} = \frac{\hat{I}_L(\Omega_1 - \Omega_2)}{\hat{I}(\Omega_1 - \Omega_2)} = \frac{\gamma^2(\gamma - 1)}{1 + \gamma^3}. \quad (3.44)$$

Substituting (3.43) and (3.44) in (3.39), we have:

$$\frac{CIMD_{2,L}}{CIMD_2} = 1 + \frac{1}{\gamma}. \quad (3.45)$$

Figure 3.22 (upper left) shows the results computed for (3.43)-(3.45) against the electrical power penalty  $EP = 20 \log(\gamma)$ , [83]. As far as the fundamental term is concerned, the black trace indicates that, in principle, almost negligible optical penalty can be achieved in theory provided that an electrical penalty of over 10 dB can be assumed. In practical terms, and due to the coupling of the electrical penalty with the values of the optimized splitting ratios for the input and output Y branches of the DPMZM, (Eq. (3.42)), there is a maximum electrical penalty that can be assumed if realistic splitting ratios are to be employed. This is illustrated in the lower left part of Figure 3.22, where we plot Eq. (3.42) versus  $EP$ . If, for instance, a minimum value of  $a = 0.05$  can be assumed due to fabrication tolerances, the maximum affordable electrical penalty is around 9 dB, which results in an optical penalty slightly below 1 dB. In a similar way, the blue trace curve describes the system's behavior as related to  $IMD_2$ . The first interesting feature is that, for any value of the electrical penalty, the blue curve remains above the black curve. This means that upon this third-order linearization process the  $IMD_2$  photocurrent always suffers a higher attenuation than that of the fundamental tone. The solid red line indicates that, at the same time that  $IMD_3$  is suppressed, the  $IMD_2$  term experiences a greater attenuation as compared to that experienced by the fundamental tone. This means that as far as  $IMD_2$  is concerned, the system linearity is also improved.



Case 2:  $\psi_1 = \pi$  and  $\psi_2 = 0$ ,  $\varphi_{dc,1} = \varphi_{dc,2} = \pi/2$ ,  $b = 1/2$

This is a particular condition of Case 1, where  $b$  is fixed to  $1/2$  to obtain two balanced modulated outputs. Since now there is one variable less than in (3.40), we obtain a direct relation that yields the optimum operation:

$$a = \frac{1}{1 + \gamma^6}; \quad (3.46)$$

$$\frac{C_L}{C_{\max}} \Big|_{\text{max}} = \frac{\gamma(\gamma^2 - 1)}{\sqrt{2(1 + \gamma^6)}}. \quad (3.47)$$

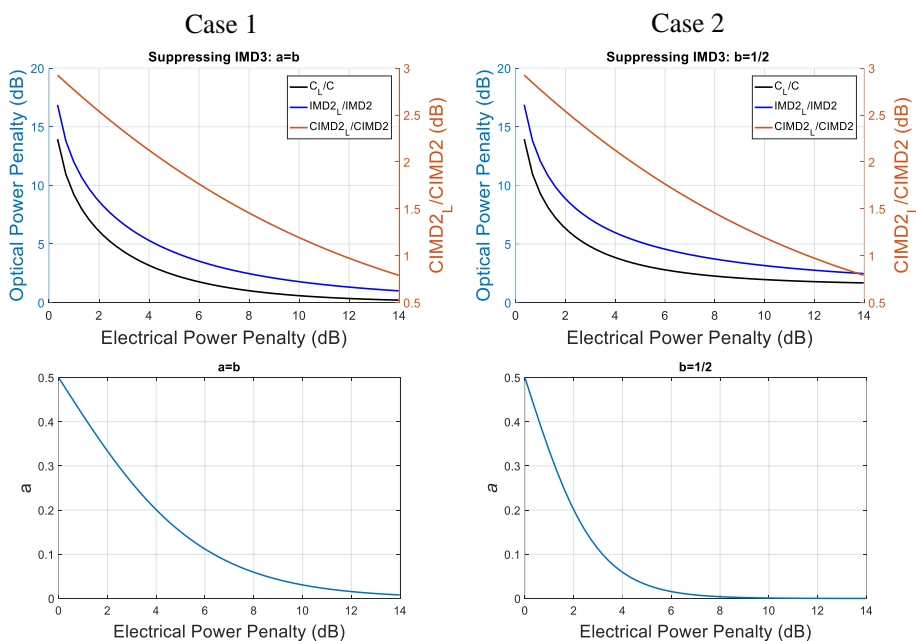


Figure 3.22 Case 1. (Upper) Optical penalties vs Electrical Penalties, (Lower) Coupler coefficient vs Electrical Penalty for Case 1 (left) and Case 2 (right).

$$\frac{IMD_{2,L}}{IMD_2} = \frac{\gamma^2(\gamma - 1)}{\sqrt{2(1 + \gamma^6)}}. \quad (3.48)$$

Following a similar process, we obtain exactly the same expression of  $CIMD_{2,L}/CIMD_2$  than in Eq. (3.45). The right part of Figure 3.22 shows the results for this case, where we observe a similar behavior as in case 1. However, the range of allowed electrical penalty values is reduced (5 dB as compared to 8 dB of case 1), while the minimum optical penalty for the fundamental tone is increased of (around 4.5 dB as compared to 1 dB of case 1). As in case 1, the behavior as compared to  $IMD_2$  is improved and, in fact, the relative improvement is the same in both equalization methods.

### Discussion

Both linearization cases are in principle capable of cancelling third-order intermodulation distortion from the modulation stage while, at the same time, improve the linearity of the system as related to second-order intermodulation distortion. Note that whereas the standard/commercial DPMZMs are usually symmetric, it is feasible to obtain asymmetric coupling in Y-branches by proper design [53]. In the first case, a better performance is obtained in terms of optical power penalty for the fundamental tone (i.e. smaller than in case 2 for the same amount of electrical power penalty). This is achieved at the expense of a more complex design of the DPMZM since both the input and output Y-branch splitting ratios are asymmetric. However, as a result from the optimization process, both have the same value (Eq. (3.42)). In case 2, one of the two Y-branches can be symmetric, however this does not render any significant advantage in terms of fabrication. Since case 2 is more restrictive in terms of affordable electrical power penalty, the conclusion is that the approach of case 1 is preferable from the practical point of view. Note however that the optimum bias point for  $IMD_3$  suppression should be kept fixed and this requires the stabilization of the bias voltages for the upper and lower MZMs as well as for the phase shifters to avoid the drifting of the optimum operation conditions.

It should be pointed out as well that none of the two cases can obtain simultaneous cancellation of second- and third-order intermodulation distortion despite the fact that both MZMs at the two DPMZMs are biased in quadrature. This is not surprising as second-order intermodulation distortion cancellation at quadrature biasing points is only achieved for the case of direct detection, that is for intensity modulators, while the system under consideration here works under self-beating coherent detection, that is for electric field modulators. In fact, the topic of linearized electric field modulators has been scarcely addressed in the literature but is currently raising increased interest, as coherent systems are becoming commonplace in optical fiber communications. A possible configuration for a near linear field response modulator (NLFRM) has been reported very recently in [86], which proposes a two-stage modulator.

### 3.5 Implementation of different modes of operation

In this chapter, we have proposed the first integrated MWP processor architecture that can perform the main MWP functionalities by software definition. Moreover, a field-based end-to-end model has been developed accounting for both MWP and RF stages that computes the fundamental and intermodulation terms to obtain the figures of merit that characterise the system. It allows system evaluation as well as a powerful designing tool to properly programme the photonic processor.

To conclude this chapter, we illustrate in Figure 3.23 to Figure 3.26 the configurations of the proposed architecture to work in different modes of operation depending on the frequency domain of the signal to be processed at the input and output processor ports: electrical/electrical, electrical/optical, optical/electrical, and optical/optical.

Electrical/Electrical operations are typically employed in MWP functionalities such as RF-filtering, instantaneous frequency measurement, frequency mixing, RF and millimetre-wave arbitrary signal generation to cite a few. It requires the processor to enable the optical source, the electro/optic and optoelectronic converters as well as the reconfigurable optical core. Figure 3.23 depicts the signal flow within the processor. Note that if a second modulator is integrated, it can be enabled to perform the frequency mixing operations based on the cascade of 2 EO modulators.

Sometimes, the processed signal has to be distributed. The processor can leverage the inherent properties of optical fibres for distribution purposes. Figure 3.24 illustrates the electrical/optical operational mode that is widely employed in radio-over-fiber MWP links. At the receiver point of the link, another multipurpose MWP processor with the same architecture can be employed. In this case, it would be working in optical/electrical mode. The receiver, shown in Figure 3.25 has the chance to process the signal before the photodetection stage. In addition, the processor working in O/E mode can enable its own optical source to act as a local oscillator.

The last working mode, depicted in Figure 3.26, is the optical/optical. In this case, the input signal can be processed directly in the optical domain. Optical channel management such as add/drop, switching and broadcasting operations are common optical processing operations.

Finally, all the modes may coexist for a certain multi-task functionality. For example, a modulated signal could be divided after being processed and both distributed through the optical ports and downconverted by the photodetectors.

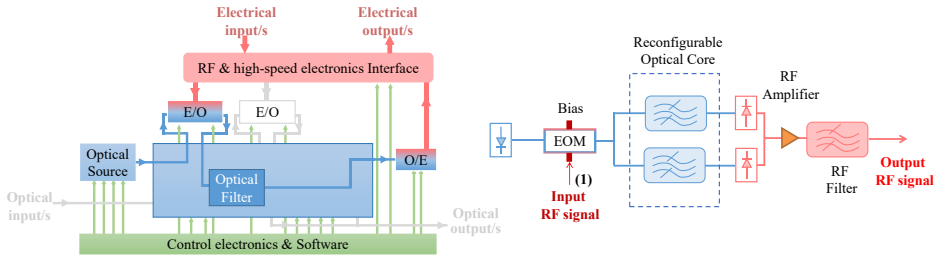


Figure 3.23 Generic purpose MWP processor architecture in Electrical/Electrical operation mode. (Left) Processor settings and signal flow, (right) targeted operation scheme.

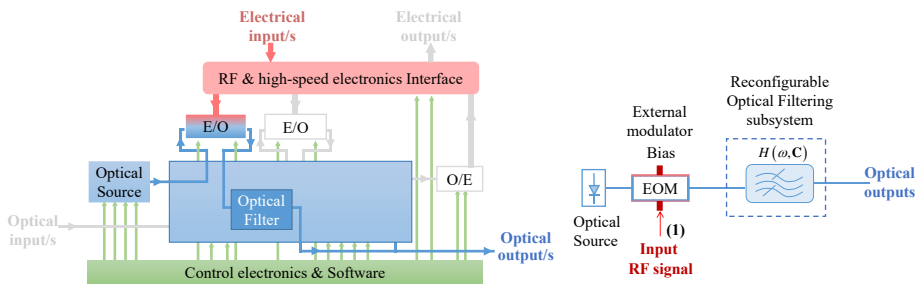


Figure 3.24 Generic purpose MWP processor architecture in Electrical/Optical operation mode. (Left) Processor settings and signal flow, (right) targeted operation scheme.

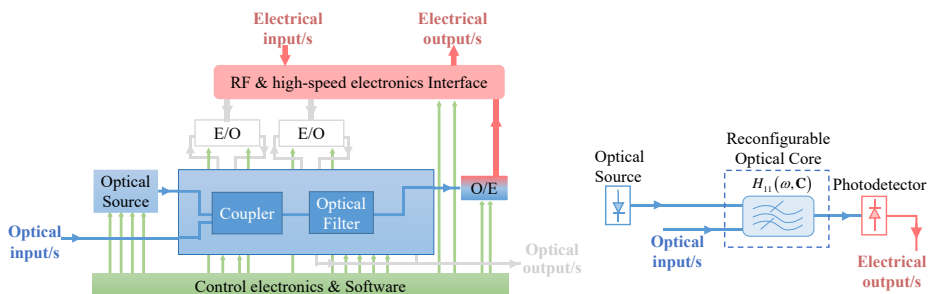


Figure 3.25 Generic purpose MWP processor architecture in Optical/Electrical operation mode. (Left) Processor settings and signal flow, (right) targeted operation scheme.

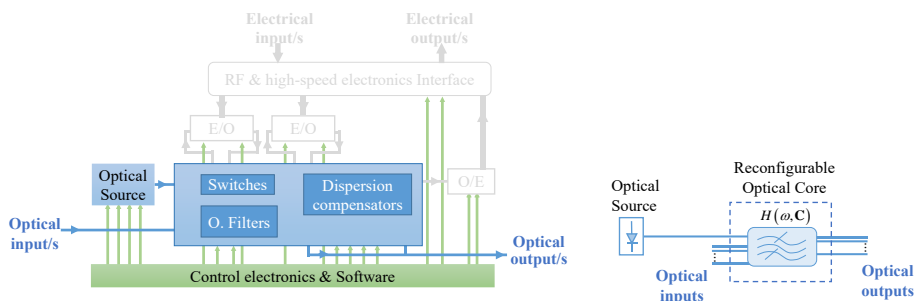


Figure 3.26 Generic purpose MWP processor architecture in Optical/Optical operation mode. (Left) Processor settings and signal flow, (right) targeted operation scheme.

### 3.6 Discussion

Due to the considerable number of parameters involved in the generic MWP system equations developed in this chapter, it is difficult to test here the dependence of each FoM for each parameter variation. However, the final equations allow to quantitatively determine their impact in an intuitive way. The generic analytical model developed here aims to be a practical tool applicable for most of the MWP systems reported to date as well as a dynamic tool for the programmable photonic processor configuration. The reported model is developed for typical architectures. However, the model, in its current form, is limited to passive RF links. The extension of the model to incorporate amplified MWP links/systems has been identified as future work. The main impact of the integrated SOA will be the reduction of RF losses (RF gain increment) at the expense of added amplified spontaneous emission (ASE) noise and nonlinearities from the four-wave mixing effect created by carrier population oscillations, [87].

For each application, the model allows the designers to know the minimum conditions for each subsystem to obtain the desired specifications. Reduced-loss systems aiming at least 0 dB gains, reduced noise figures and larger dynamic ranges are desired for most MWP applications. In this sense, on-going research on on-chip optimum modulators, photodetectors, integrated sources and on-chip optical amplification presents year by year more efficient devices.

Current ASPICs have demonstrated reduced RF gains, noise figures and large dynamic ranges. However, these figures have not been demonstrated within a single chip. Moreover, reported values of FoM account for systems that are not fully integrated and cannot be easily compared. A recent publication [20] integrates all the subsystems, but E/E measurements are not available.

In current ASPICs, the gain issue has been solved by the inclusion of external optical amplification prior / after the integrated optical processing core. Some remarkable chips, employ on-chip optical amplification, [43].

In a medium-term, it should be feasible to simultaneously achieve operation bandwidths up to 60 GHz, internal RF losses  $<20$  dB, Noise figures between 3-15 dB and spurious free dynamic ranges  $>110$  dB.Hz<sup>2/3</sup>, reducing current discrete-based MWP systems SWaP values to  $<3 \cdot 10^{-5}$  m<sup>2</sup>,  $<0.02$  kg and  $<3$  W, respectively, with the optimum configuration and design of a generic-purpose programmable MWP processor.

# Chapter 4

## Optical Core Design for RF-Photonic Processors

### 4.1 Introduction

The central element of the reconfigurable optical processor is the optical core, where the main signal processing tasks are carried in the photonic domain. Ideally, the optical core should be built upon a versatile architecture capable of implementing different functionalities in response to different electronic control signals. In practice, among the reconfigurable photonic circuits proposed in the literature, the ones that could especially emerge as candidates for this core are either based on the cascade of finite (i.e. Mach-Zehnder interferometers) or infinite (i.e. Ring Cavity) impulse response cells or a combination of both. Some examples are illustrated on Figure 4.1, which correspond to configurations limited to the synthesis of 1-input/1-output or 2-input/2-output periodic filters and allow for bandwidth reconfiguration and notch tunability by moving their zeros and poles along the z-plane.

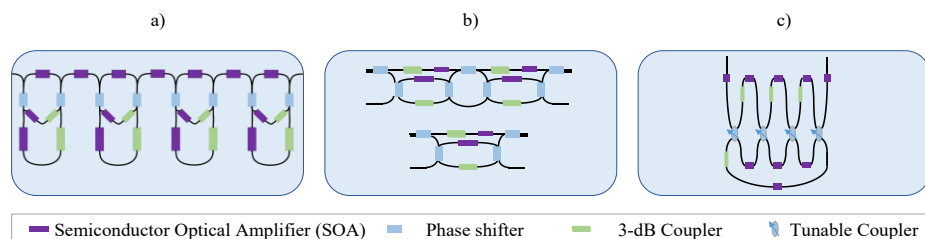


Figure 4.1 Demonstrated photonic filters allowing pole and zero reconfigurability/tunability. (a) 4-cell based reconfigurable filter [42], (b) 2- and 1-cell reconfigurable filter [82, 19] and (c) 1-cell reconfigurable filter [43].

As a first alternative to go one step further in terms of flexibility, the former approach can be extended to implement a subsystem of switched optical signal processing elements including different types of fixed and reconfigurable filtering

structures and interconnections as illustrated in Figure 4.2. This example includes finite impulse response (FIR) and infinite impulse response (IIR) filters and dispersive delay lines (DDL) that can be accessible by the correct programming of optical routing and switching elements subsystems (ORSEs) that interconnect them. This architecture is limited in terms of flexibility and scalability. The optical routing and switching elements would need to have medium-count ports depending on the number of component banks.

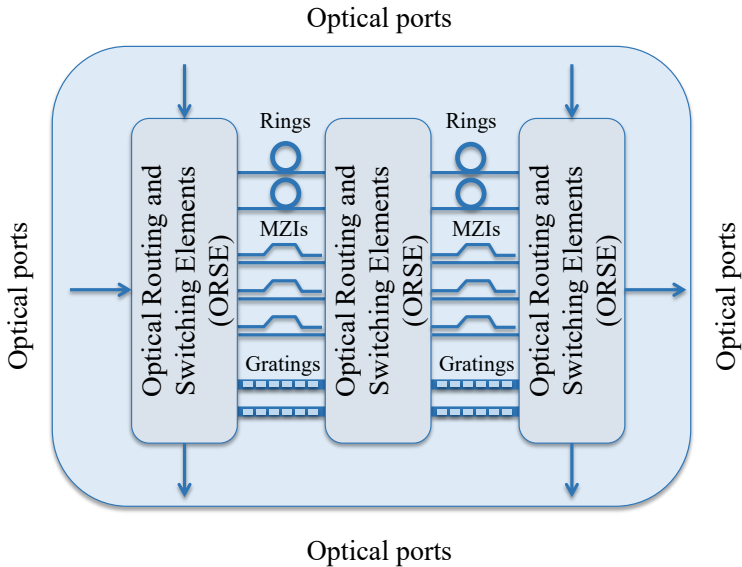


Figure 4.2 Reconfigurable Optical Core implementation based on component switching.

A more flexible architecture is the *universal multiport photonic interferometer*, which is based on planar arrangements of reconfigurable beam splitting and phase shifting devices that can implement any arbitrary unitary linear transformation between input and output optical modes. These transformations are essential to support advanced optical functions, which include, among others, linear quantum optical gates and circuits, microwave photonics signal processors, spatial mode converters, data centre connections and optical networking functionalities, [26].

The most common design for universal photonic interferometers is based on the triangular arrangement of ideal  $2 \times 2$  beam splitters with phase shifting capabilities that was proposed by Reck et al. [26]. This scheme was lately extended by Miller to include the possibility of self-reconfiguration and the use of non-ideal components [27]. Figure 4.3(a) shows, for instance, an example of  $4 \times 4$  triangular interferometer.



Very recently, however, Clements et al. [88] have proposed a new design, which is based on a rectangular arrangement of the same  $2 \times 2$  beamsplitters and requires half the optical depth as compared to the triangular arrangement. An example of a  $4 \times 4$  rectangular arrangement is shown in Figure 4.3(b). This feature makes this design more robust against losses and fabrication errors. Although universal interferometers are a powerful and versatile architecture, these structures are limited to feed-forward propagation of light and linear operations. Section 4.3.4 expands the analysis of universal couplers.

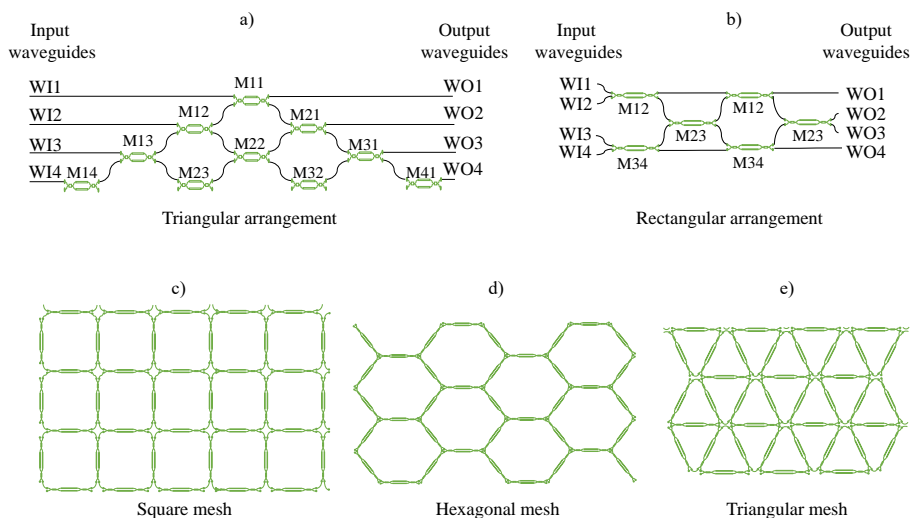


Figure 4.3 (a) Reck/Miller Triangular arrangement [26, 27], (b) Clements Rectangular arrangement, [88], (c) Square Mesh topology, [51], (d) Hexagonal Mesh Topology [52], (e) Triangular Mesh Topology, [52].

Before the publication of the enhanced rectangular universal interferometer, Zhuang and co-workers [51] pioneered a design for a programmable optical core inspired in a similar concept of that of the FPGA in electronics. This approach is based on a 2D waveguide square mesh network where the connections between waveguides are controlled by means of tunable balanced MZIs. The key difference with the previous mesh designs relies on the connectivity configuration between beamsplitters, which allows both feedforward and feedback propagation of light. By means of external electronic control signals, each MZI in the mesh can be configured to operate as a directional coupler or simply as an optical switch in a cross or bar state providing independent amplitude- and phase-controlled optical routing. In this way, the combination of different MZIs in the 2D square grid, -each individually configured as desired-, enables, in principle, the synthesis of any kind of optical core circuit topology, including finite and infinite impulse response filters,

where the sampling period can be discretely tuned by appropriate switching along the beamsplitter-based squared mesh. This mesh is potentially the most flexible candidate alternative for implementing programmable photonic processor cores.

Notwithstanding, space and power consumption constraints play a critical role in the design of photonic circuits in general and of optical meshes in particular. The limited area available for growing the optical mesh, and the need to reduce to a minimum the number of switching elements required for implementing a set of optical core topologies call for a careful analysis of possible geometries for the mesh topology implementing the optical core. In this chapter, we propose and analyse two alternative designs: the triangular and the hexagonal mesh and compare them with the square design proposed in [51]. While offering new opportunities and capabilities, the meshes allowing feedbackward propagation of the light might suffer from undesired backreflections degrading the signal processing performance or even damaging the system. This undesired effects are covered by Appendix C together with the impact consideration for non-ideal components.

## 4.2 Waveguide mesh design and comparative analysis

We propose two new configurations of tunable coupler-based meshes that can synthesize photonic integrated circuit designs. Figure 4.4 (a) and (b) illustrate a 4-cell arrangement for the novel hexagonal and triangular meshes, respectively, and their associated interconnections schemes at the bottom. As in the square-type mesh, illustrated for comparison in Figure 4.4 (c) [51], the basic building block of these meshes is a tunable coupler that must provide, independently, a complete splitting ratio tuning and phase response. This switching/tapping/dephasing mechanism can be obtained either by exploiting the electro-refraction and/or the electro-absorption effect, or by means of the thermo-optic effect, in a broadband 3-dB balanced Mach-Zehnder Interferometer (MZI). By configuring each tunable coupler placed at each side of the cell perimeter as a switch (in either its cross or bar state) or as a tunable coupler, one can synthesize a given photonic integrated circuit topology, as shown in [51].

The upper part of Figure 4.5 shows the tunable basic unit (TBU) composed by the tunable coupler and its access (input/output) waveguides. The geometry of the latter is a function of the bending radius and vary for each mesh topology due to different angle between elements. The basic unit length (BUL) is:

$$BUL = L_{access} + L_{Tunable-Coupler}, \quad (4.1)$$

where  $L_{access}$  is the overall length of the access waveguide segment and  $L_{Tunable-Coupler}$  is the length of the tunable coupler.

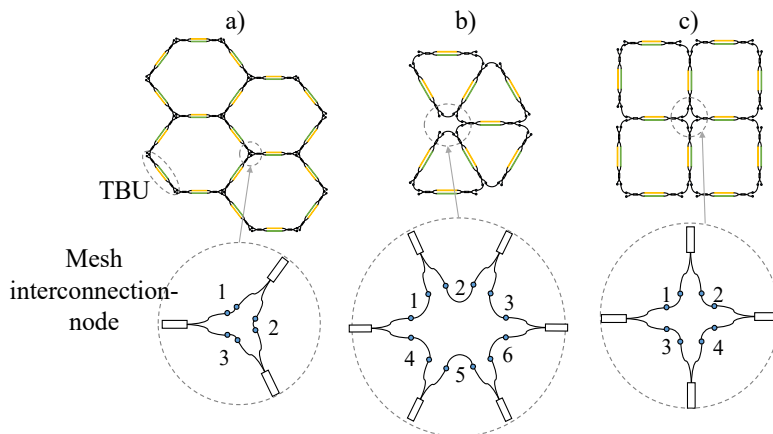


Figure 4.4 Reconfigurable Mesh designs (upper): (a) Hexagonal type, (b) triangular type, (c) square type [51], and their associated interconnections points (bottom).

Although different structures of tunable couplers can be considered in principle (balanced and unbalanced  $2 \times 2$  couplers,  $3 \times 3$ , and 3-dB MZIs) [89], we will only consider 3-dB balanced MZI structures loaded with a heater on each arm, as illustrated in the lower part of Figure 4.5. Nevertheless, the treatment is not restricted to this case and can be employed for alternative TBUs structures and tuning mechanisms.

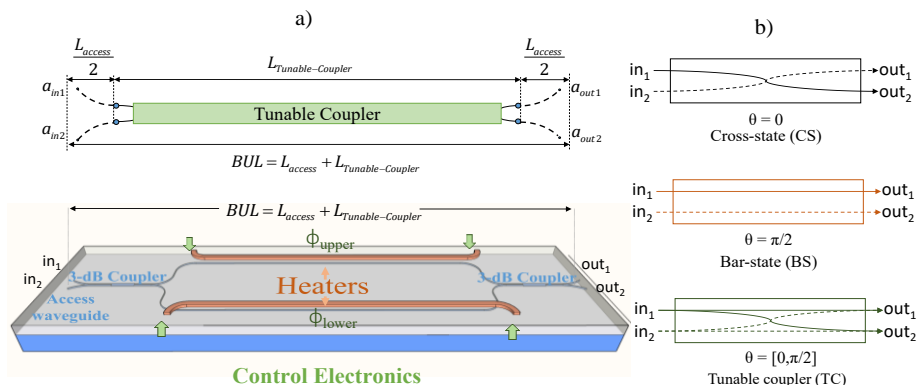


Figure 4.5 (a) (Upper) Labeled schematic of a general tunable coupler acting as the basic building block of the mesh. The Basic Unit Length (BUL) is illustrated as the sum of the tunable coupler length and the arc length of the access waveguides. (Lower) Particular case of an integrated balanced MZI-based tunable coupler. (b) Signal flow for the different TBU configuration states.

Referring to the right part of Figure 4.5, the tunable basic unit can implement 3 different states: *cross state switch* (light path connects *in1* to *out2* and *in2* to *out1*), *bar state switch* (light path connects *in1* to *out1* and *in2* to *out2*) and *tunable splitter*.

For a balanced MZI loaded with heaters on both arms, the splitting ratio is obtained by increasing the effective index due to the Joule effect in the upper or lower arm, producing a  $\phi_{upper}$  and  $\phi_{lower}$  phase shift respectively. Once set, a common drive in both heaters will provide a common phase shift, leading to independent control of the amplitude ratio and the phase. The device matrix is defined by:

$$h_{TBU} = je^{j\Delta} \begin{pmatrix} \sin \theta & \cos \theta \\ \cos \theta & -\sin \theta \end{pmatrix} \gamma, \quad (4.2)$$

where  $\theta$  is  $(\phi_{upper} - \phi_{lower})/2$  and  $\Delta$  is  $(\phi_{upper} + \phi_{lower})/2$ . The coupling factor  $K$  is then defined as  $\cos^2(\theta)$ .

The prior matrix has a general loss term  $\gamma$  that includes the effect of propagation losses in the access waveguides, the tunable coupler waveguide and the insertion losses for both 3-dB couplers. The device performance can be characterized in terms of the optical power by its insertion losses ( $IL$ ) and optical crosstalk parameters ( $CT_{Bar}$  and  $CT_{Cross}$ ):

$$IL(dB) = 20 \log_{10}(\gamma) = 10 \log_{10} \left( \frac{|a_{out1}|^2 + |a_{out2}|^2}{|a_{in1}|^2 + |a_{in2}|^2} \right), \quad (4.3)$$

$$CT_{Bar/Cross}(dB) \Big|_{\substack{|a_{in1}|^2=1 \\ |a_{in2}|^2=0}} = 10 \log_{10} \left( \frac{|a_{out2,1}|^2}{|a_{out1,2}|^2} \right).$$

These provide valuable information regarding the losses of the tunable units. Since they are connected in cascade configuration to build up the mesh, the overall  $IL$  of a certain synthesized device will be the sum of the  $IL$ s corresponding to the units across through which the light has travelled. As an example, if we assume overall device losses of 10 dB and  $IL$  of 0.2 dB for each TBU, then the longest path will be limited to 50 units. In the case of the optical crosstalk, the figure determines the leaking of signal that might cause optical reflections and undesired interferometric paths coupled to the desired photonic circuit to be programmed.

Although theoretically the TBU is in a cross state in absence of applied bias, due to fabrication phase errors the unbiased state is random. In order to reduce the footprint of the synthesized circuits, we allow the possibility of using all the unit ports independently. For example, in a cross state set both *in1/out2* and *in2/out1* connections can be employed.

We now analyse and compare the performance of the hexagonal, triangular and square mesh designs in terms of a set of figures of merit, which are relevant from a chip integration point of view. For each case, the figure of merit is defined and the quality criterion specified. Finally, we consider the overall performance of each mesh design taking into consideration all the defined figures of merit, [52].

*Spatial tuning resolution step and reconfiguration performance*

Tunable-coupler based meshes will be usually employed and reconfigured to implement either finite impulse response MZIs or infinite impulse response ORRs filters. These are spectrally periodic and their FSR is inversely proportional to the length mismatch between the two arms in the case of MZIs or the cavity length in the case of ORRs. The *spatial tuning resolution step* quantifies which is the minimum step in BUL units by which the arm length mismatch or the cavity length can be increased/decreased. The smaller the value of this figure of merit, the better, as this allows a finer discrete spatial sampling and therefore a wider range of interferometric lengths ( $L_{ORR}$  in the case of ORRs) or arm length mismatch values ( $\Delta L_{MZI}$  in the case of MZIs). The value of  $\Delta \nu_{FSR}$ , the frequency separation corresponding to the spectral period FSR of the filter is given by:

$$\Delta \nu_{FSR} = \frac{c}{n_g \cdot N \cdot BULs}, \quad (4.4)$$

where  $n_g$  is the group index of the waveguide and  $N=L_{ORR}$  or  $N=\Delta L_{MZI}$  depending on whether an ORR or a MZI is considered normalized to the BUL. Note as well that more complex configurations, like coupled resonator optical waveguides (CROWs) [60], side-coupled integrated spaced sequence of resonators (SCISSORs) [90] and ring-loaded MZIs [31, 91], can be configured with any mesh, but in principle, these will be built upon combination of the basic ORR and MZI structures.

For a fixed BUL, each mesh design has a different spatial resolution capacity for synthesising the length of the cavities and the arm length differences of the interferometric structures. For instance, Figure 4.6 and Figure 4.7 illustrate an example of particular implementations of ORRs and MZIs with hexagonal and triangular mesh designs, respectively. Notice that this particular hexagonal MZI configuration re-uses one tunable coupler inside one of the arms that is set in cross state and thus operating as an integrated waveguide crossing.

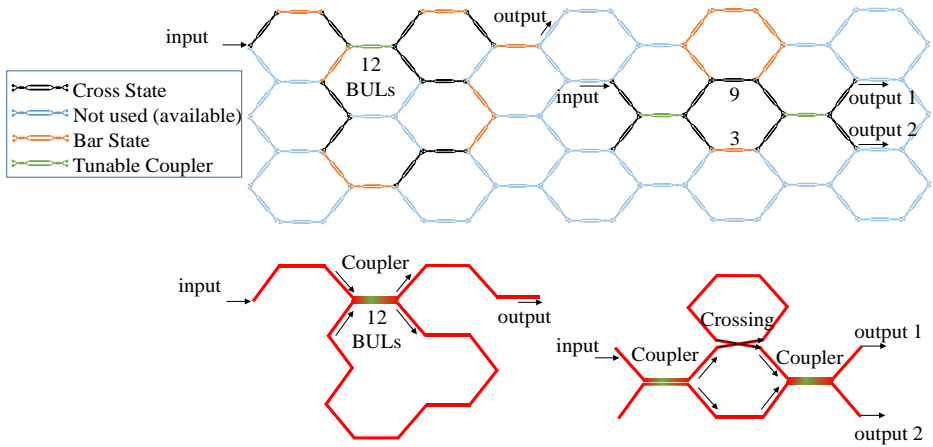


Figure 4.6 Optical Ring Resonator (left) and Mach-Zehnder Interferometer (right) configurations over a hexagonal mesh (up) and corresponding light paths (bottom).

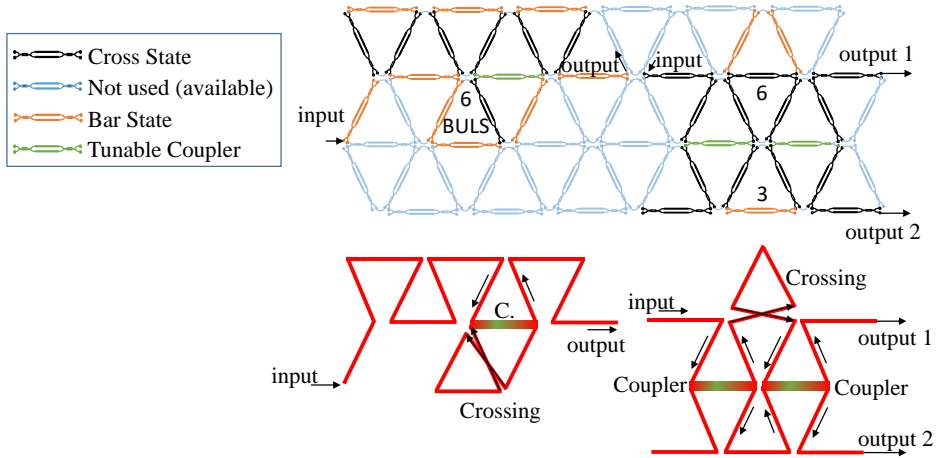


Figure 4.7 Optical Ring Resonator (left) and Mach-Zehnder Interferometer (right) configurations over a triangular mesh (up) and corresponding light paths (bottom).

The results of our comparative analysis accounting for the resolution step are shown in Table 4.1.

Table 4.1 – Values for the possible cavity lengths (ORR) and arm length mismatch (MZI) in BUL units for the different mesh designs,  $n \in \mathbb{N} \{0,1,2,\dots\}$  for MZIs and  $n \in \mathbb{N} \{1,2,3,\dots\}$  for ORRs.

	Square	Triangular	Hexagonal
MZI	$\Delta L_{MZI}^{Sq} = 4n$	$\Delta L_{MZI}^{Tr} = 3n$	$\Delta L_{MZI}^{Hx} = 2n$
ORR	$L_{ORR}^{Sq} = 4n$	$L_{ORR}^{Tr} = 3n$	$L_{ORR}^{Hx} = \{6, 10 + 2n\}$

The maximum FSR value sets the operational frequency limit for MWP applications. Regarding ORR configurations, the triangular mesh offers the maximum achievable FSR. For cavity lengths above 10 BULs, the hexagonal mesh doubles the resolution of the square mesh. As far as MZIs configurations are concerned, the hexagonal mesh offers the maximum achievable FSR and, again, doubles the resolution of the square mesh. Both the triangular and hexagonal meshes improve the spatial tuning resolution of the square mesh. The results show that, in general, the finest spatial tuning resolution corresponds to the hexagonal mesh with an incremental step of 2 BULs, although the smallest cavity value in the case of implementing an ORR is 6 BULs followed by a second step of 4 BUL units.

Given a maximum value available for  $N$ , set typically by the maximum tolerated insertion losses we define the *reconfiguration performance* of the mesh as the number of filters with different  $\Delta v_{FSR}$  values that can be implemented. Figure 4.8 plots this figure of merit for the square, triangular and hexagonal meshes as a function of  $N$  for the ORR (upper) and MZI (lower) filters. We include here a plot extension to emphasise that the limit in the maximum achievable interferometric length is given by the accumulated losses rather than by the available chip area or the number of cells. As an example, assuming a low-loss 0.3-dB TBU IL, which is quite below the state-of-the-art, a modest hexagonal mesh of 7 cells enables interferometric lengths larger than 30 BULs introducing 9-dB accumulated losses. The same area that allocates 7 hexagonal cells allows a larger number of square and triangular cells and, therefore, support larger interferometric paths. Nevertheless, an interferometric length larger than 30 suffers from more than 9-dB of accumulated losses, so the final design becomes impractical. Note that the chosen IL per TBU is below the achievable with the current state-of-the-art and that an increment in this figure implies a further reduction in the maximum allowable interferometric length for the synthesised circuits.

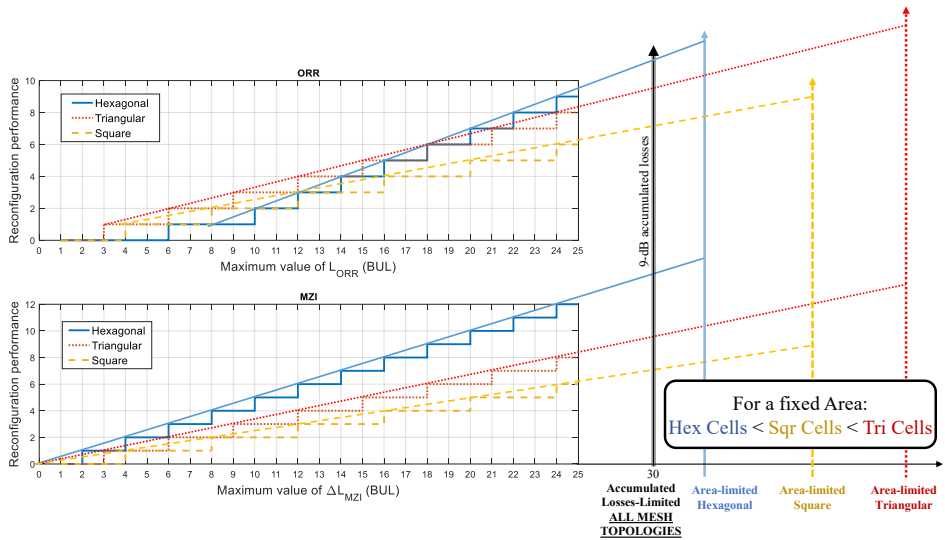


Figure 4.8 (Left) Reconfiguration performance vs available maximum value of  $N$  expressed as an integer number  $n$  of the  $BUL$  for the square, triangular and hexagonal meshes. ORR (upper) and MZI (lower) designs. (Right) Maximum Interferometric length limitation due to accumulated losses (topology-independent and more restricting) and area constrains for each alternative topology.

Note that the hexagonal configuration clearly features the best reconfiguration performance as compared to the triangular and the square meshes for MZI implementation. In the case of ORRs, the hexagonal and triangular meshes provide similar results although the hexagonal configuration outstands both the triangular and rectangular configuration for larger values of the cavity length.

#### *Number of switching elements per unit area*

From a standalone point of view of integration density, a mesh having a number of switching elements as high as possible should be preferable. However, in practice, additional factors lead to a different conclusion when taken into consideration. First of all, the maximum number of TBUs that build up the longest light path will be limited by their non-ideal propagation and coupling characteristics. In addition, if the tuning mechanism requires metal layers to route the control signals that take up the same layer level, a reduced figure of switching elements per area facilitates this task offering a reduction in the  $BUL$ , since there is no need to increase the length of the access waveguides to provide a free way to the metal tracks. If the wirebonding alternative is preferred, this is also desirable since there is more free space available to prevent the crossing of wires by increasing the separation between metal junctions. Also, in the case of using a MZI as the tunable basic unit, a reduced value of this



figure of merit offers extra free space to grow further apart the arms of each MZI, reducing the crosstalk due to the tuning mechanism, i.e., thermal crosstalk in this case. Finally, a higher number of switching elements per unit area leads to more power-hungry configurations and does not necessarily mean more flexibility in reconfiguration performance. Thus, for equal *reconfiguration performance*, a mesh design having a number of *switching elements per unit area* as low as possible is preferred.

The footprint of the mesh is obtained first by computing the area of the unitary cell and then by multiplying by the number of cells. For the sake of comparison, we normalize the polygons that define each unit cell (square, hexagon and triangle) by their side, i.e., all the meshes have sides with the same BUL. In this way, we neglect the waveguide access difference between meshes, which is the case when the BUL is large as compared to the bending radii of the technology of integration. The unit cell area can be expressed in general as  $A_{unit-cell} = kBUL^2$ , where  $k = 1$  for the square cell,  $k = 3\sqrt{3}/2$  for the hexagonal cell and  $k = \sqrt{3}/4$  for the triangular cell. For reference, as it will be shown in the next subsection, if we consider a square normalized area that could allocate a modest number of cells, it is straightforward to obtain that the number of switching elements per normalized area and its comparative increase or decrease percentage taking the square mesh as a reference. This figure yields a reduction of the 36.66% for the hexagonal mesh and an increment of 65% for the triangular mesh. This indicates that the hexagonal waveguide mesh provides the best performance in terms of this figure of merit.

*Replication flexibility: Number of possible alternative geometries for filter implementation*

Another important figure of merit is the mesh replication flexibility defined as the number of possible different alternative geometries that a given mesh design topology provides to implement a given ORR (with a fixed cavity length) or MZI configuration (with a fixed arm length imbalance). This metric is a good indicator of the potential for configuring complex devices involving cascaded photonic circuits.

When a new photonic device needs to be added in an already operational mesh, it will occupy part of its unused space, which is available. The more flexible the mesh architecture is to replicate an ORR or a MZI, the easier it will be to allocate it within the spare space. To make a fair comparison between the proposed designs, we have considered the synthesis in an infinite mesh of ORRs with cavity lengths of up to 16 BULs and MZIs with arm imbalances of up to 12 BULs. In order to account for all the MZI designs that provide the same FSR, we have limited the synthesis to MZIs whose minimum arm length is equal or shorter than 3 BULs. The results of our analysis are shown in Table 4.2. The two final rows in the table provide a cumulative figure on the total number of replication options and the replication ratio (compared to that of the triangular mesh) for ORRs and MZIs. For ORRs the square mesh

features a replication flexibility which is approximately double to that of the hexagonal mesh and approximately a 30% extra replication flexibility as compared to the triangular mesh. For MZIs, the hexagonal mesh benefits from its ability to provide shorter paths (i.e. 1 and 2 BULs) featuring approximately a 236% extra replication flexibility as compared to the triangular mesh and exceeding square mesh metrics by a 12%.

Table 4.2. Number of different devices that can be configured for each mesh design

ORRs				MZIs			
$L_{\text{ORR}}$ (BULs)	Square	Hexagonal	Triangular	$\Delta L_{\text{MZI}}$ (BULs)	Square	Hexagonal	Triangular
3	-	-	1	0	1	1	1
4	1	-	-	1	-	-	-
5	-	-	-	2	-	2	-
6	-	1	2	3	-	-	1
7	-	-	-	4	3	2	-
8	5	-	-	5	-	-	-
9	-	-	6	6	-	3	7
10	-	3	-	7	-	-	-
11	-	-	-	8	11	8	-
12	20	5	8	9	-	-	3
13	-	-	-	10	-	17	-
14	-	11	-	11	-	-	-
15	-	-	15	12	42	31	8
16	60	22	-	-	-	-	-
Total	86	42	32		57	64	19
Replication ratio	2.68	1.31	1		3	3.36	1

In order to illustrate the *replication flexibility* concept, in Figure 4.9 we plot for each mesh topology the settings to programme fixed-FSR ORRs with the cavity describing different geometries. Here, the nomenclature employed is the following: DEV[NR][ML] where DEV={ORR,MZI} stands for the device implemented, N is the cavity or arm length mismatch in BUL units, R appears if coupler reutilization is employed, M is the number of re-utilized couplers and L={A,B,C,...} is a letter that designates different designs sharing equal values for the preceding parameters in the code. In particular, we illustrate the case of setting ORRs of the same length in a bus configuration (SCISSORS). The upper left part shows, for instance, the unique 3 ways of synthesizing ORRs of normalized circumference length equal to 10 BULs using a hexagonal mesh. For the triangular mesh, the two alternatives of synthesizing ORRs of normalized circumference length equal to 6 BULs are shown in the upper right part of Figure 4.9. These results match the ones predicted by Table 4.2. Finally, the lower part of the figure shows the unique five alternatives to programme ORRs of

normalized length 8 BUL using a square mesh. Notice that the first three designs also re-use one of the TBUs.

It is also worth mentioning that different devices could also share TBUs in order to save space. For example, in the square mesh, between the ORR8A and the ORR8B an ORR8R1C could be synthesized sharing their outer bar-state-configured TBUs.

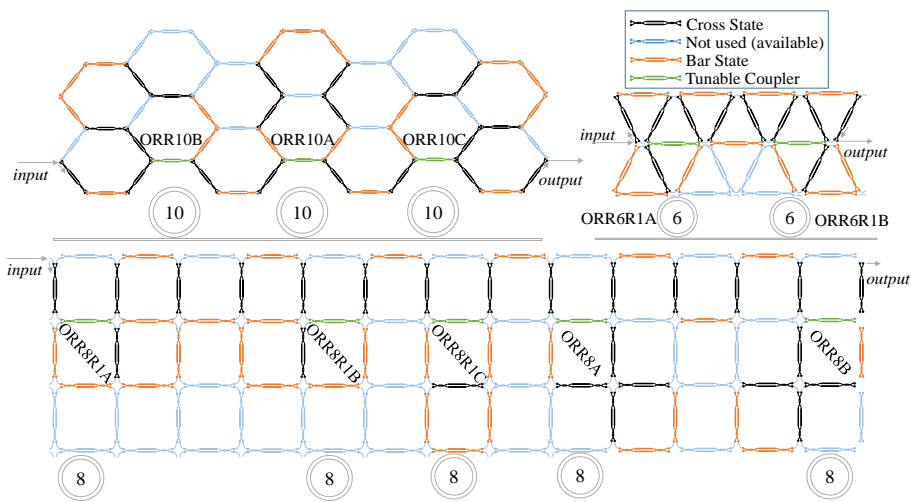


Figure 4.9 Different mesh types configured to synthesise cascaded ORRs of fixed FSR in different geometries. (Up/left) Hexagonal waveguide mesh programming three cascaded ORRs of 10-BUL cavity length, (Up/Right) triangular waveguide mesh programming two ORRs of 6-BUL cavity length and (lower) square waveguide mesh programming five ORRs of 8-BUL cavity length.

The results from Table 4.2 confirm that the square mesh is the most flexible when replicating ORRs but, at the same time, they outline that this mesh design is the most restrictive one in terms of spatial tuning resolution step. On the other hand, the triangular mesh is the most restrictive in terms of replication flexibility due to its mesh complexity and its interconnection scheme, as it is shown at the bottom of Figure 4.4. Nevertheless, its spatial tuning resolution step is better than the square mesh. Finally, the hexagonal mesh presents a good equilibrium between medium-high flexibility and the highest spatial tuning resolution step.

#### *Losses and spatial resolution associated with TBU interconnections*

Interconnections between the TBUs determine the *spatial resolution* and the *losses* due to bending radii and polarization rotation. To make a fair comparison between the meshes, we consider two benchmarking alternatives. In both cases, the tunable

coupler length of the TBU is kept constant: In the first one, the bending radii of the curves are fixed while in the second it is the BUL that is kept constant.

In the first case, the fixed radius is dictated by the integration technology platform. It ranges typically from 5-30  $\mu\text{m}$  in silicon waveguides to 100-250  $\mu\text{m}$  in Indium Phosphide, 100-1000  $\mu\text{m}$  for Silicon Nitride platforms and about 1000  $\mu\text{m}$  for Silica on Silicon. In this case, the BUL of each mesh will be different as it depends on a fixed term (the tunable coupler length) and a variable term (the access length) defined by:

$$L_{\text{access(both)}} = \frac{2\pi Ra}{(360/\alpha)}, \quad (4.5)$$

where  $\alpha$  is the angle in degrees of the arc defined by the interconnection, and  $Ra$  the radius of curvature. Both of them are illustrated in Figure 4.10 for each mesh design. Since the angle between TBUs required by the square, hexagonal and triangular meshes are  $90^\circ$ ,  $60^\circ$  and  $120^\circ$ , respectively, then the access length of the hexagonal mesh is a 33% shorter compared to the square mesh while it is a 33% longer for the triangular mesh compared to the square mesh.

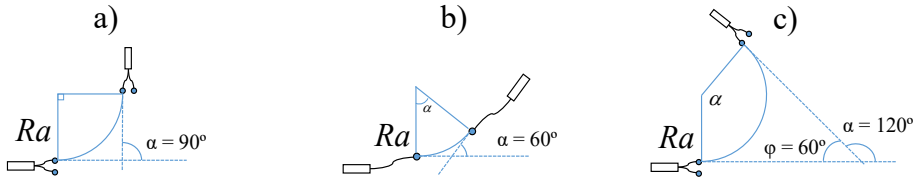


Figure 4.10 Access length and angle definition for each mesh: (a) square, (b) hexagonal, (c) triangular.

Therefore, when the radius of curvature is fixed, the BUL and, thus the spatial resolution, will be different for each mesh. Figure 4.11 shows the relation between the BUL of a given mesh design to that of the square mesh as a function of the ratio between the access waveguides and the tunable coupler length. The range of applicability of this curve depends on the material platform used to implement the mesh. For instance, in silicon photonics, the bending radii of 5-30  $\mu\text{m}$  compared with a tunable coupler length of about 500  $\mu\text{m}$ , places the region of application in the left side of the graph. In this case, the increase or decrease in the BUL associated to the triangular or the hexagonal meshes will be practically negligible as compared to that of the square mesh. In other platforms featuring higher values for the minimum bending radius, the region of application in Figure 4.11 will move towards the right part of the graph, leading to a higher spatial resolution for the hexagonal mesh.

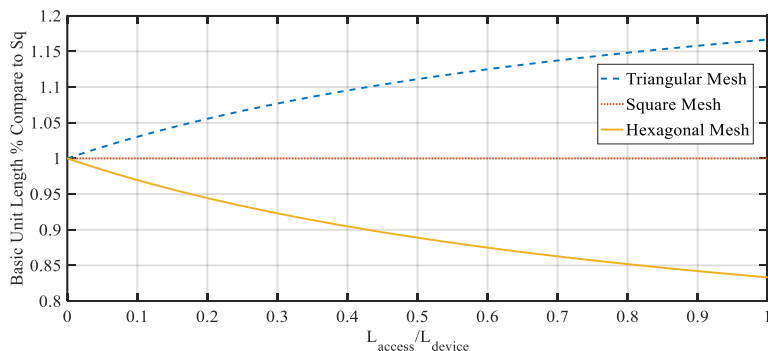


Figure 4.11 Relation between the BUL of a given mesh design to that of the square mesh as a function of the ratio between the access waveguides and the tunable coupler length.

The second case for comparison consists in fixing the value of the BUL so the product  $\alpha Ra$  shown in the right part of Eq. (4.5) remains fixed. In this case, the bending radius will be different for each mesh and, more precisely, when compared to the square mesh, the triangular will be a 25% smaller whereas the hexagonal will be a 50% higher. Here, since the losses associated to the bending radius and the polarization rotation are greater for shorter bending radii, the hexagonal mesh features, again, the best performance.

Table 4.3 summarizes the results of the previous subsections carried for the different figures of merit and the three mesh designs. With the exception of the replication ratio of ORRs, the hexagonal mesh design is the most versatile option featuring the best results in all the figures of merit. Its superior performance in terms of spatial tuning resolution step allows for a higher reconfiguration performance, that is, a wider range of spectral periods that can be implemented with complex structures built upon combining ORR and MZI based filters. The reduced value in the number of switching elements per unit area allows simpler configurations in terms of fabrication, electrode deposition, control pad interconnections and power consumption. Finally, and equally important, the hexagonal lattice mesh provides shorter curved sections for a given access waveguide bending radius and a fixed BUL value, which, in turn, results in lower propagation losses.

We conclude therefore that the hexagonal mesh is, in general, the most suitable option of the three considered for the implementation of the reconfigurable optical core in the programmable processor.

Table 4.3. Summary of values for the figures of merit of the different mesh designs

Figure of Merit	Triangular	Square	Hexagonal
ORR cavity spatial tuning resolution step in BUL units (the lower the better)	3	4	<b>2*</b> The first and second step has a resolution of 6 and 4.
MZI arm imbalance spatial tuning resolution step in BUL units (the lower the better)	3	4	2
ORR reconfiguration performance (the higher the better) (for $X=25$ BUL)	8	6	9
MZI reconfiguration performance (for $X=25$ BUL)	8	6	12
Switching elements per unit area compared to <i>square</i> % (the lower the better for a fixed value of reconfiguration performance)	+65.00%	0.00%	-36.66%
Replication Ratio for ORR structures up to 16 BUL cavity length (the higher the better).	1	2.68	1.31
Replication Ratio for MZI structures up to 12 BUL interferometric length (the higher the better).	1	3	3.36
$L_{\text{access}}/L_{\text{access square}}$ % for a fixed $Ra$ (the lower the better)	+33.33%	+0.00%	-33.33%
$Ra/Ra_{\text{square}}$ % for a fixed BUL (the higher the better)	-25.00%	+0.00%	+50.00%

#### Comparative analysis for a specific application case

Once we have analysed the three mesh designs, we provide a more detailed comparative study for a specific but representative case. Here we consider a  $5 \times 5$  BUL<sup>2</sup> available surface to implement the mesh and assume a silicon photonics platform featuring optical waveguide propagation losses of 2.5 dB/cm and a group index of  $n_g = 4.2933$  at a wavelength of  $\lambda = 1550$  nm. The TBUs are implemented by means of balanced 3-dB MZIs loaded in both arms with thermal tuners to provide independent amplitude ratio and phase tunability. The MMI couplers placed at the input/output of the MZI have excess losses of 0.1 dB each. The BUL is set to 700  $\mu\text{m}$ , which allows a phase tuning beyond  $2\pi$  preventing the burning of the tuning heater. With this value, the chip area is 12.25 mm<sup>2</sup>, which is within the state of the art range of fabrication. The area can allocate, assuming negligible the impact of the access waveguide, 25 square, 9 hexagon or 57 triangle unit cells, and the number of switching elements (tunable couplers) will be 60 for the square mesh, 38 for the hexagonal and 99 for the triangular. Taking then into consideration the area of the unit cells given in the previous section, it is straightforward to obtain that the number

of switching elements per normalized area is 2.4 for the square mesh, 1.52 for the hexagonal mesh and 3.96 for the triangular mesh. In order to compensate the greater angle of the triangular mesh access waveguides and to provide a more squared layout, we have limited the triangular mesh to 54 cells. The longest path in the mesh is in the range of 22-24 *BULs* and, therefore, the number of structures with different FSR values can be anticipated from Figure 4.8.

Figure 4.12 shows all the possible arrangements that result in different FSRs for ORRs up to 20 *BULs* in each of the three mesh designs (8 for the hexagonal, 7 for the triangular and 5 for the square), which match the results predicted by Figure 4.8.

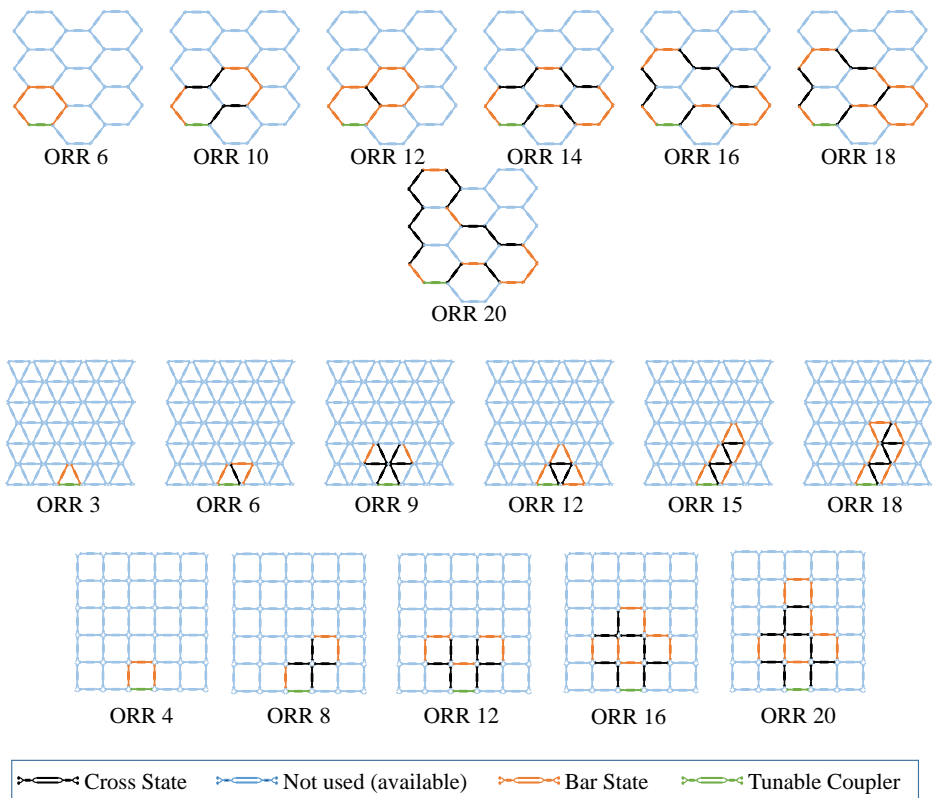


Figure 4.12 Optical Ring Resonator filters with different cavity lengths that can be implemented in a  $5 \times 5$  *BUL*<sup>2</sup> area using the hexagonal, triangular and square mesh designs. ORR *N* means an optical ring resonator filter with cavity length of *N* *BULs*.

As we can check, the hexagonal mesh provides the highest number of different cavity lengths and thus of FSR values. Note, however, that the highest FSR value corresponds to the triangular mesh. Figure 4.13 depicts the spectral characteristics attainable with each mesh design where propagation and coupler losses have been

taken into account. In each case, the coupling constant of the cavity coupler is adjusted to the critical coupling ratio set by the cavity losses. Each spectrum can be finely tuned if necessary over a whole FSR period by employing one of the TBUs inside the cavity as a phase shifter. For reference, since one BUL corresponds to a FSR of 100 GHz, a cavity with length  $k$  BUL will render a filter with a FSR of  $100/k$  GHz.

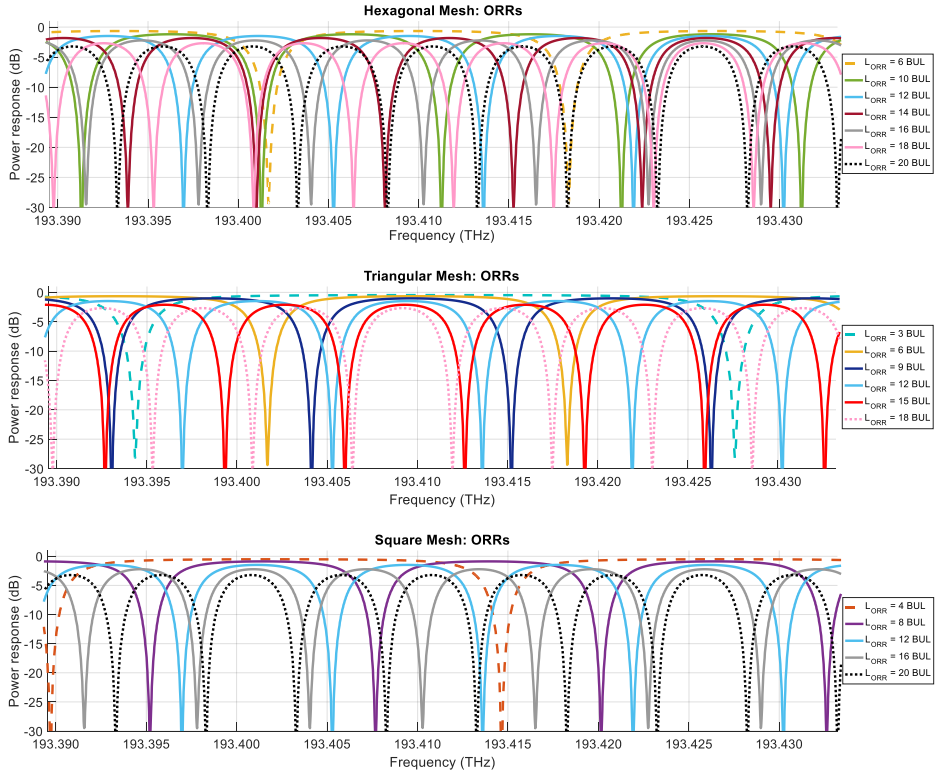


Figure 4.13 Spectra of the different ORRs available for each mesh design option. In all the cases, the cavity coupler is adjusted to attain critical coupling. Larger and shorter FSR are highlighted with dashed and dotted lines, respectively, for each mesh.

Figure 4.14 shows all the possible arrangements that result in different FSRs for MZIs with path unbalance of up to 20 BULs in each of the three mesh designs (11 for the hexagonal, 7 for the triangular and 6 for the square), which match the results predicted by Figure 4.8. Again, we can check that the hexagonal mesh provides the highest number of different cavity lengths and thus of FSR values. In this case, there is a remarkable difference in the number of available FSR values as compared to the triangular and square meshes. The highest FSR value corresponds also to the hexagonal mesh.



The spectral characteristics attainable with each mesh design are shown in Figure 4.15 where, as in the ORR case, propagation and coupler losses have been taken into account. Each spectrum can be finely tuned if necessary over a whole FSR period by employing one of the TBUs in one of the two arms of the MZI structure as a phase shifter. For reference since one BUL corresponds to a FSR of 100 GHz, a path length mismatch of  $k$  BUL will render a filter with a FSR of  $100/k$  GHz.

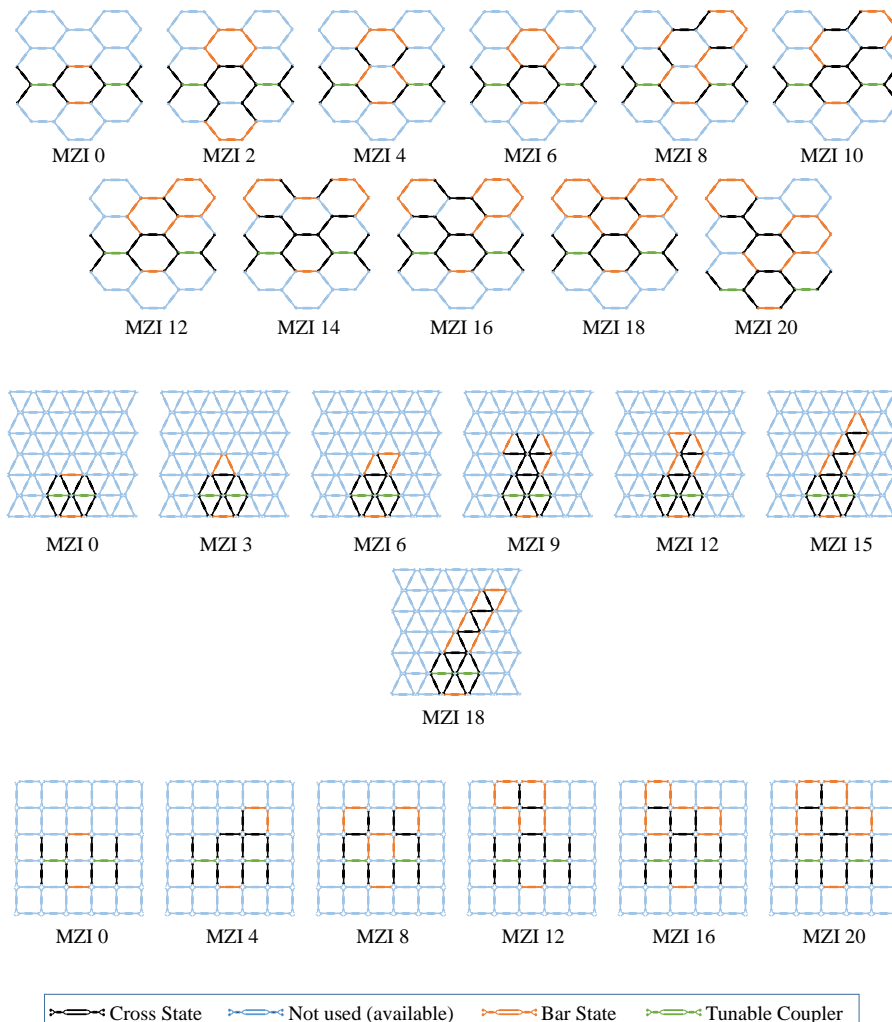


Figure 4.14 Mach-Zehnder Interferometer filters with different path length mismatch that can be implemented in a  $5 \times 5$  BUL<sup>2</sup> area using the hexagonal, triangular and square mesh designs. MZI  $Z$  means a Mach-Zehnder Interferometer filter with path length mismatch of  $Z$  BULs.

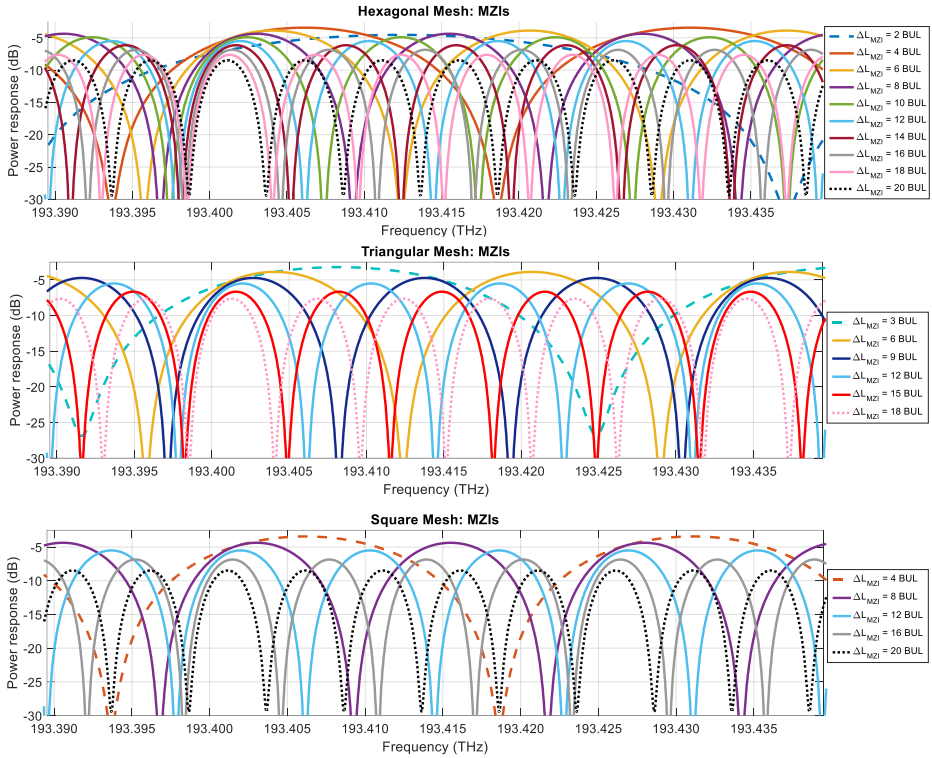


Figure 4.15 Spectra of the different MZIs available for each mesh design option. In all the cases, the output coupler is 50:50 and the input coupler is adjusted to attain maximal rejection (loss balancing).

### *Conclusions derived from the comparative analysis*

We have proposed two novel mesh design geometries for the implementation of tunable optical cores in programmable photonic processors. These geometries are the hexagonal and the triangular lattices. They have been analysed and compared to a previously proposed square mesh topology in terms of a series of figures of merit that have been defined in this chapter to account for metrics relevant to on-chip integration of the mesh.

We have found that the hexagonal mesh configuration provides the best performance for most of the relevant metrics. These results are relevant for the implementation of a versatile reconfigurable optical core in the programmable processor.

Note that for both device configurations the larger the path, the higher the IL is. This effect produced by the non-ideal characteristics of the TBUs, such as coupling and propagation losses, limits the maximum number of TBUs and, therefore, the size of the circuit.

### 4.3 The hexagonal waveguide mesh optical core

We have shown that hexagonal-shaped meshes feature improved performance in terms of spatial tuning reconfiguration step, reconfiguration performance, switching elements per unit area and losses per spatial resolution, [52] and enable the simplest implementation of both classic FIR and IIR photonic circuits. We show in this section that more complex classic filters and universal interferometers can be efficiently programmed as well in this mesh topology. For this reason, we only consider the hexagonal waveguide mesh topology for the optical core of the general-purpose software defined integrated photonic processor.

#### 4.3.1 Finite Impulse Response (FIR) filters

Unbalanced Mach-Zehnder interferometers (UMZIs) are 2-input/2-output periodic notch filters that constitute the basic building blocks for lattice and transversal filters, [32]. UMZIs find multiple applications [30], including linear phase filters, multi-channel selector biosensors, group delay compensators and biosensors. These filtering structures are all-zero filters in the z-plane.

A multi-stage filter can be realized by cascading single UMZIs structures. In order to programme the optical core to produce a one-stage FIR filter, the first step is the location and configuration of the first TBU that will operate as the input tunable coupler defined by a coupling constant  $K_1$ . Second, two synthesised waveguide paths have to be configured fulfilling two conditions: They have to maintain the desired differential path length ( $\Delta L = L_{Longer} - L_{Shorter}$ ) or a desired FSR given by Eq. (4.4) accomplishing at the same time, that both final TBUs coincide at each of the input ports of the closing coupler ( $K_2$ ) of the UMZI. By suitably tuning each TBU within the mesh, we can implement UMZI devices with path unbalances given by  $\Delta L = 2n$  BUL, for  $n = 0, 1, 2, 3, \dots$ . By taking the minimum possible value for the length of the shorter path, we can reduce the insertion losses of the filter and the number of TBUs. Figure 4.16 illustrates the targeted PICs with their corresponding settings of each TBU inside the mesh to obtain three different UMZI Filters with different FSRs. Note that the numbers accounts for the MZI arm lengths in BULs. Similarly, Figure 4.17 illustrates the implementation of two multi-stage filters by cascading single UMZIs, enabling a sixth- and fifth-order filter, respectively.

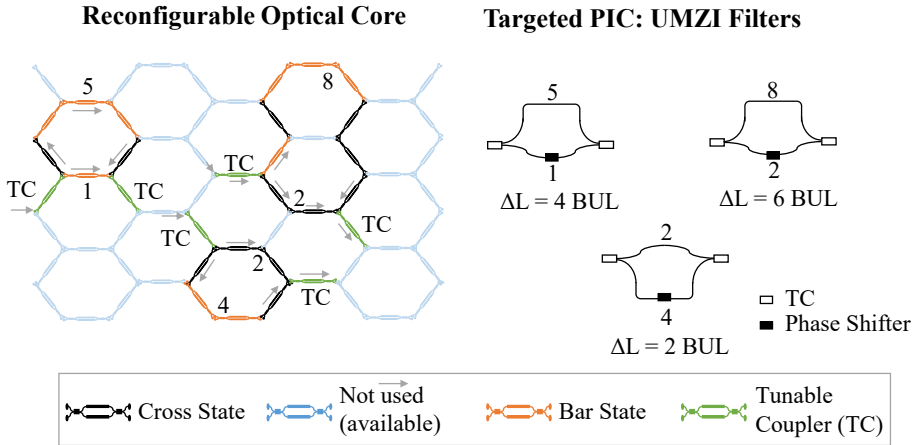


Figure 4.16 FIR filter implementations. (Left) hexagonal mesh setting for (Right) three different targeted UMZI Filters

Different values of the coupling constants  $K_1$  and  $K_2$  change the absolute magnitude of the zero in the UMZI transfer function bringing it closer or farther to the unit circle. The closer the zero is to the unit circle, the deeper are the notches in the transfer function and the higher is the phase shift step in the phase transfer function, [32]. A phase shifter can be programmed applying a common phase shift to one of the TBUs while maintaining fixed its splitting ratio. In this way, we can achieve the tuning of the resonance notch position over a complete spectral period by proper phase shifting in one of the UMZI arms. This is equivalent as moving the zero along the z-plane without changing its absolute magnitude. Pseudo-code algorithms for basic and complex FIR structures can be found in Appendix B.2.

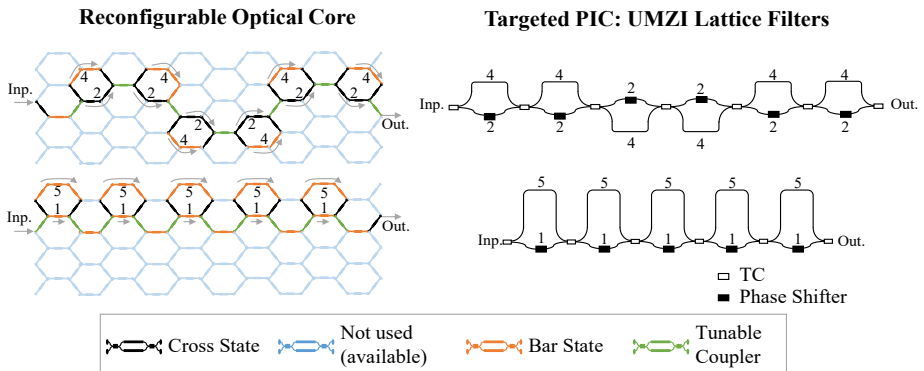


Figure 4.17 Cascaded FIR filter implementations: (left) hexagonal mesh setting for (right) two different targeted lattice UMZI Filters of 6<sup>th</sup> and 5<sup>th</sup> order.

Cascading this building block is a straightforward way to realize higher order all-zero responses in the  $z$ -plane. A wide variety of algorithms is available in the literature for the synthesis of these so-called lattice filters, which provide the values of the coupling coefficients and phase terms that render the targeted spectral magnitude or phase response, [30, 32].

### 4.3.2 Infinite Impulse Response (IIR) filters

Ring cavities are either 1-input/1-output or 2-input/2-output periodic filters. In the first case, they implement all-pole IIR notch filters, while in the second they can implement both IIR notch and FIR+IIR bandpass filters [32]. They constitute the basic building blocks for more complex filter designs such as CROWs and SCISSORS. Ring cavities find multiple applications [31] including integrators, differentiators and Hilbert transformers [49], dispersion compensators [31], as well as tunable radiofrequency phase shifters and true time delay lines, [92].

In order to program such a filter, the first step is the location and configuration of the first TBU that will operate as the input coupler defined by a coupling constant  $K_1$ . Secondly, a waveguide path has to be configured starting from one output port of the first TBU and ending in one of the input ports of the first TBU –providing the desired cavity length ( $\Delta L_{ORR}$ ) or FSR. One of the TBUs within the waveguide path can be set as a second coupler ( $K_2$ ) to implement a second input/output port and therefore enable or 2-input/2-output filter. By suitably tuning each TBU within the mesh, we can implement single optical ring resonators with cavity lengths given by  $\Delta L_{ORR} = 6, 10, 12, 14, \dots$  BULs. Different values of  $K_1$  and  $K_2$  set the values of the absolute magnitude of the zero and the pole [32]. Since any TBU in the waveguide implement the cavity can be operated as a constant-amplitude phase shifter from 0 to  $2\pi$ , we can tune the filter resonance position along a full spectral period. Figure 4.18 illustrates the mesh configuration for three IIRs filters with different FSRs with cavity lengths corresponding to 6, 10 and 12 BULs, respectively. Note that, in this example, the shorter cavity has both tunable couplers activated (i.e., it is a 2-input/2-output filter).

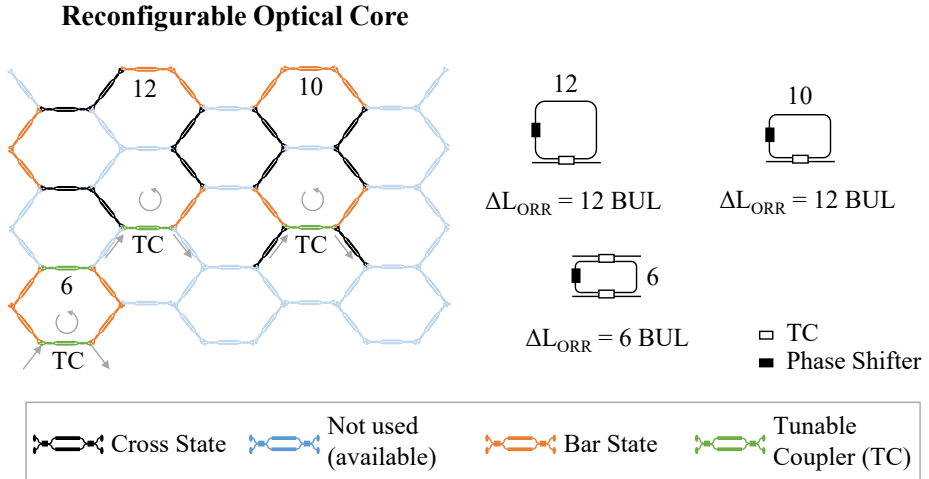


Figure 4.18 Single-cavity IIR Filter implementations. (Left) hexagonal mesh setting for (right) three different targeted ORR filters.

### 4.3.3 Complex multistage filters

We can build more complex (multicavity) signal processing structures like CROWs [93], SCISSORS [94], and ring-loaded MZIs [20] using the former basic building blocks in the waveguide mesh and activating more TBUs to provide additional propagation paths. These are usually 2-input/2-output filters that are characterized by transfer functions with a higher number of zeros and poles. By suitably tuning the coupling constants and additional phases, one can obtain, for instance, filters with special characteristics in the modulus or the phase response [31].

#### 4.3.3.1 Coupled Resonators Optical Waveguides (**CROWs**)

An  $N$ -th order CROW consists of a chain of  $N$  rings where each ring is coupled to one preceding and one succeeding ring (with the exception of the first and last in the chain). The rings in the CROW chain usually have the same length, however, to increase the overall filter FSR, rings with slightly different perimeters in a Vernier configuration can be employed, [32]. Figure 4.19 (a) illustrates the implementation of a 10-stage CROW characterized by 6-BUL cavity lengths.

#### 4.3.3.2 Side-coupled Integrated Spaced Sequence of resonators (**SCISSORS**)

Cascading ring cavities in one or two common waveguide buses leads to the implementation of higher-order response SCISSORS filters. Typically, all the ring resonators have the same cavity length. Figure 4.19 (b-d) illustrates different

SCISSOR configurations that can be implemented with the waveguide mesh: (b) is a 9-stage single-channel where all the rings are connected to the same waveguide bus, (c) is a 5-stage doubled-channel, where a second output waveguide bus collects the FIR + IRR bandpass outputs from the ring resonators and (d) is a 5-stage double cavity SCISSOR where two 6-BUL coupled cavities are connected to the collecting waveguide buses per stage. Note that, in this particular case, the signal propagation through the two collecting waveguide buses is in the same direction.

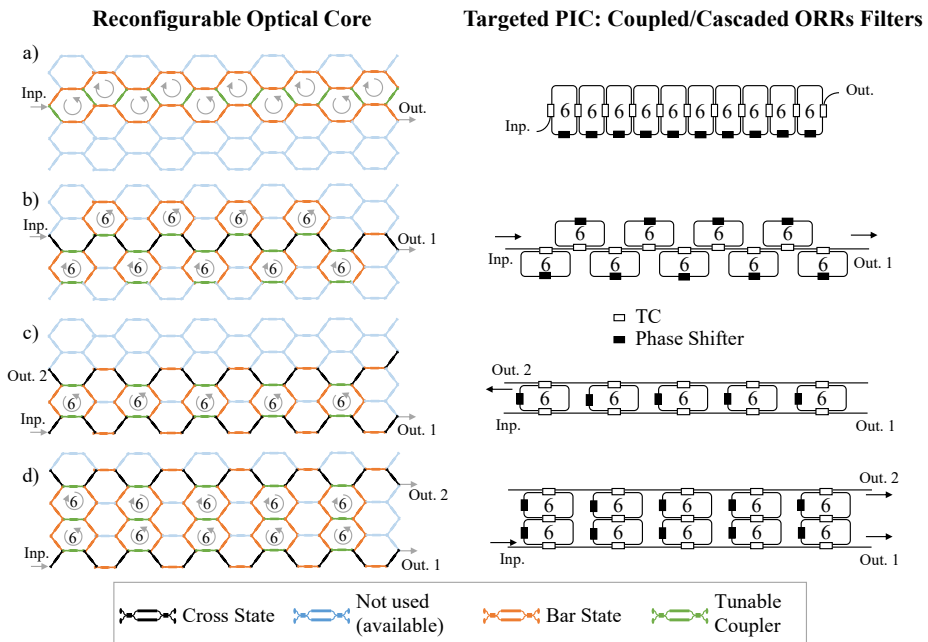


Figure 4.19 (Left) Settings for CROW & SCISSOR filter implementations in the hexagonal mesh core for (right) (a) 10<sup>th</sup>-order CROW, (b) 9<sup>th</sup>-order Single channel SCISSOR, (c) 5<sup>th</sup>-order Double channel SCISSOR, and (e) twisted double channel SCISSOR.

#### 4.3.3.3 Ring-loaded Mach-Zehnder filters (RL-MZIs)

These optical filtering architectures consist of Mach-Zehnder Interferometers with  $N$  and  $M$  optical ring resonators cascaded on each arm respectively, [31, 91]. They allow the independent setting of zeros and poles. These structures can be used for implementing compact and footprint reduced all-pass, and bandpass filters with arbitrary responses. Figure 4.20 shows two examples of single and double- RL-MZI filters where the ring cavity length is 6 BULs.

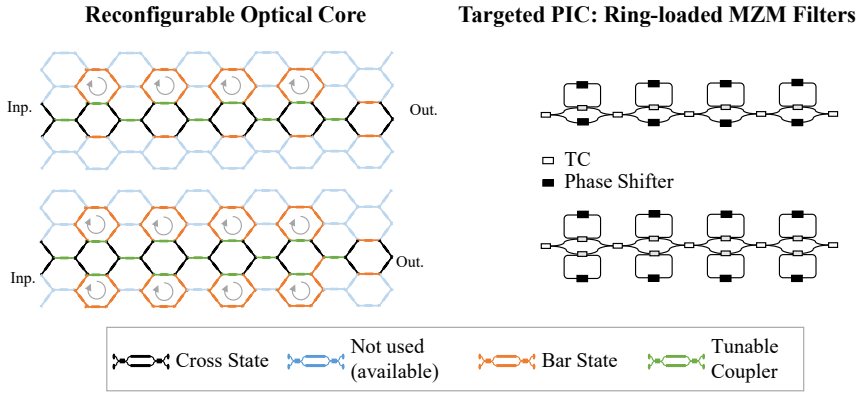


Figure 4.20 Ring-Loaded MZIs: (Left) Hexagonal mesh settings and (right) targeted single-loaded fourth order and double-loaded eighth order filter, respectively.

### 4.3.4 Universal linear optics transformers

The function of a linear optics device is to transform a series of  $N$  orthogonal modes ( $|\phi_i\rangle$ ) into the corresponding  $N$  orthogonal modes at the output ( $|\phi_o\rangle$ ), [26, 33]. This transformation, is defined by a unitary matrix  $U$  ( $|\phi_o\rangle = U|\phi_i\rangle$ ). Linear transformations are the fundamental building block of many applications in quantum information and communication systems, switching and routing, microwave photonics and optical channel management and supervision. The proposed hexagonal waveguide-mesh enables the implementation of the two layout versions of the universal linear interferometer proposed in the literature, [26, 88, 95, 34, 96, 97, 98, 99].

#### 4.3.4.1 Reck-Miller/ Triangular-arrangement interferometer

Figure 4.21(a) displays an example of a  $4 \times 4$  interferometer implemented by means of a triangular arrangement of beamsplitters and Figure 4.21(b) shows the equivalent structure implemented on a hexagonal waveguide mesh. Each beamsplitter can set a certain splitting ratio and a relative phase to the upper output. Reck et al. [26] and Miller [27] have developed algorithms to programme and configure the triangular arrangement so it can implement any desired linear unitary transformation, [27, 33]. To adapt, for example, the synthesis algorithm developed by Miller to the hexagonal waveguide mesh we, first of all, need to consider the possible different phase contributions due to the different access paths established between the interferometer inputs and the internal processing elements forming the triangular arrangement of beam splitters and, from these, to the different outputs.



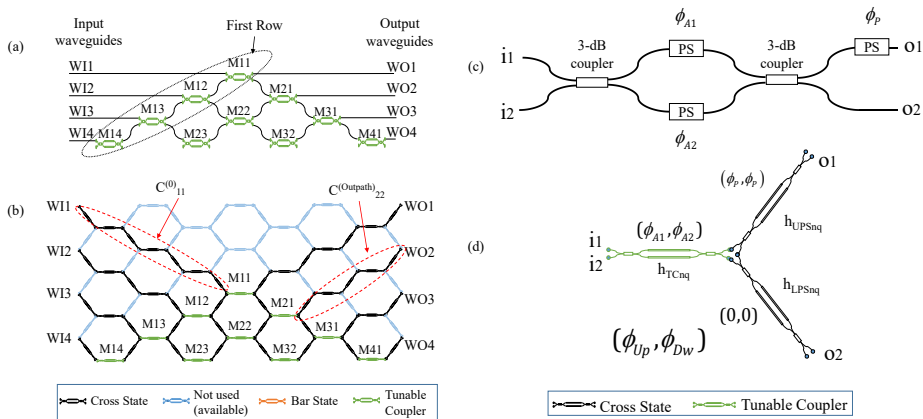


Figure 4.21 Universal interferometers: (a) Classical triangular arrangement and (b) hexagonal mesh based implementation of a 4 x4 interferometer. (c) Beamsplitter for the classical approach and (d) corresponding beamsplitter implementation with 3 TBUs for the hexagonal waveguide Mesh.

These different phase contributions must be compensated. Then, we need to establish an equivalent configuration, -using the available elements in our hexagonal waveguide mesh-, to the MZI with a phase shifter in the upper output port employed by Miller and shown in Figure 4.21(c). In our case, as illustrated in Figure 4.21(d), the equivalent “beamsplitter” is implemented using a TBU for the tunable coupler (with a transfer matrix defined by  $h_{TC}$  as in Eq. (4.2)), followed by two TBUs, which are biased in cross state and employed as output connections. In the latter, the upper TBU also implements a phase shifter and is defined by the transfer matrix  $h_{UPS}$ . The lower TBU is defined by the transfer matrix  $h_{LPS}$ .

Miller's synthesis algorithm is based on writing any of the input basis functions as a linear combination of each input port or rectangular functions ( $|\phi_{1n}\rangle$ ), and configuring sequentially each row of beam couplers for each input mode. These input modes can be obtained from the columns of the Hermitian Adjoint of the matrix  $U$ . A procedure describing the synthesis algorithm adaptation and the related equations is provided in the Appendix B.1.

Figure 4.22 illustrates an application example that includes the corresponding coupling and additional phase's values to configure the hexagonal core for a Hadamard transformation of size 4x4, defined as:

$$U_{Hadamard} = \frac{1}{\sqrt{2^2}} \begin{pmatrix} 1 & 1 & 1 & 1 \\ 1 & -1 & 1 & -1 \\ 1 & 1 & -1 & -1 \\ 1 & -1 & -1 & 1 \end{pmatrix}. \quad (4.6)$$

The actual implementation of the triangular arrangement for a 4x4 interferometer using a hexagonal mesh with the labelled configuration for each TBU is depicted, for the previous matrix, specifying: ID, for the TBU identification label,  $K$ , for the coupling constant,  $\phi$  for the additional phase shift. The letter P is used to indicate that the TBU remains in passive state (both phase shifters are unbiased). The coefficients and phase terms are found using the configuration algorithm developed in Appendix B.1.

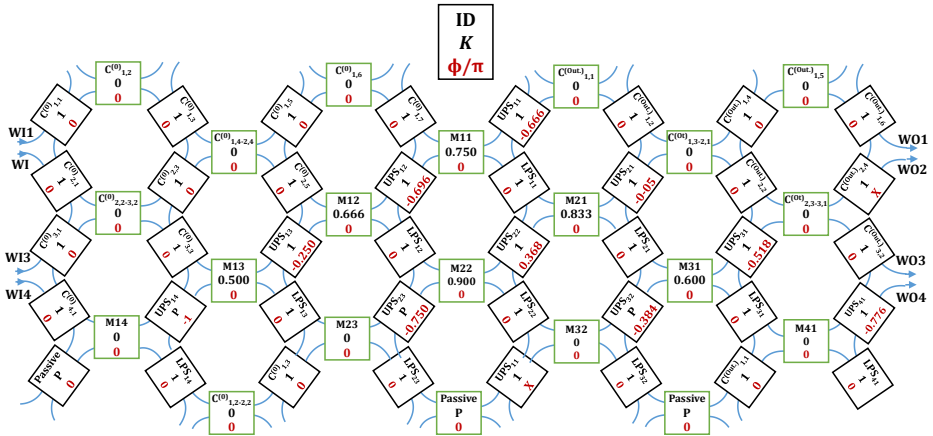


Figure 4.22 Universal interferometer: TBU settings of the hexagonal mesh for the Triangular arrangement implementation programming a Hadamard 4x4 linear transformation. ID: TBU identification Label,  $K$ : coupling constant,  $\phi$ : additional phase shift,  $P$ : coupling constant when both phase shifters are unbiased. Green-colour edges for TBUs acting as a tunable coupler and Black-colour for the cross state.

#### 4.3.4.2 Clements/Rectangular-arrangement interferometer

Figure 4.23(a) displays an example illustrating the implementation of a more compact 4 x 4 multiport interferometer based on the rectangular arrangement proposed by Clements et al. [88]. Figure 4.23(b) shows the equivalent structure implemented on a hexagonal waveguide mesh. In the algorithm developed by Clements, each beamsplitter (Figure 4.23(c)) sets a certain splitting ratio and a relative phase sequentially to programme and configure the whole rectangular arrangement so it can implement any desired linear unitary transformation efficiently, [88].

To adapt this layout and its synthesis algorithm to the hexagonal waveguide mesh, we need to perform a few modifications. First of all, we must use a different matrix for the beam coupler/TBU structure. In our case, as can be seen in Figure 4.23 (d), we employ a TBU for the tunable coupler (coloured in green), defined by a transfer function  $h_{TC}$ , and the two precedent TBUs (coloured in black) for the required connections. Here, the upper one operates in cross mode providing an extra phase shifting (Upper Phase Shifter,  $h_{UPS}$ ), while the lower one operates in cross mode.

Note that incidentally, both the classical and hexagonal approaches of rectangular arrangements need an extra phase shifter at each channel output that is required for certain applications, indicated as (\*) in Figure 4.23(b). Finally, some of the outer TBUs that build up the interferometer must be configured to be phase-transparent featuring the phase-shift values indicated in Appendix B.1, where together with a procedure describing the synthesis algorithm adaptation, we provide the related equations, incorporating the special case where the element to be null is already equal to 0.

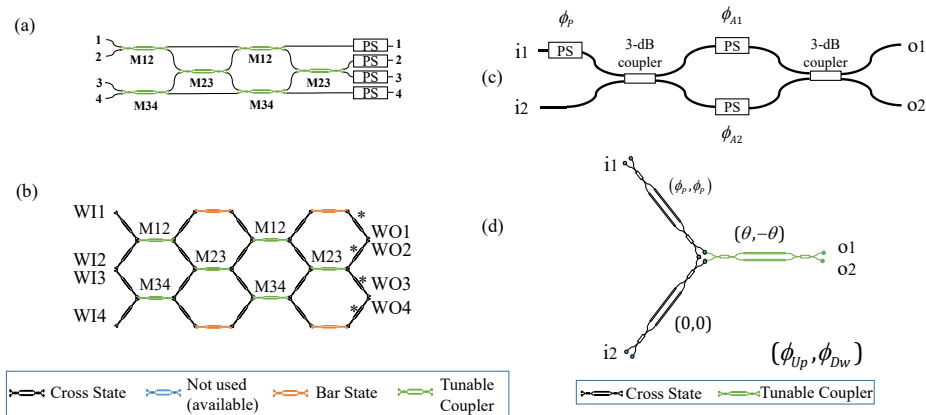


Figure 4.23 Universal interferometer: TBU settings of the hexagonal mesh for the rectangular arrangement implementation programming a Hadamard 4x4 linear transformation. ID: TBU identification Label, K: coupling constant,  $\phi$ : additional phase shift, P: coupling constant when both phase shifters are unbiased. Green-colour edges for TBUs acting as a tunable coupler, black colour for the cross state and orange colour for the bar state.

Figure 4.24 illustrates an application example that includes the corresponding coupling and additional phase's values to configure the same Hadamard transformation as in the previous case defined by (4.6).

Note that the rectangular arrangement is the most compact topology for the synthesis of a certain  $N \times N$  linear transformation.

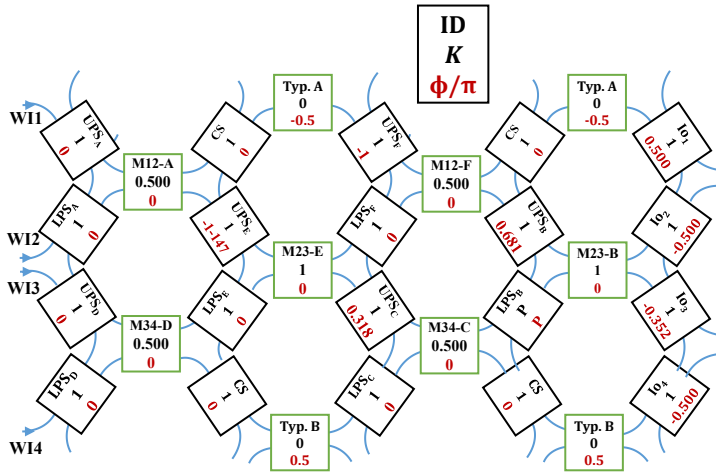


Figure 4.24 Universal interferometer: Rectangular arrangement TBU settings on hexagonal mesh based programming a Hadamard  $4 \times 4$  linear transformation.

A key advantage of this hexagonal mesh is the possibility to flexibly combine universal interferometers with other classic photonic integrated circuit structures that can be programmed over the mesh as well, such as Mach-Zehnder Interferometers or interferometric cavities. This comes at the expense of more beamsplitters for a certain  $N \times N$  linear transformation, that will increase from  $N(N-1)/2$  (triangular and rectangular arrangements), to  $(3*N*(N-1)/2) + 2*N$  for hexagonal applications. As previously outlined, a phase shifter/TBU must be added to each output, increasing the previous numbers by  $N$ .

Another advantage of the hexagonal mesh implementation is that, assuming equal losses for all the TBUs, the overall path losses for each configured channel will be equal, as the number of TBUs where the signal goes through is the same.

#### 4.3.4.3 4-sides interferometer: Channel management

Rectangular arrangements can be programmed to manage different optical channels enabling broadcasting, add/drop configurations, multiplexing and demultiplexing functions to cite but a few. A different device can be obtained if we add optical ports, in not only the left and right side of the arrangement, but also in the top and bottom sides of the rectangular arrangement thanks to the hexagonal mesh topology.

The main difference is that functionalities that are more compact can be achieved with this configuration. Consider that, for the standard rectangular arrangement, an Add/drop functionality would require  $N$  input ports equal to the number of channel inputs ( $I$ ) and  $add$  channels ( $A$ ). In the same way, the number of outputs ports will be

equal to the number of output channels ( $O$ ) and *drop* channels ( $D$ ). Figure 4.25 (top) illustrates this new configuration that places *add* and *drop* channels in the upper and bottom part respectively enabling a more efficient device. The TBUs from  $H1$  to  $H5$  are set in bar state performing the add/drop operation for the matrix illustrated in Figure 4.25 (top/right). In particular, corresponds to an Add (drop) operation for  $A1(D1)$  to  $A4(D4)$  while channel 5 bypasses the device.

Figure 4.25 (lower) illustrates the fully reconfigurable interconnection matrix that can be programmed. Each block is a tunable coupler and can be configured as a switch or define a desired splitting ratio in order to enable broadcasting, multiplexing, demultiplexing, and switching operations.

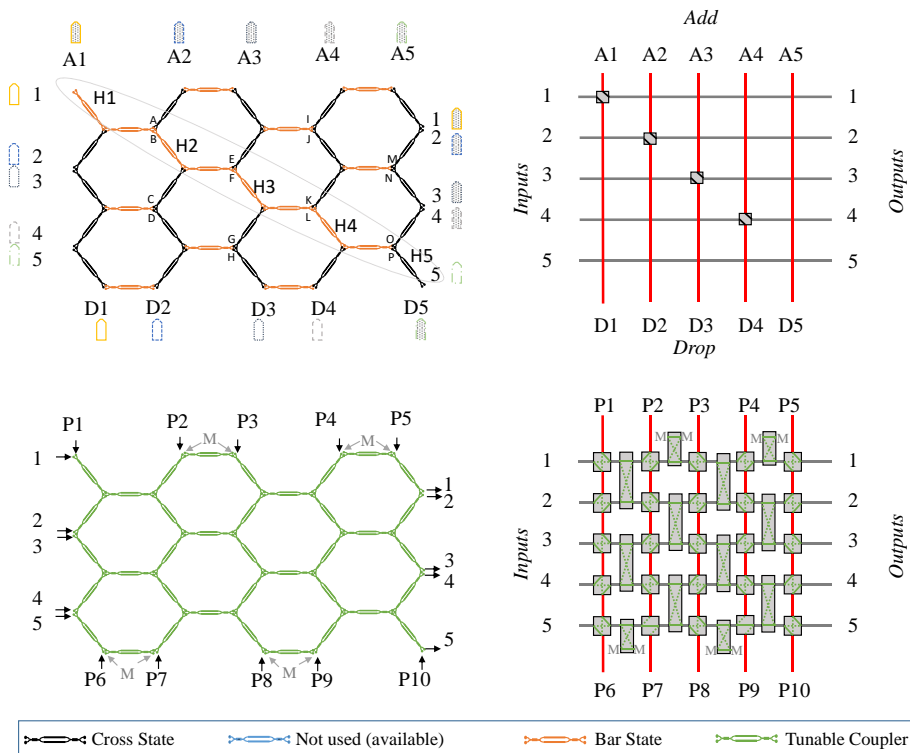


Figure 4.25 Waveguide mesh settings for channel management application: (up) Add-drop configurations for channels 1-4. Channel 5 bypasses the device. (Lower) fully reconfigurable channel management station that allows channel broadcasting, add/drops, channel combinations and demultiplexing. M: Signal monitoring points.

### 4.3.5 Functional designs for MWP applications

As introduced in Chapter 3, the generic-purpose photonic processor architecture employs several subsystems that can be activated or configured by software

definition: The optical source, electro/optic modulators, opto/electronic photodetectors and a reconfigurable optical core. The main tasks of the last subsystem are to interconnect the previous elements between them and perform versatile optical processing operations.

In this Chapter, we have shown that the hexagonal waveguide core is the best candidate to perform switching operations between the processor elements and to synthesize photonic integrated circuits enabling versatile optical processing operations. We propose here the first general-purpose photonic integrated processor that can be software-defined to perform multiple MWP applications with a reconfigurable optical core based on a hexagonal waveguide mesh. By suitable tuning each element on the processor, the same hardware can be configured to perform the main functionalities in MWP: Optical delay lines, RF-photonics filtering, optical generation of radiofrequency and millimetre waves, photonic-assisted RF-mixing, instantaneous frequency measurements, etc.

Figure 4.26 represents the processor architecture for a wide range of RF-photonics applications. All the elements are connected to the reconfigurable optical core in such a way that, not only they produce the desired filtering or delay schemes, but also connect the internal and the external elements required for different functionalities. As highlighted in the right part of the figure, a hybrid design might be needed to achieve the most efficient performance. In this case, we choose the silicon photonics platform (ochre colour) for the passive devices and the Indium Phosphide (red colour) for the active devices. Note that an array of optical amplifiers in this platform would be required to overcome the large conversion losses when moving from the radiofrequency to the optical domain. These losses are mainly related to the conversion efficiency of modulators and photodetectors as well as the propagation losses.

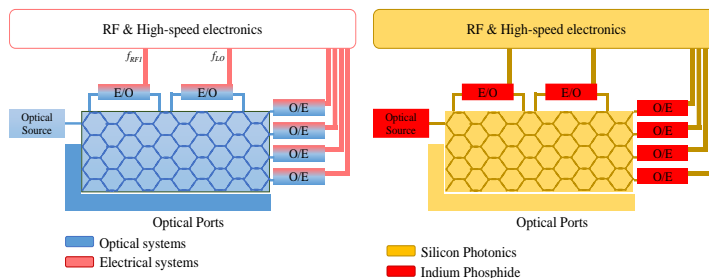


Figure 4.26 General-purpose photonic integrated processor architecture and candidate fabrication platforms for each subsystem.




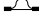
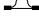


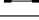



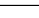



In this subsection, our proposal relies on the demonstrated performance of on-chip lasers, modulators and photodetectors together with the complex mesh devices

proposed and experimentally demonstrated within the framework of this Thesis. Simulations to test the specific performance of the programmed functionalities to be compared to an ASPIC counterpart are not addressed and are stated as on-going research work in Chapter 6. However, we identify and envision the main performance penalties.

In order to test the benchmark of the multi-purpose processor in terms of frequency we will consider four different BULs for a silicon photonics platform with a group index of 4.18.  $BUL_1 = 119.5 \mu\text{m}$ ,  $BUL_2 = 239.7 \mu\text{m}$ ,  $BUL_3 = 358.6 \mu\text{m}$  and a larger one of  $BUL_4 = 597.7 \mu\text{m}$ .

Some of the MWP applications described in this section will be limited to a set of FSR values, a discrete frequency grid or delay given by the chosen BUL. For these examples featuring different BUL values, the resulting FSRs of the filters (ORRs and MZIs) that can be synthesised on the hexagonal mesh are shown in Table 4.4. The ITU frequency grid has been highlighted for comparison. Radiofrequency bands ranging from the K (20 GHz) up to the E (60 GHz) band are covered by all of the proposed examples. In addition, the Vernier effect [100] could be exploited to overcome this limitation and produce greater FSRs.

Table 4.4. Frequency grid associated to 4 different BULs. The interferometric structure available for the hexagonal core is also indicated.

Interferometric length (BULs)	$BUL_1 = 119.5 \mu\text{m}$ FSR(GHz)	$BUL_2 = 239.7 \mu\text{m}$ FSR(GHz)	$BUL_3 = 358.6 \mu\text{m}$ FSR(GHz)	$BUL_4 = 597.7 \mu\text{m}$ $\mu\text{m}$ FSR(GHz)
 2	300.00	150.00	<b>100.00</b>	60.00
 4	150.00	75.00	<b>50.00</b>	30.00
 6	<b>100.00</b>	<b>50.00</b>	33.33	20.00
 8	75.00	37.50	<b>25.00</b>	15.00
 10	60.00	30.00	20.00	12.00
 12	<b>50.00</b>	<b>25.00</b>	16.67	10.00
 14	42.86	21.43	14.29	8.57
 16	37.50	18.75	12.50	7.50
 18	33.33	16.67	11.11	6.67
 20	30.00	15.00	10.00	6.00
 22	27.27	13.64	9.09	5.45
 24	<b>25.00</b>	12.50	8.33	5.00
 26	23.08	11.54	7.69	4.62
 28	21.43	10.71	7.14	4.29
 30	20.00	10.00	6.67	4.00

#### 4.3.5.1 True time delay lines

Together with tunable RF phase shifting, the tunable optical true time delay line is a key basic functionality required in complex signal processing applications. It constitutes actually an essential building block in a considerable number of filtering and optical beamforming schemes that will be described in following subsections. It is worth noticing that the first optical true time delay lines were implemented using optical fibres of different lengths and, therefore, resulted in bulky devices. During the last twenty years, however, different schemes of integrated delay lines have been reported [79, 92], where some of them enable tunable delays. The objective is to achieve long tunable time delays while maintaining high-bandwidth operability, reduced footprint and reduced losses per delay unit.

Using optical switches, discretely tunable time delays can be implemented selecting integrated waveguides with different lengths. They enable large bandwidth operation that is typically independent of the selected delay value. Nevertheless, some applications would benefit from continuously tunable delay lines.

An alternative approach to achieve continuous time delay relies on overlapping the group delay of cascaded optical filters such as ORRs loaded with a phase shifter. In this case, there is a trade-off between the bandwidth of the delay line and the time delay provided. In order to achieve longer continuous delays without reducing the bandwidth, a continuous delay ranging from 0 to  $\tau$  seconds in series with switched discrete delay lines offering  $\tau$ ,  $2\tau$ , and  $4\tau$  can provide an increased continuous delay line ranging from 0 to  $8\tau$ , [92]. In this case, since waveguide-based discrete delay lines enable large bandwidth transmission, the delay line bandwidth will be mainly limited by the coupled ORRs maximum bandwidth provided by the first continuous delay stage. In general, demonstrated losses per delay value are between 3.3 and 60 dB/ns, depending on the selected optical delay line scheme.

Another approach enabling continuous delays is the Separate Carrier Tuning (SCT) technique, [11, 101]. It consists of two independent blocks: a tunable delay line for the modulation sideband and a separate carrier tuning phase shifter for the optical carrier that extrapolates the linear phase characteristic of the sideband delay line. Varying the group time delay while independently applying a full phase shift in the separate carrier allows higher bandwidths. This technique has demonstrated delays up to 400 ps for small signal *bandwidth  $\times$  delay*. The hexagonal waveguide-mesh is a natural discrete optical delay line. If by switching different TBU we can set a light path corresponding to  $N$  BULs, then, the corresponding delay  $\tau$  is as:

$$\tau = \frac{n_g \cdot N \cdot BUL}{c}. \quad (4.7)$$



The basic unit delay for BULs values considered above and a group index of 4.18 are:  $\tau_1 = 1.66$  ps,  $\tau_2 = 3.34$  ps,  $\tau_3 = 5.00$  ps and  $\tau_4 = 8.33$  ps. The losses per delay value figure can be obtained as the ratio between the TBU insertion losses and its associated basic unit delay.

The techniques enabling continuously tunable delays reviewed above can be programmed as well in the hexagonal waveguide mesh. Figure 4.27(a) illustrates the group-delay overlapping of the cascaded ORRs approach. In the first case, each tunable coupler that connects the rings to the bus waveguide should have a small/moderate coupling constant maintaining a trade-off related to resonant insertion losses and group delay. Next, a phase shift is applied to each ring resonator to obtain the desired group delay overlapping profile for each wavelength. Note that the more overlapped they are, the higher group delay and the smaller bandwidth are achieved. Figure 4.27(b) depicts the implementation of the SCT technique, where the first two rings correspond to the carrier tuning and the two remaining provide the subcarrier phase shift. Finally, the waveguide mesh includes an optical filter based on a doubled loaded MZI to suppress one of the modulated sidebands. The signal bandwidth for this application will be limited by the passband response of this optical filter or the ORR stages corresponding to a few GHz for the selected example BULs.

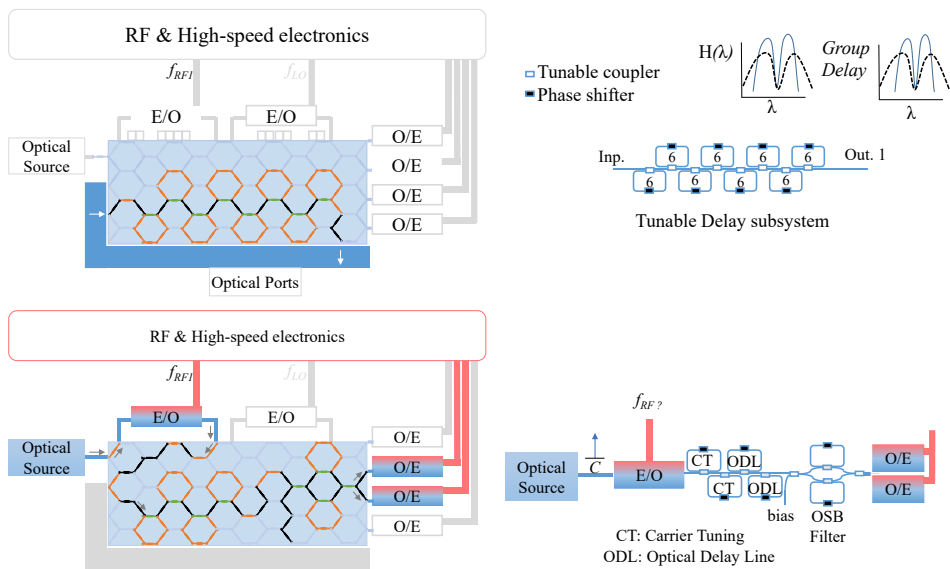


Figure 4.27 True Time delay line implementation for two different techniques: (top) Overlapping group delays of 7 cascaded ORRs, (bottom) SCT technique. The left part depicts the processor configuration and the right part shows the targeted scheme.

#### 4.3.5.2 Filtering applications

All-optical microwave signal filtering is probably the most widespread application in integrated MWP processors. Specifically, this application brings the possibility of designing fully integrated tunable photonic devices to meet flexible wideband spectral processing requirements for actual and future RF communication bands.

The general scheme of a microwave photonic system consists of an optical source modulated by an external modulator with the RF signal to be processed, followed by an optical core where the RF signal, up-converted to the optical region of the electromagnetic spectrum (at hundreds of THz), is processed by optical techniques and components, such as filters and amplifiers. Finally, the signal can be distributed to large distances or can be down-converted back to the RF domain with a high-speed photodetector resulting in the processed signal in the electrical domain. This scheme leverages on the unique characteristics inherent to photonics like high bandwidth, low losses, tunability and reconfigurability.

Depending on the operation regime, the filter can be based on a summation of optical intensities (ruling out the optical phases) in the case of incoherent operation, or a summation of electric fields, where optical phases are key, in the coherent regime case. In the first one, the shortest delay experienced by the signal inside the filter is much longer than the coherence time of the optical source. It is commonly implemented with discrete and large optical components, where the coefficients are set by optical amplification or attenuators and the delay is given by tunable delay lines to obtain tunable frequency responses. Filters built using optical discrete delay lines and fibre Bragg gratings reach up to 40 dB of Extinction Ratio and quality factors up to 325 with a high number of taps and, hence, require a considerable number of components. Some of them have demonstrated reconfigurability and tunability up to around tens of GHz, but it is quite difficult to maintain the resulting bulky system stable in temperature. Implementation of integrated incoherent MWP is not easy on a chip scale as the inherent small footprint delays call for the use of broadband optical sources to meet the incoherent operation condition.

On the other hand, coherent filters, where the longest delay experienced by the signal is much shorter than the coherence time of the optical source are amenable for integration. Integrated optics circuits have been demonstrated recently for the implementation of tunable coherent optical filters [82, 19, 43, 51, 20].

Optical Single Side Band Modulation (OSSBM) is an interesting particular approach for the implementation of coherent MWP filters as it allows the direct transmission of the transfer filter implemented by the optical core to the RF region of the spectrum. In this case, the detected photocurrent is then proportional to the frequency response of the optical filter at the carrier frequency multiplied by the

optical filter response at the RF sideband, mapping the shape of the optical filter transfer function into the electrical domain [102]:

$$i(t) \propto s |H(f_o)| \cdot |H(f_o + f_{RF})| \cdot \cos(2\pi f_{RF} - \angle H(f_o) + \angle H(f_o + f_{RF})), \quad (4.8)$$

where  $H(f)$  is the optical filter response at a given RF frequency  $f$ .

Furthermore, different modulation and detection schemes can be employed to increase the tunability range, the dynamic range, the gain and the noise figure of the whole system, such as self-heterodyning systems [81] where full-FSR frequency response tunability can be achieved by adding a phase shift into the optical filter and employing a copy of the carrier that was sent to a different path prior modulation.

Coherent filters are usually based on optical filters built from the concatenation of single unit cells such as Mach Zehnder interferometers (zeros), ring resonators (poles) and ring-loaded MZI. As shown in the previous section, tuning can be achieved by adding a simultaneous phase to all the filtering structures. Optimum passband filters like Chebyshev, Butterworth, and Elliptic are possible, where the filter order is related to the number of ring resonators in the structure [32]. The concatenation of unit cells increases the insertion losses of the whole device (if each cell has no zero insertion losses), but, on the other hand, can produce more selective filters as the result of multiplication of their individual frequency responses. Integrated solutions outstand due to their versatility and low SWaP, offering at the same time similar figures of extinction ratio and selectivity comparing to bulk optics designs.

Figure 4.28 illustrates an application example of the multi-purpose processor hexagonal core for the implementation of MWP filters. It corresponds to a RF-photonics filter employing a self-homodyne modulation/detection scheme. The optical filter stage synthesises, in this case, a 6<sup>th</sup> order optical filter based on a SCISSOR structure. For the case of RF-photonics filters, the limitation will depend on the modulation scheme: Double side band modulations would have the half-FSR of the optical filter whereas Single-side band modulations map the full FSR of the optical filter to the electrical domain. Following the Table 4.4, the optical filter corresponds to an FSR associated to ORRs of 6 BULs of 100, 50, 33.33 and 20 GHz for each selected BUL. A wide variety of optical filters that can be synthesised on the hexagonal waveguide core reviewed in the previous sections are amenable to be translated to RF.

When compared to its ASPIC counterpart, the programmable processor suffers from extra excess losses due to the waveguide lattice mesh, reducing the total RF gain. To overcome this limitation, the integration of optical amplifiers must be considered. In contrast, the reconfigurability of the filter is increased, resulting in a

more powerful and versatile device. Although the noise figure and the dynamic range could be deteriorated, the programmable processor could take advantage from its high-reconfigurability degree to perform optimum filtering and linearization over the whole system in the optical or in the RF domain, as stated in Chapter 2.

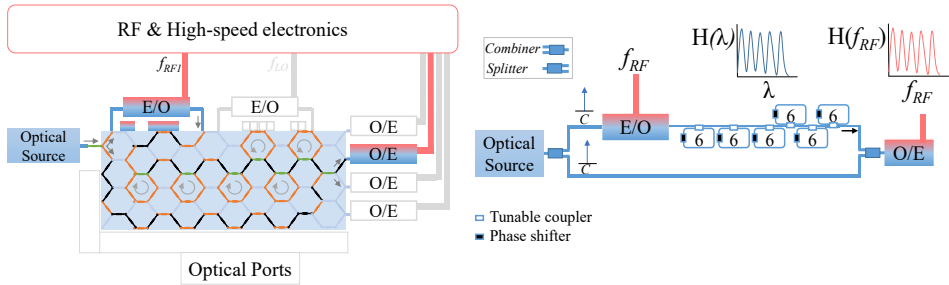


Figure 4.28 General-purpose signal processor configuration for RF filtering implementation (left) based on a self-homodyne modulation/detection scheme (right). The optical filter is composed of six cascaded ORRs defined by a cavity length of 6 BULs.

#### 4.3.5.3 Optical Generation of continuous microwave & millimetre wave signals

The optical generation of high-quality CW microwave and millimetre-wave (mm-wave) signals can be applied in many fibre-supported microwave and mm-wave systems (including antenna remoting and phased array antennas) with a special interest in the upcoming 5G radio access networks [52, 79]. This functionality allows the generation and distribution of high-frequency RF signal by taking advantage of inherent properties of optics, such as low propagation losses of standard fibres and the availability of fibre amplifiers. Actually, the purely electrical approach faces problems in the generation of signals above 25 GHz, while their distribution is highly challenging due to the propagation losses of coaxial cables. In addition, the increasing bandwidth demand in communications has driven the attention towards the mm-wave band because of the wide bandwidth available for high-data-rate wireless transmission where propagation losses are even higher for purely electrical/RF systems.

The main performance figures of photonic-generated RF signals systems are the frequency range where the signal can be generated and the linewidth of the tone. As in every PIC, it is also important to evaluate the power consumption and the potential integration percentage of the whole system.

There are different reported approaches to generate microwave and mm-wave signals, but most of them are based on optical heterodyning, in which two optical waves of different wavelengths beat at a photodetector generating a tone up to the THz band with a frequency coincide on the difference between the two tones. The

phase of the resulting tone will be the difference between the two phases. Thus, in order to generate low-phase noise, the use of correlated optical waves is advisable.

The maximum achievable frequency is mainly limited by the photodetector bandwidth (among other specific limits related to each approach). Figure 4.29 shows the performance of the demonstrated devices for each technique reported during the last years. They can be classified into six groups: Optical injection locking, optical phase locking, optical injection phase locking, external modulator based, optoelectronic oscillators and dual parallel MZMs. The first three have not been able to break the 42-GHz barrier and need two lasers to be working at the same time.

The approach employing an external modulator takes advantage of the frequency up-conversion inherent when a continuous wave signal provided by a laser is modulated by an RF tone. By employing different modulation biasing points, the input frequency can be doubled or even quadrupled by suppressing the odd- or even-order modes, (together with the use of an optical filter to suppress the optical carrier). The linewidth is limited by the input signal and can be as low as 5 Hz. The lowest frequency is limited by the bandwidth of the filter employed to suppress the carrier, while the highest achievable frequency is limited by the photodetector bandwidth and the modulator bandwidth. This technique has reached tone generation up to 60 GHz. The use of a phase modulator instead of an intensity modulator avoids the bias drift problem that would need a control circuit in order to increase the robustness, [103].

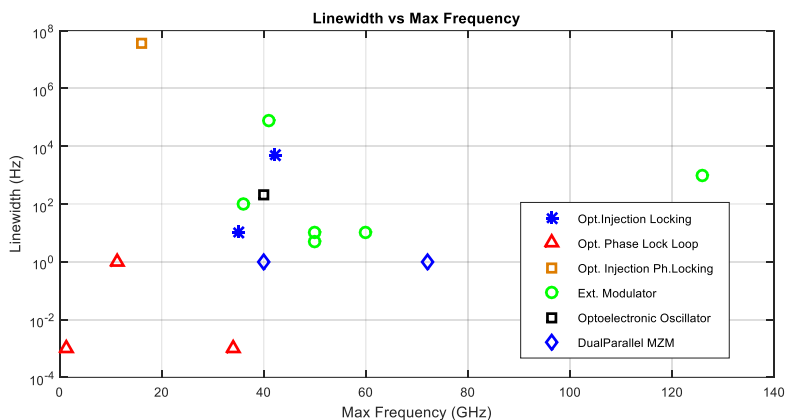


Figure 4.29 Linewidth vs maximum frequency of the different demonstrated techniques for optical generation of microwave and millimetre-wave signals, [79].

An interesting alternative that has achieved an outstanding integration degree is optoelectronic oscillation. The oscillator operates by modulating a continuous wave signal from a laser with an external intensity modulator. The signal goes through a high-Q optical storage stage (Fabry Perot filter or optical delay line) in order to

suppress the unwanted modes and provide a cavity round-trip delay. The photodetected signal is injected again into the modulator after the electrical stage as a feedback loop. This architecture has provided a linewidth under 200 Hz and tones ranging from 10 up to 40 GHz, [104].

Finally, the use of a Dual Parallel Mach-Zehnder Modulator (DPMZM) maintains a good trade-off between linewidth obtained, (in the range of tens of Hz), and achievable frequency, (that ranges from very low frequencies up to 60 GHz and is actually limited by the photodetector and the modulator bandwidth). In this case, a MZM is connected at each arm of an outer MZM forming a third interferometric structure. This structure can provide Optical Carrier Suppressed modulations without using an optical filter. The generated tone is then the difference between the optically modulated tones. Regarding power consumption, this structure only needs an optical source and an optical amplifier to increase the conversion gain.

None of the aforementioned analysed structures have been completely integrated on a complex PIC. However, integrated optical lasers and modulators are already available. Standalone integrated modulators and photodetectors up to 50 GHz have been demonstrated in many of the platforms we described in Chapter 2.

Our proposed multi-purpose programmable MWP processor architecture enables the synthesis of different schemes for carrying out this task. Figure 4.30 illustrates the processor configuration implementing different approaches: (a) the external modulator approach, (b) the optoelectronic oscillator approach. Note that if a DPMZM was included in the architecture, this technique could be integrated as well. The achievable frequencies would mainly depend on the modulator and photodetector performance. Particularly, the bandwidth limitation in (a) due to the optical filter might be determined by the UMZI FSR of  $\Delta L = 2$  BULs, ranging from 300 up to 60 GHz for the selected BUL examples.

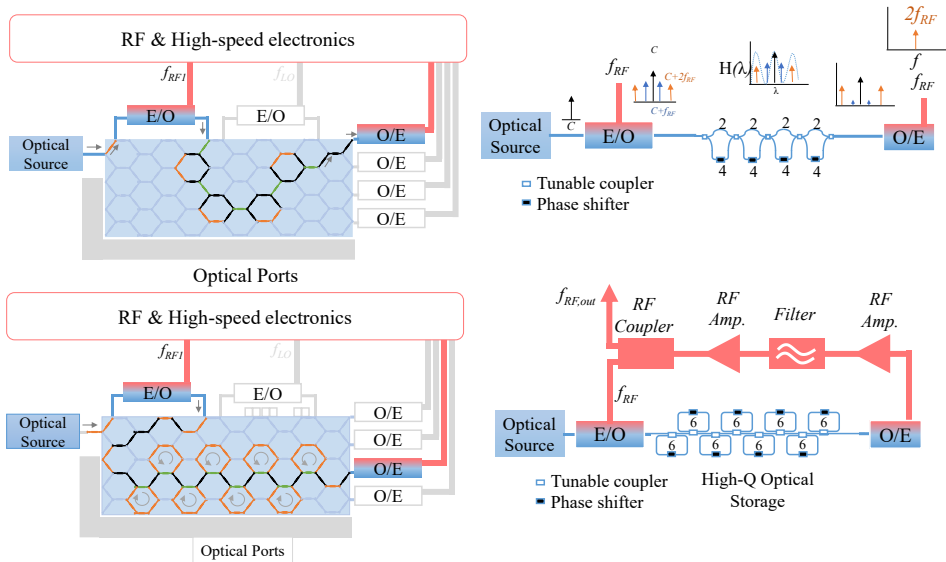


Figure 4.30 General-purpose signal processor configuration for microwave and mm-wave tone generation based on (upper) External modulator approach, (bottom) Optoelectronic oscillation approach. The right figures illustrate the targeted configuration schemes.

#### 4.3.5.4 Optical mixing: Radio-frequency upconversion/downconversion

Frequency up- and/or down- conversion of RF signals is usually required in many radio-over-fibre and intermediate-frequency-over-fibre communication systems. Different architectures have been proposed focusing on the modulation scheme of both the laser and the local oscillator signal, i.e., direct or external modulation, [105, 106]. The use of an optical modulator is equivalent to the use of an electrical mixer, but without the limitation to an intermediate frequency bandwidth of less than a few GHz. The use of an external modulator for both the RF input frequency and the local oscillator (LO) increases their maximum frequency at both system inputs.

Dual parallel Mach-Zehnder modulators [106] can up-convert signals to high frequencies as well. They can double the frequency by biasing the DPMZM to obtain Optical Double Side Band - Carrier Suppressed (ODSB-CS) modulation without employing optical filters providing destructive interference for the carrier.

The main figures of merit to be evaluated in these systems are the RF Gain (conversion losses), the Noise Figure and the spurious free dynamic range (SFDR). The approach based on two cascaded intensity modulators with frequency doubling [105] has worse figures of merit than the one built upon the DPMZM. The latter

improves 10 dB the NF, near 20 dB the Gain and  $10 \text{ dB} \cdot \text{Hz}^{2/3}$  the third-order SFDR (SFDR<sub>3</sub>), [106].

For this application, it might be more efficient to have a DPMZM instead of two E/O intensity modulators in the photonic processor. Nevertheless, we leave this option as a future work and consider the two modulators approach here.

Figure 4.31 illustrates the processor configuration for optical mixing and the targeted scheme. An optional optical filter is employed in this case to suppress the possible intermodulation contributions prior to the second modulator input. An optical amplifier array prior to the photodetection stage would improve the overall gain of the RF signal output, which is particularly necessary to overcome the electrooptic and optoelectronic conversion losses.

Another approach employing a pure-optical local oscillator would require the integration of another optical source. Also, the LO signal can be introduced externally by the optical ports.

The maximum bandwidth will be given again by the modulation and photodetector bandwidths. When compared to its ASPIC counterpart, only the programmed optical filter will decrease the RF gain of the system. However, this filtering stage can benefit from a higher reconfigurability degree and increase the system linearity.

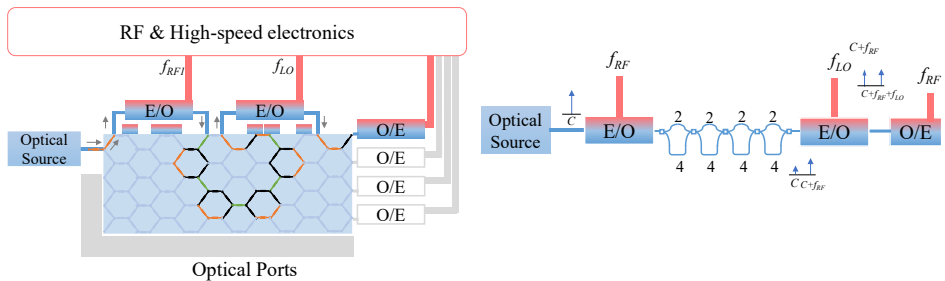


Figure 4.31 General-purpose signal processor configuration for RF-mixing scheme example (left) for a targeted configuration scheme composed of 2 electrooptic modulators and an optical filter implemented by four cascaded MZIs (right).

#### 4.3.5.5 Arbitrary waveform generation

This application pursues generating ultra-broad bandwidth RF waves with arbitrary and reconfigurable phase or amplitude characteristics. Applications like pulsed radar, medical imaging, modern instrumentation systems and ultrawideband (UWB) communications need a system for the generation of arbitrary waveforms. Again, the electronic counterpart is limited in frequency and bandwidth to few GHz. A solution is to take advantage of the high speed and broadband characteristics



offered by photonic devices and generate the microwave arbitrary waveform in the optical domain. There are four main techniques: direct space-to-time pulse shaping, spectral shaping and wavelength-to-time mapping, temporal pulse shaping as well as microwave signal processing shaping. MWP techniques have been demonstrated in bulky devices [107], lacking on full programmability and reconfigurability that is essential in arbitrary waveform generation.

The use of an optical filter to implement a spectral shaper followed by a dispersive element to implement the wavelength-to-time mapping is a promising solution and can be integrated on a chip [48]. Even though, the main difficulty remains in the dispersive element that is not easy to integrate in a small footprint while providing, at the same time, long differential delays.

Arbitrary waveform generators should have a wide range of tunability and reconfigurability and the hexagonal core enables this capability. Ultra-reconfigurable filter topologies and design parameters can be tuned to produce the spectral shaper followed by a dispersive component that can be programmed with cascaded lattice filters of unbalanced MZIs creating the desired dispersion profile, as shown in Figure 4.32. In contrast, more insertion losses will be added when compared to an ASPIC solution. If a certain application needs a higher differential delay, the optical ports can be employed to connect dispersive fibre reels.

For the BULs selected as an example, the FSR limitation of the optical filter will be again between 100 and 20 GHz for each BUL, limited by the shortest FSR that in this case is determined by the ORRs.

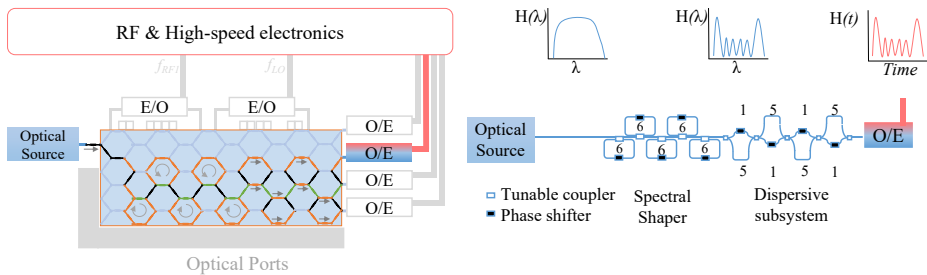


Figure 4.32 General-purpose photonic processor settings for the implementation of Arbitrary waveform generation (left) and targeted system scheme composed of an spectral shaper and a dispersive subsystem (right).

#### 4.3.5.6 Beamforming networks

In phased array antennas, the circuit that feeds the radiating elements is known as the beamforming network. It is possible to modify the radiation characteristics of an array of equal radiating elements simply by changing their electrical excitations. The beam

is then steered by adjusting the phase relationship between the different feeding paths. The angle of transmission or reception  $\theta$  is given by:

$$\theta = \arcsin\left(\frac{\lambda \cdot \Delta\phi}{2 \cdot \pi \cdot d}\right),$$

where  $d$  is the distance between array radiating elements,  $\lambda$  the optical wavelength and  $\Delta\phi$  is the differential phase shift introduced between the different array elements. There are two alternatives to perform the phase shift. The first one is by directly applying the differential phase by an integrated phase shifter. In this case, the pointing angle varies with the input RF frequency. The second approach is to use tunable delay lines, where the pointing angle  $\theta$  remains independent of  $f_{RF}$  offering a squint-free approach suitable for wideband operation, [108].

This field has raised a considerable attention for the last 30 years, moving from the military field to civil radars, remote sensing platforms, satellite or airborne communications, air traffic control, radio astronomy and flexible cellular wireless communications. From the first bulky fibre-based devices, integrated MWP approaches have been proposed based on ORRs as tunable optical delay lines elements [109]. They can provide up to 2.5-GHz bandwidth, limited by the ring performance. Furthermore, a more complex integrated beamforming based on SCT to provide de delay has been proposed for a 2D array system of 16 antennas, [11, 18].

Figure 4.33 corresponds to the implementation of a beamformer based on the natural discrete delay lines of the hexagonal core. In this case, the bandwidth is wide and will mainly be limited by the modulator or photodetector bandwidths. The pointing angle can be varied modifying the differential length between the paths feeding the photodetectors ( $\Delta L$ ). The tilt angle tuning will be limited to discrete values. Figure 4.34 shows the tilt angle for the BULs taken as an example at the beginning of this section and a group index of 4.18. Larger BULs produce less angle resolution. Negative waveguides lengths refer to the case where the lower antennas have a shorter feeding path. Note that continuously tunable delays can be added to overcome this problem, as described in the previous subsection *Optical delay lines*.

If a certain application requires more antennas to enable 2D tunability, more multi-purpose chips can be employed and connected between their optical ports.

In addition, pure optical beamforming can be done as well employing exclusively the optical core.

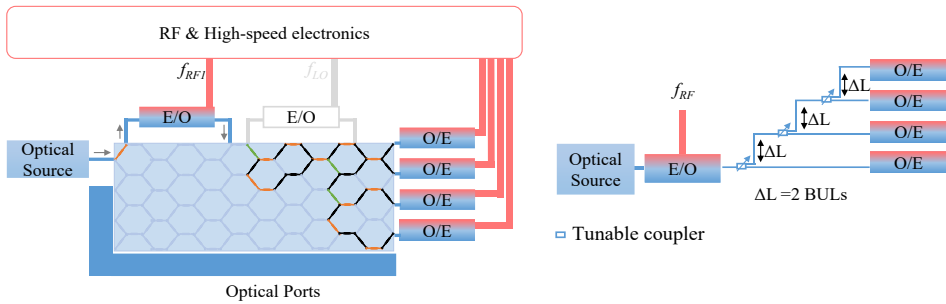


Figure 4.33 General-purpose photonic processor settings (left) for the implementation of beamforming networks based on discrete optical delay lines with a differential length of  $\Delta L$  (right).

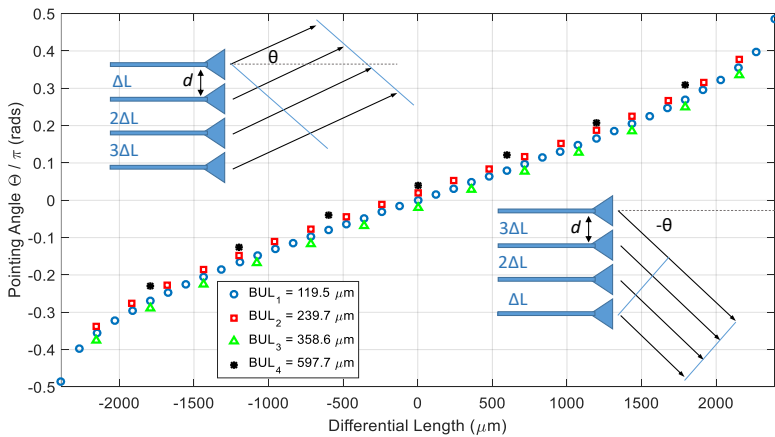


Figure 4.34 Beamforming networks based on discrete delay line implementation for broadband operation. A differential of  $0.04 \text{ rads}/\pi$  on the y-axis has been applied to improve readability. For this example, we consider a distance between radiating elements  $d = 1 \text{ cm}$ .

#### 4.3.5.7 Instantaneous frequency measurement (IFM)

The ability of measuring in real-time applications the frequency of microwave signals is enabled by photonic-assisted devices. Integrated photonics devices take advantage not only of low cost, weight and power consumption, but also of the reduced measurement latency due to the short optical paths when comparing to bulk-optics-based-systems. Large bandwidths up to 40 GHz (limited among others by the

bandwidth of the modulator), and high accuracy (represented by an error below 1% in the measured range), have been demonstrated increasing the range and capacity of electronic-based IFM systems, [39, 38, 23].

Demonstrated devices follow two main approaches clearly differentiated. On the one hand, the basic principle is to map the unknown microwave frequency to an optical power ratio by establishing a unique relationship, which is commonly referred as the amplitude comparison function (ACF) that is independent of both the laser and input RF powers. The reported devices have been partially fabricated on Silicon Nitride [23], InP [39] and Silicon [110]. On the other hand, Four Wave Mixing (FWM) approaches map the input frequency to the power of an idle tone generated by a non-linear process like the Kerr effect on thick silicon or ChG waveguides [38]. Neither of them includes the optical source nor the modulator and the detector on-chip. Thus, a maximum 20% of the components have been integrated. The ones that employ interferometric structures are limited in range to the quality factor and the free spectral range, while the FWM-based IFM depends on obtaining a high on-chip non-linearity coefficient in order to avoid the use of fibre. Figure 4.35 reports the error and achievable bandwidth demonstrated by different IFM devices. Obviously, a low measurement error for a wide bandwidth is desired. The best results exhibit sub-1% error rates for up to 34 GHz for both approaches.

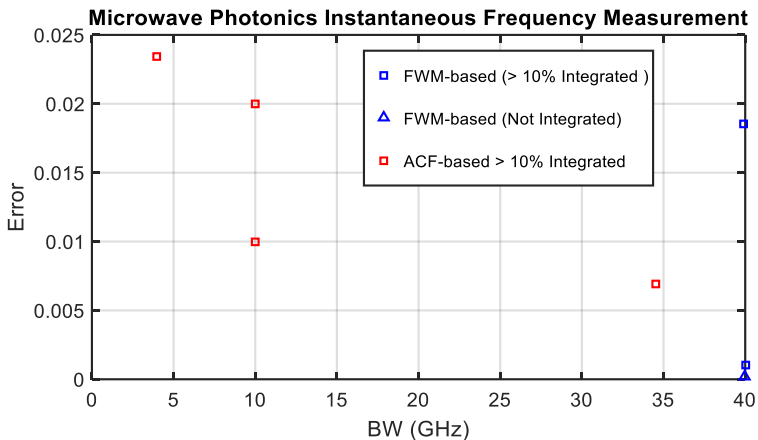


Figure 4.35 Bandwidth vs Error (%) for partially integrated IFM systems demonstrated in the literature.

The approach that employs interferometric structures like ORRs exhibits a trade-off between the measured frequency range and the error while maintaining a real-time process due to the FSR limitation in frequency and the quality factor. Some of them use a coarse and a fine measure after setting a narrower range as an effective method to increase the accuracy while giving up a faster response time. All the

processing is taken in the photonic domain but an integrated electrical circuit is needed to map the optical power versus frequency function. These approaches open the door to highly accurate IFM systems with a reduced quantity of active components. A high-performance IFM has been demonstrated with DSB-CS based on the use of only one non-tunable optical source, an intensity modulator, a simple ORR-based add-drop and two photodetectors [110].

Figure 4.36 illustrates the configuration of the generic-purpose photonic integrated processor. In this case, the optical source, one E/O modulator producing a Carrier-suppressed Double Side-band modulation and two photodetectors are enabled. The reconfigurable core leads the signal from the optical source to the modulator and performs the complementary function on the interferometric filter structure for the ACP function. In this case, it consists of two stages of double-loaded MZIs. Considering the previous example BULs, the frequency range of this device would be limited to a range up to of 50, 25, 16 and 10 GHz respectively, which is half the FSR of the 6-BULs ORR.

A key advantage of the reconfigurable processor is that the ACF can be made reconfigurable. Sharper functions lead to an increase in the resolution at the expense of reducing the frequency range, so multiple measurements can be done while reconfiguring an ACP function for each frequency range of measurement. In contrast, the increment in the optical filter insertion losses might degrade the system sensitivity.

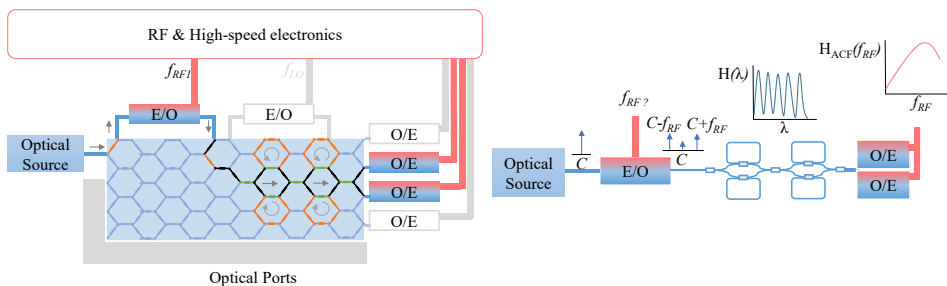


Figure 4.36 General-purpose photonic processor settings for the implementation of instantaneous frequency measurement based on ACP function mapping (left) and targeted system scheme (right).

#### 4.4 The software layer

The software-defined tag has been used in microwave photonics [111], and the software-radio [80] communities for the last years. It implies that a particular architecture or system can be programmed/reconfigured after fabrication and provide a sort of adaptability degree to the escorted word.

The generic-purpose processor architecture proposed in Chapter 3, and particularly, its internal subsystems, can be reconfigured by means of its electronic control signals. These signals can be grouped together into the processor state vector  $\mathbf{C} = (c_1, c_2, c_3, \dots, c_N)$ , where each  $c_i$  identifies a particular parameter of a given photonic or RF component. For example, in the context of optical modulators,  $c_i = \{0, V_{\pi/2}, V_{\pi}\}$  could define the voltage values for null, quadrature and maximum bias point of an internal modulator;  $c_i = \{V_X, V_{\parallel}, V_K\}$  the voltage values for cross and bar operation of a 2x2 optical switch or TBU defined by a K coupling factor;  $c_i = \{V_0, V_{\pi/2}, V_{\pi}, V_{3\pi/2}\}$  the voltage values required to achieve a given phase within an optical phase shifting element in the optical core, etc. The common hardware platform would then implement different functionalities by changing the values of the components in its state vector. Depending on the software capabilities, for a targeted functionality, the processor might be able to configure itself to optimally perform the application.

Figure 4.37 illustrates the processor's workflow. As an initial step, the pre-evaluation or characterization of the subsystems in general and the reconfigurable optical core in particular are essential for the correct processor's performance. After this task, which can be performed by the processor during its initialisation, the device is ready to programme diverse functionalities. First, the subsystems implied in the operation must be enabled with the correct control signals. Next, the circuit topology and/or optical interconnections to be synthesized in the reconfigurable optical core must be chosen together with the high-level design parameters. In the case of an optical filter synthesis based on cascaded ring resonators, the number of rings, coupling constants and differential phase applied to each ring must be computed. Once obtained these results, these settings have to be programmed in the reconfigurable optical core. Dynamic operation based on signal monitoring can be employed to optimise and improve the overall performance in real time.

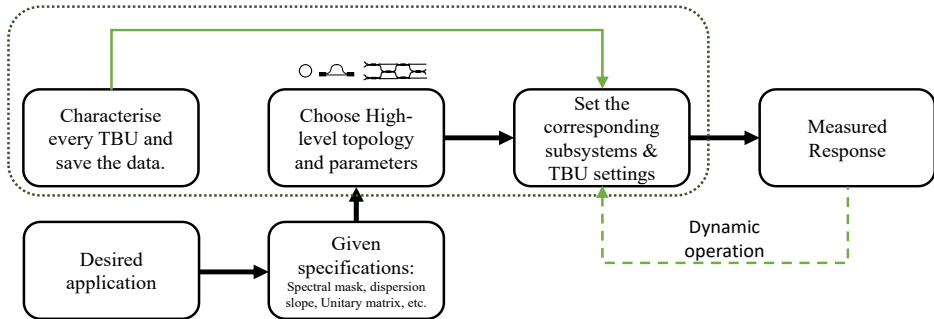


Figure 4.37 Processor workflow including optional dynamic operation.

The software capabilities of the processor determine the complexity level of the tasks that it can perform independently. In our case, we could define three tiers of software-definition: *Tier one*, implies the user ability to change the lower layer settings such as TBU phase-shifter currents that are directly related to the TBU coupling coefficient and the additional phase response. In this case, the circuit topology and design parameters are chosen by the user, which must enable and configure each TBU to obtain the desired light path. The user oversees enabling and configuring all the subsystems required for the desired operation. *Tier two* is defined as the one that includes the capacity of the processor to choose the best alternative to synthesize/emulate a certain configuration. If the user decides to programme, for example, an optical ring resonator of a certain FSR, and extinction ratio, the processor will internally configure itself the circuit topology and design parameters in an efficient way. In this case, the processor performs a system pre-evaluation that allows knowing the status of each subsystem. For the reconfigurable optical core, the processor performs an algorithm to optimally allocate the synthesised circuit and to set the suitable high-level design parameters. In *Tier three*, in contrast, the user specifies a desired application and the specifications, while the processor chooses the best topology to accomplish the previous requirements allowing the user to become totally disregarded of the internal configuration. The last two levels could optionally provide self-healing attributes. This characteristic can be achieved if the processor automatically detects a defective phase shifter, TBU, waveguide or port and prevent the signal to go through this element. These software-defined tiers can actually coexist together and are represented in Figure 4.38.

Several examples of software procedures are included in Appendix B.3.

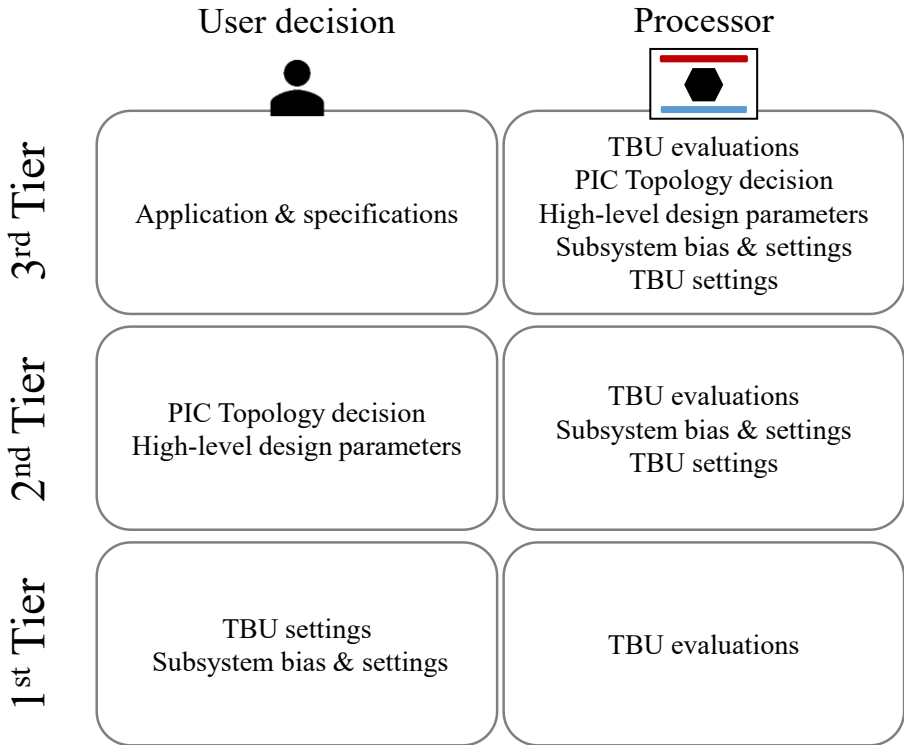


Figure 4.38 Software-definition levels depending on the capabilities of the signal processor to perform configuration and evaluation tasks.



# Chapter 5

## Design, fabrication and demonstrations

### 5.1 Introduction

In this chapter, we address the design, fabrication and measurement process of the first hexagonal photonic waveguide mesh reconfigurable core. The device has been fabricated in Silicon on Insulator (SOI). As mentioned in earlier chapters, this core is the key part of a reconfigurable photonic processor. In our case, the remaining elements will not be integrated in the same chip. Considering the fabrication technologies reviewed in Chapter 2, a fully integrated version of the proposed multi-purpose processor could be realized, either in a monolithic Indium Phosphide (InP) platform or by considering a hybrid design including the silicon photonic platform for the passive devices and the electronics and InP for the active elements.

The waveguide mesh reported here is composed of 7 hexagonal cells. By suitable programming each of the 30 TBUs that build up the core, we analysed both measured and simulated optical responses of more than 30 different photonic integrated circuits, demonstrating, to the best of our knowledge, the highest versatility of a photonic integrated circuit to date. This figure is limited by the number of current sources available at the moment of measurement (18 sources) and could be extended up to 100 different photonic integrated circuits programmed with the addition of 12 extra current sources.

After the fabrication stage, during the testing period, the device performance displayed, as expected, several undesired effects related to the non-ideal behaviour of the integrated devices. These were mainly caused by optical crosstalk and thermal crosstalk inherent to the tuning mechanism. We analyse them and identify their origin and impact on waveguide mesh-based reconfigurable optical cores.

Finally, we provide a discussion on the TBU influence on the processor performance and the optimal Basic Unit Length.

### 5.2 Chip design

The photonic chip layout was designed using a code-programming software called *Optodesigner: Phoenix Software*© for the creation of a Graphic Database System file (.GDS). Due to the symmetry, replicability and recursive properties of the waveguide meshes, the design process can take advantage of code loops provided by any code-based design software package.

Before starting the design stage, we considered 6 different layouts. Figure 5.1 illustrates the candidate layouts together with their associated number of cells, TBUs, phase shifters and electrical DC Pads considering, in principle, single-point ground at PIC level. A quick analysis shows that a good trade-off is achieved for the 7-cell layout as related to complexity, risk and versatility allowing, in principle, the synthesis of over 100 different configurations. Despite the fact that the 8-cell layout is apparently the most complex layout of the ones we considered, we found that it was not able to synthesise double-loaded ORRs MZIs, unlike the 7-cell configuration. We also considered layouts with a lower degree of complexity. For instance, the 6-cell provides the possibility of implementing more than 50 different devices, while both 4-cell devices enable the synthesis of around 18 different devices. All in all, we finally chose the layout with 7 hexagonal cells.

The aim of the design was to demonstrate the synthesis of more than 20 different configurations including optical ring resonators, MZIs, complex combinations of cascaded/coupled photonic integrated circuits, universal linear interferometers and optical delay lines as theoretically anticipated in Chapter 4. Since we aimed a proof-of-concept device, we decided to choose the thermo-optic effect as the tuning mechanism to configure each TBU, as its design is easier, less risky and does not produce undesired extra losses if the metal layer is far enough from the optical waveguide core.

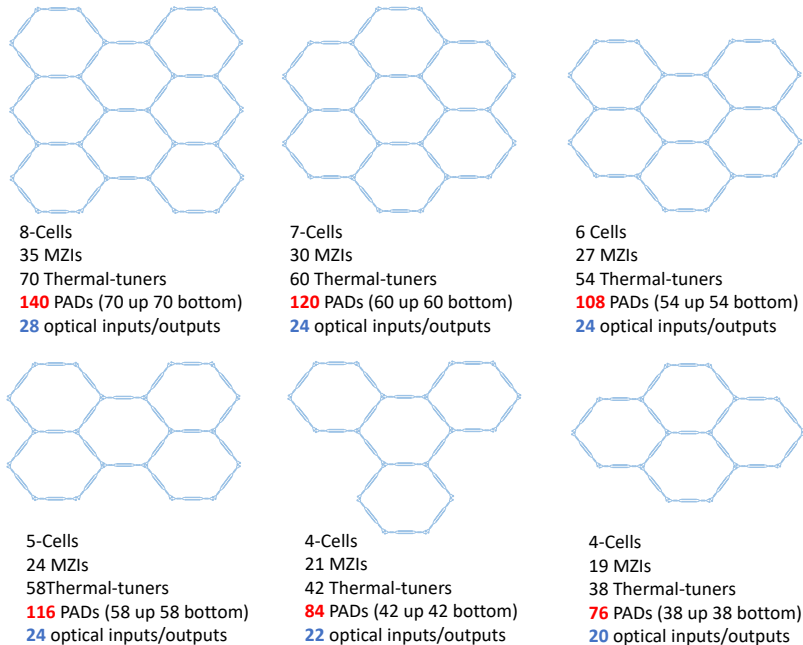


Figure 5.1 Different layout candidates for the hexagonal mesh-based optical reconfigurable core.

---

The circuit design is divided into three different layers: The photonic layer, the metal layer and the thermal-isolation layer.

### 5.2.1 Photonic layer

The designed photonic integrated circuit is a tunable coupler-based waveguide mesh, composed of 3-dB balanced Mach-Zehnder Interferometers, which are employed as TBUs. The basic operation principles have been described in Chapter 4. The present device includes the following elements:

- 7 hexagonal cells.
- 24 Optical inputs/outputs.
- 30 Tunable Basic Units.
- 60 Thermal tuners.
- 120 Pads (Electrical DC inputs).

Also, the PIC includes as separate test structures:

- 2 Independent Tunable Basic Units.
- 1 hexagonal cell.
- 8 Tunable Basic Units.
- 16 Thermal tuners.
- 32 Pads (Electrical DC inputs).
- Test bed of passive structures (propagation losses, MMIs losses, bend losses).

The cross-section of the SOI waveguides that we employed in the chip design is illustrated in Figure 5.2. The waveguide employs silicon for the core and silicon oxide for the cladding. The refractive index difference of these two materials confines the light that travels through the waveguide. Standard width of  $W = 500$  nm was considered for the optical waveguide core and  $W_h = 10$   $\mu$ m for the heater section.

Waveguide bending is fundamental for the integration of large optical circuits in a limited area. If the bend radius is too small, the guided signal is partially radiated, leading to bend-sensitive losses. Depending on the light confinement in the waveguide, every fabrication technology sets a minimum bend radius in order to neglect/reduce the losses produced by bending. Although for the employed silicon platform, the minimum bend radius is approximately 10-20  $\mu$ m, a conservative 30  $\mu$ m was employed in the design.

As mentioned in Chapter 4, for the TBU design we have considered a balanced Mach-Zehnder Interferometer loaded with one thermal tuner on each arm. This 3-dB balanced design offers full and independent splitting ratio setting and phase tunability. The whole TBU can be discretised in different sections accounting for the

MMIs, straight waveguide sections, and bend sections. The symmetry in both axes enables natural balanced losses necessary for the correct unit performance.

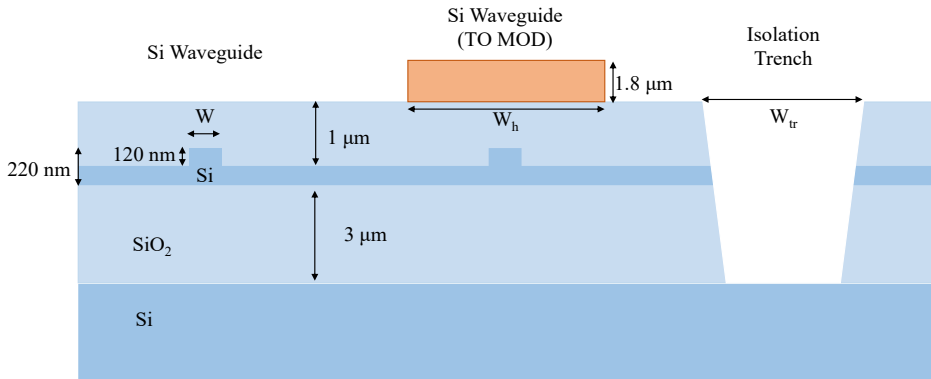


Figure 5.2 Silicon platform cross-section. Waveguide, thermal tuner, thermal isolation trench.

Figure 5.3 illustrates the position of two  $2 \times 2$  MMIs, at the input and output of the TBU. In principle, they are designed to provide reduced insertion losses ( $< 0.1$  dB) and 50:50 splitting ratio. Pursuing a conservative design, straight waveguide sections are also added at each MMI port and at each bend section port. The motivation behind this waveguide extension is to increase the distance between the upper and the lower arm and to increase the distance between TBUs in order to enable the signal DC routing at the metal layer.

The total Basic Unit Length is equal to  $975 \mu\text{m}$  and accounts for the length of the MMIs, the access waveguides, the MZI arms, and the extra-added straight waveguides. A reduction of the Basic Unit Length is possible and its impact is discussed at the end of this chapter. The overall access length, defined by the arc length of the access ports is  $31.416 \mu\text{m}$ . The MZI arms waveguide section was kept long enough to allocate a  $466\text{-}\mu\text{m}$  straight heater length.

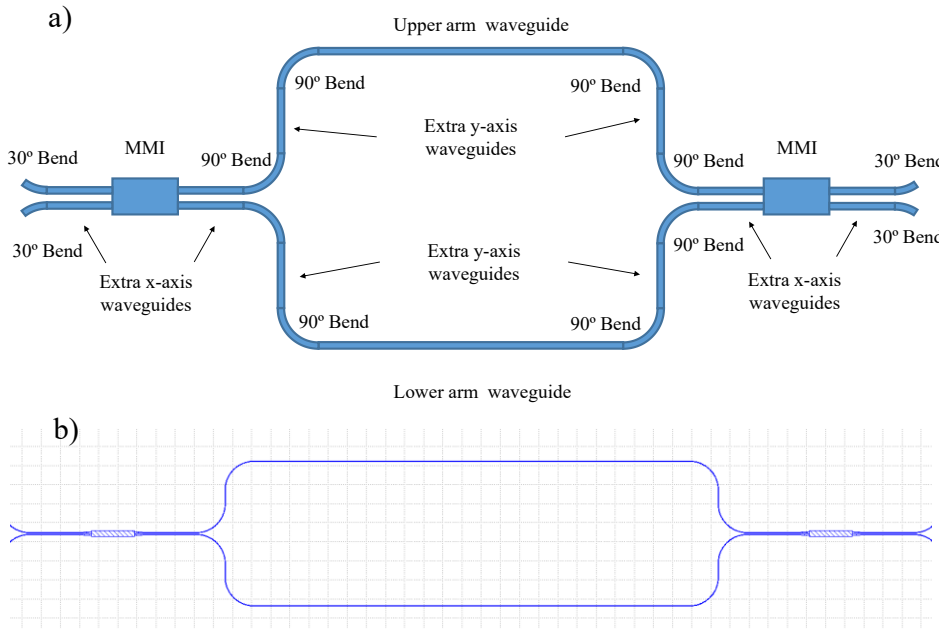


Figure 5.3 Photonic layer: (a) Tunable Basic Unit Design: Schematic and (b) GDS layout.

For the optical inputs/outputs, this PIC employs vertical coupling based on standard integrated gratings. The grating consists of 50 periods of deep-etched waveguides and a taper waveguide that accommodates the injected light to the employed waveguide width. The grating incorporates and extracts the optical signal from a fibre to the integrated waveguide and vice versa. We extended the initial 25 periods to 50 in order to avoid signal reflections. Since the propagation losses in silicon are mainly produced by the roughness of the lateral walls of the optical core, we worked with a waveguide width of  $2\ \mu\text{m}$  the longest possible for the straight access waveguides that connect the grating couplers to the mesh ports. Figure 5.4 (a,c) illustrates the concept and the layout of the on-chip gratings with a zoomed vision of a single grating coupler.

In order to increase the speed in the chip measurement, the use of a fibre array is advisable. This structure is a group of equispaced fibres. With the purpose of anticipating the array requirements, we initially designed the 16 left ports and the 16 right ports with a standard  $250\text{-}\mu\text{m}$  pitch. The outer ports have a feedback loop that is employed for the correct alignment of the fibre array by maximizing the measured optical gain in this loop as illustrated in Figure 5.4(b).

The technology-test structures included in the chip (propagation losses, MMI and bend insertion losses) do not have these array structures.

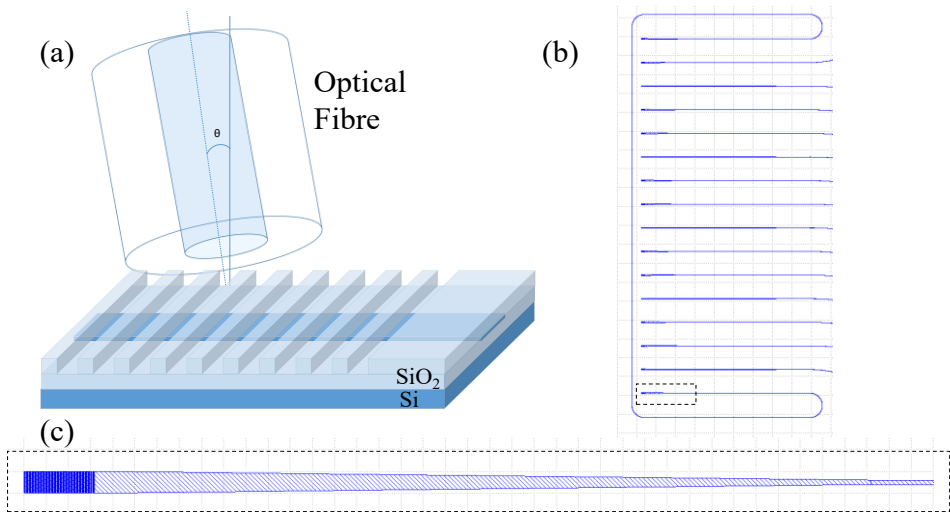


Figure 5.4 Photonic layer: Fibre-to-chip grating coupler (a) schematic and (b,c) GDS layout.

Note that these grating couplers are designed for an incoming angle of  $10^\circ$ . A non-ideal design or an angle error can produce a wavelength shift in the operational window of the vertical coupler.

To provide a measure of the passive optical performance parameters, such as the coupling losses, the propagation losses, the insertion losses (IL) of the bend sections for a radius  $R = 30 \mu\text{m}$  and the IL of the MMIs, we incorporated a testbed of passive structures in the same chip, which comprised the following elements:

A waveguide array with different lengths ( $\Delta L = 0, 4, 8, 12, 16, 20 \text{ mm}$ ) was designed to compute propagation losses, offering an estimation of grating coupler losses. Different numbers of cascaded whole bends: 90, 80, 60, 40 and 20 enable the linear fitting to compute the losses per bend. For the MMIs, there is not a perfect test structure to obtain their insertion losses and coupling factor. For this reason, we employed two different structures to estimate both figures. They consist of an array of cascaded MMIs (32, 24, 16, 8 and 4), and a distribution line of MMIs (up to 8). Some of these are schematised in Figure 5.5. The designed die footprint was  $15 \times 20 \text{ mm}^2$ . Figure 5.6 displays to the complete optical layout.

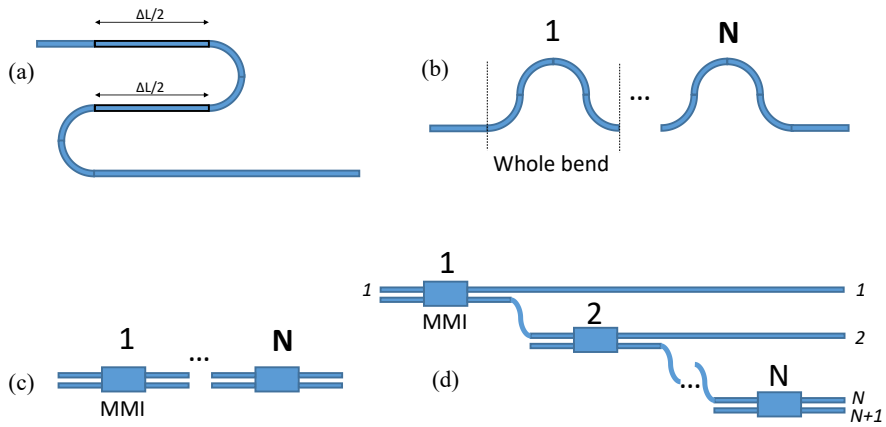


Figure 5.5 Photonic layer: Test structures schematic for optical properties characterisation. (a) Propagation losses, (b) bend losses, (c) MMI insertion losses, and (d) MMI coupling and insertion losses.

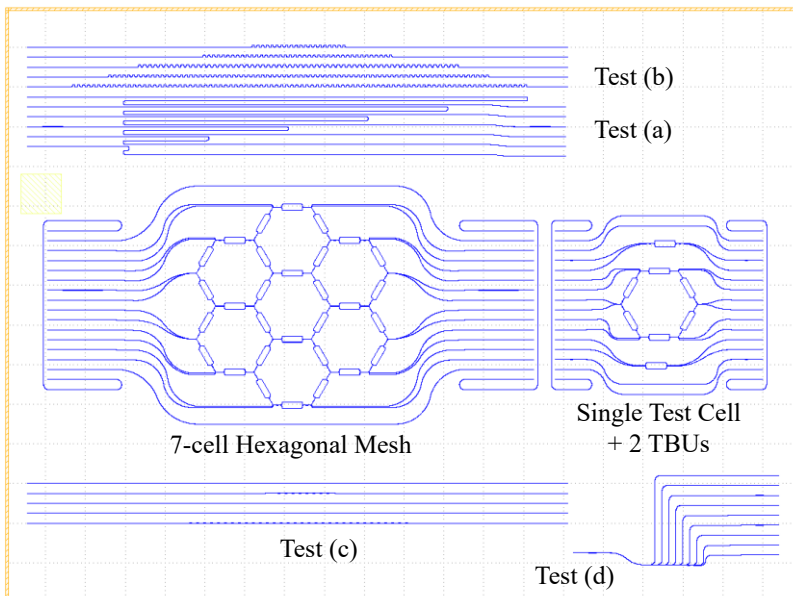


Figure 5.6 Reconfigurable optical core photonic layer: Complete optical layer labelled layout.

### 5.2.2 Electrical layer

The phase shifter operation is based on exploiting the thermo-optic effect. A temperature gradient ( $\Delta T$ ) produced by an electrical current going through a thin metal layer (*Joule effect*) will heat the optical waveguide producing a positive effective index variation  $\Delta n_{eff} = (dn_{eff}/dT) \Delta T$ , where  $dn_{eff}/dT$  is the thermo-optic coefficient of the technology platform. The phase shift ( $\Delta\phi$ ) is then computed as:

$$\Delta\phi = 2\pi \frac{\Delta n_{eff}}{\lambda}, \quad (5.1)$$

where  $\lambda$  is the optical wavelength. The dissipated electrical power in form of heat is directly proportional to the metal resistance ( $R_{metal}$ ). The resistance of a straight metal layer is:

$$R_{metal} = \rho \frac{L}{W \cdot t}, \quad (5.2)$$

where  $\rho$  is the metal resistivity ( $\Omega \text{ m}$ ) and,  $L$ ,  $W$  and  $t$  are the length, the width and thickness in metres of the metal layer, respectively.

The heaters have a length of 466  $\mu\text{m}$ , a width of 10  $\mu\text{m}$  and a thickness of 1.8  $\mu\text{m}$ . As illustrated in Figure 5.7 (a), the heater is connected to large trapezoidal pads by electrical access paths. These access tracks are implemented by means of a bend section with a linear-tapered width with the purpose of concentrating the dissipated power only at the heater section. The current design shares the metal layer that allocates both thermal tuners and DC tracks. Due to the full-layout complexity and the high density of components for only one metal layer, not all the TBUs could be connected by metallic tracks to the chip perimeter. For this reason, internal TBUs were wire-bonded from their PADs to an *internal DC pad circumference* that can be appreciated in Figure 5.7 (b, c), which finally connects them to the chip perimeter via metal tracks.

Another consequence of employing a unique metal layer is that the routing metal DC-tracks must be as wide as possible in order to reduce the undesired power dissipation in form of heat over the chip surface. For the TBU interconnections, the routing track widths are linear tapers from 160 to 100  $\mu\text{m}$  and from 100 to 40  $\mu\text{m}$  for the electrical paths that connect the outer *chip perimeter* to the *internal DC circumference* and for the *DC pad-circumference* to the *external TBUs* respectively.

The internal circumference contains 48 DC pads, which were wire-bonded, and 72 DC pads to be routed (for the TBUs placed at the external perimeter). The former are identified in Figure 5.7 (b) with a  $W$ . The *DC pad circumference* with a radius of



3.4 mm distributes the wire-bonding pads (as far as possible between them) to make easier the wire-bonding task and increase its probability of success.

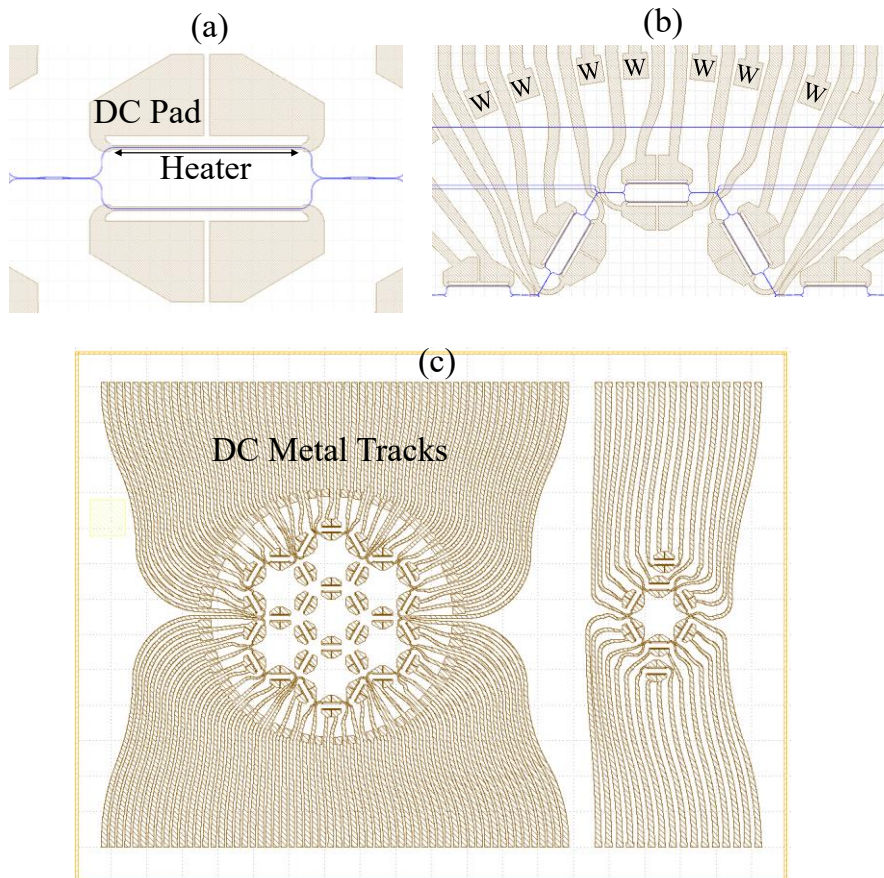


Figure 5.7 Reconfigurable optical core electrical layer layout: (a) Internal TBU, (b) external TBU and (c) complete electrical layout.

Although the DC routing tracks are made as wide as possible, only the 26-58% of the heating power remains in the heater area off each thermal tuner, resulting in a temperature gradient over almost all the circuit. We employ a simplified formula that assumes all-straight non-width tapered sections to estimate the thermal tuner efficiency as:

$$Eff = \frac{R_{heater}}{R_{total}} = \frac{\frac{L_h}{W_h}}{\frac{L_h}{W_h} + \frac{L_{DC-TRACK-EXT}}{W_{DC-TRACK-EXT}} + \frac{L_{DC-TRACK-INT}}{W_{DC-TRACK-INT}}} \approx 26 - 58\%, \quad (5.3)$$

where  $L_{DC-TRACK-EXT}$  is the external DC track with length between 3100-8000  $\mu\text{m}$  and a width of 100  $\mu\text{m}$  and  $L_{DC-TRACK-INT}$  is the internal DC track with length between 100-800  $\mu\text{m}$  and a width of 40  $\mu\text{m}$ . This problem could be overcome employing a different metal layer for the DC routing and the thermal tuners. A thicker metal for the DC routing increases the efficiency of the phase shifters and reduces the thermal crosstalk. In addition, reducing the heater width will drastically improve the thermal tuner efficiency. In contrast, a too narrow heater cross section may suffer from electro-migration and derive in a less robust design that might burn during operation.

### 5.2.3 Thermal isolation layer

When the heaters and DC tracks dissipate power in form of heat, they can produce undesired phase shifts in the adjoining TBUs through thermal crosstalk. The objective of this layer is to increase the thermal resistance in the core plane and force the heat to flow in the direction of the bottom of the PIC. Under the Printed Circuit Board that holds the PIC, we introduced a heat sink to control and keep a fixed temperature.

Figure 5.2 (right) illustrates the cross-section of a deep-etched isolation trench. As a conservative design rule, the security distance between all the elements and the trenches must be over 10  $\mu\text{m}$  to prevent from mask misalignment. Note that the deep etch includes the lower cladding of the waveguide cross-section.

Thermal simulations reveal a 3.16% of thermal crosstalk between the arms of a MZI placed at 150  $\mu\text{m}$  when an isolation trench is placed between them. This will influence the power consumption of each TBU and will produce an undesired common phase shift for both outputs ports.

We employed a multiphysics solver (COMSOL MP <sup>®</sup>) to estimate theoretically the thermal crosstalk between different TBUs to be less than a 1.68% when isolation trenches are employed. For these simulations, we did not take into account the effect of the PIC carrier, which deteriorates the previous performance since the distance to the heater sink and the thermal resistance increases. Moreover, the dissipation of the metal DC tracks was neither considered.

Figure 5.8 illustrates the zoomed vision of the thermal isolation layer layout. The metal layer is illustrated as well for reference.

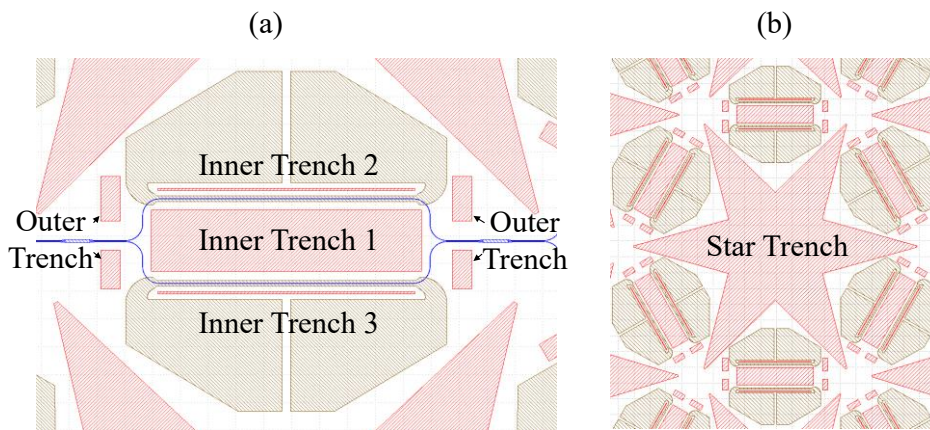


Figure 5.8 Reconfigurable optical core isolation trenches layout (red-coloured), and metal layer layout (gold-coloured). (Left) Inner TBU distribution, (right) Inner Cell distribution.

The objective of *Inner Trench 1* is to isolate thermally both heaters of the same TBU. *Inner Trenches 2* and *3* aim to focus the heat over the objective waveguide and prevent heat leaking into other structures. *Outer Trenches* and *Star Trench* increase the thermal isolation between adjacent TBUs.

### 5.3 Chip Fabrication

Chip fabrication was carried at the Optoelectronic Research Centre (ORC) of the University of Southampton. The processor core based on a hexagonal waveguide reconfigurable mesh was fabricated in SOI and wire-bonded to a chip carrier for experimental demonstration. In particular, SOI wafers with a 220-nm thick silicon overlayer and a 3- $\mu\text{m}$  thick buried oxide layer were used and e-beam lithography performed to define the grating couplers. Dry etching of 70 nm into the silicon overlayer to form the grating couplers was then carried out followed by resist stripping. Another e-beam lithography and 120-nm silicon dry etching step was performed to produce the optical waveguides. Following resist stripping, 1  $\mu\text{m}$  of plasma-enhanced chemical vapour deposition (PECVD) silicon dioxide was deposited to act as the upper cladding layer of the waveguides. Photolithography was then performed to define isolation trench openings, followed by a deep dry etching process to etch through the top cladding, silicon overlayer and buried oxide layer. These trenches provided thermal isolation to adjacent devices and improved the efficiency of the heaters. A 1.8- $\mu\text{m}$  thick metal layer was deposited after the resist had been stripped. A subsequent photolithography and dry etching step realised electrodes used to provide localised heating to tune the devices and the DC-metal tracks. The resist was then stripped and the wafers diced into individual dies. These

dies were then mounted onto 3 PCBs and a wire bonding process was used to provide electrical connections both within the die and between the die and the PCB, [112].

Figure 5.9 (a) shows the fabricated chip, which occupies a surface of  $15 \times 20 \text{ mm}^2$ . Figure 5.9 (b), (c) and (d) display zoomed views of the 7-hexagonal mesh, a single cell and an optical interconnection node respectively, where the MZI and the tuning electrodes are clearly distinguishable. Figure 5.9 (e) and (f) show the chip mounted on a printed circuit board (PCB), which occupies a surface of  $60 \times 120 \text{ mm}^2$ , where the internal and external wire bonding can be appreciated.

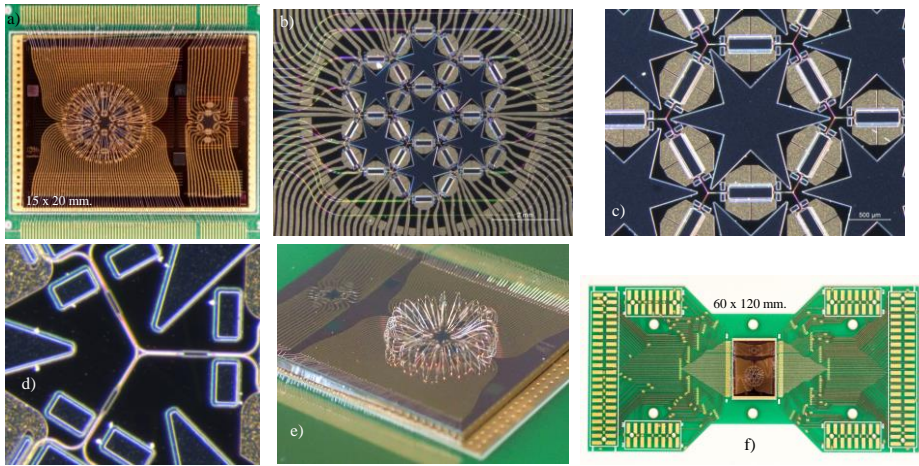


Figure 5.9 Fabricated hexagonal waveguide mesh chip. a, Fabricated SOI chip. b, zoomed vision of the 7-cell hexagonal waveguide mesh. c, zoomed image of a single hexagonal cell showing the MZI, tuning heaters and star-type thermal isolation trenches. d, zoomed image of an optical interconnection node of 3 TBUs. e, wire bonded PIC. e, f, Printed circuit board with the waveguide mesh chip mounted and wired bonded.

## 5.4 Chip experimental characterization

We started the characterisation of the static optical properties of the integrated waveguides by measuring the integrated test-bed structure in four different dies. As illustrated in Figure 5.10, a tunable laser (ANDO AQ4321D) featuring a 1 pm wavelength resolution was connected to the input grating coupler of the test die and scanned to provide a wavelength range characterization. The test die output grating coupler was connected to an optical spectrum analyser (ANDO AQ6217C). As pointed above, measurements included: differential path length to characterize propagation losses, cascaded bends structures to characterize bend losses and 2 different cascaded and coupled MMI structures to characterize MMI insertion losses and bandwidth.

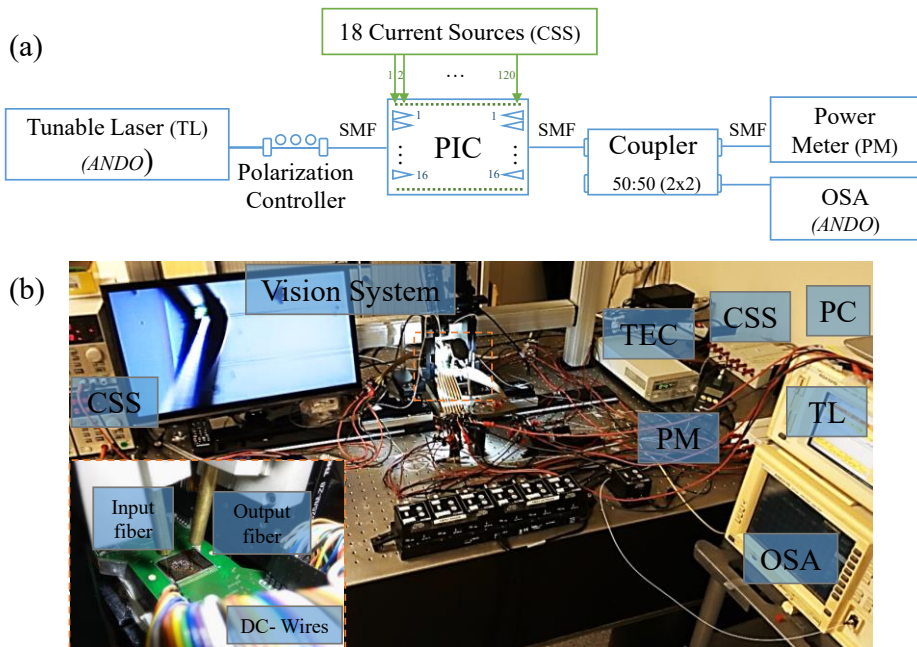


Figure 5.10 Characterization and measurement setup: (a) Scheme and (b) Lab picture.

To illustrate the measurements, we have selected one representative result from each of the 4 measured test dies. As we can see in the left column of Figure 5.11, each die has a different wavelength operational window. Notice that the resulting window is the overlapping function of the input and the output grating coupler responses. This undesired effect can be overcome by designing the waveguide gratings more efficiently, by choosing butt coupling or by offering a more packaged solution via optimised chip encapsulation.

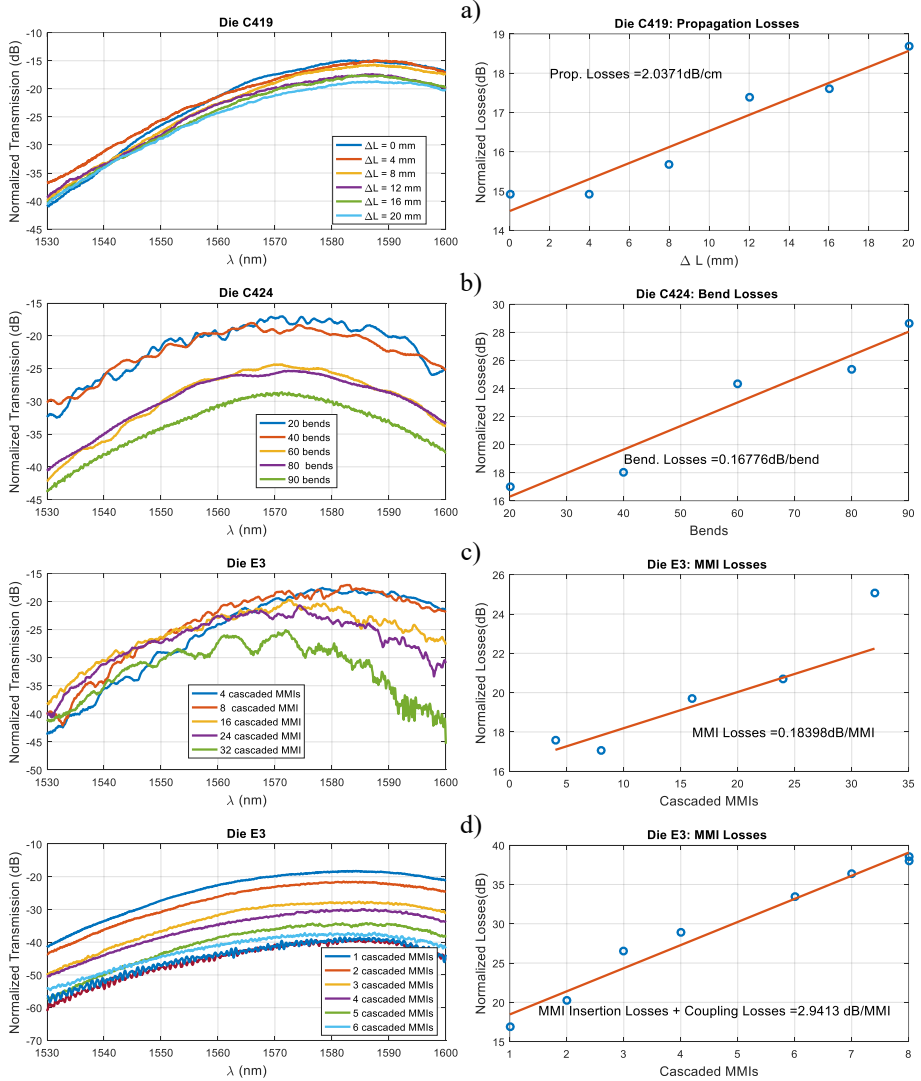


Figure 5.11 (Left) Operational window for each test structure and (right) Linear fitting for the passive properties characterisation of specific dies (a) Measured propagation losses, (b) Measured bend losses, (c) Measured cascaded MMIs, (d) Measured distributed MMIs.

The examples of measured propagation, bend and MMI losses are illustrated in the right-hand column of Figure 5.11. Note, for example that the bend relative losses account for a whole bend that contains four-cascaded 90° bends. Referring to the MMIs, there is not a perfect test structure to characterise them. In Figure 5.11

(right/c), we see that the cascaded configuration suffering from phase errors during fabrication leads to the formation of an interferometric structure that increases the insertion losses of the MMI. In Figure 5.11 (right/d), the two points at the last MMI outputs refer to each final MMI output confirming that the 50:50 splitting ratio is nearly satisfied. All the previous measurements contain a deviation produced by the coupling efficiency variability due to the error relative to the fibre and grating position. Nevertheless, it results in a good estimation of around 2.5 dB/cm for the waveguide propagation losses, negligible bend relative losses and low-loss MMIs. The summarised results are provided in Table 5.1.

Table 5.1. Main characterization figures.

Figures	Measured
Synthesized Waveguide Losses	$2.38 \pm 0.30$ dB/cm
MMI Losses	$0.15 \pm 0.10$ dB
Whole Bend Losses	$0.10 \pm 0.02$ dB
Grating Coupler Losses	$6.50 \pm 0.50$ dB
Grating Coupler Central Window Deviation	$1580 \pm 15$ nm
Grating Coupler 3-dB bandwidth	$35 \pm 2$ nm
Thermo-optic efficiency ( $P_\pi$ )	$110 \pm 15$ mW
TBU Optical Crosstalk	$40 \pm 5$ dB
TBU Insertion Losses	$0.60 \pm 0.10$ dB

Prior to the synthesis of any photonic integrated circuit, we need to characterise each TBU. For each one, we performed a full process that consisted in injecting optical power into one of the optical ports of the TBU while sweeping the electrical current applied to one of the two TBU heaters. For this electro-optical characterization, we employed current sources of different resolution and quality: 3 Keithley2401, 13 Thorlabs LDC8010 and 2 TECMA 72-2535. This process was carried out for the 76 thermal tuners present on each of the 3 characterized PCBs. Together with resistance and output optical power, we obtained as a result the normalized coupling constant calibration curves as a function of the injected current of each TBU. A characterisation example is shown in Figure 5.12. Through this method, we also extracted the phase shift calibration curves as a function of the injected current to each thermal tuner. For characterisation of the inner TBUs, we had to bias outer TBUs properly so access could be granted to the internal units.

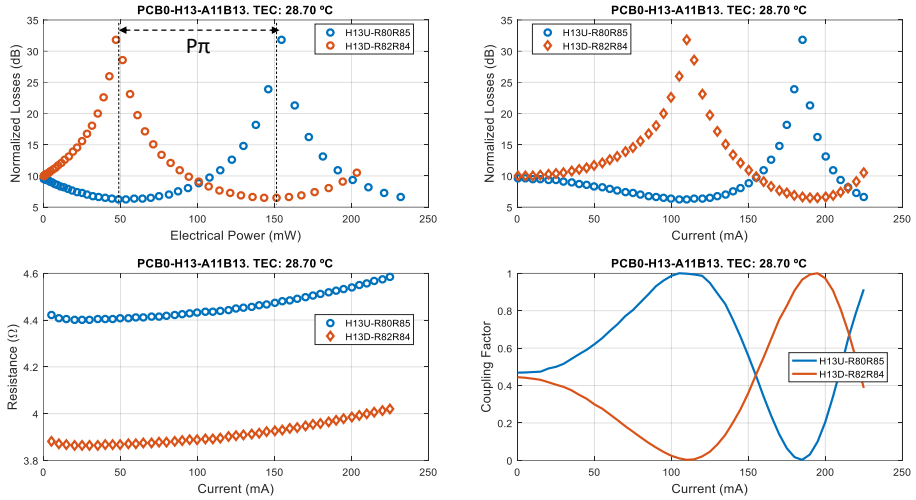


Figure 5.12 Characterisation output of a tunable basic unit. Up/Left, Normalised losses versus electrical power applied for each heater. Up/Right, Normalised losses vs electrical current. Bottom/Left, Resistance vs electrical current. Bottom/Right, Coupling Factor vs electrical current.

The TBU Insertion Losses ( $0.60 \pm 0.10$  dB) include the propagation losses across the Mach Zehnder interferometer and the bend relative losses. They were computed by fitting the losses of paths relative to different TBUs numbers. As a result, we extrapolated this measurement to an average *synthesized waveguide* loss value of  $6.1 \pm 0.3$  dB/cm. The main contributions for this figure are the insertion losses of the 20 MMIs present inside the 10 TBUs required for 1 cm of synthesized waveguide. The longterm robustness of the heaters was tested applying an electrical power sweep up to  $2P_{\pi}$  (over more than 2000 steps) and obtaining no-resistance variation.

## 5.5 Measurement results
















Once we have characterized each TBU, we could use their respective calibration curves to program each TBU for synthesising different photonic integrated circuits. In this section, we show the measured results corresponding to several functionalities that we could demonstrate with the fabricated processor core. Different photonic integrated circuits like 1 and 2 input/output filters, dispersion compensator delay lines and universal interferometers can be implemented. The software-definition is low-level (machine-code or assembly language). This means that commands or functions in the language map closely to processor instructions. First, the coupling and phase shifters values are obtained by programming the well-known equations or adapted algorithms of the synthesized structures in *MATLAB*®. Next, by employing the



database containing the TBU calibration curves (coupling constant and phase vs injected current), we set the TBUs bias by a *Python* programme that controls the external current sources, the laser and capture and read the data from the optical spectrum analyser.

In case of optical filters, we can set the FSR by changing the interferometric lengths. In this case, the range of available FSRs are provided in Table 5.2.

Table 5.2. Frequency grid associated to the fabricated BULs. The interferometric structure available for the hexagonal core is also indicated.

Interferometric length (BULs)	BUL = 975 $\mu\text{m}$ FSR(GHz)	BUL = 975 $\mu\text{m}$ FSR(pm)
 2	<b>36.78</b>	294.75
 4	18.39	147.37
 6	12.26	98.25
 8	9.19	73.69
 10	7.36	58.95
 12	6.13	49.12
 14	5.25	42.11
 16	4.60	36.84
 18	<b>4.09</b>	32.75
 20	3.68	29.47
 22	3.34	26.79
 24	3.06	24.56
 26	2.83	22.67
 28	2.63	21.05
 30	2.45	19.65

Unless otherwise specified, all the measured spectral responses in the following sections are normalised to the measured insertion losses corresponding to an integrated waveguide that connects the grating couplers to the input and output ports of one TBU in *all-pass* state. These losses include the input and output grating coupler losses, the propagation losses of the mesh access paths and the loss corresponding to one TBU, resulting in a figure of 17.5 dB.

### 5.5.1 Finite Impulse Response (FIR) filters

By suitably tuning the TBUs in the 7-cell waveguide mesh, we have been able to implement UMZI devices with path unbalances given by 0, 2, 4, 6 and 8 BULs, limited by the number of current sources available at the moment of measurement. Figures 5.13 to 5.15 show, as an example, the results for the 2-, 4- and 8-BUL UMZI cases. For each case, (a) shows the 7-cell hexagonal waveguide mesh configuration, where each TBU is represented by a given colour depending on whether it is activated as a cross (black) or bar (orange) switch, a tunable coupler (green) or if it is not used and is therefore available for another potential circuit implementation (blue). In (b) we show the circuit layout of the implemented structure. These figures also include the measured modulus and corresponding phase (calibrated by the shortest path), where the input is in the IN port and the output is in the OUT1 port for different coupling and phase shifter values.

Measured curves are displayed for different values of the coupling constant  $K_1$  and a fixed value of  $K_2$  equal to 0.5, which are tuned by changing the injection currents to the heater elements of the input and output TBU devices of the UMZI. Changing these values alters the absolute value of the zero in the UMZI transfer function bringing it closer or farther to the unit circle. The closer the zero is to the unit circle, the deeper are the notches in the transfer function are (up to 35 dB of extinction ratio) and the higher the phase shift step in the transfer function is. Note that the periodicity in the transfer function changes according to the path unbalance (36.8 GHz for the 2-BUL UMZI in Figure 5.13, 18.4 GHz for the 4-BUL UMZI in Figure 5.14 and 9.2 GHz for the 8-BUL UMZI in Figure 5.15). As illustrated in Appendix B.4, in each case, we compared the experimental results with those provided by the theoretical expressions of the transfer functions [32] obtaining an excellent agreement. We also checked the tuning of the notch position over a complete spectral period without changing its absolute value, by proper phase shift addition to one of the UMZI arms as illustrated in Figure 5.13(d) and Figure 5.14(d).

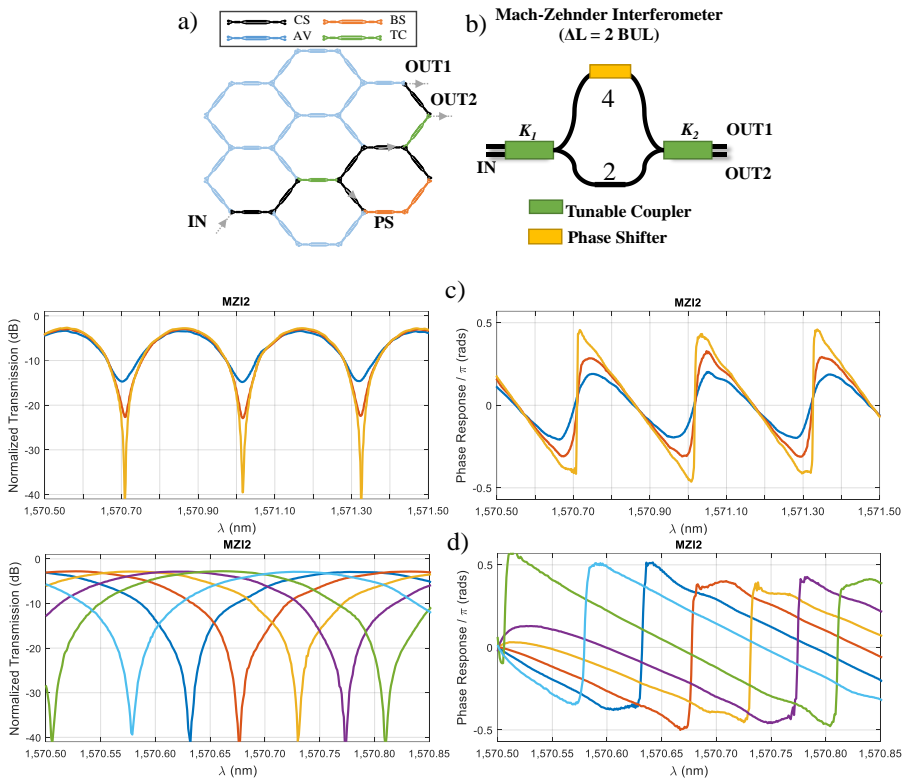


Figure 5.13 Experimental results for tunable UMZIs of  $\Delta L = 2$  BULs. (a) Waveguide mesh connection diagram, (b) circuit layout indicating the normalized waveguide length in BULs and measured modulus and phase transfer function for (c) different values of the coupling constants  $K_1$  and  $K_2$ , and (d) for fixed coupling factors and active phase shifter tuning.

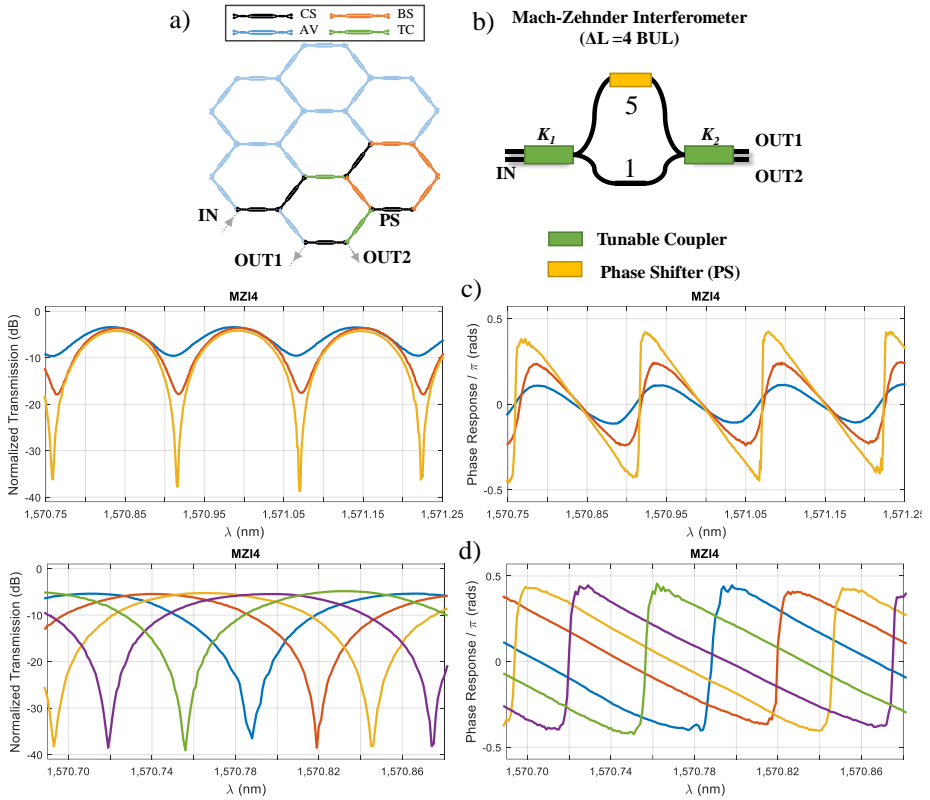


Figure 5.14 Experimental results for tunable UMZIs of  $\Delta L = 4$  BULs. (a) Waveguide mesh connection diagram, (b) circuit layout indicating the normalized waveguide length in BUL units and measured modulus and phase transfer function for (c) different values of the coupling constants  $K_1$  and  $K_2$ , and (d) for fixed coupling factors and active phase shifter tuning.

Although the waveguide mesh has a limited number of cells, we were also able to implement a lattice filter by serially cascading UMZI units and a 3-tap transversal filter by the parallel cascade of UMZI units. Figure 5.16 shows these results: In the first one, corresponding to a FSR of 36.8 GHz, by changing the values of  $K_1$  to  $K_3$ , we tuned the positions of the two zeros provided by the cascaded structure and, therefore, reconfigured its transfer function. For the last one, characterised by a FSR of 18.4 GHz we also changed the values of  $K_1$  to  $K_4$  to tune the positions of the two zeros provided by the structure reconfiguring again its transfer function. Note that in this case, we have directly represented the relative (to the optical carrier) frequency assuming a self-beating modulation/detection scheme as the ones proposed in Chapter 3.

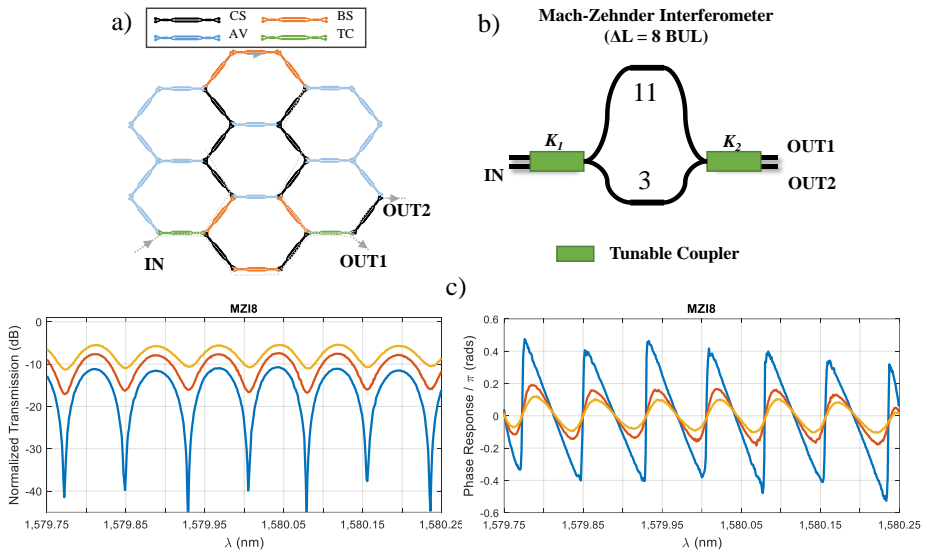


Figure 5.15 Experimental results for tunable UMZIs of  $\Delta L = 8$  BULs. (a) Waveguide mesh connection diagram, (b) circuit layout indicating the normalized waveguide length in BUL units, and measured modulus and phase transfer function for (c) different values of the coupling constants  $K_1$  and  $K_2$ .

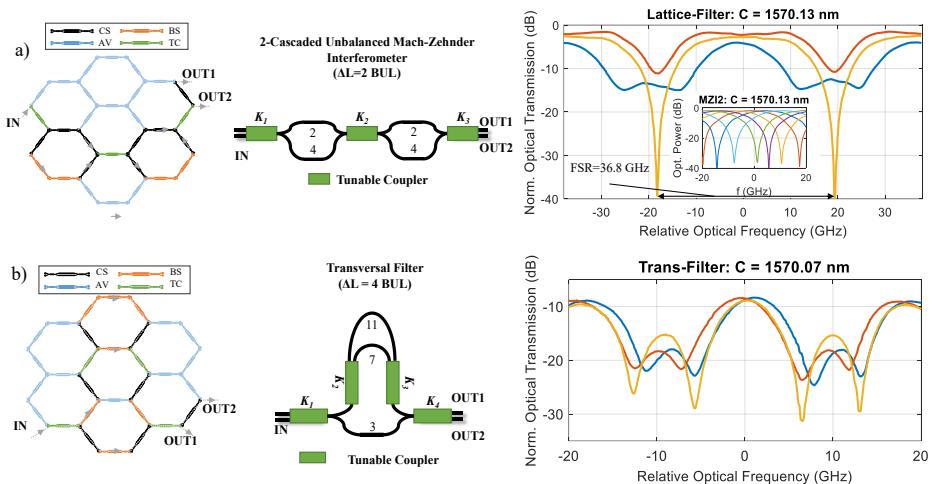


Figure 5.16 Experimental results for cascaded tunable UMZIs and FIR Filters. Waveguide mesh connection diagram, circuit layout and measured modulus for different values of the coupling constants  $K_1$  and  $K_2$ ,  $K_3$  (and  $K_4$ ) in the case of **a**, two cascaded 2-BUL lattice UMZI filters, including full-FSR tunability (inset); **b**, a 4-BUL UMZI transversal filter. C: Optical Carrier wavelength.

### 5.5.2 Infinite Impulse Response (IIR) filters

By suitably tuning the TBUs in the 7-cell waveguide mesh, we have been able to programme single cavity optical ring resonators with cavity lengths given by 6, 10, 12, 14, 16 and 18 BULs. Figures 5.17 to 5.19 show some of the relevant measured results for the 6-, 12- and 18-BUL cavity length cases. The figures show in (a) the waveguide mesh configurations (with the TBU device status according to the color code previously described), (b) the circuit layouts and (c) the modulus as well as phase shift responses for the OUT1 port. The measured results correspond to different values of  $K_1$  and  $K_2$ , which settle the positions of the zero and the pole. The OUT2 response is depicted in Figure 5.17 (d) (FIR+IIR filter). The IIR filter tunability, which is shown in Figure 5.17 (e), is achieved by exploiting the fact that the coupling constant and the phase shift in any TBU of the mesh can be adjusted independently. Hence, any TBU inside the cavity can be operated as a constant-amplitude phase shifter. Figure 5.18 and Figure 5.19 correspond to the 12- and 18-BUL ORR length case, respectively.

Appendix B4 includes the comparison between our experimental results with those predicted by the theory employing the well-known transfer function of ORRs [32], showing an excellent agreement

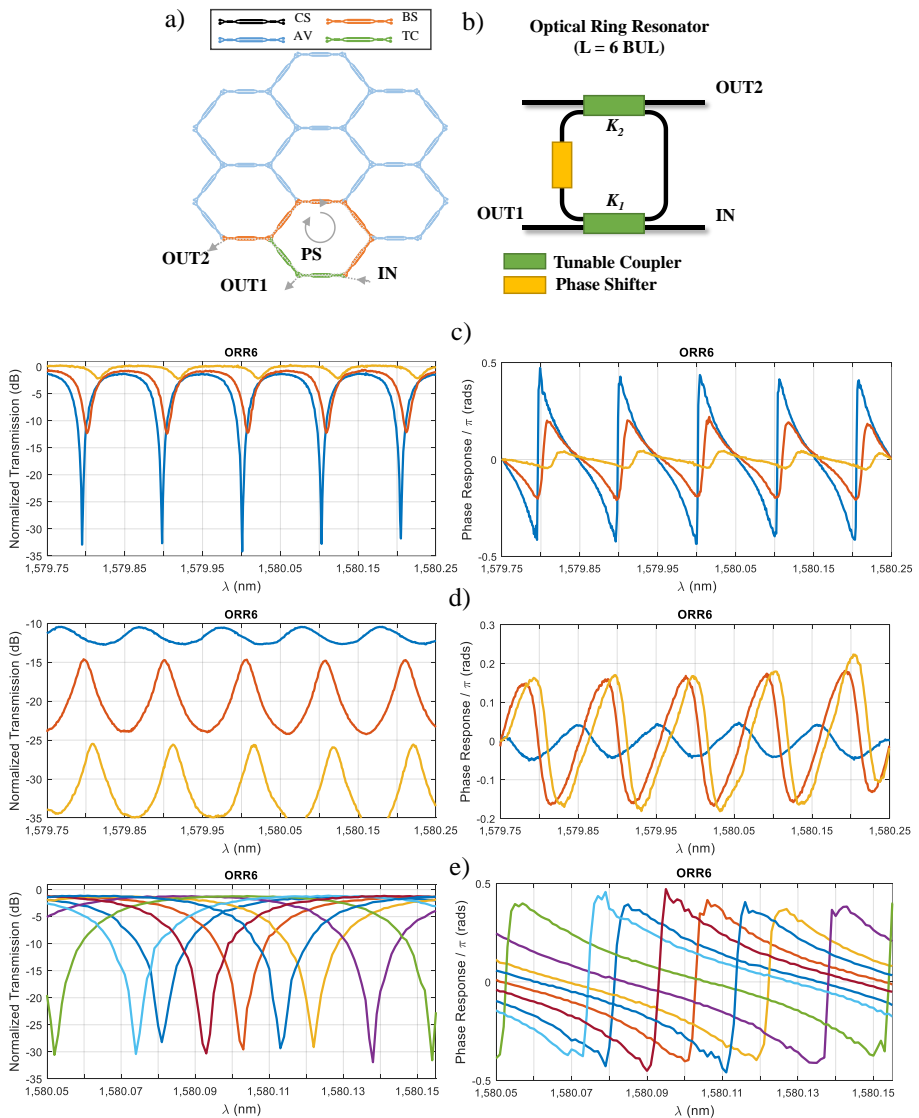


Figure 5.17 Experimental results for 6 BUL ring resonator IIR and FIR+IIR filters. (a) Waveguide mesh connection diagram, (b) circuit layout and measured modulus and phase transfer function for a, (c) IIR filter for different values of the coupling constants  $K_1$  and  $K_2$ , (d), FIR+IIR filter for different values of the coupling constants  $K_1$  and  $K_2$ , (e) IIR filter along a full spectral period for different values of the optical ring resonator round-trip phase shift.

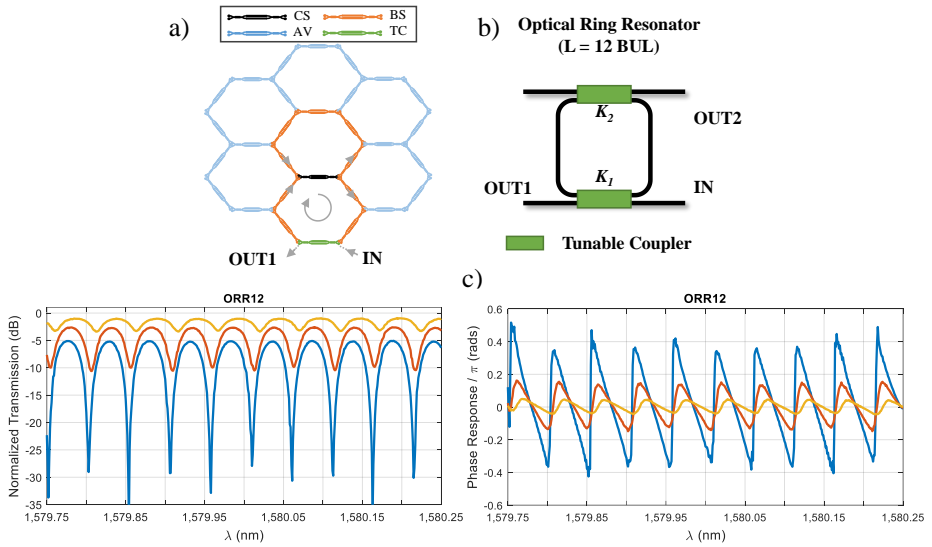


Figure 5.18 Experimental results for 12 BUL ring resonator IIR filters. (a) Waveguide mesh connection diagram, (b) circuit layout and (c) measured modulus and phase transfer function for different values of the coupling constants  $K_1$  and  $K_2$ .

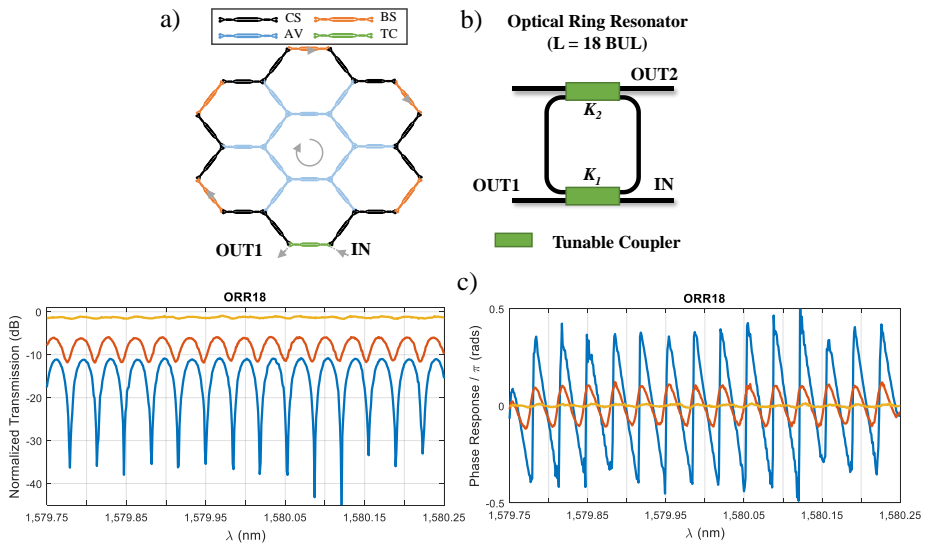


Figure 5.19 Experimental results for 18 BUL ring resonator IIR filters. (a) Waveguide mesh connection diagram, (b) circuit layout and (c) measured modulus and phase transfer function for different values of the coupling constants  $K_1$  and  $K_2$ .



### 5.5.3 Complex tunable and reconfigurable filters

We can build more complex (multicavity) signal processing structures as, for instance, CROWs, SCISSORS and ring-loaded MZIs using the former basic building blocks in the 7-cell waveguide mesh and activating more TBU devices to provide additional propagation paths. The number of current sources allowed us to programme 2- and 3-ORR CROWs (6-BUL ORR length), 2-ORR SCISSORS (6-BUL cavity length) and a double ring-loaded MZI with reconfigurable coupling factors and phases. Figure 5.20 shows three examples of complex filters that employ two 6 BUL ring cavities.

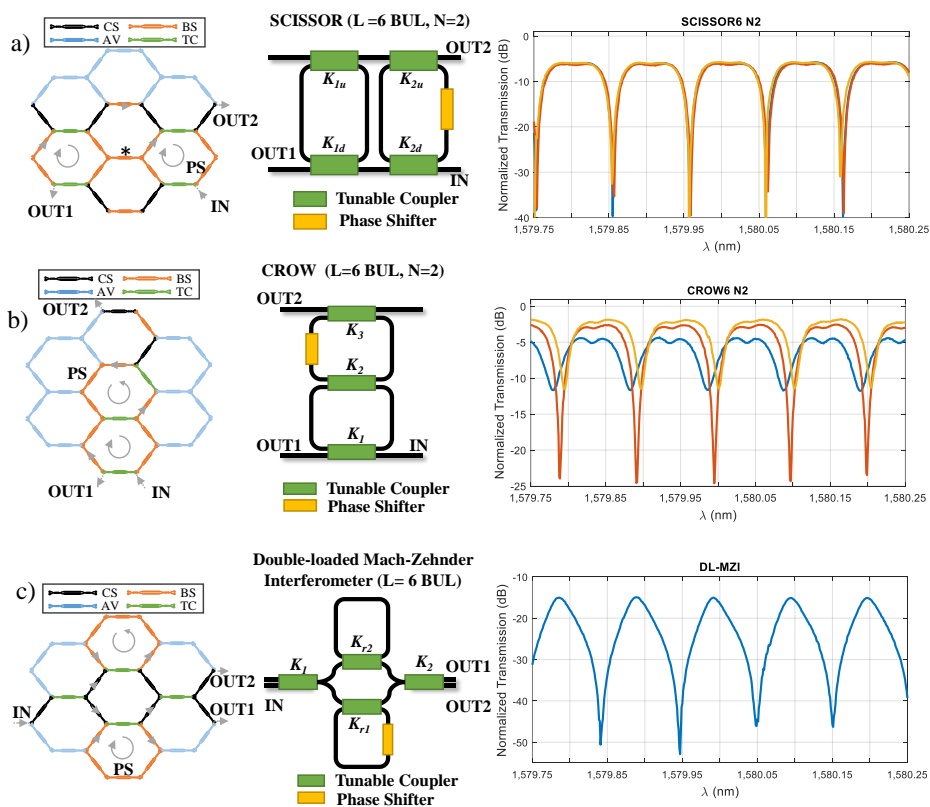


Figure 5.20 Experimental results for complex double ring-loaded 6-BUL optical ring resonator filters. Waveguide mesh connection diagram, circuit layout and measured modulus and phase transfer function for a, a 6-BUL double ORR SCISSOR filter and different values of the coupling constants  $k_1$  and  $k_2$ ; b, a 6-BUL double ORR CROW filter and different values of the coupling constants  $k_1$  and  $k_2$ ; c, a 6-BUL double ORR ring-loaded MZI.

Figure 5.20 (a) corresponds to a notch SCISSOR filter, Figure 5.20 (b) to a bandpass CROW structure and Figure 5.20 (c) to a double ring-loaded MZI. As in

the previous cases, the first column shows the 7-cell hexagonal waveguide mesh configuration where each TBU is represented by a given color depending on its activation state, the second column shows the layout of the implemented structure and the third column shows the measured modulus. In the measured results shown in Figure 5.20. Label (a), correspond to a SCISSOR structure (input: IN, output: OUT 1), the phase shifter flattens the spectral region in between two consecutive notches and provides two slightly parabolic phase shifts of opposed concavity in that region, which correspond to two linear group delay regions of opposed slopes. Within this region, the structure can be employed as a tunable dispersion compensator or as a true time delay line. The TBU marked with an asterisk is an example of how TBUs can be configured to extract non-ideal leaking due to optical crosstalk from the circuit. Anyway, no deteriorated performance was observed in form of internal reflections. A similar concept is employed in the Figure 5.20 (b) that corresponds to a CROW structure (input: IN, output: OUT 2). Here, the different traces correspond to different values of the phase shifter, which move one ORR resonance with respect to the other. When the phase shift is 0, then the resonances of the two cavities are located in the same frequency and the narrowest bandpass is achieved (red trace). As a small phase shift is added to one of the cavities, one of the resonances is slightly displaced but there is still a considerable overlapping. This technique is employed to broaden the response of bandpass filters providing a controlled ripple value, [32]. Figure 5.20 (c) shows the measured results for a double ring-loaded MZI. This structure is employed as a building block for the implementation of special configurations such as maximally flat high-order Butterworth and Chebyshev filters, [32, 31, 20, 39].

Figure 5.21 shows the particular application of three multicavity filters to coherent self-beating MWP bandpass filtering. We express the transfer function results in terms of the relative (to the optical carrier) RF frequency. Each figure contains the measured bandwidths and the resulting Side Lobe Level (SLL). Bandwidth reconfiguration from 4.40 to 6.05 GHz is demonstrated for a fixed FSR of 12.26 GHz. As mentioned, the SCCISOR architecture corresponding to Figure 5.20 (a) can be programmed to operate as a parabolic dispersion compensator. Figure 5.22 shows the theoretical and measured normalized transmission and relative group delays for this case.

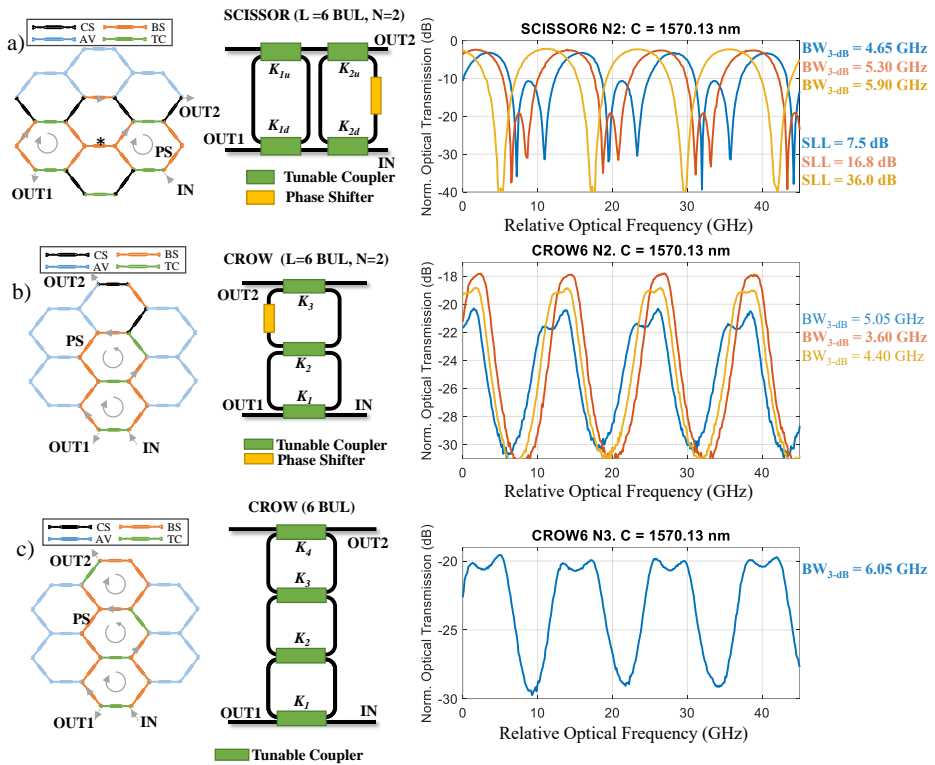


Figure 5.21 Layout of fabricated 7-cell hexagonal mesh and TBU settings (left) for the implementation of 2 cascaded 6 ORRs (up), for the implementation of 2 coupled 6 ORRs (middle) and 3 coupled 6 ORRs (bottom) and its respective Normalized Optical Response (right). The 3-dB bandwidth is indicated for each example. All FSR corresponds to 12.26 GHz. Note that a direct optical-to-radiofrequency conversion has been applied to the frequency axis. SLL: Side Lobe Level. C: Optical Carrier

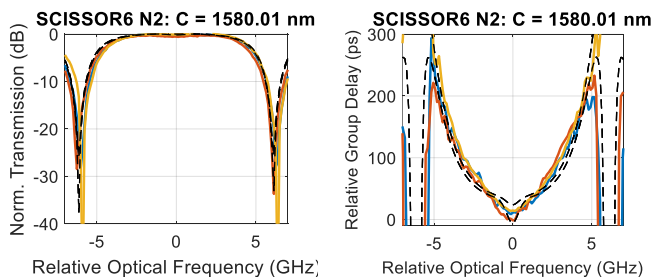


Figure 5.22 Experimental (solid-line) and theoretical (dashed-line) results for 6-BUL ring resonator IIR filter. 2 cascaded 6 ORRs transmission response and associated group delay.

### 5.5.4 Multiple input multiple output linear optic transformation devices:

A wide variety of signal processing operations involve mode transformations, which can be described in terms of multiple input/multiple output linear optics operations given by an  $N \times N$  unitary matrix, [26, 88, 33, 113]. We programmed the 7-cell waveguide mesh to demonstrate several  $3 \times 3$  and  $4 \times 4$  linear unitary transformations. These are relevant examples of signal processing tasks that are needed in different applications and the results are shown in Figures 5.23 to 5.30. Figure 5.23 shows an example of a  $3 \times 3$  column swapper between inputs 1 and 3 leaving column 2 invariant. Any phase relationship between the three output modes can be selected by proper biasing the TBUs M21 and M31. Figure 5.24 shows another  $3 \times 3$  transformation example. In this case, a backward input swapper where input 1 is routed to output 2, input 2 to output 3 and input 3 to output 1. The former examples are particular cases that illustrate the application of the waveguide mesh as a programmable signal router. In both cases, the measured results show an excellent agreement with the targeted matrices for the operation wavelength of  $\lambda = 1571$  nm with an extinction ratio  $> 25$  dB between the 1 and 0 coefficients. The required values for the coupling constants and phases of the TBUs used in the former implementations were obtained by the synthesis algorithm adaptation presented in Chapter 4 and developed in the Appendix B.1. We have incorporated the resulting coupling and phase coefficients as an example in the corresponding appendix section. These coefficients are translated into the required injected currents to the phase shifters according to the calibration curves obtained for each TBU during the chip characterization.

Incidentally, the degree of freedom in the phase can be employed to implement linear transformations involving complex coefficients as required by Z, X or Y Pauli or Hadamard gates [114] as illustrated in Figure 5.25 to Figure 5.27, normalised to a 5-BUL waveguide loss. Phase shifts are implemented by one or two TBUs marked as PS and shown in the figure. Again, we have added a table containing the corresponding coefficients and phases for each TBU in Appendix B.1.

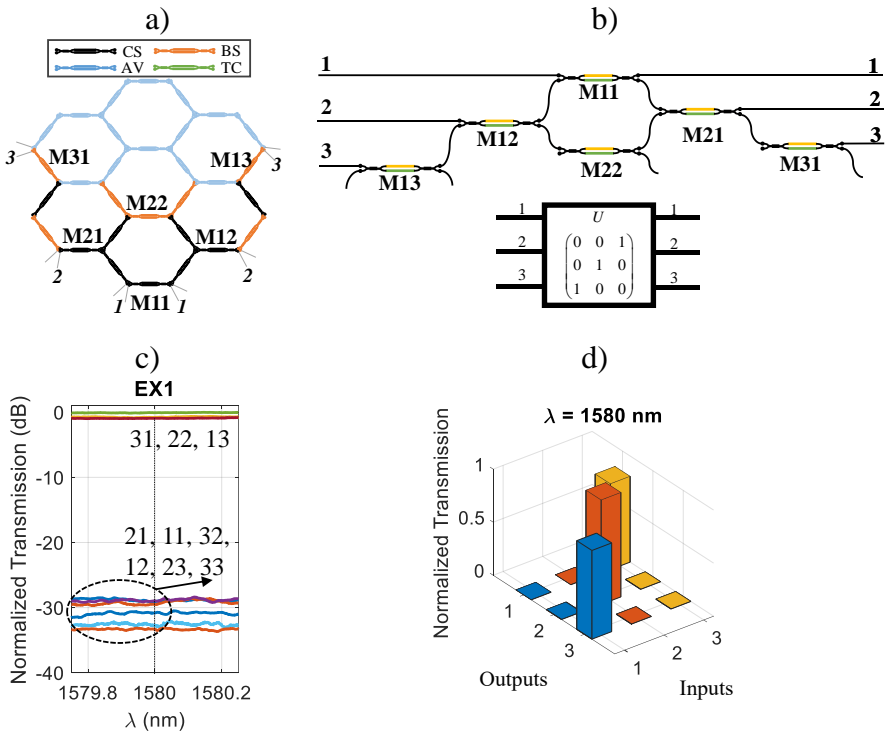


Figure 5.23 Experimental results for the hexagonal waveguide mesh configuration of a  $3 \times 3$  interferometer based on a triangular arrangement. (a) Hexagonal core settings for 1-3 input mode swapping unitary transformation (CS = TBU in cross state, BS = TBU in bar state, TC = TBU in tunable coupler state, AV = TBU not employed), (b): circuit layout of the implemented interferometer, (c) spectral measurement of all input/output port connections, (d) normalized bar diagram of the resulting measured unitary matrix for  $\lambda = 1571 \text{ nm}$ .

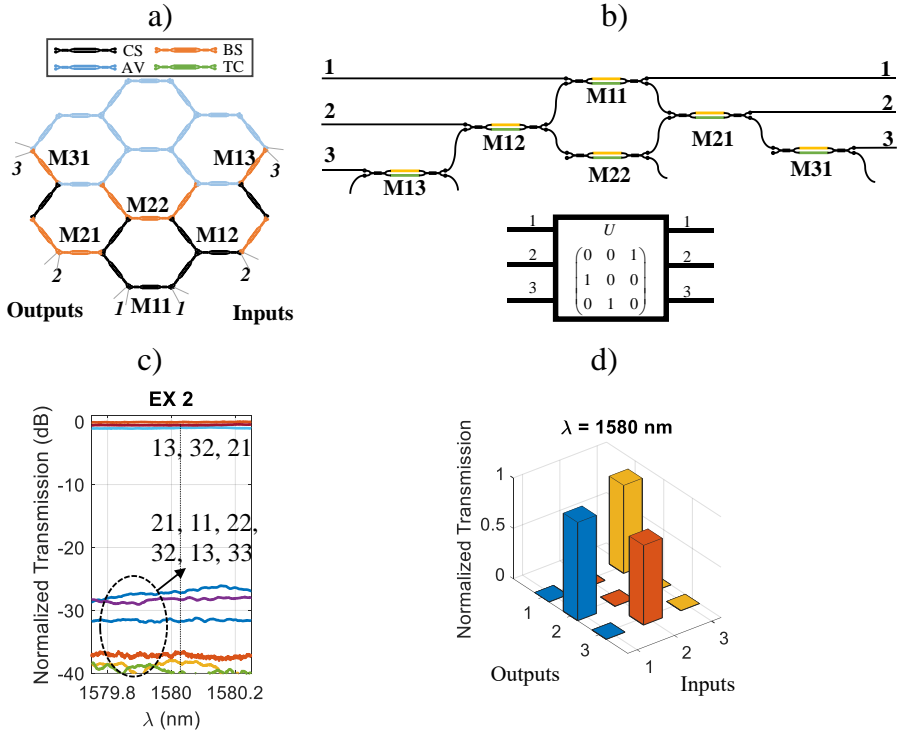


Figure 5.24 Experimental results for the hexagonal waveguide mesh configuration of a  $3 \times 3$  interferometer based on a triangular arrangement. (a) Hexagonal core settings for 1-2, 2-3 and 3-1 input mode swapping unitary transformation. (CS = TBU in cross state, BS = TBU in bar state, TC = MZI in tunable coupler state, AV = TBU not employed), (b): circuit layout of the implemented interferometer, (c): Spectral measurement of all input/output port connections. (d) Normalized Bar diagram of the resulting measured unitary matrix for  $\lambda = 1571$  nm.

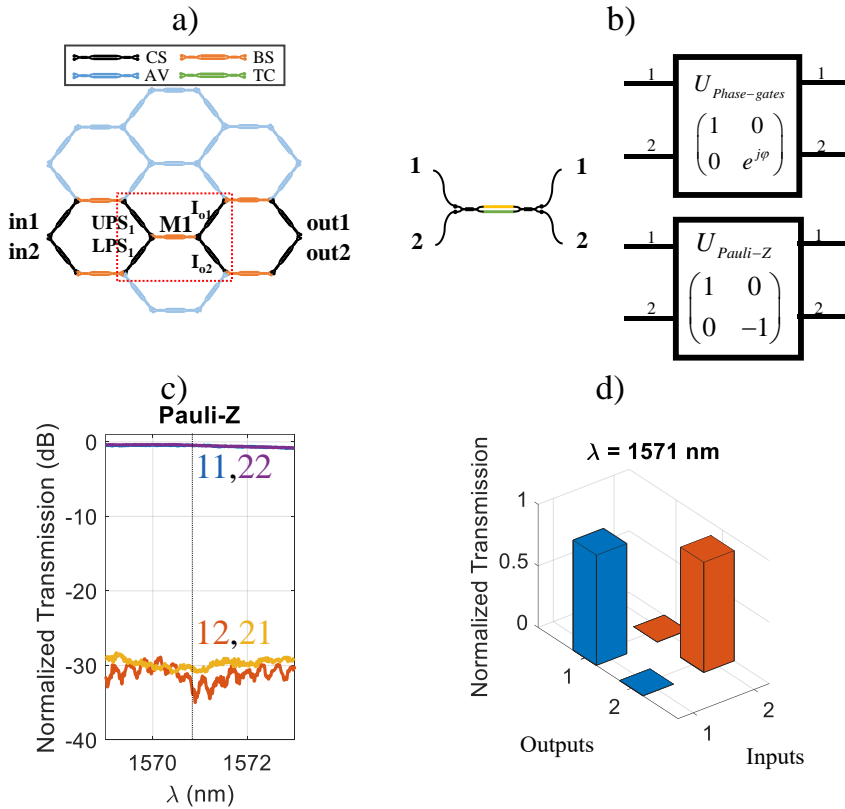


Figure 5.25 Pauli-Z  $2 \times 2$  transformation experimental results involving complex-valued matrix coefficients using the hexagonal waveguide mesh, (a): 7-cell configuration (CS = MZI in cross state, BS = MZI in bar state, TC = MZI in tunable coupler state, AV = MZI not employed, PS = Phase shifter), (b) circuit layout of the implemented interferometer, (c) spectral measurement of all input/output port connections, (d) normalized bar diagram of the resulting measured unitary matrix for  $\lambda = 1571$  nm.

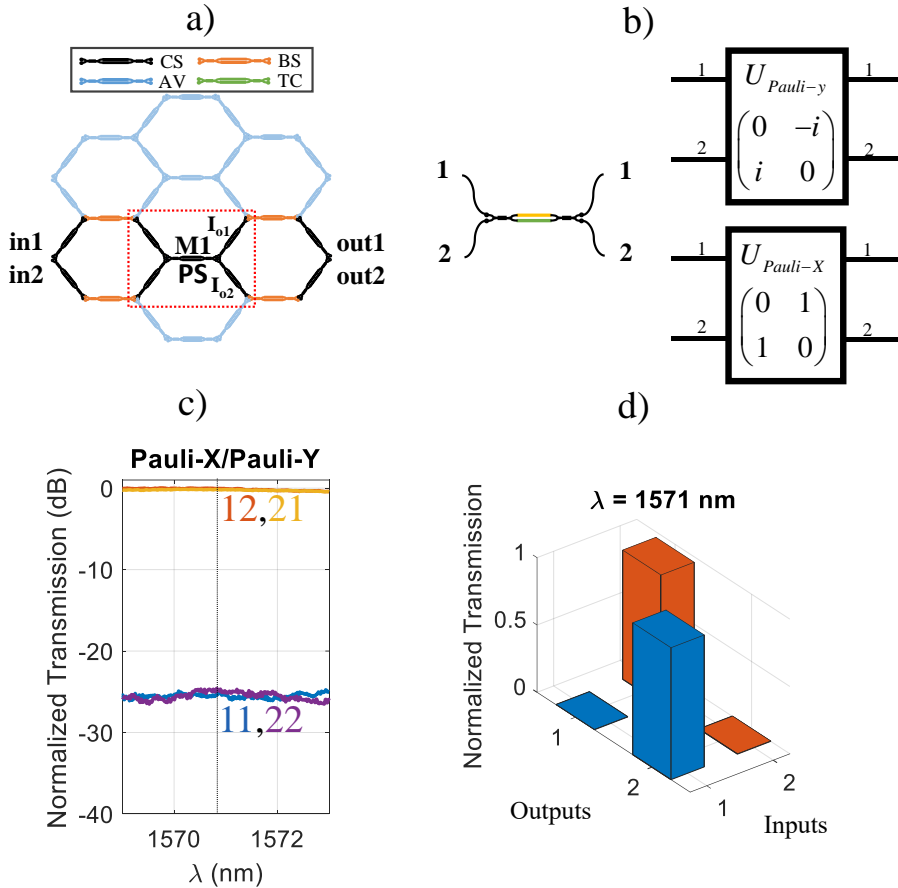


Figure 5.26 Pauli X and Pauli Y  $2 \times 2$  transformations experimental results involving complex-valued matrix coefficients using the hexagonal waveguide mesh, (a) 7-cell configuration (CS = TBU in cross state, BS = TBU in bar state, TC = TBU in tunable coupler state, AV = TBU not employed, PS = Phase shifter), (b): circuit layout of the implemented interferometer, (c): spectral measurement of all input/output port connections, (d) normalized bar diagram of the resulting measured unitary matrix for  $\lambda = 1571$  nm.



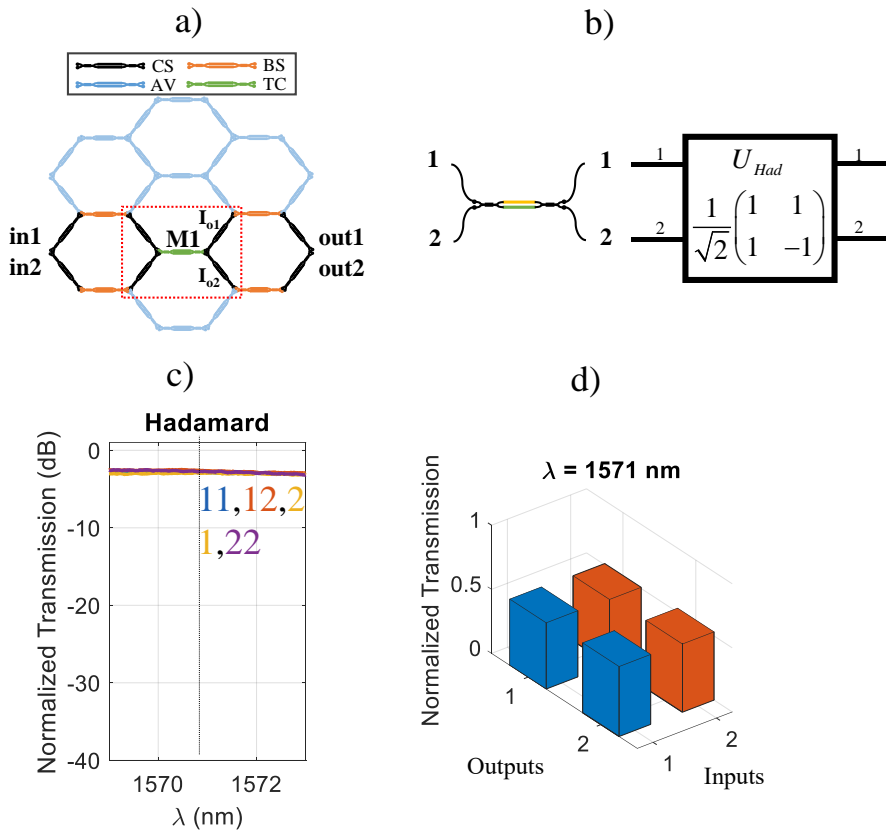


Figure 5.27 Hadamard  $2 \times 2$  transformation involving complex-valued matrix coefficients using the hexagonal waveguide mesh. (a) 7-cell configuration (CS = MZI in cross state, BS = TBU in bar state, TC = TBU in tunable coupler state, AV = TBU not employed, PS = Phase shifter), (b) circuit layout of the implemented interferometer, (c) spectral measurement of all input/output port connections, (d) normalized bar diagram of the resulting measured unitary matrix for  $\lambda = 1571 \text{ nm}$ .

We finally present the measured results corresponding to the implementation of rectangular  $4 \times 4$  interferometers. Figures 5.28 to 5.30 show the results obtained for three different unitary transformations [114] (as required by identity, C-NOT and swap gates), normalized to a 5 BUL waveguide loss. As with the former cases, an excellent agreement is obtained between the theoretical and measured matrix coefficients with extinction ratios above 25 dB for the targeted 1 and 0 coefficients. Note that due to the number of TBUs of the fabricated PIC, this device will be limited to interferometric structures where  $M_B$  coupling constant setting is equal to 1 (Bar State) for  $4 \times 4$  transformations. These examples are, to the best of our knowledge, the

first demonstration of a linear transformation based on a rectangular arrangement of beam splitters theoretically proposed in [88].

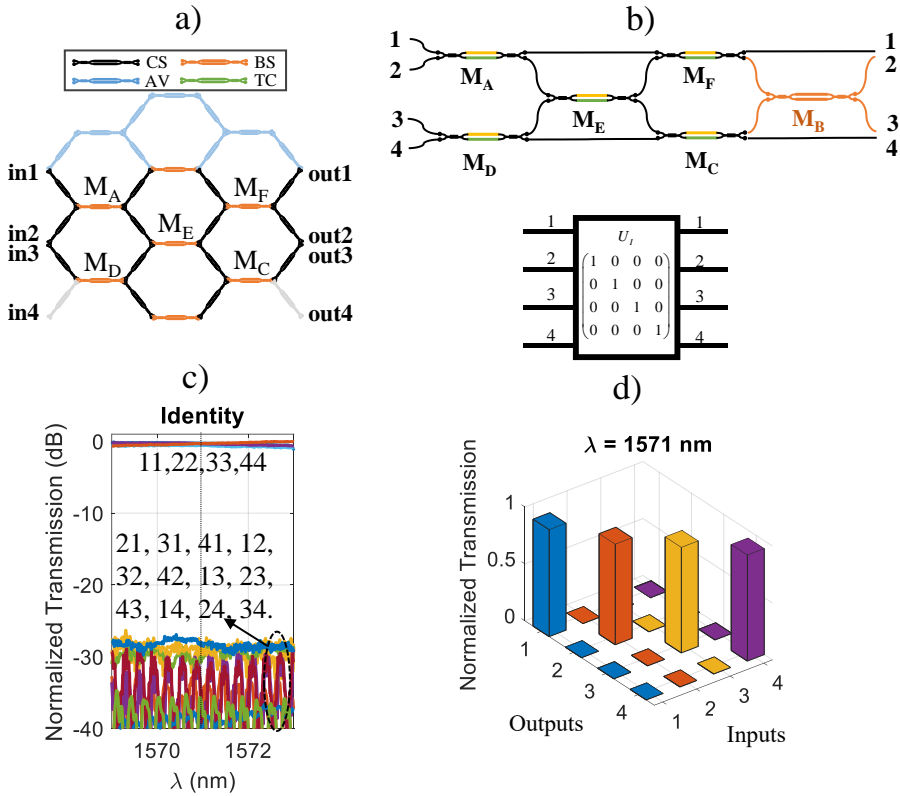


Figure 5.28 Identity transformation configuration of a 4 x 4 interferometer based on a rectangular arrangement. (a) 7-cell configuration (CS = TBU in cross state, BS = MZI in bar state, TC = TBU in tunable coupler state, AV = TBU not employed), (b) circuit layout of the implemented interferometer, (c) spectral measurement of all input/output port connections, (d) normalized bar diagram of the resulting unitary matrix for  $\lambda = 1571$  nm.

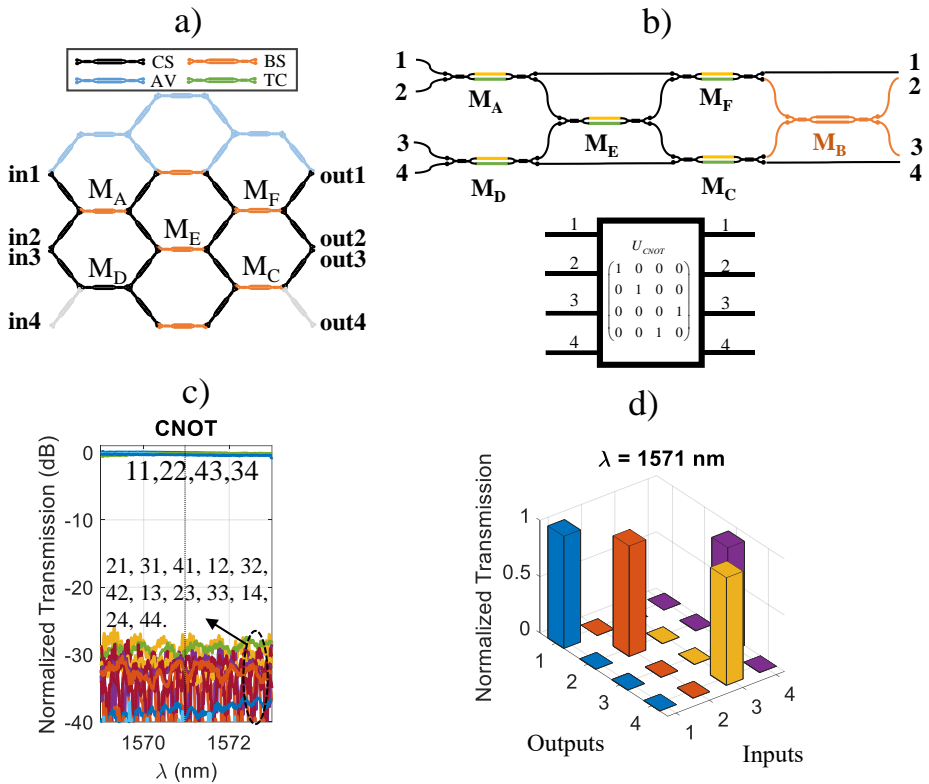


Figure 5.29 C-NOT transformation configuration of a 4 x 4 interferometer based on a rectangular arrangement. (a) 7-cell configuration (CS = TBU in cross state, BS = MZI in bar state, TC = TBU in tunable coupler state, AV = TBU not employed), (b) circuit layout of the implemented interferometer, (c) spectral measurement of all input/output port connections, (d) normalized bar diagram of the resulting unitary matrix for  $\lambda = 1571$  nm.

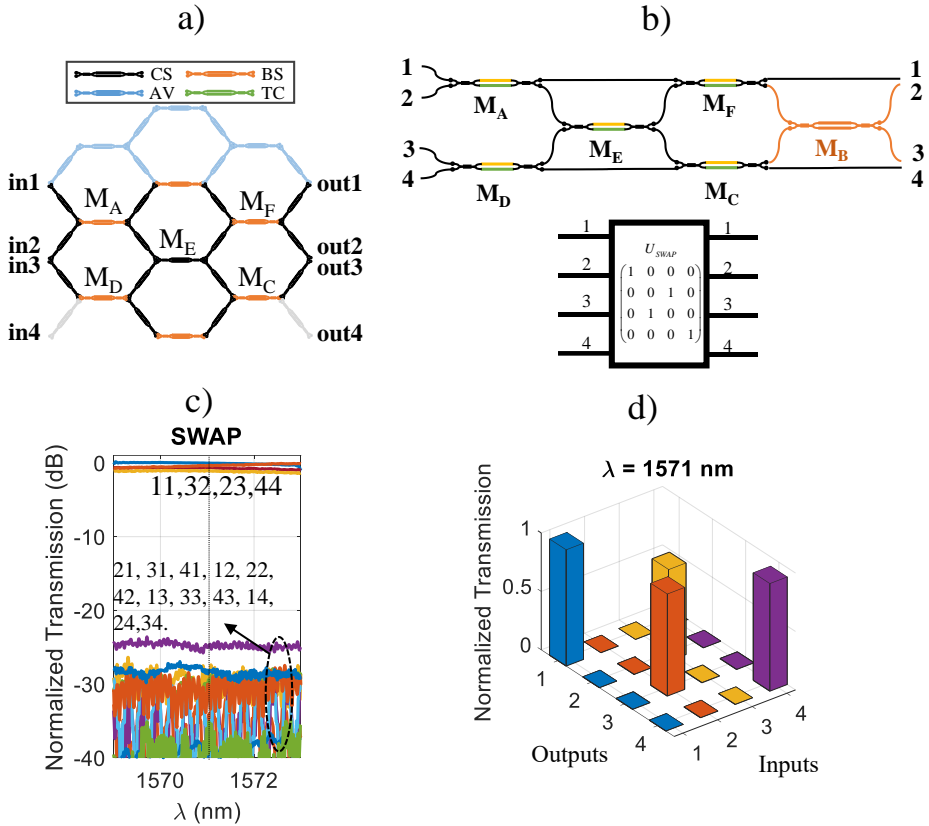


Figure 5.30 SWAP transformation configuration of a 4 x 4 interferometer based on a rectangular arrangement. (a) 7-cell configuration (CS = TBU in cross state, BS = MZI in bar state, TC = TBU in tunable coupler state, AV = TBU not employed), (b) circuit layout of the implemented interferometer, (c) spectral measurement of all input/output port connections, (d) normalized bar diagram of the resulting unitary matrix for  $\lambda = 1571$  nm.

### 5.5.5 Optical Delay Lines:

Optical delay line chips can be used to temporally store optical signals and are a key basic building block for optical processing in digital and microwave photonics applications. We report here the measurements related to the inherent discrete delay line capability of our fabricated hexagonal waveguide processor core. For these results, we have employed an Optical Vector Analyzer (OVA) from LUNA®.

We start by visualizing the time response of two previously synthesized circuits corresponding to a 6-BUL ORR in Figure 5.31, and to a 4-BUL UMZI in Figure 5.32

In the ORR case, we show the reflection response where the coupling factor is being changed. In the top/left we can see that the TBU performing the tunable coupler is in Bar State. In this case, the signal is not travelling through the ring cavity and is directly transmitted to the output. The inset shows a planar spectrum response since there is not any interferometric structure. The top/right figure shows that if we increase the coupling factor, the different contributions for successive signal recirculations will appear delaying the signal. The overall delay is characterised by a time value given by the propagation across the entire ring cavity length, 81 ps. Moving to the bottom/left figure, we can see that we achieve the critical coupling condition resulting in the highest extinction ratio. In this case, we reduce the power of the first contribution and increase the optical power in the ring cavity to overcome the travelling losses inside it. The last figure corresponds to an over-coupled condition. Note that the second contribution is greater than the first one.

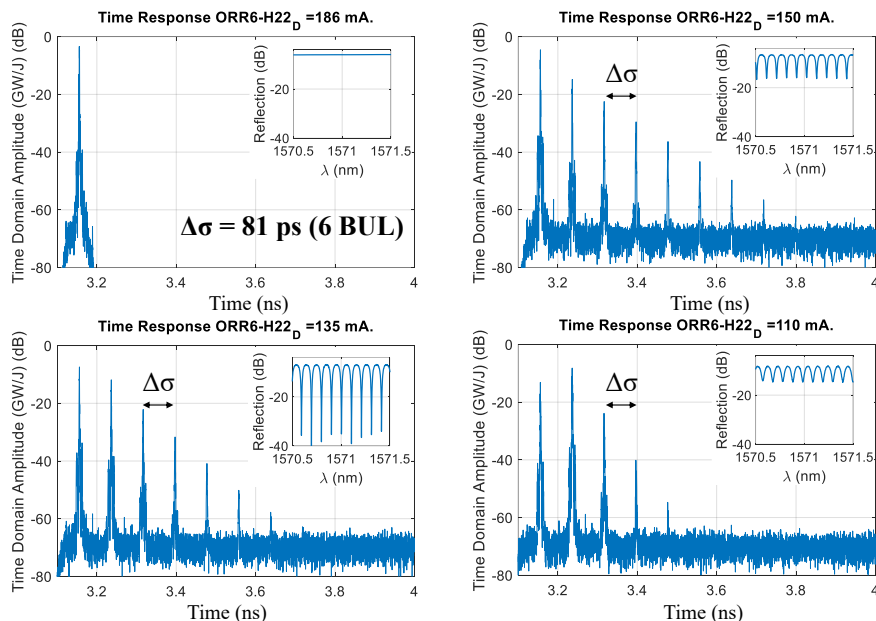


Figure 5.31 Measured time response of an ORR corresponding to 6 BULs. Each figure corresponds to a different coupling factor. The inset shows the corresponding spectral response. (Top/left) the tunable coupler is in bar state so no signals travel through the cavity, (Top/right) the tunable coupler sets a coupling ratio below the critical coupling of the cavity, (Bottom/left) the tunable coupler sets the critical coupling condition in the cavity, (Bottom right) the tunable coupler sets an over-coupling condition in the cavity.

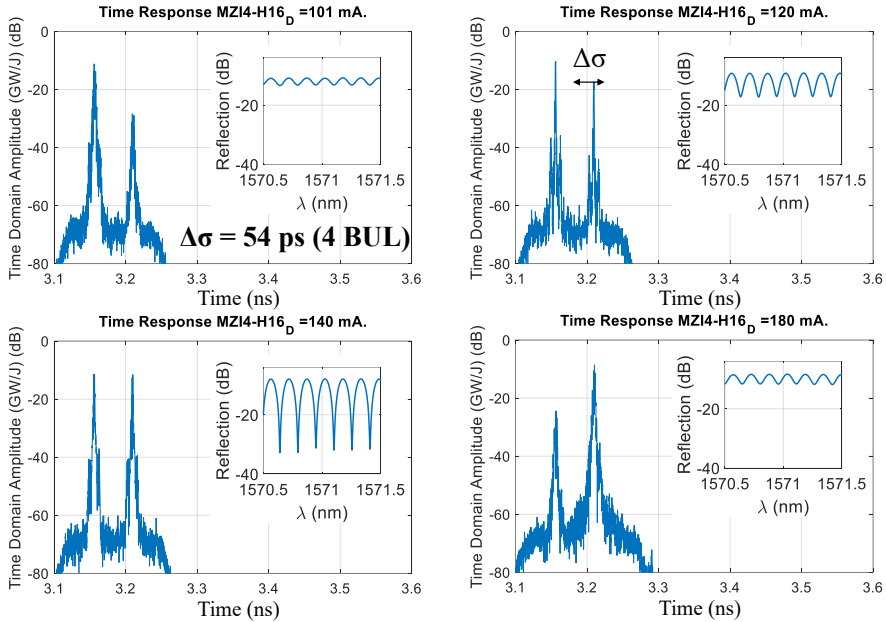


Figure 5.32 Measured time response of a MZI corresponding to 4 BULs. Each figure corresponds to a different input coupling factor and a fixed value of 50:50 for the output coupler division factor. The inset shows the corresponding spectral response. (Top left) The input tunable coupler introduces more power in the shortest path to obtain a difference of 20-dB at the MZI output, (Top right) the input tunable coupler introduces more power the shortest path to obtain a 5-dB difference at the MZI output, (Bottom left) The input tunable coupler sets the critical coupling condition in the MZI to obtain equal power contributions at the output, (Bottom right) the tunable coupler introduces more power to the long path.

In the UMZI case depicted in Figure 5.32, we show the temporal response (i.e. a two-tap discrete time filter) corresponding to one of its two outputs. The coupling constant of the TBU acting as the input tunable coupler is varied while the one acting at the output coupler is maintained fixed with a coupling ratio of 50:50. In the top/left we can see a case where most of the signal is travelling through the shorter UMZI path. The inset shows a low extinction ratio in the spectrum response. The remaining figures illustrate how the splitting ratio changes for each contribution when we increase the coupling ratio. When both contributions are equal (like in bottom/left), the highest extinction ratio is achieved. In this case, the coupling ratio is set to compensate the losses in the largest path with respect to the shorter one. The time delay given by the differential path length is 54 ps. The last figure corresponds to the scenario where the contribution from the longer arm in the UMZI is greater than the first one.

Larger discrete delay lines can be programmed by suitably tuning the TBUs involved in the light path. As an example, Figure 5.33 illustrates two different settings for the 7-cell layout. In the first case, the light is travelling through 5 BULs which results in a delay of 67.5 ps. When the light path is modified as in the companion figure, we increase the light path length to 9 BULs, which corresponds to 121.5 ps. In the right side of the figure, we have included some of the experimental delays obtained by changing the light path length from 3 to 12 TBUs (40.5-162 ps). Our device loss per delay figure is 44.44 dB/ns.

This device would benefit from the integration of an optical amplifier before leaving the chip to compensate the losses.

It could also be possible to employ a continuous delay section implemented with a programmed cascaded-ring delay line followed by a discrete delay line to obtain a larger continuous delay, [92].

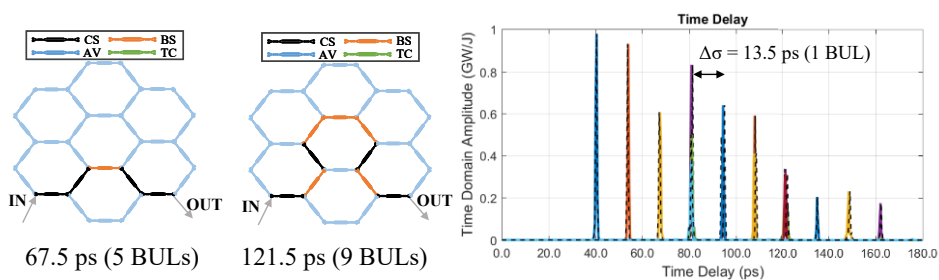


Figure 5.33 Discrete optical delay lines. (Left) 7-cell layout and settings for two different time delays. (Right) Measured delays up to 12 BULs.

Simple optical beamforming configurations based on optical delay lines can be as well programmed in our 7-cell core. By configuring some of the TBUs as tunable couplers, it is possible to create adjacent light-paths with an incremental length  $\Delta L$ . This incremental length will define the tilt angle of the antennas placed at the outputs as shown in Chapter 4. Figure 5.34 illustrates two measured cases that implement a different optical delay  $\Delta\tau$  corresponding to 2 and 3 BULs.

Optical Beamforming networks based on providing a differential phase shift to each output can be as well programmed in the hexagonal-mesh core, either by using a tree-scheme with a phase shifter at each output or by programming a linear interferometer for the beamsplitting section. In this case the output signal frequency and the tilt angle will not be independent, [108].

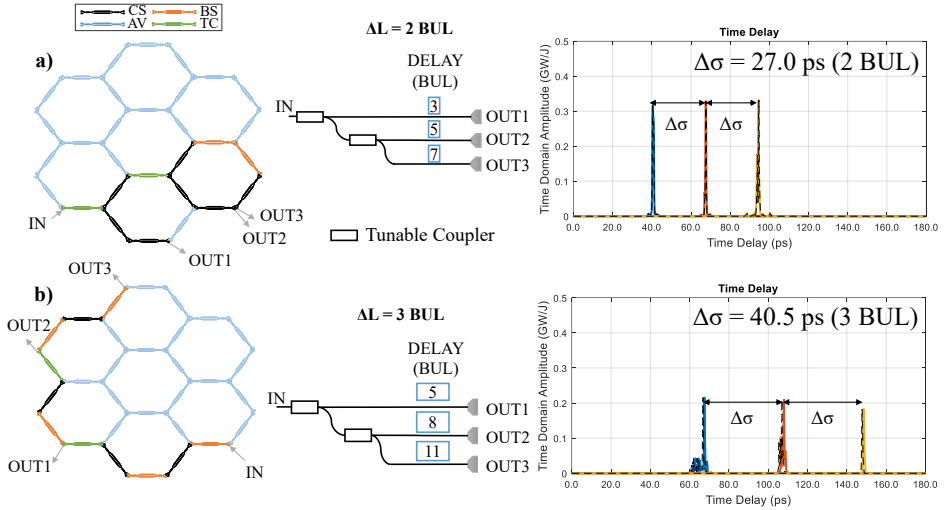


Figure 5.34 Measured optical beamformer network: (a) 2-BUL delay, (b) 3-BUL delay.

## 5.6 Discussion

As we have pointed out in Chapter 4 and demonstrated experimentally in this chapter, the proposed waveguide mesh photonic processor can implement a wide variety of signal processing functionalities. Thanks to the hexagonal layout and its geometric properties described in Chapter 4, even a relatively modest chip with a low cell count design, such as the one reported in this chapter, can be programmed to implement over 100 different configurations. In practice, there were a limited number of available current sources required to tune the TBUs. This restricted the number of configurations that we could demonstrate to a figure around 30. More complex structures like higher-order cascade lattice filters and more complex quantum logic gates than the ones demonstrated here would be possible, if the fabricated chip were to include more unit cells.

Our experimental results have shown the potential of the hexagonal waveguide mesh for implementing 1,2 inputs/outputs ports optical tunable filters structures with an exceptional reconfigurability, optical delay lines as well as 2 x 2, 3 x 3 and 4 x 4 linear optic real and complex-valued unitary transformations.

In the case of optical filters, full-FSR tuning of the notch position is achieved by applying a continuous phase shift to the interferometric structure by suitably configuring a TBU to perform as a constant-amplitude phase shifter. FSR reconfiguration from 36.8 to 4.1 GHz has been demonstrated by modifying the



interferometric length of the programmed structures. The synthesis of more complex structures like 2 cascaded MZIs lattice filters, coupled and side coupler resonators and ring-loaded MZIs have demonstrated the capacity of programming complex PICs. The versatility of the mesh to program optical filters is limited to a fixed number of FSRs. In other words, only a system that can be discretized over the mesh is susceptible to be programmed. Accumulated losses limit further system scalability and the synthesis of more complex circuits.

For the optical delay lines, a discrete range of 13.5 ps steps from 0 up to 162 ps has been measured featuring a loss per delay figure of 44.44 dB/ns. We can improve this figure if some sort of on-chip amplification can be incorporated. In addition, beamforming networks of 3 taps with differential delays of 27 and 40.5 ps have been demonstrated. As for optical filter synthesis, programmed optical delay lines are limited by losses and a reduction of the TBU insertion losses would dramatically upgrade the ODL performance.

Regarding the linear unitary operations implemented, which cover 2x2, 3x3 and 4x4 transformations, it is important to outline that the same hardware architecture can support either a triangular or a rectangular arrangement for multiport interferometers. Moreover, full matrix reconfiguration is achieved by translating the values of the coupling constants and phase shifters (obtained by means of the synthesis algorithms adapted to this architecture) into proper injection currents to the tuning elements according to calibration curves. In this respect, this configuration can help to reduce fabrication costs as the same layout is fabricated regardless the targeted transformation.

A key advantage of this hexagonal mesh compared to the rectangular and triangular beamsplitters arrangements is the possibility to flexibly combine universal interferometers with other classic photonic integrated circuit structures that can be programmed over the mesh as well, such as Mach-Zehnder Interferometers or interferometric cavities. This comes at the expense of more beamsplitters for a certain  $N \times N$  transformation, that will increase from  $N(N-1)/2$  (triangular and rectangular arrangements), to  $(3*N*(N-1)/2) + 2*N$ .

An important question that needs to be addressed is related to the structure scalability. In the structure reported in this work, the number of cells in the chip limits the maximum number of ports in the universal interferometer structures, the number of elements that can be synthesized at the same time and the possibility to integrate complex designs. The number of unit cells could be increased at the expense of increasing the complexity on the three design layers, the software layer and the chip area. For a fixed TBU and BUL design, the required chip area increases with the number of cells. Nevertheless, the TBU can be re-designed to provide a more compact hexagonal cell design for a fixed BUL. Based on our results, further increasing the number of TBUs to be integrated would require two different metal

layer levels to enable on-chip electrical routing. For larger hexagonal waveguide meshes featuring more cells than those actually required for a certain operation, it will be necessary to program access paths to access inner programmed devices, leading to additional balanced losses for all the channels. In contrast, the unused TBUs will be left as redundant components that can be employed in case of failure over a certain chip area, leading to a more robust final device. The number of cells for a particular design will depend on the size of the targeted circuits to be synthesized/programmed. In practice, the number of electrical DC Pads and its associated control system might limit the number of available TBUs present on the circuit. Figure 5.35 plots the number of required electrical ports versus the number of cells. For the reported device, we employed 120 single-point (ground) pads for the electrical control of 60 phase shifters. Out of the chip, some of them were connected to a common ground. Having a common ground port on the circuit can reduce the amount of electrical ports by a factor of two. The main drawback would then be the appearance of electrical noise, which can be pre-characterized considering the differential resistance of each path, [113].

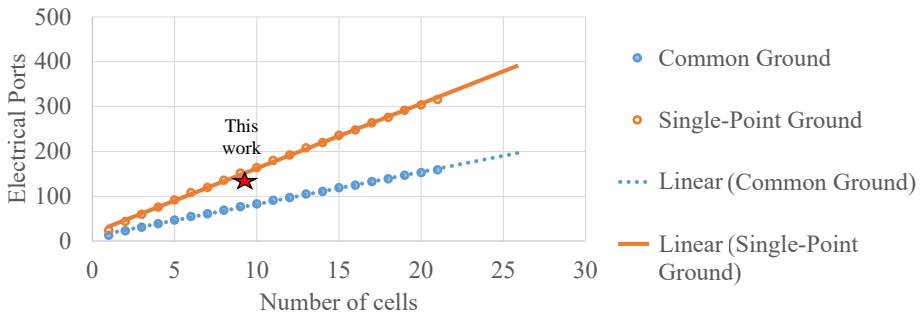


Figure 5.35 Electrical ports vs number of cells for 2 different ground configurations. (Up), Single-Point Ground. (Bottom), Common Ground.

Although a miniaturization of the BUL is possible, we must consider the resulting operational trade-off. The impact of the BUL miniaturization is four-fold. To start with the positive aspects, first, the maximum Free Spectral Range of the interferometric devices programmed will be limited by the inverse of 2-BULs and 6 BULs for the MZIs and the ORRs cases, respectively. This limitation affects the maximum operational frequency of most of the microwave photonics applications. Secondly, the resolution step will be finer so the probability to be closed to a desired FSR, delay, or length will increase. Two negative aspects may arise for miniaturised BULs. First, a programmed waveguide of a certain length will have more propagation losses for shorter BULs, as a greater number of TBUs will be needed for a required length. As illustrated by Figure 5.36, the insertion losses of the 2 MMIs of each TBU

are dominant over the propagation losses. Secondly, the integration density and thus the number of switching elements per area will increase, leading to a thermal crosstalk increment, since it is proportional to the proximity between TBUs. Additionally, it results in a more complex metal layer design. In practice, reducing the BUL is technically feasible. Thermal tuners offering continuous  $[0 - 2\pi]$  phase shift shorter than  $62 \mu\text{m}$  have been demonstrated recently, [115]. State-of-the-art 3-dB couplers in silicon have insertion losses around  $0.15 \pm 0.1 \text{ dB}$  [116, 117], so the losses due to the 2 cascade couplers will dominate over state-of-the-art propagation losses, which are around  $1 \text{ dB/cm}$  [118].

Since the roughness on the lateral walls of the optical waveguide dominates the propagation losses, an alternative for our TBU design would be to increase the width on the straight waveguide sections, enabling even lower propagation losses.

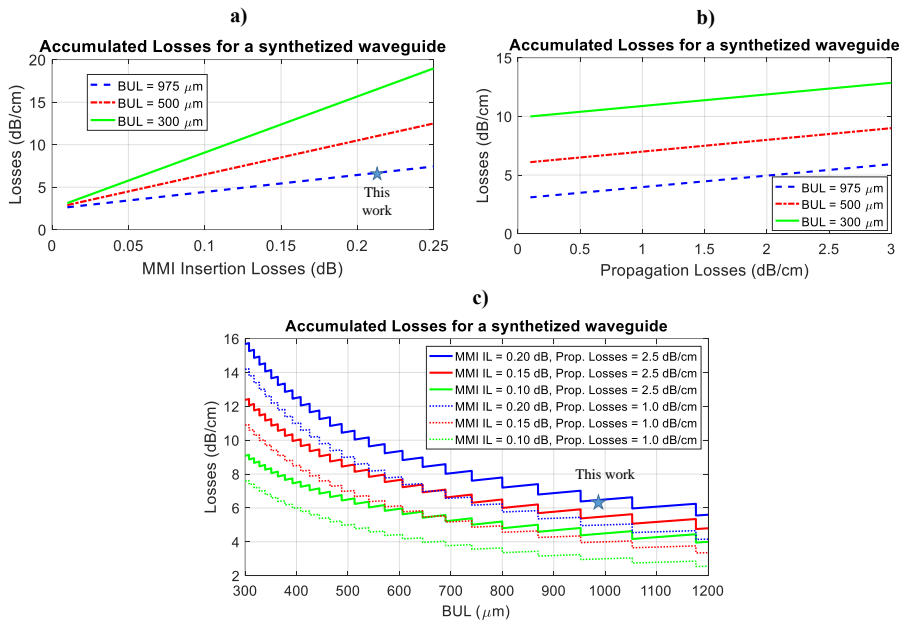


Figure 5.36 Synthesized waveguide losses impact due to: (a), MMI Insertion Losses for propagation losses of  $2.5 \text{ dB/cm}$ . (b), propagation losses for a fixed MMI IL of  $0.15 \text{ dB}$ . (c), discretization due to Basic Unit Length variation and relative path losses.

For practical operation, it is fundamental to thermally stabilize the TBUs so their programmed values remain stable in time once selected and to manage the impact of thermal crosstalk from neighbouring TBUs, a complete analysis regarding these issues for the presented hexagonal waveguide core is included in [112]. In addition, it is essential to make the chip operation robust against departures of the TBUs from

their designed values. A recent work [119] has reported practical solutions to overcome this limitation in CMOS-compatible silicon photonics platforms, enabling potential dynamic regime operation by tracking the deviations in the device parameters and providing corrective signals to stabilize the operation. Hybrid integration with III-V materials would be necessary in order to incorporate the optical sources and the modulator to the proposed optical core. Future work on electronic integration is required to integrate the current sources.

Another important issue is related to how the input signal is directed into a specific input port of the mesh network and how a signal is directed from a port of the mesh to a photodetector. These operations require some degree of optical interconnection that can be provided by the mesh itself provided its size is large enough as depicted in Chapter 4.

In contrast to application-specific devices, multi-purpose photonic processors enable a wide variety of applications on the same chip, providing flexible and fast adaptive designs topologies and circuit parameters. Fabricated in a CMOS compatible technology, multi-task processors enable high-production volume reducing the price per chip. The unused/available TBUs perform as spare components that will potentially enable self-healing photonic integrated circuits.

# Chapter 6

## Summary, Conclusions and Future Work

### 6.1 Summary and Conclusions

In this thesis, we have proposed the new concept of *generic-purpose software-defined integrated MWP photonic processor*. Being a radically different approach from ASPICs, this new PIC class enables the programmability of the main MWP functionalities on the same hardware platform.

In Chapter 2, we have reviewed the evolution and state of the art of IMWP. To date, the activity in this research area has almost focused on particular circuits and chip configurations designed to optimally perform a single MWP functionality. Only three material platforms: Indium Phosphide, Silicon Nitride, and Silicon photonics have reached the required degree of maturity to be considered as viable options for the implementation of complex photonic integrated circuits, either monolithic or hybrid. We have reviewed their strengths and weaknesses regarding the integration of optical active components, optical passive components as well as radiofrequency and electronic subsystems.

In Chapter 3, we have presented the photonic processor system architecture together with a full end-to-end model for the evaluation of the main figures of merit: RF gain, noise figure and dynamic range. It allows the complete system evaluation and provides, at the same time, a powerful tool to properly design and programme the photonic processor. Some examples of operational modes have been outlined for the processor configuration.

The generic-purpose photonic processor relies on a powerful and versatile optical core to perform the reconfigurable optical interconnects and the photonic filtering tasks. Chapter 4 is focused on this key subsystem. We believe that reconfigurable waveguide lattice meshes [51, 52] are optimal candidates for the optical core of the photonic processor, since they provide the required versatility. In that chapter, we

have proposed two alternative lattice topologies to the existing square mesh design: the hexagonal and triangular waveguide meshes. We have presented an extensive analysis of the three mesh topologies and defined several figures of merit that account for photonic integration efficiency and versatility when programming PICs: *flexibility*, *switching elements per area* and *reconfiguration performance*. We obtained as a result that the hexagonal mesh topology outperforms both the square and triangular meshes. We have illustrated the processor configuration, whose optical core is based on a hexagonal waveguide mesh, for several MWP functionalities like RF and optical filtering, instantaneous frequency measurement, optical beamforming, arbitrary signal generation and frequency mixing.

In Chapter 5, we have presented the design, fabrication and testing process of the first integrated hexagonal waveguide lattice mesh. This 7-cell layout integrated on silicon has achieved, to the best of our knowledge, several records beyond the current state of the art. First, it is the first integrated hexagonal mesh ever reported. Secondly, it is the mesh-based PIC with a higher cell count number: Whereas the previous one integrated 2 square cells (7 Tunable Basic Units), our design features 7 hexagonal cells (30 Tunable Basic Units). Finally, this higher cell count number allows the demonstration of a record number of 30 different functionalities, which is only limited by the current sources available at the moment of measurement (18 current sources). With 12 additional current sources, we estimate that over 100 different functionalities can be programmed in our fabricated PIC. Moreover, our optical core enable for the first time the synthesis of filtering structures like ORRs and MZIs as well as the universal interferometers. The latter enable the synthesis of any operation defined by a linear unitary matrix of size limited by the number and distribution of the cells. Here, we were able to synthesize the two arrangements proposed for this linear operation: the triangular beamsplitter and, for the first time, the rectangular beamsplitter.

All in all, we believe that the work presented here opens a new paradigm in photonic integration. Similarly to the development and further market expansion experienced by the electronic integrated circuits given by the fabrication and design processes standardization as well as the migration to application agnostic integrated systems, we believe that this work sets the base for a new era of generic-purpose photonic integrated systems.

## 6.1 Future work

Although a considerable amount of work has been done for the last three years related to the near-unexplored field of generic-purpose photonic processors, there are still many open questions and issues that need to be addressed and solved before achieving a fully-integrated software-defined MWP processor. Some of these

problems are inherent to photonic integration and have been studied by the scientific community in the preceding years, [53, 3], while others have not been addressed yet:

- *The design of a fully integrated processor version:* To date, there is no material platform that enables, simultaneously, the integration of the different components present in IMWP systems, such as active and passive microwave components as well as active and passive photonic components, together with electronics. This might call for a hybrid integration design, but to date, there is not a clear optimal solution, [3, 55].
- *Tunable Basic Unit optimization and optimal number of cells:* Depending on the targeted operations complexity, the reconfigurable optical core might need the integration of a considerable number of Tunable Basic Units, [59]. Since the reconfigurable optical core relies on the cascade interconnection of this element, a minimum improvement in the tunable basic unit results in a huge quality increment of the overall processor. This calls for the exploration of TBU design alternatives aiming low insertion losses, high-bandwidth, and reduced crosstalk (optical and thermal) as well as power consumption, [120]. In this regard, we have designed a new hexagonal waveguide mesh that is currently under fabrication at the  $\text{Si}_3\text{N}_4$  illustrated in Figure 6.1. The reduced value of the group index (1.92) and a BUL of 1270  $\mu\text{m}$  provides maximum FSRs of 61.37 and 20.45 GHz for MZIs and ORRs, respectively.
- *Exploring alternative tuning mechanisms for the TBUs:* Electro-optic effects based on the effective index change to the presence of electrical carriers [74], (carrier depletion [75], injection and accumulation), graphene-based [121] and micro-opto-mechanical structures using gradient electric force phase shifters [76]. In Figure 6.2, we show the impact of the power consumption of the optical core for different number of activated TBUs vs the average TBU power consumption percentage, assuming two different  $P_\pi$  values. The average TBU power depends on the design topology selected.
- *Experimental demonstration and validation of the processor:* This would constitute an achievement well beyond the current state of the art. Some of the targeted functionalities are: reconfigurable MWP filters with a self-beating scheme, the realization of integrated reconfigurable and tunable mm-wave delay lines for beamforming applications, arbitrary waveform generation, frequency up/down conversion, instantaneous frequency measurement as well as tone generation based on optoelectronic oscillation. The use of the model developed in Chapter 3 will be essential.
- *Demonstration of the applicability of the proposed tunable core to other areas of Photonics:* for instance, in quantum information systems, routing or switching. The universal linear interferometers demonstrated here can be employed to sustain reconfigurable quantum applications, [49]. This would expand the already-powerful capabilities of the photonic processor.

- *Extension and programming of the software-layer capabilities:* to obtain self-healing attributes and optimise the processor performance enabling dynamic operation.

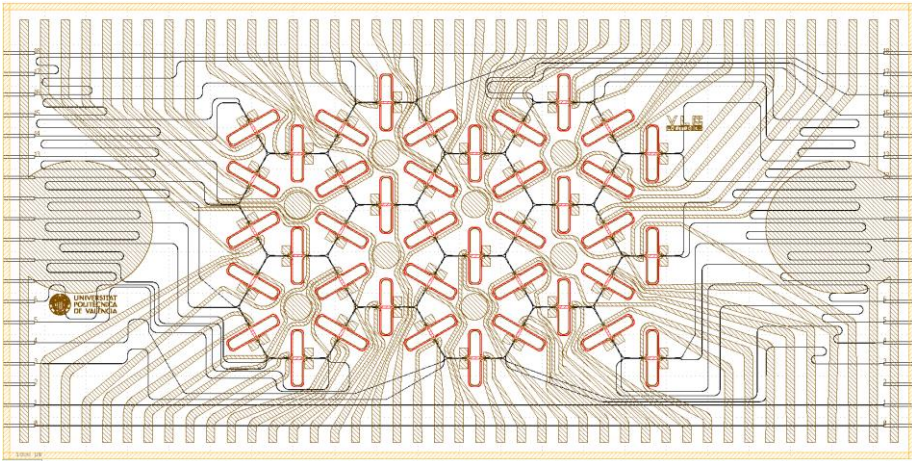


Figure 6.1 5.5 x 11 mm<sup>2</sup> optical layout of a hexagonal waveguide mesh to be integrated in Si<sub>3</sub>N<sub>4</sub> at VLC Photonics – CNM Platform. (Black) optical layer, (copper-coloured) metal layer, (red) thermal isolation layer.

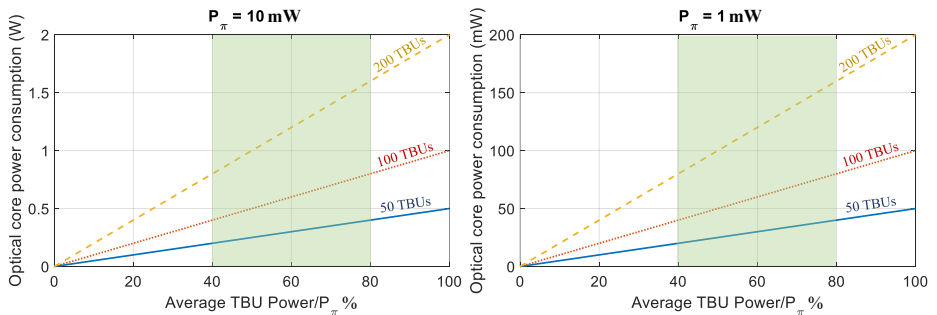


Figure 6.2 Optical core power consumption estimation vs average TBU power for the synthesis of circuits involving 50, 100 and 200 TBUs assuming a  $P_\pi$  of: (left) 10 mW and (right) 1 mW. A green area between 40-60 % of the average TBU power represents typical feeding values depending on the synthesised circuit.

The recent award of the ADVANCED GRANT ERC-ADG2016-741415, *Universal microwave photonics programmable processor for seamlessly interfacing wireless and optical ICT systems* UMWP-CHIP, provides a unique opportunity for addressing and developing the future research lines outlined here to achieve a fully-integrated version of a generic-purpose programmable MWP processor.







# Appendix A

## Analytical model of a MWP system/link

For the sake of completeness, we will incorporate the step-by-step process to derive the figures of merit presented in Chapter 3. The corresponding to direct detection schemes (IM-DD, PM-DD and PM-BD) were previously demonstrated in [40]. Here, we include the IM-BD scheme, as well as a heterodyne (self-beating) configuration schemes. For all of them, we include the end-to-end model corresponding to the contributions of the MWP system and the RF stage in the last section.

Appendix A.4 deals with the intermediate steps on the linearization process of MWP systems/links employing a DPMZM described in Chapter 3.

### A.1 Detailed derivation of photocurrents and RF power for Direct Detection systems/links

For a modulating signal composed of two sinusoidal functions at different electrical angular frequencies  $\Omega_1$  and  $\Omega_2$ , (point (1) of Figure 3.4), the photocurrent term at the output of the MWP part (point (2) of Figure 3.4) considering up to the second-order and the most relevant third-order frequency contributions is given by:

$$\begin{aligned}
 x(t) = & i_1 \sin(\Omega_1 t + \theta_1) + i_2 \sin(\Omega_2 t + \theta_2) + i_{11} \sin(2\Omega_1 t + \theta_{11}) + i_{22} \sin(2\Omega_2 t + \theta_{22}) + \\
 & i_{12} \sin[(\Omega_1 - \Omega_2)t + \theta_{12}] + i_{21} \sin[(\Omega_2 - \Omega_1)t + \theta_{21}] + i_{xx} \sin[(\Omega_1 + \Omega_2)t + \theta_{xx}] + \\
 & i_{112} \sin[(2\Omega_1 - \Omega_2)t + \theta_{112}] + i_{221} \sin[(2\Omega_2 - \Omega_1)t + \theta_{221}],
 \end{aligned} \tag{A.1}$$

where the terms  $i$  and  $\theta$  refer, respectively, to the amplitude and phase of each different frequency term. Following the derivation reported in [40] for small-signal approximation, we obtain the following expressions for the amplitude of the linear and nonlinear terms of the previous equation, referred to the real current:

- Signal contribution, either at the angular frequency  $\Omega_1$  or  $\Omega_2$ :

$$i'_{1,2} = \frac{I_{dc}\phi_{rf}}{2} \sin(\phi_{dc}) |A'_{\Omega_{1,2}}| \quad \text{and} \quad i'_{1,2}{}^\Phi = 2I_{dc}\phi_{rf} |A^\Phi_{\Omega_{1,2}}|. \quad (\text{A.2})$$

- Second-order distortion, considering both the harmonic and intermodulation products:

$$\begin{aligned} i'_{112} &= \frac{I_{dc}\phi_{rf}^2}{8} |A'_{2\Omega_{1,2}}|, \quad i'_{12,21} = \frac{I_{dc}\phi_{rf}^2}{8} |A'_{\Omega_{1,2}-\Omega_{2,1}}| \quad \text{and} \quad i'_{ix} = \frac{I_{dc}\phi_{rf}^2}{8} |A'_{\Omega_1+\Omega_2}|; \\ i^\Phi_{112} &= I_{dc}\phi_{rf}^2 |A^\Phi_{2\Omega_{1,2}}|, \quad i^\Phi_{12,21} = I_{dc}\phi_{rf}^2 |A^\Phi_{\Omega_{1,2}-\Omega_{2,1}}| \quad \text{and} \quad i^\Phi_{ix} = I_{dc}\phi_{rf}^2 |A^\Phi_{\Omega_1+\Omega_2}|. \end{aligned} \quad (\text{A.3})$$

- Third-order distortion, considering both the harmonic and intermodulation products:

$$i'_{112,221} = \frac{I_{dc}\phi_{rf}^3}{32} \sin(\phi_{dc}) |A'_{2\Omega_{1,2}-\Omega_{2,1}}| \quad \text{and} \quad i^\Phi_{112,221} = \frac{I_{dc}\phi_{rf}^3}{2} |A^\Phi_{2\Omega_{1,2}-\Omega_{2,1}}|. \quad (\text{A.4})$$

where  $I$  and  $\Phi$  refer to the possible operation regimes (including single or balanced detection for each case),  $I_{dc}$  is the average photocurrent,  $\phi_{rf}$  the signal modulation index,  $\phi_{dc}$  the bias point for the case of intensity modulation, and  $A_{\Omega}^{Mod}$  the spectral coefficients for a frequency tone defined by  $\Omega$ , which were defined in Chapter 3.

The RF photodetected power for each signal contribution term of frequency  $\Omega$  into a load defined by  $R_{out}$  Ohms is:

$$P_{RF}^{Mod}(\Omega_x) = \frac{[i_x^{Mod}]^2 R_{out}}{2}, \quad (\text{A.5})$$

while the RF input power is, for both modulation types:

$$P_{RF}^{Mod}(\Omega) = \frac{V_{rf}^2}{2R_{in}}, \quad (\text{A.6})$$

where  $V_{rf}$  is the amplitude of the voltage signal applied to the external modulator and  $R_{in}$  is the input resistance.

## A.2 Detailed derivation of photocurrents and the figures of Merit of Self-Beating scheme

We consider the self-beating MWP link shown in Figure 3.6. Referring to this figure, the system parameters given in Chapter 3, and the vector field at the output of the upper link  $\mathbf{E}_{out}(t)$  for the electromagnetic field (prior to the second coupler), the output photocurrent can be computed yielding:

$$\begin{aligned}
 i_{RF,out}(t) &= \Re(2K_2 - 1) |E_{out}(t)|^2 - \Re(2K_2 - 1) \alpha_L K_1 P_o \\
 &\quad + 2\Re \sqrt{K_1 K_2 (1 - K_2)} \alpha_L P_o e^{-j\omega_o t} \vec{E}_{out}(t) \cdot \vec{e}_d + \\
 &\quad + 2\Re \sqrt{K_1 K_2 (1 - K_2)} \alpha_L P_o e^{j\omega_o t} \vec{E}_{out}^*(t) \cdot \vec{e}_d \\
 &= i_{dd}(t) + i_b(t),
 \end{aligned} \tag{A.7}$$

where  $\vec{e}_d$  is the vector representing the state of polarization of the CW laser. The first term in Eq. (A.7) is  $i_{dd}(t)$ , the contribution due to direct detection and its impact over the figures of merit has been evaluated in [40]. Although, in principle, this contribution has to be taken into account in the derivations, in practice it is the second and third terms that correspond to the beating between the signal and local oscillator  $i_b(t)$  which are expected to dominate.

The action of the modulator is described in the time and frequency domains by [40]:

$$\begin{aligned}
 E_{out}|_{MZM}(t) &= j\sqrt{\alpha_{MZM}} E_{in}(t) \sin\left[\phi_{dc} + (\phi_{rf}/2)\sin\Omega t\right], \\
 E_{out}|_{MZM}(\omega) &= 2\pi\sqrt{\alpha_{MZM}} \sum_{n=-\infty}^{\infty} B_n J_n(\phi_{rf}/2) E_{in}(\omega - n\Omega), \\
 B_n &= (-1)^n j^{|n|+1} \sin(\phi_{dc}/2 + |n|\pi/2),
 \end{aligned} \tag{A.8}$$

where  $B_n$  are the spectral coefficients of the modulator. Introducing Eq. (A.8) in Eq. (A.7)(4.7) and taking into account that  $\mathbf{E}_{out}(\omega) = H(\omega) \mathbf{E}_{out}|_{MZM}(\omega)$ , we have after a straightforward but lengthy calculation:

$$\begin{aligned}
 i_b(t) &= \{\vec{e}_u \cdot \vec{e}_d = \cos\varphi\} = \\
 &= 2\Re P_o \sqrt{K_1 K_2 (1 - K_2) (1 - K_1)} \alpha_L \alpha_U \\
 &\quad \sum_{n=-\infty}^{\infty} \sum_{k=-\infty}^{\infty} J_{|n|}\left(\frac{\phi_{RF}}{2}\right) J_{|k|}\left(\frac{\phi_{RF}}{2}\right) \left[ B_{n,k} H(\omega_o + n\Omega_1 + k\Omega_2) + \right. \\
 &\quad \left. (-1)^{|n|+|k|} B_{-n,-k}^* H^*(\omega_o - n\Omega_1 - k\Omega_2) \right] e^{j(n\Omega_1 + k\Omega_2)t} \cos\varphi.
 \end{aligned} \tag{A.9}$$

Equation (A.9) provides the value of the fundamental and intermodulation terms required for the computation of the contribution of the self-beating current to the Figures of Merit of the MWP link. In combination with equation (6) of [40], they provide the overall output current. For example, under small signal modulation approach, the phasor for the fundamental RF photocurrent at  $\Omega_1$  is given by:

$$\begin{aligned}\widehat{I}(\Omega_1) &= \widehat{I}_{dd}(\Omega_1) + \widehat{I}_b(\Omega_1) = \\ &= I_{dc} \sqrt{\alpha_U(1-K_1)} \left( \frac{\phi_{RF}}{4} \right) \sin(\phi_{DC}) \left[ \begin{array}{l} 2\sqrt{K_1 K_2(1-K_2)} \alpha_L A_{\Omega_1}^{I,SB} - \\ j(2K_2-1) \sqrt{\alpha_U(1-K_1)} A_{\Omega_1}^I \end{array} \right],\end{aligned}\quad (\text{A.10})$$

where:

$$A_{\Omega_1}^{I,SB} = \frac{[H(\omega_o + \Omega_1) - H^*(\omega_o - \Omega_1)]}{\sin(\phi_{dc}/2)} \cos \varphi, \quad (\text{A.11})$$

and  $A_{\Omega_1}^I$ ,  $A_{\Omega_1}^{I,SB}$ , are the spectral coefficient for the fundamental, terms for intensity modulated direct detection and the self-beating filtered MWP systems that are defined in Chapter 3 and in Eq. (A.13), respectively.

In the same way, the phasors for the second- and third-order RF intermodulation terms are given by:

$$\begin{aligned}\widehat{I}(\Omega_1 - \Omega_2) &= \widehat{I}_{dd}(\Omega_1 - \Omega_2) + \widehat{I}_b(\Omega_1 - \Omega_2) = \\ &= I_{dc} \sqrt{(1-K_1)} \alpha_U \left( \frac{\phi_{RF}}{4} \right)^2 \left[ \begin{array}{l} \sqrt{(1-K_1)} \alpha_U (2K_2-1) A_{\Omega_1-\Omega_2}^I + \\ j2\sqrt{K_1 K_2(1-K_2)} \alpha_L A_{\Omega_1-\Omega_2}^{I,SB} \end{array} \right],\end{aligned}\quad (\text{A.12})$$

$$\begin{aligned}\widehat{I}(2\Omega_1 - \Omega_2) &= \widehat{I}_{dd}(2\Omega_1 - \Omega_2) + \widehat{I}_b(2\Omega_1 - \Omega_2) = \\ &= I_{dc} \sqrt{(1-K_1)} \alpha_U \left( \frac{\phi_{RF}}{4} \right)^3 \sin(\phi_{dc}) \left[ \begin{array}{l} j(2K_2-1) \sqrt{(1-K_1)} \alpha_U A_{2\Omega_1-\Omega_2}^I + \\ 2\sqrt{K_1 K_2(1-K_2)} \alpha_L A_{2\Omega_1-\Omega_2}^{I,SB} \end{array} \right],\end{aligned}$$

where:

$$\begin{aligned}A_{\Omega_1-\Omega_2}^{I,B} &= 2[H(\omega_o + \Omega_1 - \Omega_2) - H^*(\omega_o - \Omega_1 + \Omega_2)] \sin(\phi_{dc}/2) \cos \varphi, \\ A_{2\Omega_1-\Omega_2}^{I,B} &= \frac{[H(\omega_o + 2\Omega_1 - \Omega_2) - H^*(\omega_o - 2\Omega_1 + \Omega_2)]}{2\sin(\phi_{dc}/2)} \cos \varphi,\end{aligned}\quad (\text{A.13})$$

and  $A'_{\Omega_I-\Omega_2}$  and  $A'_{2\Omega_I-\Omega_2}$  are the spectral coefficients, respectively, for the second- and third-order intermodulation terms for intensity modulated direct detection MWP systems, which were defined in Chapter 3. From Eqs. (A.10) and (A.12), one can directly compute the RF powers corresponding to the fundamental term:

$$\begin{aligned} P_{RF}(\Omega_1) &= 2|\widehat{I}(\Omega_1)|^2 Z_{out} = \\ &= 2I_{dc}^2 Z_{out} \alpha_U (1-K_1) \left(\frac{\phi_{RF}}{4}\right)^2 \sin^2(\phi_{DC}) \left| \left( \frac{2\sqrt{K_1 K_2 (1-K_2)} \alpha_L A'_{\Omega_1}{}^{I,B} - j(2K_2-1)\sqrt{\alpha_U (1-K_1)} A'_{\Omega_1}{}^I}{j(2K_2-1)\sqrt{\alpha_U (1-K_1)} A'_{\Omega_1}{}^I} \right) \right|^2. \end{aligned} \quad (\text{A.14})$$

From Eq. (A.14), we can directly obtain the end-to-end RF gain as defined in Chapter 3. Note that this time, the power has been computed from the phasor of the current instead of from the real current term, like in Eq. (A.5).

#### Noise contributions

Regarding the noise contributions, and using the *RIN* definition, we first need to determine the value of the average current which from (A.9) is given by:

$$I_{dc,total} = \frac{DI_{dc}}{X} \left[ (-1)^p D |H(\omega_o)|^2 (1 - \cos \phi_{DC}) + Y + 4C \sin\left(\frac{\phi_{DC}}{2}\right) \cos \varphi \text{Im}\{H(\omega_o)\} \right], \quad (\text{A.15})$$

where the exponent  $p$  takes the value 0 for single detection and 1 for balanced detection, and  $D$ ,  $X$ ,  $Y$ ,  $C$  are the coupling and losses coefficients defined in Chapter 3. From Eq. (A.15) and the *RIN* definition, we get the different contributions:

$$\begin{aligned} RIN_{\text{Thermal input}} &= \frac{N_{\text{Thermal input}}^{\text{output}}}{I_{dc,Total}^2 Z_{out}} \\ &= \frac{k_B T \left[ \frac{\pi \sin(\phi_{DC})}{2V_\pi} \right]^2 |jDA'_{\Omega_1}{}^I + CA'_{\Omega_1}{}^{I,B}|^2 Z_{in}}{\left[ (-1)^p D |H(\omega_o)|^2 (1 - \cos \phi_{DC}) + Y + 4C \sin\left(\frac{\phi_{DC}}{2}\right) \cos \varphi \text{Im}\{H(\omega_o)\} \right]^2}, \end{aligned} \quad (\text{A.16})$$

$$\begin{aligned}
 RIN_{\text{Thermal input}} &= \frac{N_{\text{Thermal input}}^{\text{output}}}{I_{dc, \text{Total}}^2 Z_{out}} \\
 &= \frac{k_B T \left[ \frac{\pi \sin(\phi_{DC})}{2V_\pi} \right]^2 |jDA_{\Omega_1}^I + CA_{\Omega_1}^{I,B}|^2 Z_{in}}{\left[ (-1)^p D |H(\omega_o)|^2 (1 - \cos \phi_{DC}) + Y + 4C \sin\left(\frac{\phi_{DC}}{2}\right) \cos \varphi \operatorname{Im}\{H(\omega_o)\} \right]^2}, \quad (\text{A.17})
 \end{aligned}$$

$$\begin{aligned}
 RIN_{\text{Thermal output}} &= \frac{N_{\text{Thermal output}}^{\text{output}}}{I_{dc, \text{Total}}^2 Z_{out}} \\
 &= \frac{2k_B T}{\left( \frac{DI_{dc}}{X} \right)^2 Z_{out} \left[ (-1)^p D |H(\omega_o)|^2 (1 - \cos \phi_{DC}) + Y + 4C \sin\left(\frac{\phi_{DC}}{2}\right) \cos \varphi \operatorname{Im}\{H(\omega_o)\} \right]^2}, \quad (\text{A.18})
 \end{aligned}$$

$$\begin{aligned}
 RIN_{\text{Shot}} &= \frac{N_{\text{shot}}^{\text{output}}}{I_{dc, \text{Total}}^2 Z_{out}} \\
 &= \frac{2e}{\left( \frac{DI_{dc}}{X} \right) \left[ (-1)^p D |H(\omega_o)|^2 (1 - \cos \phi_{DC}) + Y + 4C \sin\left(\frac{\phi_{DC}}{2}\right) \cos \varphi \operatorname{Im}\{H(\omega_o)\} \right]}, \quad (\text{A.19})
 \end{aligned}$$

from which  $RIN_{\text{Total}}$  can be computed as the sum of all of them together with the  $RIN_{\text{laser}}$  contribution.

Finally, the optical interception points are obtained from RF powers of the intermodulation terms:



$$\begin{aligned}
P_{RF}(\Omega_1 - \Omega_2) &= 2|\widehat{I}(\Omega_1 - \Omega_2)|^2 Z_{out} = \\
&= 2I_{dc}^2 Z_{out} (1 - K_1) \alpha_U \left( \frac{\phi_{RF}}{4} \right)^4 \left( \frac{\sqrt{(1 - K_1) \alpha_U (2K_2 - 1) A'_{\Omega_1 - \Omega_2}} + j2\sqrt{K_1 K_2 (1 - K_2) \alpha_L A'^{I,B}_{\Omega_1 - \Omega_2}}}{j2\sqrt{K_1 K_2 (1 - K_2) \alpha_L A'^{I,B}_{\Omega_1 - \Omega_2}}} \right)^2,
\end{aligned} \tag{A.20}$$

$$\begin{aligned}
P_{RF}(2\Omega_1 - \Omega_2) &= 2|\widehat{I}(2\Omega_1 - \Omega_2)|^2 Z_{out} = \\
&= 2I_{dc}^2 Z_{out} (1 - K_1) \alpha_U \left( \frac{\phi_{RF}}{4} \right)^6 \sin^2(\phi_{dc}) \left( \frac{j(2K_2 - 1)\sqrt{(1 - K_1) \alpha_U A'_{2\Omega_1 - \Omega_2}} + j2\sqrt{K_1 K_2 (1 - K_2) \alpha_L A'^{I,B}_{2\Omega_1 - \Omega_2}}}{2\sqrt{K_1 K_2 (1 - K_2) \alpha_L A'^{I,B}_{2\Omega_1 - \Omega_2}}} \right)^2.
\end{aligned}$$

Equating them to the fundamental RF power given by Eq. (A.14) we can obtain the OIP for each distortion term by:

$$\begin{aligned}
OIP_2 &= 2 \left( I_{dc} \sin^2(\phi_{DC}) \frac{D}{X} \right)^2 Z_{out} \frac{|jDA'_{\Omega_1} + CA'^{I,B}_{\Omega_1}|^4}{|jDA'_{\Omega_1 - \Omega_2} + CA'^{I,B}_{\Omega_1 - \Omega_2}|^2}, \\
OIP_3 &= 2 \left( I_{dc} \sin(\phi_{DC}) \frac{D}{X} \right)^2 Z_{out} \frac{|jDA'_{\Omega_1} + CA'^{I,B}_{\Omega_1}|^3}{|jDA'_{2\Omega_1 - \Omega_2} - CA'^{I,B}_{2\Omega_1 - \Omega_2}|}.
\end{aligned} \tag{A.21}$$

### A.3 Detailed derivation of photocurrents and the End-to-End figures of Merit including the RF stage

The input current from the optical part of the MWP system referred to Point (2) in Figure 3.14 is defined by  $i(t)$ .

$$\begin{aligned}
i(t) &= i_1 \sin(\Omega_1 t + \theta_1) + i_2 \sin(\Omega_2 t + \theta_2) + i_{11} \sin(2\Omega_1 t + \theta_{11}) + i_{22} \sin(2\Omega_2 t + \theta_{22}) + \\
& i_2 \sin[(\Omega_1 - \Omega_2)t + \theta_{12}] + i_{21} \sin[(\Omega_2 - \Omega_1)t + \theta_{21}] + i_{\alpha\alpha} \sin[(\Omega_1 + \Omega_2)t + \theta_{\alpha\alpha}] + \\
& i_{112} \sin[(2\Omega_1 - \Omega_2)t + \theta_{112}] + i_{221} \sin[(2\Omega_2 - \Omega_1)t + \theta_{221}],
\end{aligned} \tag{A.22}$$

It has been conveniently derived in the previous subsections for *direct IM/PM* and *self-beating intensity modulation* for *single/balanced* detection schemes.

This current enters the RF amplifier of gain  $a$  that is characterized by a nonlinear characteristic defined by the nonlinear term  $b$ . The output current is:

$$y(t) = ai(t) + bi^2(t) + \dots \quad (\text{A.23})$$

The output current can be grouped into several terms, of which we will only consider those corresponding to the signal, the second and third order intermodulation:

$$\begin{aligned}
 y_{\Omega_1}(t) &= ai_1 \sin(\Omega_1 t + \theta_1) + bi_1 i_{11} \cos(\Omega_1 t + \theta_{11} - \theta_1) - bi_2 i_{12} \cos(\Omega_1 t + \theta_2 + \theta_{12}), \\
 &\quad + bi_2 i_{21} \cos(\Omega_1 t + \theta_2 - \theta_{21}) + bi_2 i_{xx} \cos(\Omega_1 t + \theta_{xx} - \theta_2), \\
 y_{\Omega_2}(t) &= ai_2 \sin(\Omega_2 t + \theta_2) + bi_1 i_{12} \cos(\Omega_2 t + \theta_1 - \theta_{12}) - \\
 &\quad bi_1 i_{21} \cos(\Omega_2 t + \theta_1 + \theta_{21}) + bi_2 i_{22} \cos(\Omega_2 t + \theta_{22} - \theta_2) + \\
 &\quad + bi_1 i_{xx} \cos(\Omega_2 t + \theta_{xx} - \theta_1), \\
 y_{\Omega_1 - \Omega_2}(t) &= ai_{12} \sin((\Omega_1 - \Omega_2)t + \theta_{12}) + bi_1 i_2 \cos((\Omega_1 - \Omega_2)t + \theta_1 - \theta_2) + \\
 &\quad bi_{11} i_{xx} \cos((\Omega_1 - \Omega_2)t + \theta_{11} - \theta_{xx}), \\
 y_{\Omega_2 - \Omega_1}(t) &= ai_{21} \sin((\Omega_2 - \Omega_1)t + \theta_{21}) + bi_{22} i_{xx} \cos((\Omega_2 - \Omega_1)t + \theta_{22} - \theta_{xx}), \\
 y_{\Omega_1 + \Omega_2}(t) &= ai_{xx} \sin((\Omega_1 + \Omega_2)t + \theta_{xx}) - bi_1 i_2 \cos((\Omega_1 + \Omega_2)t + \theta_1 + \theta_2) + \\
 &\quad bi_{11} i_{12} \cos((\Omega_1 + \Omega_2)t + \theta_{11} - \theta_{12}) - bi_{11} i_{21} \cos((\Omega_1 + \Omega_2)t + \theta_{11} + \theta_{21}) \\
 &\quad - bi_{22} i_{12} \cos((\Omega_1 + \Omega_2)t + \theta_{22} + \theta_{12}) + bi_{22} i_{21} \cos((\Omega_1 + \Omega_2)t + \theta_{22} - \theta_{21}), \\
 y_{2\Omega_1 - \Omega_2}(t) &= ai_{112} \sin((2\Omega_1 - \Omega_2)t + \theta_{112}) - bi_1 i_{12} \cos((2\Omega_1 - \Omega_2)t + \theta_1 + \theta_{12}) \\
 &\quad + bi_1 i_{21} \cos((2\Omega_1 - \Omega_2)t + \theta_1 - \theta_{21}) + bi_2 i_{11} \cos((2\Omega_1 - \Omega_2)t + \theta_{11} - \theta_2), \\
 y_{2\Omega_2 - \Omega_1}(t) &= ai_{221} \sin((2\Omega_2 - \Omega_1)t + \theta_{221}) + bi_1 i_{22} \cos((2\Omega_2 - \Omega_1)t + \theta_{22} - \theta_1) \\
 &\quad - bi_2 i_{21} \cos((2\Omega_2 - \Omega_1)t + \theta_2 + \theta_{21}) + bi_2 i_{12} \cos((2\Omega_2 - \Omega_1)t + \theta_2 - \theta_{12}).
 \end{aligned} \quad (\text{A.24})$$

### Output RF Power

The output RF power over one load impedance  $R_{LOAD}$  placed after the RF filter can be computed as:

$$P_{RF} = \left\langle \left( \bar{y}_{\Omega_1}(t) + \bar{y}_{\Omega_2}(t) + \bar{y}_{\Omega_1 - \Omega_2}(t) + \bar{y}_{\Omega_2 - \Omega_1}(t) + \bar{y}_{2\Omega_1 - \Omega_2}(t) + \hat{y}_{2\Omega_2 - \Omega_1}(t) + \dots \right)^2 \right\rangle R_{LOAD}, \quad (\text{A.25})$$

where  $\bar{y}$  is the signal at the RF filter ( $H_e(\Omega)$ ) output for each frequency contribution considered in time domain. We perform a time average over  $T$ . It has to be enough large to cancel the cross-product terms once averaged.

$$\langle y \rangle = \frac{1}{T} \int_0^T y(t) dT, \quad (\text{A.26})$$

$$\begin{aligned} P_{RF} = & \left\langle \left( \bar{y}_{\Omega_1}(t) \right)^2 \right\rangle R_{LOAD} + \left\langle \left( \bar{y}_{\Omega_2}(t) \right)^2 \right\rangle R_{LOAD} + \dots \\ & \dots + \left\langle \left( \bar{y}_{2\Omega_1 - \Omega_2}(t) \right)^2 \right\rangle R_{LOAD} + \left\langle \left( \bar{y}_{2\Omega_2 - \Omega_1}(t) \right)^2 \right\rangle R_{LOAD} + \dots \end{aligned} \quad (\text{A.27})$$

Furthermore, for each of the above terms, there are contributions with different phases so a second average over the phases has to be performed, which eliminates the contribution of cross products if phases are assumed to be uniformly distributed in the  $[0, 2\pi]$  range. Hence, each RF power contribution is given by:

$$\begin{aligned} P_{RF}(\Omega_1) &= \left\langle \left( \bar{y}_{\Omega_1}(t) \right)^2 \right\rangle R_{LOAD} = \\ &= \left\{ \frac{a^2 i_1^2 + b^2 \left[ i_1^2 i_{11}^2 + i_2^2 i_{12}^2 + i_2^2 i_{21}^2 + i_2^2 i_{xx}^2 \right]}{2} \right\} |H_e(\Omega_1)|^2 R_{LOAD} \\ &\approx \frac{a^2 i_1^2 |H_e(\Omega_1)|^2 R_{LOAD}}{2}, \end{aligned} \quad (\text{A.28})$$

$$\begin{aligned} P_{RF}(\Omega_2) &= \left\langle \left( \bar{y}_{\Omega_2}(t) \right)^2 \right\rangle R_{LOAD} = \\ &= \left\{ \frac{a^2 i_2^2 + b^2 \left[ i_2^2 i_{22}^2 + i_1^2 i_{12}^2 + i_1^2 i_{21}^2 + i_1^2 i_{xx}^2 \right]}{2} \right\} |H_e(\Omega_2)|^2 R_{LOAD} \\ &\approx \frac{a^2 i_2^2 |H_e(\Omega_2)|^2 R_{LOAD}}{2}, \end{aligned} \quad (\text{A.29})$$

$$\begin{aligned}
 P_{RF}(\Omega_1 - \Omega_2) &= \left\langle \left( \bar{y}_{\Omega_1 - \Omega_2}(t) \right)^2 \right\rangle R_{LOAD} = \\
 &= \left\{ \frac{a^2 i_{12}^2 + b^2 \left[ i_1^2 i_2^2 + i_1^2 i_{xx}^2 \right]}{2} \right\} |H_e(\Omega_1 - \Omega_2)|^2 R_{LOAD}, \tag{A.30}
 \end{aligned}$$

$$\begin{aligned}
 P_{RF}(\Omega_2 - \Omega_1) &= \left\langle \left( \bar{y}_{\Omega_2 - \Omega_1}(t) \right)^2 \right\rangle R_{LOAD} = \\
 &= \left\{ \frac{a^2 i_{21}^2 + b^2 \left[ i_1^2 i_{xx}^2 \right]}{2} \right\} |H_e(\Omega_2 - \Omega_1)|^2 R_{LOAD}, \tag{A.31}
 \end{aligned}$$

$$\begin{aligned}
 P_{RF}(2\Omega_1 - \Omega_2) &= \left\langle \left( \bar{y}_{2\Omega_1 - \Omega_2}(t) \right)^2 \right\rangle R_{LOAD} = \\
 &= \left\{ \frac{a^2 i_{12}^2 + b^2 \left[ i_1^2 i_2^2 + i_1^2 i_{21}^2 + i_2^2 i_{11}^2 \right]}{2} \right\} |H_e(2\Omega_1 - \Omega_2)|^2 R_{LOAD}, \tag{A.32}
 \end{aligned}$$

$$\begin{aligned}
 P_{RF}(2\Omega_2 - \Omega_1) &= \left\langle \left( \bar{y}_{2\Omega_2 - \Omega_1}(t) \right)^2 \right\rangle R_{LOAD} = \\
 &= \left\{ \frac{a^2 i_{22}^2 + b^2 \left[ i_1^2 i_{22}^2 + i_2^2 i_{21}^2 + i_2^2 i_{12}^2 \right]}{2} \right\} |H_e(2\Omega_2 - \Omega_1)|^2 R_{LOAD}. \tag{A.33}
 \end{aligned}$$

*Overall figures of merit*

### RF Gain

$$\begin{aligned}
 G_{RF}(\Omega_1) &= \frac{P_{RF}(\Omega_1)}{P_{RFin}(\Omega_1)} = \frac{a^2 i_1^2 |H_e(\Omega_1)|^2 R_{LOAD}}{2P_{RFin}(\Omega_1)} = \\
 &= \left( \frac{i_1^2 R_{LOAD}}{2P_{RFin}(\Omega_1)} \right) a^2 |H_e(\Omega_1)|^2 = a^2 G_{RF}^{MWP}(\Omega_1) |H_e(\Omega_1)|^2. \tag{A.34}
 \end{aligned}$$

That is, irrespective of the configuration of the MWP segment, the overall gain is the product of the RF gain of the MWP segment multiplied by the squared (power) gain of the RF amplifier and the squared modulus of the RF optical filter.

In logarithmic we have:

$$G_{RF}(\Omega_1)(dB) = G_{RF}^{MWP}(\Omega_1)(dB) + 20 \log a + 20 \log |H_e(\Omega_1)|. \tag{A.35}$$

### Noise Figure

The noise figure is defined as the signal to noise ratio difference at the input and output of the system. In our case, it is computed as:

$$NF = \frac{\left(\frac{S}{N}\right)_{in}}{\left(\frac{S}{N}\right)_{out}} = \frac{\left(\frac{S}{N}\right)_{in}}{\left(\frac{S}{N}\right)_{in,MWP}} \frac{\left(\frac{S}{N}\right)_{in,MWP}}{\left(\frac{S}{N}\right)_{out,MWP}} \frac{\left(\frac{S}{N}\right)_{out,MWP}}{\left(\frac{S}{N}\right)_{out}}. \quad (\text{A.36})$$

We will assume that the first segment, connecting the RF input to the external modulator is not noisy, hence:

$$NF = \frac{\left(\frac{S}{N}\right)_{in}}{\left(\frac{S}{N}\right)_{out}} = NF_{MWP} \cdot NF_{RF}, \quad (\text{A.37})$$

where:

$$NF_{MWP} = \frac{\left(\frac{S}{N}\right)_{in,MWP}}{\left(\frac{S}{N}\right)_{out,MWP}} \quad (\text{A.38})$$

defines the noise figure of the MWP segment and:

$$NF_{RF} = \frac{\left(\frac{S}{N}\right)_{out,MWP}}{\left(\frac{S}{N}\right)_{out}} \quad (\text{A.39})$$

is the noise figure of the RF stage placed after the MWP segment.

### Dynamic Range:

As described in Chapter 3, the dynamic range is defined as

$$SFDR_2 = \left[ \frac{OIP_2}{N_{\text{output Total}}} \right]^{\frac{1}{2}}, \quad SFDR_3 = \left[ \frac{OIP_3}{N_{\text{output Total}}} \right]^{\frac{2}{3}}, \quad (\text{A.40})$$

First, we compute the total output spectral density  $N_{tot}$ . Since:

$$NF = \frac{N_{tot}}{G_{RF}^2 N_{in}} \Rightarrow N_{tot} = NF \cdot G_{RF} N_{in} = NF_{RF} NF_{MWP} a^2 G_{RF}^{MWP} (\Omega_1) |H_e(\Omega_1)|^2 N_{in}, \quad (\text{A.41})$$

and:

$$N_{tot, MWP} = NF_{MWP} G_{RF}^{MWP} (\Omega_1) N_{in}. \quad (\text{A.42})$$

Then:

$$N_{tot} = NF_{RF} N_{tot, MWP} a^2 |H_e(\Omega_1)|^2. \quad (\text{A.43})$$

$OIP_2$  and  $OIP_3$  are the second and third-order optical interception points respectively and are defined as the linearly extrapolated input powers at which the fundamental (Eq. (A.28)) and their respective intermodulation terms  $-IMD_2$  (Eq. (A.30)) and  $IMD_3$  (Eq. (A.32))- output powers are equal. A lengthy but straightforward process renders the expression for the second order spurious free dynamic range specified here in linear units:

$$SFDR_2^{Mod} = \frac{SFDR_{2, MWP}^{Mod}}{\sqrt{NF_{RF} (1 + T_{2Mod})}} \left[ \frac{|H_e(\Omega_1)|}{|H_e(\Omega_1 - \Omega_2)|} \right],$$

$$T_{2X} = \varepsilon_{Mod} \left( \frac{b}{a} \right)^2 \frac{|A_{\Omega_1}^{Mod}|^2 |A_{\Omega_2}^{Mod}|^2}{|A_{\Omega_1 - \Omega_2}^{Mod}|^2} = \frac{P_{IMD2, RF}}{P_{IMD2, MWP}} \quad (\text{A.44})$$

$$\begin{cases} \varepsilon_I = 4I_{dc}^2 \sin^4(\phi_{dc}) \\ \varepsilon_{\Phi} = 16I_{dc}^2 \\ \varepsilon_{I, SB} = 4I_{dc}^2 \sin^4(\phi_{dc}) \alpha_U \alpha_L C^2 D^2 \end{cases}$$

$$SFDR_3^{Mod} = \frac{SFDR_{3,MWP}^{Mod}}{\sqrt[3]{NF_{RF}^2 (1 + T_{3Mod})}} \left[ \frac{|H_e(\Omega_1)|}{|H_e(2\Omega_1 - \Omega_2)|} \right]^{2/3}.$$

$$T_{3X} = \varepsilon_{Mod} \left( \frac{b}{a} \right)^2 \frac{\left[ |A_{\Omega_1}^{Mod}|^2 |A_{\Omega_1 - \Omega_2}^{Mod}|^2 + |A_{\Omega_1}^{Mod}|^2 |A_{\Omega_2 - \Omega_1}^{Mod}|^2 + |A_{2\Omega_1}^{Mod}|^2 |A_{\Omega_2}^{Mod}|^2 \right]}{|A_{2\Omega_1 - \Omega_2}^{Mod}|^2} = \frac{P_{IMD3,RF}}{P_{IMD3,MWP}} \quad (A.45)$$

$$\begin{cases} \varepsilon_I = 4I_{dc}^2 \\ \varepsilon_{\Phi} = 16I_{dc}^2 \\ \varepsilon_{I,SB} = 4I_{dc}^2 \alpha_U \alpha_L C^2 D^2 \end{cases}$$

For the last case of self-beating modulation scheme, we have assumed that the self-beating term was dominant.

#### A.4 Derivation of the linearization process employing a Dual Parallel MZM (DPMZM).

By developing the same analytical procedure used in Appendix A.2 and [81], but including the DPMZM, the fundamental tone phasor  $C$  at the frequency  $\Omega_1$  is given by the photocurrent beating term  $\hat{I}_b(\Omega_1)$ :

$$C(\Omega_1) = \hat{I}_b(\Omega_1) = -I_{dc} \sqrt{\alpha_U \alpha_L} CD \left( \frac{\phi_{RF1}}{4} \right) \left[ \frac{\sqrt{(1-a)(1-b)} \sin(\phi_{DC1}) A_{1,\Omega_1}^{I,B}}{\gamma \sqrt{ab} \sin(\phi_{DC2}) A_{2,\Omega_1}^{I,B}} + \right], \quad (A.46)$$

where

$$A_{i,\Omega_1}^{I,B} = \cos \varphi \frac{\left[ H_i(\omega_o + \Omega_1) - H_i^*(\omega_o - \Omega_1) \right]}{\sin\left(\frac{\phi_{DCi}}{2}\right)}, \quad (A.47)$$

$$H_i(\omega) = H(\omega) e^{j\nu_i}.$$

The second-order intermodulation component  $IMD_2$  at frequency  $(\Omega_1 - \Omega_2)$  is given by the photocurrent beating term  $\hat{I}_b(\Omega_1 - \Omega_2)$ :

$$\begin{aligned}
IMD_2(\Omega_1 - \Omega_2) &= \widehat{I}_b(\Omega_1 - \Omega_2) = \\
&= -jI_{dc} \sqrt{\alpha_U \alpha_L} CD \left( \frac{\phi_{RF}}{4} \right)^2 \left[ \sqrt{(1-a)(1-b)} A_{1,\Omega_1-\Omega_2}^{I,B} + \right. \\
&\quad \left. \gamma^2 \sqrt{ab} A_{2,\Omega_1-\Omega_2}^{I,B} \right].
\end{aligned} \tag{A.48}$$

Finally, the third-order intermodulation component  $IMD_3$  at frequency  $(2\Omega_1 - \Omega_2)$  is given by the photocurrent associated to the beating term  $\widehat{I}_b(2W_1 - W_2)$ :

$$\begin{aligned}
IMD_3(2\Omega_1 - \Omega_2) &= \widehat{I}_b(2\Omega_1 - \Omega_2) = \\
&= -I_{dc} CD \sqrt{\alpha_U \alpha_L} \left( \frac{\phi_{RF}}{4} \right)^3 \left[ \sin(\phi_{dc1}) \sqrt{(1-a)(1-b)} A_{1,2\Omega_1-\Omega_2}^{I,B} \right. \\
&\quad \left. + \gamma^3 \sin(\phi_{dc2}) \sqrt{ab} A_{2,2\Omega_1-\Omega_2}^{I,B} \right],
\end{aligned} \tag{A.49}$$

For the linearization process described in Chapter 3, we employ a Lagrangian equation. We aim to maximize Eq. (3.41) subject to the condition given by Eq. (3.40). The Lagrangian is thus given by:

$$L(a, b) = \sqrt{(1-a)(1-b)} - \gamma \sqrt{ab} + \lambda \left[ \sqrt{(1-a)(1-b)} - \gamma^3 \sqrt{ab} \right], \tag{A.50}$$

where  $\lambda$  is the Lagrange multiplier. We now compute:

$$\begin{aligned}
\frac{\partial L}{\partial a} &= -\frac{\sqrt{(1-b)}}{2\sqrt{(1-a)}} + \frac{\gamma\sqrt{b}}{2\sqrt{a}} + \lambda \left[ \frac{\sqrt{(1-b)}}{2\sqrt{(1-a)}} + \frac{\gamma^3\sqrt{b}}{2\sqrt{a}} \right] = 0, \\
\frac{\partial L}{\partial b} &= -\frac{\sqrt{(1-a)}}{2\sqrt{(1-b)}} + \frac{\gamma\sqrt{a}}{2\sqrt{b}} + \lambda \left[ \frac{\sqrt{(1-a)}}{2\sqrt{(1-b)}} + \frac{\gamma^3\sqrt{a}}{2\sqrt{b}} \right] = 0, \\
\frac{\partial L}{\partial \lambda} &= \sqrt{(1-a)(1-b)} - \gamma^3 \sqrt{ab} = 0.
\end{aligned} \tag{A.51}$$

The first equality in Eq. (A.51) leads to:

$$\frac{\partial L}{\partial a} = 0 \Rightarrow \lambda = \frac{-\sqrt{a(1-b)} + \gamma\sqrt{(1-a)b}}{\sqrt{a(1-b)} - \gamma^3\sqrt{(1-a)b}}. \tag{A.52}$$

The second equality in Eq. (A.51), taking into consideration Eq. (A.50), leads to:

$$\frac{\partial L}{\partial b} = 0 \Rightarrow \frac{1-a}{a} = \frac{1-b}{b} \Rightarrow a = b. \tag{A.53}$$



Finally, the third equality in Eq. (A.51) yields:

$$\frac{\partial L}{\partial \lambda} = 0 \Rightarrow (1-a) - \gamma^3 a = 0 \Rightarrow a = b = \frac{1}{1+\gamma^3}. \quad (\text{A.54})$$



---

## Appendix B

# Reconfigurable optical core algorithms

In Chapter 4, we have proposed different implementations of photonic integrated circuits programed over the hexagonal waveguide mesh. This mesh is based on the interconnection of MZI-type beamsplitters defined by its ideal transfer matrix:

$$h_{TBU} = je^{j\Delta} \begin{pmatrix} \sin \theta & \cos \theta \\ \cos \theta & -\sin \theta \end{pmatrix}. \quad (\text{B.1})$$

where  $\theta$  is  $(\phi_{upper} - \phi_{lower})/2$  and  $\Delta$  is  $(\phi_{upper} + \phi_{lower})/2$ .

By means of external electronic control signals applied to the heaters deposited on top of each MZI arm, each TBU can be configured to provide independent power splitting ratio and overall phase shift. This ability enables the operation as a directional coupler or simply as an optical switch/DDL in a cross or bar. Using this principle, this waveguide mesh architecture can be reconfigured to support different connection paths between its input and output ports and, hence, any kind of linear transformation, much in the same way as a FPGA operates in electronics.

### B.1 Universal Coupler (Triangular and Rectangular)

#### TRIANGULAR ARRANGEMENT IMPLEMENTATION

Here, we describe the transformation of the algorithm for the triangular beamsplitter arrangement proposed by Miller [27], for the synthesis of universal linear interferometers in the hexagonal waveguide mesh.

First of all, we need to consider the possible different phase contributions due to the different access paths established between the interferometer inputs and the internal processing elements forming the triangular arrangement of beam splitters and, from these, to the different outputs. These different phase contributions must be compensated.

Secondly, we need to establish an equivalent configuration to the phase shifted MZI employed by Miller as shown in Chapter 4. In our case, the equivalent “beamsplitter” is implemented using a TBU for the tunable coupler (with a transfer matrix defined by  $h_{TC}$  as in (B.1)), followed by two TBUs, which are biased in cross state and employed as output connections. In the latter, the upper TBU also implements a phase shifter and is defined by the transfer matrix  $h_{UPS}$ . The lower TBU is defined by the transfer matrix  $h_{LPS}$ .

The function of a linear optics device is to transform a series of  $N$  orthogonal modes ( $|\phi_I\rangle$ ) into the corresponding  $N$  orthogonal modes at the output ( $|\phi_O\rangle$ ) [26]. This transformation is defined by a unitary matrix  $U$  ( $|\phi_O\rangle = U|\phi_I\rangle$ ).

Miller's synthesis algorithm is based on writing any of the input basis functions as a linear combination of each input port or rectangular functions ( $|\phi_{In}\rangle$ ), and configuring sequentially each row of beam couplers for each input mode. These input modes are obtained from the columns of the Hermitian Adjoint of the matrix  $U$ .

We consider, first of all, the impact of the access paths by multiplying the first input mode by a diagonal matrix  $C^{(0)}$  accounting for each input access path:

$$|\phi_{DI1}^{(I)}\rangle = C^{(0)}|\phi_I\rangle. \quad (\text{B.2})$$

where  $|\phi_{DI1}^{(I)}\rangle$  is the first input mode, modified by each access path, that arrives to the first row of beamsplitters.

The element  $C^{(0)}_{nm}$  in  $C^{(0)}$  represents the coefficient for the  $n$ -input access path. Similarly, a  $C^{(OutPath)}$  matrix is required to account for the output paths set after the processing elements. The path responses ( $C^{(0)}_{nm}$ ,  $C^{(OutPath)}_{nm}$ ) can be computed by multiplying the proper TBU matrix element (Eq. (B.1)) for each of the TBUs that build up the path. Both access paths elements can be identified in Fig. B.1.

Now, we express  $|\phi_{DI1}^{(I)}\rangle$  as a linear combination of each input port of the triangular arrangement of beam splitters ( $|\phi_{In}\rangle$ ).

$$|\phi_{D11}^{(1)}\rangle = \sum_{n=1}^M a_{1n} |\phi_{1n}\rangle, \quad (\text{B.3})$$

where  $a_{1n}$  are the linear coefficients that represent the field (amplitude and phase) in the input waveguides of the first row of beamsplitters.

The algorithm starts configuring the first row of beam couplers, illustrated in Figure 4.21(a), for the first mode. Taking into account Eqs. (B.2) – (B.3) and the definitions of the overall transfer matrices for the equivalent TBUs (Figure 4.21(d)), we get:

$$a_{11}^* = h_{TC11\_11} \cdot h_{UPS11\_21} \cdot c_{11}^{(OutPath)}. \quad (\text{B.4})$$

The algorithm first computes the modulus of  $h_{TC11\_11}$  satisfying Eq. (B.4). Note that the notation here is  $h_{ELEMENTqn\_xy}$ , where  $n$  represents the row in the beam splitter arrangement and  $q$  the beam coupler order inside a given row;  $x$  and  $y$  indicate the output and input ports of the beam splitter, respectively. Note that the modulus of the TBUs implementing phase shifters, interconnections and access paths will be 1. The phase shift of  $h_{UPS}$  is adjusted to equalize the overall phase in the left and right hand-side members of Eq. (B.4).

Once  $|h_{TC11\_11}|$  and the phase shift of  $h_{UPS}$  are obtained, an iterative process will render the remaining  $|h_{TC}|$  values and the  $h_{UPS}$  phases for the remaining beam splitters in the row:

$$\begin{aligned} |h_{TC1n\_11}| \cdot e^{i\angle(h_{UPS1n\_21})} &= \\ &= \frac{a_{1n}^*}{c_{11}^{(OutPath)} \prod_{q=1}^{n-1} |h_{TC1q\_12}|} e^{-i\left(\angle(h_{TC1n\_11}) + \sum_{n=1}^{n-1} \angle(h_{TC1q\_12}) + \sum_{n=1}^{n-1} \angle(h_{UPS1n\_21})\right)}. \end{aligned} \quad (\text{B.5})$$

In a similar way to the Miller's algorithm, the subsequent input modes will be affected by the previously configured rows of beam splitters. To take this fact into account, the mode has to be multiplied by the corresponding transfer function. In this case, it is defined by a triangular  $C^{(n)}$  matrix where the diagonal elements are:

$$c_{ss}^{(n)} = h_{TCns\_21} \cdot h_{LPSns\_12}, \quad (\text{B.6})$$

and the upper-triangular matrix terms are:

$$c_{sj}^{(n)} = h_{TCnj\_11} \cdot h_{TCns\_22} \cdot \prod_{p=s+1}^{j-1} (h_{TCnp\_12}) \cdot h_{LPSns\_12} \cdot \prod_{p=s+1}^j (h_{UPSnp\_21}). \quad (\text{B.7})$$

The rest of the terms of  $C^{(n)}$  are 0. For the input mode  $n$ , the C matrix will incorporate  $C^{(k)}$  matrices with ( $k = 1, 2, n-1$ ) computed for previous modes:

$$|\phi_{Din}^{(n)}\rangle = C^{(n-1)} \dots C^{(2)} C^{(1)} C^{(0)} |\phi_{Din}\rangle. \quad (\text{B.8})$$

Some cases of special interest must be programmed apart. When the rectangular mode absolute value is  $|a_{qn}| = 1$ , then all tunable couplers  $|h_{TC\_11}|$  in the following equivalent beam splitters in the row must be set to 0 except the one corresponding to the last equivalent beam splitter that will be set to 1 as well.

When the algorithm has finished, we transform the resulting values of  $|h_{TC\_q,n}|$  and the phases of  $h_{UPS\_qn}$  to the actual phase shifts that have to be programmed for each TBU according to Eq. (B.1):

$$\begin{aligned} \phi_{TCupper} &= 2 \arcsin(|h_{TCqn\_11}|), \\ \phi_{TCslower} &= 0, \\ \phi_{UPSupper} &= \phi_{UPSlower} = \angle h_{UPS} - \frac{\pi}{2}, \\ \phi_{LPSupper} &= \phi_{LPSlower} = 0. \end{aligned} \quad (\text{B.9})$$

The synthesis algorithm described here for the triangular arrangement implementation of the universal multiport interferometer can be summarized by the procedure:

```

1: procedure Programme (U)
2:   for  $n$  from 1 to N do
3:     % compute  $|h_{TC}|(1,n)$ 
4:     % compute  $\angle h_{TC}(1,n)$ 
5:     % compute  $\angle h_{UPS}(1,n)$ 
6:
7:     if (N-I is greater than 0) then
8:       for  $q$  from 2 to N - i + 1 do
9:         if ( $|h_{TC11}|$  is equal to 1) then
10:          %  $|h_{TC11}|(q:N-i,n)=0$ 
11:          %  $|h_{TC11}|(N-i+1,n)=1$ 
12:          break
13:         else

```

---

```

14:          % compute |hTC12|(q-1,n)
15:          % compute |hTC|(q,n)
16:          % compute ∠hTC(q,n)
17:          % compute ∠hUPS(q,n)
18:          %compute C(n)
19:          %C=C(n)...C(2)C(1)C(0)
20:          %compute NextMode = C OriginalMode
21:          % compute Δ,φ,θ

```

In order to test the algorithm we propose several application examples.

Application examples:

We compute here the required values for the coupling constants and phases of the TBUs used in the hexagonal waveguide mesh configuration of a tunable 3 x 3 interferometer based on a triangular arrangement.

The first two examples are the matrices programmed experimentally in Chapter 5:

$$U_{EX1} = \begin{pmatrix} 0 & 0 & 1 \\ 0 & 1 & 0 \\ 1 & 0 & 0 \end{pmatrix}, \quad (\text{B.10})$$

$$U_{EX2} = \begin{pmatrix} 0 & 0 & 1 \\ 1 & 0 & 0 \\ 0 & 1 & 0 \end{pmatrix}. \quad (\text{B.11})$$

They can be employed as switching matrixes between different output and input channel combinations. The resulting values are included in Table B1. The position of each TBU is represented for the third example in Fig. B.1. In this case, it corresponds to a three-way beamsplitter defined by:

$$U_{EX3} = U_{\text{irriter}} = \frac{1}{\sqrt{3}} \begin{pmatrix} 1 & 1 & 1 \\ 1 & e^{i2\pi/3} & e^{i4\pi/3} \\ 1 & e^{i4\pi/3} & e^{i8\pi/3} \end{pmatrix}. \quad (\text{B.12})$$

Finally, we apply the algorithm to a fourth example, the identity matrix:

$$U_{EX4} = \begin{pmatrix} 1 & 0 & 0 \\ 0 & 1 & 0 \\ 0 & 0 & 1 \end{pmatrix}. \quad (\text{B.13})$$

For this last case, we will test by hand that the resulting values satisfy correctly the matrix amplitude and phase response. In this case, we will neglect the phase contributions given by the access channels. We can start with the first input, specified by blue light-path in Fig. B.2. Notice that the figure illustrates a simplified scheme, but one must understand that each beamsplitter corresponds to the combination of three TBUs, as explained in Chapter 4. Since it is an identity matrix, the output obviously must be the channel 1 as well. In addition, as it is specified by the matrix, there must be a fully phase cancellation equal to  $2\pi n$ , where  $n = 0, 1, 2, \dots$ . The first input goes through *M11*, which is composed of two TBUs. The first one, acting as a tunable coupler of value  $K = 0$ , and the second one in cross-state acting as the UPS of value  $K=1$ . The total phase contribution, is:

$$\begin{aligned} & TC_{11\_Inherent\_PS} + TC_{11\_Coupling\_derived\_PS} + \\ & + UPS_{11\_Inherent\_PS} + \phi_{UPS,11} = \frac{\pi}{2} + \frac{\pi}{2} + \frac{\pi}{2} + \frac{\pi}{2} = 0. \end{aligned} \quad (\text{B.14})$$

For the channel 2, the phase contributions are given by:

$$\begin{aligned} & TC_{12\_Inherent\_PS} + TC_{12\_Coupling\_derived\_PS} + \\ & + LPS_{12\_Inherent\_PS} + \phi_{LPS,11} + \\ & TC_{22\_Inherent\_PS} + TC_{22\_Coupling\_derived\_PS} + \\ & + UPS_{22\_Inherent\_PS} + \phi_{UPS,11} + \\ & TC_{21\_Inherent\_PS} + TC_{21\_Coupling\_derived\_PS} + \\ & + UPS_{21\_Inherent\_PS} + \phi_{UPS,21} = \\ & = \frac{\pi}{2} + 0 + \frac{\pi}{2} + 0 + \frac{\pi}{2} + \frac{\pi}{2} + \frac{\pi}{2} + \pi + \frac{\pi}{2} + 0 + \frac{\pi}{2} - \frac{\pi}{2} = 0. \end{aligned} \quad (\text{B.15})$$

Following the same process and the light-path in Fig. B.2, we can see that full phase-cancellation is achieved for the third channel as well.

The resulting values for the four previous examples are included in Table B1. Since every LPS is in cross state and only include their inherent phase shift (defined by (B.1)), they are not contained in the table.



Table B1: Required values for the coupling constants and phases of the MZIs used in the hexagonal waveguide mesh configuration of a tunable 3 x 3 interferometer based on a triangular arrangement.

TBU	(a) EX1		(b) EX2		(a) EX3		(a) EX4	
	$K$	$\phi_{UPS}/\pi$	$K$	$\phi_{UP}/\pi_S$	$K$	$\phi_{UPS}/\pi$	$K$	$\phi_{UPS}/\pi$
$M_{11}$	1	-12	1	-1/2	0.66	-0.696	0	0.5
$M_{12}$	1	-1/2	1	-1/2	0.50	-1.250	1	0
$M_{13}$	0	-1/2	0	-1/2	0	0	0	0
$M_{21}$	1	-1/2	0	-1/2	0.5	0.354	1	-0.5
$M_{22}$	0	-1	0	0	0	-0.815	0	1
$M_{31}$	0	1/2	0	-1/2	0	-0.716	0	0
CS-interconn.	1	0	1	0	1	0	1	0
BS-interconn.	0	-1/4	0	-1/4	0	0	0	$-\pi/4$
Rest	P	0	P	0	P	0	P	0

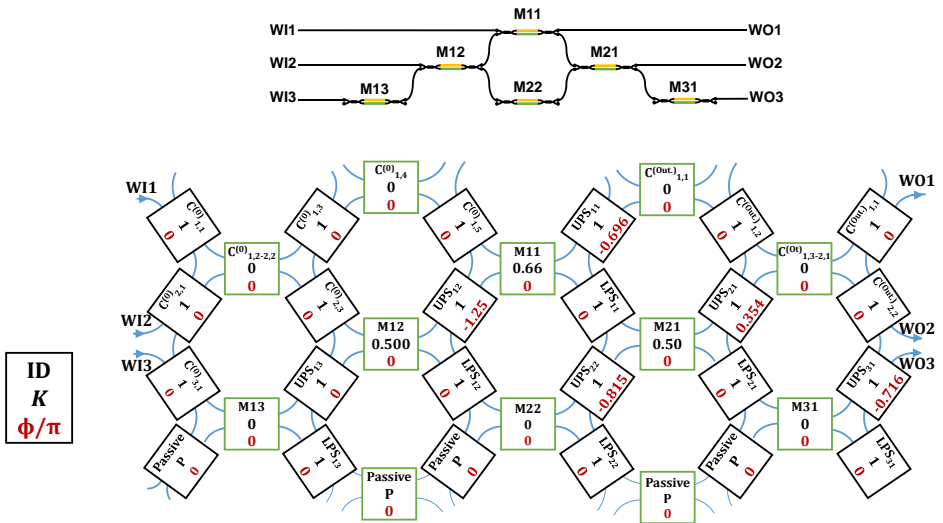


Figure B.1 Layout of the implementation of the three-way beamsplitter using a 3x3 interferometer with triangular beam splitter arrangement (Left), Actual implementation of the 3x3 interferometer using a hexagonal mesh with the labelled configuration for each Tunable Basic Unit (TBU) (right). ID: TBU identification Label,  $K$ : coupling constant,  $\phi$ : additional phase shift, P: coupling constant when both phase shifters are unbiased.

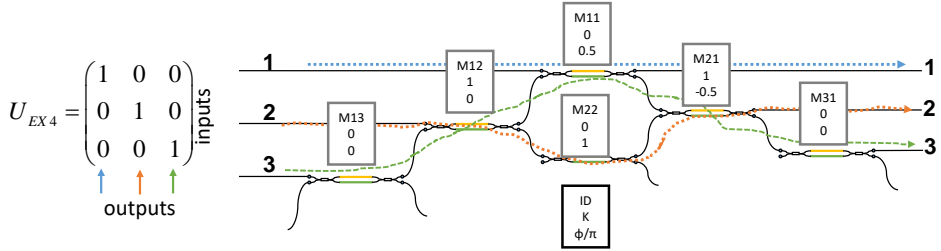


Figure B.2 Scheme of the implementation of the three-way beamsplitter using a  $3 \times 3$  interferometer with triangular beam splitter arrangement for Eq. (B.12). The coefficients are computed for the hexagonal mesh implementation with the labelled configuration for each Tunable Basic Unit (TBU) (right). ID: TBU identification Label, K: coupling constant,  $\phi$ : additional phase shift of the associated UPS, P: coupling constant when both phase shifters are unbiased. The three light path are indicated.

## RECTANGULAR ARRANGEMENT IMPLEMENTATION

To adapt this layout and its synthesis algorithm [88] to the hexagonal waveguide mesh, we need to perform a few modifications. First of all, we must use a different matrix for the beam coupler/ TBU structure. In our case, as we saw in Chapter 4 Figure 4.23(c), we employ a TBU for the tunable coupler (coloured in green), defined by a transfer function  $h_{TC}$ , and the 2 precedent TBUs (coloured in black) for the required connections. Here, the upper one operates in cross mode providing an extra phase shifting (Upper Phase Shifter,  $h_{UPS}$ ), while the lower one operates in cross mode.

Since these 2 TBUs are set in cross state, we can write the transfer matrix of the full beam coupler as:

$$\begin{aligned}
 h_{BC} &= -e^{i\Delta} \begin{pmatrix} e^{i\phi} \sin \theta & \cos \theta \\ e^{i\phi} \cos \theta & -\sin \theta \end{pmatrix} = \\
 &= - \begin{pmatrix} e^{i\phi} r & t \\ e^{i\phi} t & -r \end{pmatrix}.
 \end{aligned} \tag{B.16}$$

The algorithm proceeds by nulling successive matrix elements starting from the targeted unitary ( $N \times N$ ) matrix  $U$ . Depending on the location of the element  $U(n, m)$  to be cancelled, a row or column combination of the matrix is required.

If  $N-n-m$  is odd, then, the element to be nulled requires a combination of columns  $n$  and  $m$ , and the updating process is done by the following transformation

$$U^{Upd} = UT_{n,m}^{-1}. \quad (\text{B.17})$$

While if  $N-n-m$  is even, then, the element to be nulled requires a combination of rows  $n$  and  $m$ , and the updating process is done by the following transformation:

$$U^{Upd} = T_{n,m}U, \quad (\text{B.18})$$

where, for the case of the hexagonal waveguide mesh:

$$T_{m,n} = \begin{pmatrix} 1 & 0 & \dots & \dots & \dots & \dots & \dots & 0 \\ 0 & 1 & & & & & & \\ \cdot & & \cdot & & & & & \\ \cdot & & e^{i\phi}r & t & & & & \\ \cdot & & e^{i\phi}t & -r & & & & \\ \cdot & & & & \cdot & & & \\ \cdot & & & & & & 1 & 0 \\ 0 & \dots & \dots & \dots & \dots & \dots & 0 & 1 \end{pmatrix}. \quad (\text{B.19})$$

By further developing Eqs. (B.17) – (B.18), we can obtain an equation that relates the value of the matrix element  $U(n,m)$  to be nulled with the  $t$  and  $\phi$  values of the corresponding T-matrix. For odd parity ( $N-n-m$ ) (i. e., the matrix  $U(n,m)$  sub-diagonals nulled in the 1st, 3rd, 5th, 7th place, etc.), we have:

$$|t| = \sqrt{\frac{|U(n,m)|^2}{|U(n,m)|^2 + |U(n,m+1)|^2}}, \quad (\text{B.20})$$

$$\phi = \angle U(n,m) - \angle U(n,m+1) - \pi,$$

while for even parity ( $N-n-m$ ) elements (i. e., the matrix  $U(n,m)$  sub-diagonals nulled in the 2nd, 4th, 6th, 8th place, etc.), we have:

$$|t| = \sqrt{\frac{|U(n,m)|^2}{|U(n,m)|^2 + |U(n-1,m)|^2}}, \quad (\text{B.21})$$

$$\phi = \angle U(n,m) - \angle U(n-1,m).$$

To complete the algorithm, we must also consider the special case where the element to be nulled is a priori 0. In this case,  $t$  must be set to 0 to prevent a

mathematical error. When the algorithm has finished, the resulting  $U$  will be a diagonal matrix of unit amplitude (i. e. phase-only) elements. For a given equivalent beam splitter in the hexagonal mesh, the resulting  $t$  and phase shift  $\phi$  values are transformed into the following values for its internal phase shifters:

$$\begin{aligned}
 \phi_{TCupper} &= \theta = \arccos(|t|), \\
 \phi_{TClower} &= -\theta, \\
 \phi_{LPSupper} &= \phi_{LPStlower} = 0, \\
 \phi_{UPSupper} &= \phi_{UPStlower} = \phi, \\
 [\phi_{i01} \dots \phi_{i0N}] &= \text{diag}(U^{\text{lastupdated}}) - \frac{\pi}{2},
 \end{aligned} \tag{B.22}$$

where  $\phi_{ion}$  are the phase shifts on all individual channels at the output of the interferometer that compensate for complex values on the diagonal matrix  $U$  at the last updating step.

Finally, some of the outer TBUs that build up the interferometer must be configured to be phase-transparent featuring the phase-shift values indicated in Fig. B.3 for both possible configurations, labelled as Type A and Type B, respectively.

The synthesis algorithm described here for the rectangular arrangement implementation of the universal multiport interferometer can be summarized by the following procedure:

```

1: procedure Programme (U)
2:   for  $i$  from 1 to  $N-1$  do
3:     if  $i$  is odd then
4:       for  $j = 0$  to  $i-1$  do
5:         if  $U(N-j, i-j)$  is 0 then
6:            $t=0$ ;
7:         else
8:           %null  $U(N-j, i-j)$  by  $T^{1_{i-j}, i-j+1}$ 
9:           %update  $U T^{1_{i-j}, i-j+1}$ 
10:        else
11:          for  $j = 1$  to  $i$  do
12:            if  $U(N+j-j, i-j)$  is 0 then
13:               $t=0$ ;
14:            else
15:              %null  $U(N+j-j, i-j)$  by  $T_{N+j-i-1, N+j-i}$ 
16:              %update  $T_{N+j-i-1, N+j-i} U$ 
17:            % compute  $\Delta, \varphi, \theta$ 

```

Next, we describe several application examples to test the algorithm:

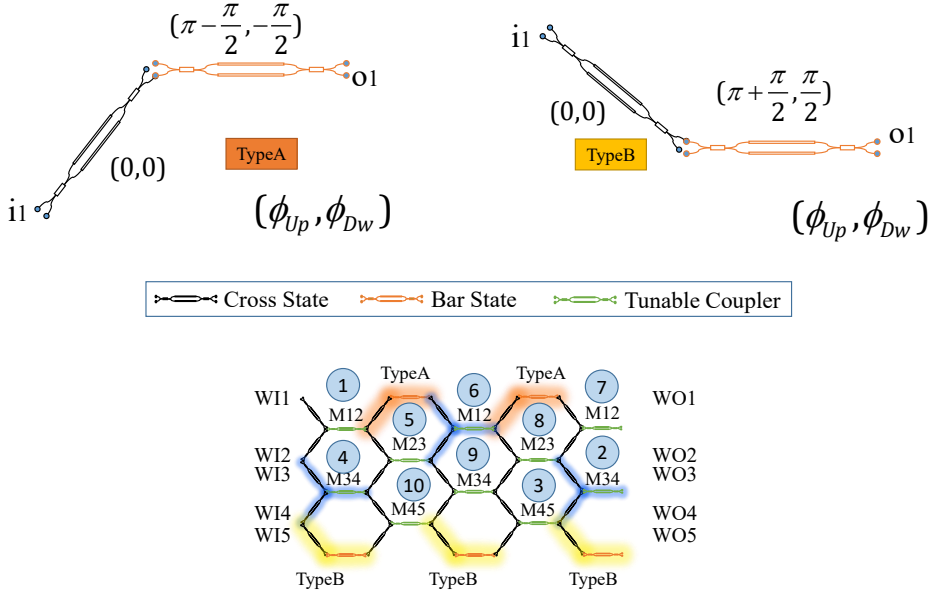


Figure B.3 Rectangular arrangement of a 5 x 5 interferometer showing the outer path configurations (up), and their location within the mesh configuration (bottom). The order of the settings followed by the synthesis algorithm are indicated

Application examples:

Here, we apply the algorithm to several matrices that were experimentally demonstrated in Chapter 5. They are unitary transformations that can potentially be applied in the quantum and information field:

$$U_{P-Z} = \begin{pmatrix} 1 & 0 \\ 0 & -1 \end{pmatrix}, \quad (\text{B.23})$$

$$U_{P-Y} = \begin{pmatrix} 0 & -i \\ i & 0 \end{pmatrix}, \quad (\text{B.24})$$

$$U_{P-X} = \begin{pmatrix} 0 & 1 \\ 1 & 0 \end{pmatrix}, \quad (\text{B.25})$$

$$U_{Id} = \begin{pmatrix} 1 & 0 & 0 & 0 \\ 0 & 1 & 0 & 0 \\ 0 & 0 & 1 & 0 \\ 0 & 0 & 0 & 1 \end{pmatrix}, \quad (\text{B.26})$$

$$U_{CNOT} = \begin{pmatrix} 1 & 0 & 0 & 0 \\ 0 & 1 & 0 & 0 \\ 0 & 0 & 0 & 1 \\ 0 & 0 & 1 & 0 \end{pmatrix}, \quad (\text{B.27})$$

$$U_{SWAP} = \begin{pmatrix} 1 & 0 & 0 & 0 \\ 0 & 0 & 1 & 0 \\ 0 & 1 & 0 & 0 \\ 0 & 0 & 0 & 1 \end{pmatrix}. \quad (\text{B.28})$$

Table B2: Required values for the coupling constants and phases of the MZIs used in the hexagonal waveguide mesh configuration of a  $2 \times 2$  interferometers. P indicates that the TBU remains unbiased.

	(a) P-Z		b1) P-X		b2) P-Y		(c) Had	
TBU	$K$	$\phi/\pi$	$K$	$\phi/\pi$	$K$	$\phi/\pi$	$K$	$\phi/\pi$
M1	0	$-1/2$	1	0	1	0	0.5	$-1/4$
UPS	1	0	1	$-1/2$	1	$-1$	1	0
LPS	1	0	1	0	1	0	1	0
$Io_1$	1	$1/2$	1	0	1	$1/2$	1	$1/2$
$Io_2$	1	$1/2$	1	$-1/2$	1	$-1/2$	1	$1/2$
CS-interconn.	1	0	1	0	1	0	1	0
BS-Type A interconn.	0	$-1/2$	0	$-1/2$	0	$-1/2$	0	$-1/2$
BS-TypeB interconn.	0	$1/2$	0	$1/2$	0	$1/2$	0	$1/2$
Rest	P	0	P	0	P	0	P	0

Table B3: Required values for the coupling constants and phases of the MZIs used in the hexagonal waveguide mesh configuration of a tunable 4 x 4 interferometer based on a rectangular arrangement: P indicates that the TBU remains unbiased.

	Identity		C-NOT		SWAP		Tritter	
	$K$	$\phi/\pi$	$K$	$\phi/\pi$	$K$	$\phi/\pi$	$K$	$\phi/\pi$
TBU								
$M_A$	0	-1/2	0	-1/2	0	-1/2	0.5	0
A-UPS	1	-1	1	-1	1	-1	1	-0.33
$M_B$	0	-1/2	0	-1/2	0	-1/2	0.5	0
B-UPS	1	0	1	0	1	0	1	0.33
$M_C$	0	-1/2	0	-1/2	0	-1/2	0.66	0
C-UPS	1	0	1	0	1	0	1	-1.66
$M_D$	0	-1/2	1	0	0	-1/2	-	-
D-UPS	1	-1	1	-1	1	-1	-	-
$M_E$	0	-1/2	0	-1/2	1	0	-	-
E-UPS	1	0	1	-1	1	0	-	-
$M_F$	0	-1/2	0	-1/2	0	-1/2	-	-
F-UPS	1	-1	1	0	1	-1	-	-
A,B,C,D,E,F-LPS	1	0	1	0	1	0	1	0
$Io_1$	1	-1/2	1	1/2	1	-1/2	1	0
$Io_2$	1	-1/2	1	1/2	1	-1/2	1	-0.16
$Io_3$	1	1/2	1	-1/2	1	-1/2	1	0.16
$Io_4$	1	-1/2	1	-1/2	1	-1/2	-	-
CS-interconn.	1	0	1	0	1	0	1	0
BS-Typ. A interconn.	0	-1/2	0	-1/2	0	-1/2	0	-1/2
BS-Typ. B interconn.	0	1/2	0	1/2	0	1/2	0	1/2
Rest	P	0	P	0	P	0	P	0

## B.2 Pseudo-Codes for FIRs and IIRs

In this subsection, we give examples of several pseudo-codes to programme the reconfigurable optical core. Depending on the software layer properties and capabilities, these examples can be suitably extended and modified.

*FIR 1 stage:*

```

1: procedure placeFIR, (InterLength, PS)
2:   set (TBU_number, TC) % Set input_coupler
3:   for i from 1 to Nshort do
4:     set (TBU_number, DDL) % Set short path
5:     set (TBU_number, TC) % Set output_coupler
6:   for i from 1 to Nshort+ InterLength do
7:     while % closed path between input_coupler and output_coupler
8:       set (TBU_number, DDL) % Set long path
9:   if PS is distinct from 0 then
10:    set (TBU_number, PS) % Set short path/long path phase shift

```

*FIR N stages:*

```

1: procedure placeFIR_N, (InterLength, PS,N)
2:   for i from 1 to N do
3:     placeFIR (InterLength, PS,N) % Set input_coupler
4:     %last_TBU_output_coupler is the next TBU_number (input coupler)

```

*IIR 1 stage:*

```

1: procedure placeIIR, (InterLength, PS)
2:   set (TBU_number, TC) % Set input_coupler
3:   for i from 1 to InterLength-1 do
4:     set (TBU_number, DDL) % Set cavity
5:     set (TBU_number, TC) % Set output_coupler
6:   if PS is distinct from 0 then
7:     set (TBU_number, PS) % Set short path/long path phase shift

```

*IIR N stages (single-bus SCISSOR):*

```

1: procedure placeIIR_N, (InterLength, busLength ,PS,N)
2:   for i from 1 to bus_length do
3:     set (TBU_number, DDL) % Set bus channel
2:   for i from 1 to N do
3:     placeIIR (InterLength, PS,N) % Set input_coupler

```



*IIR N stages (CROW):*

```

1: procedure placeCROW_N, (InterLength, PS, N)
2:   for i from 1 to N do
3:     placeIIR (InterLength, PS, N) % Set input_coupler
4:     %last_TBU_output_coupler is the next TBU_number (input coupler)

```

### **B.3 Pseudo-Code for complete mesh characterization**

As stated in Chapter 4, the first task to be performed before programming the reconfigurable optical core is a TBU characterization. Due to fabrication errors, they might not be in their ideal cross-state when remaining unbiased.

For this reason, a characterization/evaluation task is required. This process needs to sweep the TBU electrical biasing parameter at the time a certain optical power at the input is measured at the output of the TBU, as explained in Chapter 5.

For evaluation/monitoring each TBU, we propose 3 alternatives. The first one requires the integration of at least one photodetector inside the TBU port, as implemented in [59]. The second approach monitors only along the external perimeter of the mesh. Finally, an intermediate solution from the two previous approaches is the incorporation of several checkpoint photodetectors distributed over the mesh.

To start the characterization, first, we need to introduce optical power into one of the inputs of the TBU to be characterized. For this reason, the outer TBUs are firstly considered. Then, we start evaluating the shortest paths between the mesh port illuminated by an optical source and the nearest photodetector. Once done, we continue with the inner TBUs that are accessible by the lowest number of uncharacterized TBUs. Typically this number is from 2 to 3 TBUs and never greater than 4. In this way, it is possible to run an algorithm to sweep each uncharacterized TBU at a time in order to perform the characterization. Although by this method, the uncertainties are minimum, it is advisable to perform various characterizations (different ports of the same TBU) during the characterization round to double-check the measurements.

If a photodetector is embedded into the TBU ports, it results in a more complex reconfigurable optical core, but enables dynamic operation as well as direct and efficient characterization. If external photodetectors are employed, the characterization task might be performed for several iterations to overcome the multiple-path problem. This occurs when the number of TBUs is too high for the

number of photodetectors in the chip. In this case, if the synthesised access path to the targeted TBU is too long, and several TBUs are uncharacterised yet, the signal might distributed to several paths. Thus, the different path alternatives hinder the characterization process. A possible solution is to employ simultaneously the photodetected signal from different points in order to reduce the degrees of freedom of the process. Thus, internal photodetectors inside the mesh are recommended for larger meshes.

Again, depending on the software layer properties and capabilities, these examples can be suitably extended and modified.

```

1: procedure Characterise_Core, (Niter)
2:   for each TBU, for iter = 1...Niter
3:     if nextTBU inside the next shorter path defined by (o.source-a photodetector) then
4:       set [TBU_number,DDL] % Set the access path to the targeted TBU if known
5:       [K]=sweep (TBU_number) % Init evaluation
6:     %repeat and switch to alternative paths for each TBU if it is possible

```

## B.4 Characterization of Photonic Integrated Circuits

The proposed architecture can implement both traditional feedforward/feedbackward Finite (FIR) and Infinite (IIR) impulse response filters as well as universal multiple input/multiple output optical linear transformers. FIR filters are based either on cascades/lattices of 3-dB tunable MZIs or transversal filter configurations. For both FIR filter alternatives, synthesis and recursive scaling algorithms have been developed in the literature [32, 30] that are directly applicable since the hexagonal waveguide mesh can implement both 3-dB tunable MZI cascade lattices and transversal filter configurations. For IIR filters, either simple/compound optical ring cavities of ring-loaded 3-dB tunable MZI cascades are employed. Again, synthesis algorithms have been reported in the literature [32, 31] that are directly applicable since the hexagonal waveguide mesh can implement either simple or multiple cavity ring filters or ring-loaded 3-dB tunable MZI cascades.

We compared each measured case to its well-known analytical transfer function that can be derived following the methods described and obtained an excellent match for both amplitude and phase responses. For example, in the case of the tunable 3-dB MZI structure, the analytical transfer function connecting input port 1 and output port 2 is given by:

$$\begin{aligned}
 h_{21}^{NMZI}(\lambda) = & j\sqrt{(1-\gamma_a)(1-\gamma_b)}e^{-j\beta_d^{(P)}(\lambda)L_d^{(P)}} \\
 & \left[ \sqrt{K_b^{(P)}(\lambda)(1-K_a^{(P)}(\lambda))}e^{-j\Delta\phi_{ud}^{(P)}} + \sqrt{K_a^{(P)}(\lambda)(1-K_b^{(P)}(\lambda))} \right],
 \end{aligned} \tag{B.29}$$

where

$$\begin{aligned} \Delta\phi_{ud} &= \beta_u^{(P)} L_u^{(P)} - \beta_d^{(P)} L_d^{(P)} = \beta_u^{(P)} \cdot (n_u - \Delta\beta_{ud}^{(P)} n_d) \cdot BUL, \\ &(|n_u - n_d| = N). \end{aligned} \quad (\text{B.30})$$

The parameters  $\gamma_{a,b}$  and  $K_{a,b}^{(P)}$  represent the excess losses and coupling factor of the input and output couplers in the MZI structure respectively,  $\beta_{u,d}$  the propagation coefficient of the upper and lower waveguide, and  $L_{u,d}$  the length of the upper and lower paths. In the case of the ring cavity structure, the reflection and transmission transfer functions are given by:

$$\begin{aligned} h_{\text{ref}}^{\text{NORR}}(\lambda) &= \sqrt{(1-\gamma)(1-K^{(P)}(\lambda))} \cdot \\ &\frac{1-(1-\gamma)e^{-j\beta^{(P)}(\lambda)L^{(P)}}}{1-(1-\gamma)(1-K^{(P)}(\lambda))e^{-j\beta^{(P)}(\lambda)L^{(P)}}}, \\ h_{\text{trans}}^{\text{NORR}}(\lambda) &= \frac{-(1-\gamma)K^{(P)}(\lambda)e^{-j\beta^{(P)}(\lambda)L^{(P)}/2}}{1-(1-\gamma)(1-K^{(P)}(\lambda))e^{-j\beta^{(P)}(\lambda)L^{(P)}}}, \end{aligned} \quad (\text{B.31})$$

where,

$$\beta^{(P)} L^{(P)} = \beta^{(P)} \cdot N \cdot BUL. \quad (\text{B.32})$$

The parameters  $\gamma$  and  $K^{(P)}$  represent the excess loss and coupling factor of the ORR coupler, respectively. The superscript  $(P)$  indicates that this parameter can be tuned in the TBU.

Figure B.4 shows, as an example, the results for two different filters, a 4-BUL UMZI and a 6 BUL ring cavity filter. For the UMZI, we configured and simulated  $K_1 = 0.5$ , while  $K_2$  took the values 0.11 (yellow), 0.26 (red) and 0.34 (blue). For the ring cavity, we selected  $K_2 = 0$  while  $K_1$  took the values 0.15 (yellow), 0.50 (red) and 0.65 (blue). Coupler positions can be identified in the experimental demonstrations in Chapter 5.

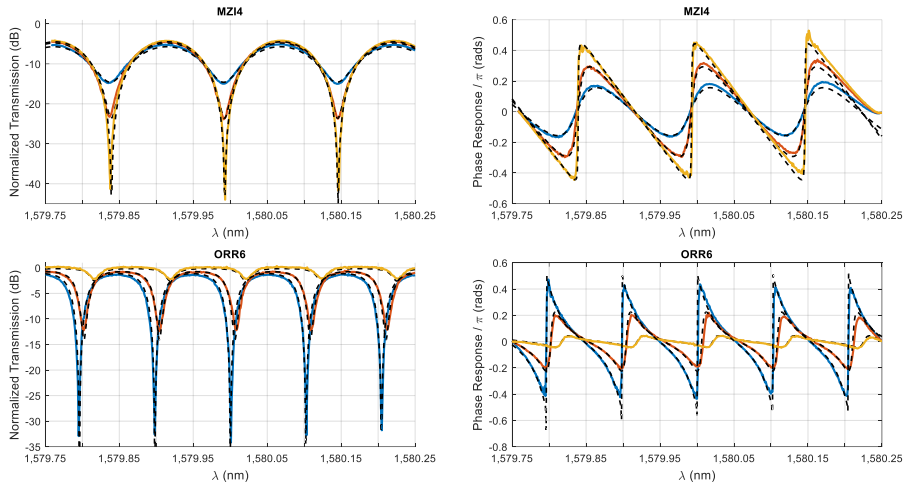


Fig. B.4 Comparison between simulated and measured filters. Up, Power and phase responses of a MZI, Bottom, Power and phase responses of an optical ring resonator. Dashed lines correspond to simulated values whereas solid lines correspond to measured traces.

# Appendix C

## Non-ideal effects in mesh-based circuits

In Chapter 4, we have proposed different implementations of photonic integrated circuits programed over the hexagonal waveguide mesh. This mesh is based on the interconnection of MZI-type beamsplitters. The ideal behaviour of the TBU lead to the perfect performance of the programmable processor. However, in practice, several considerations must be taken into account: imperfect splitting ratios, phase control, parasitic backreflections, loss imbalances, fabrication errors (gradients through the circuit in thickness or temperature), and drift in time.

### C.1 Internal reflections and non-ideal states

One of the drawbacks associated to cascaded circuits are internal back-reflections and signal leakage produced by non-ideal light coupling in bar- or cross-state TBUs. Furthermore, if the tunable-coupler based waveguide mesh allows recirculation of the propagated signals this effect can deteriorate the system's performance by inserting the reflected and leakage signals at different points in the circuit. According to the photonic integrated circuit point of view, this effect would be similar to the addition of interferometric structures through different points in the ideal circuit with reduced coupling coefficients as illustrated in Figure 1 (b).

Figure 1(a) shows the synthesis of a Finite Impulse Response filter representing the light path in black and the signal back-reflections and leakages in red and grey. The signal leakage guided through the non-used TBUs is susceptible of damaging the signal performance. Undesired paths containing reflected/leaked signals will suffer

from more leaking and propagation losses. We can define first grade leakage (FGL) as the aggrupation of reflected and non-ideally coupled signals that go through a number of TBUs lower than 6 before going into the ideal-light path again. They are represented in red.

We can define the second grade leakage (SGL) as the aggrupation of reflected and non-ideally coupled signals that go through a number of TBUs greater than 5 before going into the ideal-light path again. They are represented in grey.

Figure 1(c) represents the ideal response and an estimated total response of a two cascaded UMZIs of differential length equal to 4 BULs, where the non-ideal effects (due to leakage) are identified. Note that the First Grade Leakage effects will add a ripple with a Free Spectral Range larger than the one produced by the Second Grade Leakage. Nevertheless, the effect is expected to be stronger (worse) for the First Grade Leakage since the leakage signal is likely to be greater. Both effects will typically affect inside the FSR of interest.

Zero-Grade Leakage is the one produced inside the TBU. Reflections inside this structure will generate a perturbation with a FSR greater than the frequencies of interest.

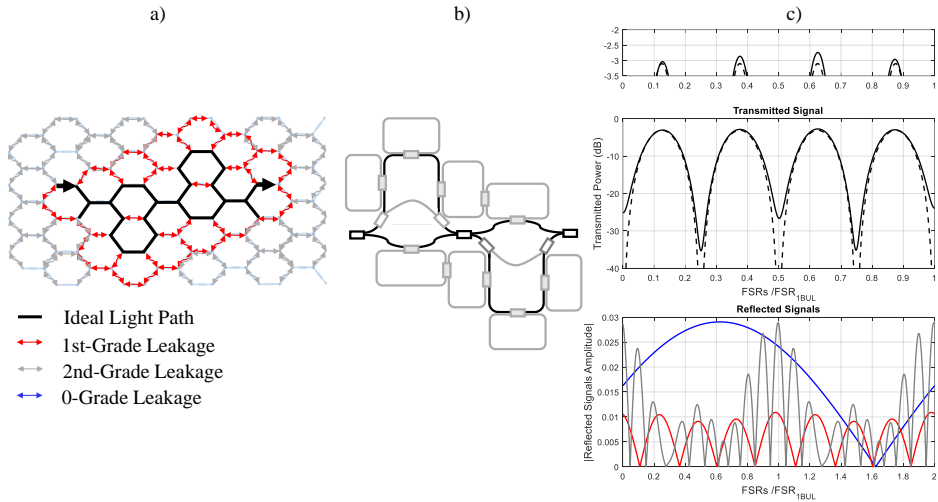


Figure C.1 Layout and mesh-configuration for two cascaded UMZI, (b) Schematic illustrating the associated undesired interferometric structures, (c) Ideal Transmitted responses (dashed-line), total transmitted response (solid-line) and reflected signals example.

For this example, we have simplified the contributions and considered the addition of 3 reflected sinusoidal signals of 0.01 amplitude, and random phase for each defined leakage grade of frequencies defined by differential paths of 1; 2,4;

8,10,12 BULs, respectively. The ideal signal was defined by the response of 2 cascaded MZIs.

The same conditions are applied to a programmed straight waveguide obtaining the results contained in Figure 2.

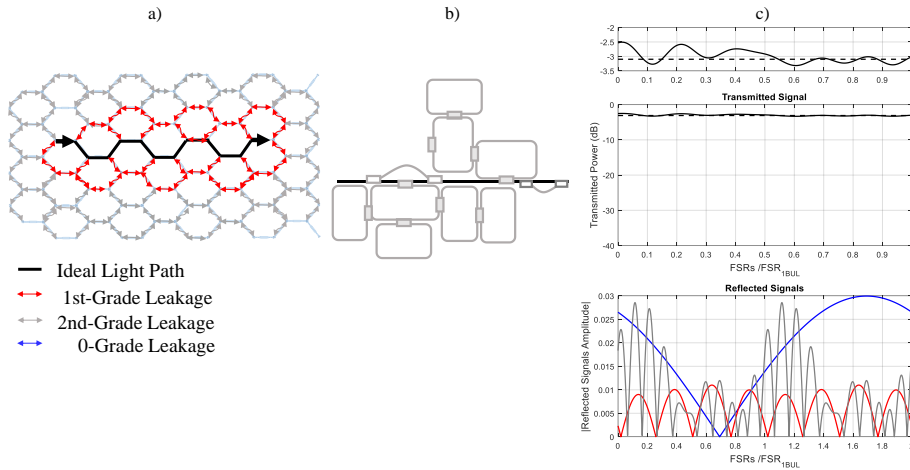


Figure C.2 Layout and mesh-configuration for a programmed waveguide. (b) Schematic illustrating the associated undesired interferometric structures.

In practice, one can tune the non-used TBUs to guide the reflected and leakage signals as far as possible from the defined circuit or to a defined drain optical ports. As shown in Chapter 5, in our experiments no real evidences of strong reflected signals have been measured. The main reason is that, the extinction ratio of a single TBU was measured to be more than 30 dB.

The ideal extinction ratio is infinite. If the 3-dB couplers at the input and the output of the TBU have not ideal 90 ° phase difference between its outputs or the effective index of the lower and upper arms are different, the targeted unbalanced MZI becomes a balanced MZI. In our experimental demonstration, the wavelength window where the TBU remains constant is greater than the 37 nm window offered by the vertical couplers.

## C.2 Thermal stability and crosstalk

Photonic integrated circuits require, in general, thermal management. A typical strategy is to maintain the bottom of the PIC at a constant temperature for which the PIC has been designed. In our case, we have designed a copper thermal chuck coupled

to a heat sink that has been employed to support a Peltier cell and a heat-sensitive resistor to perform the thermal stabilization at 28.7 °C. This structure holds the PCB that, in turn, carries the PIC. Gold vias allow the heat to flow from the bottom to the upper part of the PCB at the PIC area.

First of all, we checked the thermal stability of our setup by synthesizing a simple optical ring resonator in the mesh and by measuring the wavelength drift of a particular spectral notch for 2 different temperatures. Figure 3 shows that after 45 minutes a maximum deviation of less than 7 pm could be observed for both cases. In addition we obtained the temperature drift of the notch versus temperature resulting in 105 pm/°C, which is in good agreement with typical temperature deviation figures in silicon photonics circuits<sup>1</sup>.

Neighbouring TBUs may introduce undesired phase shift due to thermal crosstalk. The heat will flow, not only to the targeted waveguide underneath, but also to the adjacent ones producing a given phase shift. In order to minimize this effect, thermal isolation trenches were introduced in the design and fabrication to increase the thermal resistance in the waveguide plane, increasing the heat flow to the thermal sink. The results obtained for the coupling constant versus injection current seem to be reasonably immune to thermal crosstalk. We attribute this to the fact that the arms of the MZI implementing the TBU are so close that both will experience almost the same crosstalk-induced temperature variation.

Nevertheless, we noticed the presence of an extra phase shift that might be caused by 2 effects: The main one is due to the use of the same metal layer for heating and DC-signal routing. Although the DC routing tracks were made as wide as possible, only the 25% of the heating power remains in the heater area for each thermal tuner, resulting in a temperature gradient over almost all the circuit. Secondly, there might be an imperfect thermal junction between both faces of the PCB, which might need additional check and re-design. This effect is greater the closer the waveguide is from the adjacent heater, as shown in Figure 4. Anyway, this additional phase shift can be overcome by adding a compensating additional corrective phase shift with any of the TBUs involved in the synthesized circuit.

The fully-integrated design must prevent a temperature gradient over the PIC, produced typically by the optical source and the optical amplifiers for the correct chip behaviour.



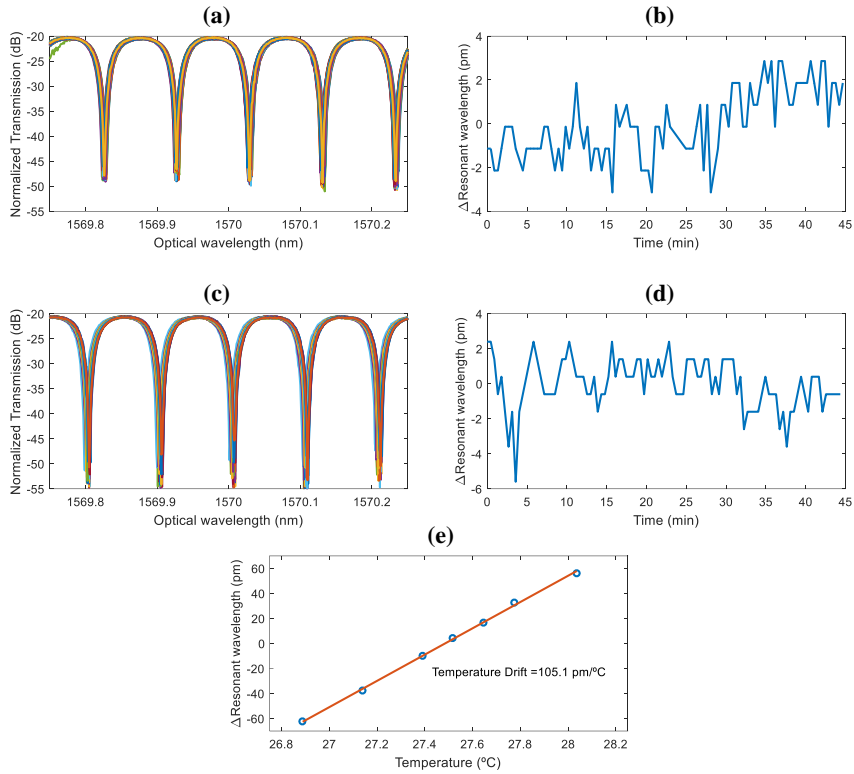


Figure C.3 Thermal stability of the setup. (a) & (c) Normalized Transmission vs optical wavelength. (b) & (d) Wavelength deviation of the notches due to thermal instability. (e) Wavelength deviation of the notch due to the photonic integrated circuit temperature variation. ORR: optical ring resonator, TEC: Temperature in Celsius Degrees,

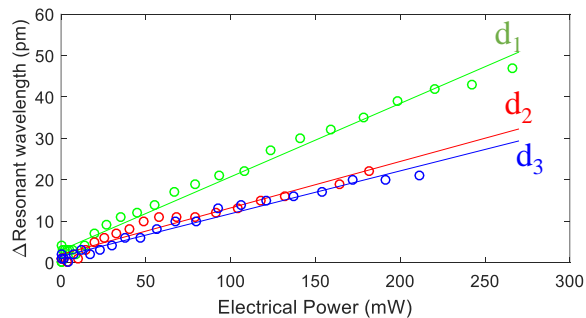


Figure C.4 Thermal crosstalk of the setup for different distances ( $d_1 = 1.511$ ,  $d_2 = 3.176$  and  $d_3 = 8.876$  mm) between the closest ring waveguide and the adjacent heater.

## Author's Publication List

### Peer-reviewed international Journal Publications

1. D. Perez, I. Gasulla and J. Capmany, "Towards Programmable Microwave Photonics Processors," submitted to Journal of Lightwave Technology, (2017) (INVITED).
2. D. Pérez, I. Gasulla, L. Crudgington, D. J. Thomson, A. Z. Khokhar, K. Li, W. Cao, G. Z. Mashanovich and J. Capmany, "General-purpose silicon photonics signal processor core," to be published in Nature Communications, (2017).
3. J. Capmany, D. Pérez and I. Gasulla, "Software-defined universal microwave photonic processors," SPIE Newsroom Optoelectronics & Communications, DOI: 10.1117/2.1201609.006705, (2016), (INVITED).
4. D. Pérez, I. Gasulla, J. Capmany, J. S. Fandiño, P. Muñoz and A. Hossein, "Third-order linearization for self-beating filtered microwave photonic systems using a Dual Parallel Mach-Zehnder modulator", Optics Express 24 (18), 20632-20640, (2016).
5. D. Perez, I. Gasulla and J. Capmany, "Microwave Photonics: The programmable processor," Nature Photonics, 10, 6-8, (2016), (INVITED).
6. D. Pérez, I. Gasulla, J. Capmany and R.A. Soref, "Reconfigurable lattice mesh designs for programmable photonic processors" Optics Express 24 (11), 12093-12106, (2016).
7. D. Pérez, D. Domenech, P. Muñoz and J. Capmany, "Electro-Refraction Modulation Predictions for Silicon Graphene Waveguides in the 1540–1560 nm Region," IEEE Photonics Journal 8 (5), 1-13, 2016.
8. D. Pérez, I. Gasulla, J. Capmany, J. S. Fandiño, P. Muñoz and H. Alavi, "Figures of merit for self-beating filtered microwave photonic systems", Optics Express 24 (9), 10087-10102, (2016).
9. D. Perez, I. Gasulla and J. Capmany, "Software-defined universal microwave photonics processor", OSA Optics Express, vol. 23, no. 11, pp. 14640-14654, (2015).

---

### International Conference Publications

1. D. Pérez, I. Gasulla, F. J. Frailem L. Crudgington, D. J. Thomson, A. Z. Khokhar, K. Li, W. Cao, G. Z. Mashanovich and J. Capmany, “Integrated RF-Photonic Delay Lines using Reconfigurable Photonic Waveguide Meshes,” submitted to International Topical Meeting on Microwave Photonics (IEEE-MWP), Beijing, China, October, 2017.
2. D. Pérez, I. Gasulla, L. Crudgington, D. J. Thomson, A. Z. Khokhar, K. Li, W. Cao, G. Z. Mashanovich and J. Capmany, “Silicon RF-Photonics Processor Reconfigurable Core,” to be presented at 43rd European Conference on Optical Communication ECOC 2017, Gothenburg, Sweden, 2017.
3. D. Pérez, I. Gasulla, L. Crudgington, D. J. Thomson, A. Z. Khokhar, K. Li, W. Cao, G. Z. Mashanovich and J. Capmany, “Compact programmable RF-photonic filters using integrated waveguide mesh processors,” to be presented at 20th International Conference on Transparent Optical Networks ICTON, Girona, Spain, 2017, (INVITED).
4. D. Pérez, I. Gasulla and J. Capmany, “Multi-purpose programmable optical chips,” to be presented at OSA Advanced Photonics Congress, New Orleans, US, 2017, (INVITED).
5. D. Pérez, I. Gasulla and J. Capmany, “Towards Programmable Microwave Photonics Processors,” Optical Fiber Communication Conference 2017, Los Angeles, US, 2017, (INVITED).
6. D. Pérez, I. Gasulla and J. Capmany, “Integrated Microwave Photonics: The evolution from ASPICs to Universal Processors,” European Conference on integrated optics (ECIO) 2017, Eindhoven, 2017, (INVITED).
7. G. Micó, L. Bru, D. Pastor, D. Pérez, D. Domenech, A. M. Sánchez, C. Domínguez and P. Muñoz, “C-band linear propagation properties for a 300 nm film height Silicon Nitride photonics platform,” European Conference on integrated optics (ECIO) 2017, Eindhoven, 2017.
8. D. Pérez, I. Gasulla, J. Capmany and R. A. Soref, “Integrated microwave photonics: The quest for the universal programmable processor”, Photonics Society Summer Topical Meeting Series (SUM), 2016 IEEE, 144-145, Newport Beach, US, 2016, (INVITED).
9. D. Pérez, I. Gasulla, J. Capmany and R. Soref, “Reconfigurable lattice mesh designs for programmable photonic processors and universal couplers” 18th International Conference on Transparent Optical Networks ICTON, Trento, Italy, 2016, (INVITED).

10. J. Capmany, D. Perez and I. Gasulla, "Waveguide Mesh Inspired Integrated Microwave Photonics", Asia Communications and Photonics Conference (APC), AF1H. 1, Wuhan, China, 2016, (INVITED).
11. D. Pérez, I. Gasulla and J. Capmany, "Integrated microwave photonics", IEEE Photonics Conference (IPC) 2016, 5-6, Hawaii, US, 2016, (INVITED).
12. D. Pérez, I. Gasulla, J. Capmany and R. Soref "Hexagonal Waveguide Mesh Design for Universal Multiport Interferometers", IEEE Photonics Conference (IPC) 2016, 5-6, Hawaii, US, 2016.
13. D. Perez, I. Gasulla and J. Capmany, "Honeycomb lattice meshes for reconfigurable universal microwave photonics processors", SPIE/COS Photonics Asia 2016, 2016, (INVITED).
14. D. Perez, I. Gasulla, J. Capmany and R.A. Soref, "Hexagonal Reconfigurable Lattice Mesh for Programmable Photonic Processors," 42nd European Conference on Optical Communication ECOC 2016, Düsseldorf, Germany, 2016.
15. D. Pérez, I. Gasulla and J. Capmany, "Recent advances in Integrated Microwave Photonics," The 2nd International Conference on Microwave Photonics Technology and Application (MPTA 2016), Shanghai, China, 2016, (INVITED).
16. D. Pérez, D. Domenech, C. Domínguez, I. Gasulla, J. Capmany, and P. Muñoz, "Thermal tuners on Silicon Nitride: performance and crosstalk analysis," 20th Annual Symposium of the IEEE Photonics Benelux Chapter, Brussels, Belgium, 2016.
17. D. Pérez, J. Fernández et al., "Switching and cross-talk characteristics of compact thermal tuners on a Silicon Nitride Platform", European Conference on Integrated Optics (ECIO), Warsaw, Poland, 2016.
18. D. Pérez, I. Gasulla and J. Capmany, "Software-defined reconfigurable microwave photonics processor: concept and design equations", in Proc. ECOC 2015, paper P 3.6, Valencia, Spain, (2015).
19. D. Pérez, I. Gasulla and J. Capmany, "Software-defined integrated microwave photonics for Radio Access Networks", 36th Progress in Electromagnetics Research Symposium, Prague, Czech Republic, 2015, (INVITED).
20. D. Pérez, I. Gasulla and J. Capmany, "Microwave Photonics Transistor Design Equations", in 2014 International Topical Meeting on Microwave Photonics (IEEE-MWP) Technical Digest, pp. 82-85, Sapporo, Japan, October, 2014.

21. P. Muñoz, J. Capmany, D. Pérez, J. H. den Besten, J. S. Fandiño and J.D. Doménech, “Integrated microwave photonics: State of the art and future trends,” 16th International Conference on Transparent Optical Networks (ICTON), Graz, Austria, 2014, (INVITED).

**Patent:**

1. J. Capmany, I. Gasulla, D. Pérez and S. Sales, “Compact broadband tunable photonic dispersive delay line,” Application no. R-19150 -2017 under revision. Priority country: Spain.

## References

- [1] C. A. Mack, «Fifty years of Moore's Law,» *IEEE Transactions on Semiconductor Manufacturing*, vol. 24, n° 2, pp. 202-207, 2011.
- [2] R. Waterhouse y D. Novack, «Realizing 5G: Microwave photonics for 5G mobile wireless systems,» *IEEE Microwave Magazine*, vol. 16, n° 8, pp. 84-92, 2015.
- [3] S. Iezekiel, M. Burla, J. Klamkin, D. Marpaung y J. Capmany, «RF Engineering meets optoelectronics,» *IEEE Microwave Magazine*, vol. 16, n° 8, pp. 28-45, 2015.
- [4] S. Shinjo, K. Nakatani, K. Tsutsumi y H. Nakamizo, «Integrating the Front End: A Highly Integrated RF Front End for High-SHF Wide-Band Massive MIMO in 5G,» *IEEE Microwave Magazine*, vol. 18, n° 5, pp. 31-40, 2017.
- [5] M. M. Rathore, A. Ahmad, A. Paul y S. Rho, «Urban planning and building smart cities based on the Internet of Things using Big Data analytics,» *Computer Networks*, vol. 101, pp. 63-80, 2016.
- [6] M. Lehofer, M. Heiss, S. Rogenhofer, C. W. Weng, M. Sturm, S. Rusitschka y S. Dippl, «Platforms for Smart Cities – connecting humans, infrastructure and industrial IT,» de *IEEE Science of Smart City Operations and Platforms Engineering (SCOPE) in partnership with Global City Teams Challenge (GCTC) (SCOPE - GCTC), 2016 1st International Workshop on*, Vienna, Austria, 2016.
- [7] «Technology focus on microwave photonics,» *Nature Photonics*, vol. 5, n° 723, 2011.
- [8] P. Ghelfi, F. Laghezza, F. Scotti, G. Serafino, A. Capria, S. Pinna, D. Onori, C. Porzi, M. Scaffardi, A. Malacarne, V. Vercesi, E. Lazzeri, F. Berizzi y A.

- 
- Bogoni, «A fully photonics-based coherent radar system,» *Nature*, vol. 507, n° 7492, pp. 341-345, 2014.
- [9] J. Capmany y D. Novak, «Microwave photonics combines two worlds,» *Nature Photonics*, vol. 1, pp. 319-330, 2007.
- [10] M. Burla, L. R. Cortés, M. Li, X. Wang, L. Chrostowski y J. Azaña, «Integrated waveguide Bragg gratings for microwave photonics signal processing,» *Optics Express*, vol. 21, n° 21, pp. 25120-25147, 2013.
- [11] M. Burla, M. R. H. Khan, D. A. I. Marpaung, L. Zhuang, C. H. Roeloffzen, A. Leinse, M. Hoekman y R. Heidenman, «Separate carrier tuning scheme for integrated optical delay lines in photonic beamformers,» de *Microwave Photonics, 2011 International Topical Meeting on & Microwave Photonics Conference*, Singapore, Singapore , 2011.
- [12] J. Capmany, J. Mora, P. Muñoz y S. Sales, «A microwave photonics transistor,» de *IEEE Topical meeting on MWP*, Alexandria, USA, 2013.
- [13] J. Fandiño, J. D. Domenech, P. Muñoz y J. Capmany, «Integrated InP frequency discriminator for phase-modulated microwave photonic links,» *Optics Express*, vol. 21, n° 3, pp. 3726-3736, 2013.
- [14] A. Seeds, M. Natrella, H. Shams, L. Ponnampalam, K. Balakier, C. Graham, C.-P. Liu, H. Liu, C. Renaud y M. Fice, «Microwave Photonics: Present Status and Future Outlook,» de *Microwave Photonics (MWP), 2015 International Topical Meeting on*, Paphos, Cyprus, 2015.
- [15] R. Slavík, Y. Park, N. Ayotte, S. Doucet, T.-J. Ahn, S. LaRochelle y J. Azaña, «Photonic temporal integrator for all-optical computing,» *Optics Express*, vol. 16, n° 22, pp. 18202-18214, 2008.
- [16] D. Marpaung, C. Roeloffzen, R. Heideman, A. Leinse, S. Sales y J. Capmany, «Integrated microwave photonics,» *Laser & Photonics Reviews*, vol. 7, n° 4, pp. 506-538, 2013.
- [17] M. Burla, L. R. Cortés, M. Li, X. Wang, L. Chrotowski y J. A. , «On-chip ultra-wideband microwave photonic phase shifter and true time delay line

- based on a single phase-shifted waveguide Bragg grating,» de *IEEE Microwave Photonics Conference*, Alexandria, VA, USA , 2013.
- [18] M. Burla, L. Zhuang, D. Marpaung, M. R. Khan, A. Leinse, W. Beeker, M. Hoekman, R. Heideman y C. Roeloffzen, «On-chip, CMOS-compatible, hardware-compressive integrated photonic beamformer based on WDM,» de *Microwave Photonics (MWP), 2013 International Topical Meeting on*, Alexandria, VA, USA , 2013.
- [19] H. Chen, A. W. Fang, J. D. Peters, Z. Wang, J. Bovington, D. Liang y J. E. Bowers, «Integrated microwave photonic filter on a hybrid silicon platform,» *IEEE Transactions on Microwave Theory and Techniques*, vol. 58, n° 11, pp. 3213-3219, 2010.
- [20] J. S. Fandiño, P. Muñoz, D. Doménech y J. Capmany, «A monolithic integrated photonic microwave filter,» *Nature Photonics*, vol. 11, pp. 124-129, 2016.
- [21] P. Samadi, L. R. Chen, C. Callender, P. Dumais, S. Jacob y D. Celo, «RF arbitrary waveform generation using tunable planar lightwave circuits,» *Optics Communications*, vol. 284, n° 15, pp. 3737-3741, 2011.
- [22] K. Wang, Y. Wang, S. Gao, A. Nirmalathas, C. Lim, K. Alameh y E. Skafidas, «2x2 silicon integrated optical phased array for beam steering applications,» de *International Topical Meeting on Microwave Photonics (MWP)*, Paphos, 2015.
- [23] D. Marpaung, «On-Chip Photonic-Assisted Instantaneous Microwave Frequency Measurement System,» *IEEE Photonics Technology Letters*, vol. 25, n° 9, pp. 837-840, 2013.
- [24] S. D. Brown, J. R. Francis, J. Rose y Z. G. Vranesic, *Field-programmable gate arrays*, Springer Science & Business Media, 2012.
- [25] O. Graydon, «Birth of the programmable optical chip,» *Nature Photonics*, vol. 1, 2016.



- 
- [26] M. Reck, A. Zeilinger, H. J. Bernstein y P. Bertani, «Experimental realization of any discrete unitary operator,» *Physical Review Letters*, vol. 73, nº 58, p. 58–61, 1994.
- [27] D. A. Miller, «Self-configuring universal linear optical component,» *Photonics Research*, vol. 1, nº 1, p. 1–15, 2013.
- [28] C. Cox, E. Ackerman, G. Betts y J. Prince, «Limits on the performance of RF-over-fiber links and their impact on device design,» *IEEE Transactions on Microwave Theory and Techniques*, vol. 54, nº 2, pp. 906-920, 2006.
- [29] E. I. & C. C. H. Ackerman, «Microwave photonic links with gain and low noise figure,» de *Lasers and Electro-Optics Society, 2007 (LEOS). The 20th Annual Meeting of the IEEE (pp. 38-39). IEEE, 2007.*
- [30] K. Jinguji y M. Kawachi, «Synthesis of coherent two-port lattice-form optical delay-line circuit,» *Journal of Lightwave Technology*, vol. 13, nº 1, pp. 73-82, 1995.
- [31] K. Jinguji, «Synthesis of coherent two-port Optical delay-line circuit with ring waveguides,» *Journal of lightwave technology*, vol. 14, nº 8, pp. 1882-1898, 1996.
- [32] C. K. Madsen and J. H. Zhao, *Optical filter design and analysis: A signal processing approach*, John Wiley & Sons, Inc., 1999.
- [33] D. A. B. Miller, «All linear optical devices are mode converters,» *Optics Express*, vol. 20, nº 21, pp. 23985-23993, 2012.
- [34] D. A. B. Miller, «Self-aligning universal beam coupler,» *Optics Express*, vol. 21, nº 5, pp. 6360-6370, 2013.
- [35] «RF Photonic Links,» PHARAD, LLC, 2017. [En línea]. Available: <http://www.pharad.com/rf-photonic-transceivers.html>.
- [36] D. J. Blumenthal, J. Barton, N. Beheshti, J. E. Bowers, E. Burmeister, L. A. Coldren, M. Dummer, G. Epps, A. Fang, Y. Ganjali, J. Garcia, B. Koch, V.

- La, E. Lively, J. Mack, M. Mašanović, N. McKeown, K. Nguyen, S. C. Nicholes, H. Park y B. Stam, «Integrated photonics for low-power packet networking,» *IEEE Journal of selected topics in quantum electronics* , vol. 17, n° 2, pp. 458-471, 2011.
- [37] C. Doerr y K. Okamoto, «Advances in Silica Planar Lightwave Circuits,» *Journal of Lightwave Technology*, vol. 24, n° 12, pp. 4763 - 4789, 2006.
- [38] M. Pagani, K. Vu, D.-Y. Choi, B. J. E. S. J. Madden y D. Marpaung, «Instantaneous microwave frequency measurement using four-wave mixing in a chalcogenide chip,» *Optics Communications*, vol. 373, pp. 100-104, 2016.
- [39] J. S. Fandiño y P. Muñoz, «Photonics-based microwave frequency measurement using a double-sideband suppressed-carrier modulation and an InP integrated ring-assisted Mach–Zehnder interferometer filter,» *Optics Letters*, vol. 38, n° 21, pp. 4316-4319, 2013.
- [40] I. Gasulla y J. Capmany, «Analytical model and figures of merit for filtered microwave photonic links,» *Optics Express*, vol. 19, n° 20, pp. 19758-19774, 2011.
- [41] P. Muñoz, J. Capmany, D. Pérez, J. H. d. Besten, J. S. Fandiño y J. D. Domenech, «Integrated microwave photonics: sstate of the art and future trends,» de *Proceedings of International Conference on Transparent Networks (ICTON)*, Graz, Austria, 2014.
- [42] E. J. Norberg, R. S. Guzzon, S. Nicholes, J. Parker and L. Coldren, "Programmable Photonic Lattice Filters in InGaAsP-InP," *IEEE Photonics Technology Letters*, vol. 22, no. 2, pp. 109-111, 2010.
- [43] R. S. Guzzon, E. J. Norberg, J. S. Parker, L. A. Johansson and L. A. Coldren, "Integrated InP-InGaAsP tunable coupled ring optical bandpass filters with zero insertion loss," *Optics Express*, vol. 19, no. 8, pp. 7816-7826, 2011.
- [44] F. Ferdous, H. Miao, D. E. Leaird, K. Srinivasan, J. Wang, L. Chen, L. T. Varghese y A. M. Weiner, «Spectral line-by-line pulse shaping of on-chip microresonator frequency combs,» *Nature Photonics*, vol. 5, pp. 770-776, 2011.

- 
- [45] C. Sun, M. Georgas, J. Orcutt, B. Moss, Y.-H. Chen, J. Shainline, M. Wade, K. Mehta, K. Nammari, E. Timurdogan, D. Miller, O. Tehar-Zahav, Z. Sternberg, J. Leu, J. Chong, R. Bafrali, G. Sandhu, M. Watts, R. Meade y M. Popović, «A Monolithically-Integrated Chip-to-Chip Optical Link in Bulk CMOS,» *IEEE Journal of Solid-State Circuits*, vol. 50, n° 4, pp. 828 - 844, 2015.
- [46] C. Sun, M. T. Wade, Y. Lee, J. S. Orcutt, L. Alloatti, M. S. Georgas, A. S. Waterman, J. M. Shainline, R. R. Avizienis, S. Lin, B. R. Moss, R. Kumar, F. Pavanello, A. H. Atabaki, H. M. Cook, A. J. Ou, J. C. Leu, Y.-H. Chen, K. Asanović y R. J. Ram, «Single-chip microprocessor that communicates directly using light,» *Nature*, vol. 528, n° 7583, pp. 534-538, 2015.
- [47] S. Assefa, W. M. J. Green, A. Rylyakov, C. Schow, F. Horst y Y. A. Vlasov, «CMOS Integrated Nanophotonics — enabling technology for exascale computing systems,» de *Optical Fiber Communication Conference*, Los Angeles, United States, 2011.
- [48] M. H. Khan, H. Shen, Y. Xuan, L. Zhao, S. Xiao, D. E. Leaird, A. M. Weiner y M. Qi, «Ultrabroad-bandwidth arbitrary radiofrequency waveform generation with a silicon photonic chip-based spectral shaper,» *Nature Photonics*, vol. 4, pp. 117-122, 2010.
- [49] W. Liu, M. Li, R. S. Guzzon, E. J. Norberg, J. S. Parker, M. Lu, L. A. Coldren y J. Yao, «A fully reconfigurable photonic integrated signal processor,» *Nature Photonics*, vol. 10, pp. 190-195, 2016.
- [50] D. Pérez, I. Gasulla y J. Capmany, «Software-defined reconfigurable microwave photonics processor,» *Optics Express*, vol. 23, n° 11, pp. 14640-14654, 2015.
- [51] L. Zhuang, C. G. H. Roeloffzen, M. Hoekman, K.-J. Boller y A. J. Lowery, «Programmable photonic signal processor chip for radiofrequency applications,» *Optica*, vol. 2, n° 10, pp. 854-859, 2015.
- [52] D. Pérez, I. Gasulla, J. Capmany y R. A. Soref, «Reconfigurable lattice mesh designs for programmable photonic processors,» *Optics Express*, vol. 24, n° 11, pp. 12093-12106, 2016.

- [53] M. Hochberg y L. Chrostowski, *Silicon photonics design: from devices to systems*, Cambridge University, 2015.
- [54] M. Hochberg y T. Baehr-Jones, «Towards fabless silicon photonics,» *Nature Photonics*, vol. 4, pp. 492-494, 2010.
- [55] R. Soref, «The past, present and future of silicon photonics,» *IEEE Journal of Selected Topics Quantum Electronics*, vol. 12, n° 6, pp. 1678-1687, 2006.
- [56] W. Bogaerts, M. Fiers y P. Dumon, «Design Challenges in Silicon Photonics,» *IEEE Journal of Selected Topics in Quantum Electronics*, vol. 20, n° 4, p. 8202008, 2013.
- [57] W. Bogaerts, R. Baets, P. Dumon, V. Wiaux, S. Beckx, D. Taillaert, B. Luyssaert, J. V. Campenhout, P. Bienstman y D. V. Thourhout, «Nanophotonic waveguides in silicon-on-insulator fabricated with CMOS technology,» *Journal of Lightwave Technology*, vol. 23, n° 1, pp. 401 - 412, 2005.
- [58] M. Asghari, «Silicon Photonics: A Low Cost Integration Platform for Datacom and Telecom Applications,» de *National Fiber Optic Engineers Conference*, San Diego, California, United States, 2008.
- [59] D.Celo, D. J. Goodwill, J. Jiang, P. Dumais, C. Zhang, F. Zhao, X. Tu, C. Zhang, S. Yan, J. He, M. Li, W. Liu, Y. Wei, D. Geng, H. Mehrvar y E. Bernier, «32×32 silicon photonic switch,» de *OptoElectronics and Communications Conference (OECC) held jointly with 2016 International Conference on Photonics in Switching (PS)*, Niigata, Japan, 2016.
- [60] A. Melloni, A. Canciamilla, C. Ferrari, F. Morichetti, L. O'Faolain, T. F. Krauss, R. D. L. Rue, A. Samarelli y M. Sorel, «Tunable Delay Lines in Silicon Photonics: Coupled Resonators and Photonic Crystals, a Comparison,» *IEEE Photonics Journal*, vol. 2, n° 2, pp. 181 - 194, 2010.
- [61] M. J. R. Heck, J. F. Bauters, M. L. Davenport, J. K. Doylend, S. Jain, G. Kurczveil, S. Srinivasan, Y. Tang y J. E. Bowers, «Hybrid Silicon Photonic

- 
- Integrated Circuit Technology,» *IEEE Journal of Selected Topics in Quantum Electronics*, vol. 19, n° 4, p. 6100117, 2013.
- [62] S. Keyvaninia, M. Muneeb, S. Stanković, P. J. V. Veldhoven, D. V. Thourhout y G. Roelkens, «Ultra-thin DVS-BCB adhesive bonding of III-V wafers, dies and multiple dies to a patterned silicon-on-insulator substrate,» *Optical Materials Express*, vol. 3, n° 1, pp. 35-46, 2012.
- [63] R. Heideman, M. Hoekman y E. Schreuder, «TriPleX-Based Integrated Optical Ring Resonators for Lab-on-a-Chip and Environmental Detection,» *IEEE Journal of Selected Topics in Quantum Electronics*, vol. 18, n° 5, pp. 1583-1596, 2012.
- [64] C. Roeloffzen, L. Zhuang, C. Taddei, A. Leinse, R. G. Heideman, P. L. v. Dijk, R. M. Oldenbeuving, D. A. I. Marpaung, M. Burla y K. J. Boller, «Silicon nitride microwave photonics circuits,» *Optics Express*, vol. 21, n° 19, pp. 22937-22961, 2013.
- [65] G. Micó, L. Bru, D. Pastor, D. Pérez, D. Domenech, A. M. Sánchez, C. Domínguez y P. Muñoz, «C-band linear propagation properties for a 300 nm film height Silicon Nitride photonics platform,» de *European Conference on integrated optics (ECIO) 2017*, Eindhoven, the Netherlands., 2017.
- [66] «JePPIX Roadmap 2015,» 2015. [En línea]. Available: <http://www.jeppix.eu>.
- [67] A. Leinse, R. G. Heideman, M. Hoekman, F. Schreuder, F. Falke, C. G. H. Roeloffzen, L. Zhuang, M. Burla, D. Marpaung, D. H. Geuzebroek, R. Dekker, E. J. Klein, P. W. L. v. Dijk y R. M. Oldenbeuving, «TriPleX waveguide platform: low-loss technology over a wide wavelength range,» de *Proc. SPIE 8767, Integrated Photonics: Materials, Devices, and Applications II*, Grenoble, France, 2013.
- [68] W. D. Sacher, G.-Q. L. Y. Huang y J. K. S. Poon, «Multilayer Silicon Nitride-on-Silicon Integrated Photonic Platforms and Devices,» *Journal of Lightwave Technology*, vol. 33, n° 4, pp. 901-910, 2015.
- [69] M. Smit, X. Leijtens, H. Ambrosius, E. Bente, J. v. d. Tol, B. Smalbrugge, T. d. Vries, E.-J. Geluk, J. Bolk, R. v. Veldhoven, L. Augustin, P. Thijs, D. D'Agostino, K. L. H. Rabbani, S. Stopinski, S. Tahvili, A. Corradi, E. Kleijn

- y D. Dzibrou, «An introduction to InP-based generic integration technology,» *Semiconductor Science and Technology*, vol. 29, n° 8, 2014.
- [70] L. A. Coldren, S. C. Nicholes, L. Johansson, S. Ristic, R. S. Guzzon, E. J. Norberg y U. Krishnamachari, «High Performance InP-Based Photonic ICs—A Tutorial,» *Journal of Lightwave Technology*, vol. 29, n° 4, pp. 554-570, 2011.
- [71] F. Kish, R. Nagarajan, D. Welch, P. Evans, J. Rossi, J. Pleumeekers, A. Dentai, M. Kato, S. Corzine, R. Muthiah, M. Ziari, R. Schneider, M. Reffle, T. Butrie y D. Lambert, «From Visible Light-Emitting Diodes to Large-Scale III–V Photonic Integrated Circuits,» *Proceedings of the IEEE*, vol. 101, n° 10, pp. 2255 - 2270, 2013.
- [72] D. Melati, A. Alippi, A. Annoni, N. Peserico y A. Melloni, «Integrated all-optical MIMO demultiplexer for mode- and wavelength-division-multiplexed transmission,» *Optics Letters*, vol. 42, n° 2, pp. 342-345, 2017.
- [73] L. Shen, Y. Jiao, W. Yao, Z. Cao, J. v. d. Tol, G. Roelkens y M. Smit, «67 GHz uni-traveling carrier photodetector on an InP-membrane-on-silicon platform,» de *Lasers and Electro-Optics (CLEO), 2016 Conference on*, San José, CA, 2016.
- [74] R. Soref y B. Bennett, «Electrooptical effects in silicon,» *IEEE Journal of Quantum Electronics*, vol. 23, n° 1, pp. 123-129, 1987.
- [75] C. E. Png, M. J. Sun, S. T. Lim, T. Y. L. Ang y K. Ogawa, «Numerical Modeling and Analysis for High-Efficiency Carrier-Depletion Silicon Rib-Waveguide Phase Shifters,» *IEEE Journal of Selected Topics in Quantum Electronics*, vol. 22, n° 6, p. 3300208, 2016.
- [76] M. W. Pruessner, D. Park, D. A. Kozak, T. H. Stievater y W. S. Rabinovich, «Effective index tuning in micro-opto-mechanical structures using gradient electric forces,» de *Photonics Society Summer Topical Meeting Series (SUM), 2016 IEEE*, Newport Beach, CA, USA, 2016.
- [77] J. Wang, H. Shen, L. Fan, R. Wu, B. Niu, L. T. Varghese, Y. Xuan, D. E. Leaird, X. Wang, F. Gan, A. M. Weiner y M. Q., «Reconfigurable radio-

- 
- frequency arbitrary waveforms synthesized in a silicon photonic chip,» *Nature Communications*, vol. 6, n° 5957, pp. 1-8, 2015.
- [78] B. Guan, S. S. Djordjevic, N. K. Fontaine, L. Zhou, S. Ibrahim, R. P. Scott, D. J. Geisler, Z. Ding y S. J. B. Yoo, «CMOS Compatible Reconfigurable Silicon Photonic Lattice Filters Using Cascaded Unit Cells for RF-Photonic Processing,» *IEEE Journal of Selected Topics in Quantum Electronics*, vol. 20, n° 4, pp. 359-368, 2014.
- [79] D. Pérez, I. Gasulla y J. Capmany, *Software-defined Microwave Photonics Processor: Concept, Core Design, equations and performance analysis*, Universitat Politècnica de València: Master Thesis, 2015.
- [80] J. Mitola, «The software radio architecture,» *IEEE Communications Magazine*, vol. 33, n° 5, pp. 26-38, 1995.
- [81] D. Pérez, I. Gasulla, J. Capmany, J. S. Fandiño, P. Muñoz y H. Alavi, «Figures of merit for self-beating filtered microwave photonic systems,» *Optics Express*, vol. 24, n° 9, pp. 10087-10102, 2016.
- [82] E. J. Norberg, R. S. Guzzon, J. S. Parker, L. A. Johansson and L. A. Coldren, "Programmable Photonic Microwave Filters Monolithically Integrated in InP-InGaAsP," *Journal of Lightwave technology*, vol. 29, no. 11, pp. 1611-1619, 2011.
- [83] S. K. Korotky y R. M. d. Ridder, «Dual parallel modulation schemes for low-distortion analog optical transmission,» *IEEE Journal on Selected Areas in Communications*, vol. 8, n° 7, pp. 1377-1381, 1990.
- [84] Y. Zhou, L. Zhou, M. Wang, Y. Xia, Y. Zhong, X. Li y J. Chen, «Linearity characterization of a Dual-Parallel Silicon Mach-Zehnder Modulator,» *IEEE Photonics Journal*, vol. 8, n° 6, 2016.
- [85] D. Pérez, I. Gasulla, J. Capmany, J. S. Fandiño, P. Muñoz y H. Alavi, «Third-order linearization for self-beating filtered microwave photonic systems using a dual parallel Mach-Zehnder modulator,» *Optics Express*, vol. 24, n° 18, pp. 20632-20640, 2016.

- [86] H. Yamazaki, H. Takahashi, T. Goh, Y. Hashizume, T. Yamada, S. Mino, H. Kawakami y Y. Miyamoto, «Optical Modulator With a Near-Linear Field Response,» *Journal of Lightwave Technology*, vol. 34, nº 16, pp. 3796-3802, 2016.
- [87] R. S. Guzzon, E. J. Norberg y L. A. Coldren, «Spurious-Free Dynamic Range in Photonic Integrated Circuit Filters with Semiconductor Optical Amplifiers,» *IEEE Journal of Quantum Electronics*, vol. 48, nº 2, pp. 269-278, 2012.
- [88] W. Clements, P. Humphreys, B. Metcalf, W. Kolthammer y I. Walsmley, «Optimal design for universal multiport interferometers,» *Optica*, vol. 3, nº 12, p. 1460–1465, 2016.
- [89] R. A. Soref, «Silicon-based optoelectronics,» *Proceedings of the IEEE* , vol. 81, nº 12, pp. 1687 - 1706, 1993.
- [90] J. Khurgin y P. A. Morton, «Tunable wideband optical delay line based on balanced coupled resonator structures,» *Optics Letters*, vol. 34, nº 17, pp. 2655-2657, 2009.
- [91] C. K. Madsen, «General IIR Optical Filter Design for WDM Applications Using All-Pass Filters,» *Journal of Lightwave Technology*, vol. 18, nº 6, pp. 860-, 2000.
- [92] M. Rasras, C. Madsen, M. Cappuzzo, E. Chen, L. Gomez, E. Laskowski, A. Griffin, A. Wong-Foy, A. Gasparyan, A. Kasper, J. L. Grange y S. Patel, «Integrated resonance-enhanced variable optical delay lines,» *Photonics Technology Letteres, IEEE*, vol. 17, nº 4, pp. 834-836, 2005.
- [93] S. Mookherjea y A. Yariv, «Coupled resonator optical waveguides,» *IEEE Journal of Selected Topics in Quantum Electronics*, vol. 8, nº 3, pp. 448-456, 2002.
- [94] J. E. Heebner, P. Chak, S. Pereira, J. E. Sipe y R. W. Boyd, «Distributed and localized feedback in microresonator sequences for linear and nonlinear



- 
- optics,» *Journal of the Optical Society of America B*, vol. 21, nº 10, pp. 1818-1832, 2004.
- [95] A. Ribeiro, A. Ruocco, L. Vanacker y W. Bogaerts, «Demonstration of a  $4 \times 4$ -port universal linear circuit,» *Optica*, vol. 3, nº 12, pp. 1348-1357, 2016.
- [96] D. A. B. Miller, «Perfect optics with imperfect components,» *Optica*, vol. 2, nº 8, pp. 747-750, 2015.
- [97] A. Peruzzo, A. Laing, A. Politi, T. Rudolph and J. L. O'Brien, «Multimode quantum interference of photons in multiport integrated devices,» *Nature Communications*, vol. 2, no. 224, 2011.
- [98] D. Bonneau, E. Engin, K. Ohira, N. Suzuki, H. Yoshida, N. Iizuka, M. Ezaki, C. M. Natarajan, M. G. Tanner, R. H. Hadfield, S. N. Dorenbos, V. Zwiller, J. L. O'Brien y M. G. Thompson, «Quantum interference and manipulation of entanglement in silicon wire waveguide quantum circuits,» *New Journal of Physics*, vol. 14, nº 4, 2012.
- [99] B. J. Metcalf, N. Thomas-Peter, J. B. Spring, D. Kundys, M. A. Broome, P. C. Humphreys, X.-M. Jin, M. Barbieri, W. S. Kolthammer, J. C. Gates, B. J. Smith, N. K. Langford, P. G. Smith y I. A. Walmsley, «Multiphoton quantum interference in a multiport integrated photonic device,» *Nature Communications*, vol. 4, nº 1356, 2013.
- [100] R. Boeck, N. A. F. Jaeger, N. Rouger y L. Chrostowski, «Series-coupled silicon racetrack resonators and the Vernier effect: theory and measurement,» *Optics Express*, vol. 18, nº 24, pp. 25151-25157, 2010.
- [101] D. M. L. Z. C. R. M. R. K. M. Burla, A. Leinse, M. Hoekman y R. Heideman, «On-chip CMOS compatible reconfigurable optical delay-line with separate carrier tuning for microwave photonic signal processing,» *Optics Express*, vol. 19, nº 22, pp. 21475-21484, 2011.
- [102] M. Sagues, *Aplicaciones de la correspondencia entre el dominio óptico y eléctrico establecida por la modulación óptica en banda lateral única.*, Ph.D Thesis, 2009.

- [103] G. Qi, J. Yao, J. Seregelyi, S. Paquet y C. Belisle, «Generation and distribution of a wide-band continuously tunable millimeter-wave signal with an optical external modulation technique,» *IEEE Transactions on Microwave Theory and Techniques*, vol. 53, n° 10, pp. 3090 - 3097, 2005.
- [104] L. Maleki, «Sources: The optoelectronic oscillator,» *Nature Photonics*, vol. 5, pp. 728-730, 2011.
- [105] K.-P. Ho, S. Liaw y C. Lin, «Efficient photonic mixer with frequency doubling,» *IEEE Photonics Technology Letters*, vol. 9, n° 4, pp. 511-513, 1997.
- [106] Y. Gao, A. Wen, H. Zhang, S. Xiang, H. Zhang, L. Zhao y L. Shang, «An efficient photonic mixer with frequency doubling based on a dual-parallel MZM,» *Optics Communications*, vol. 321, pp. 11-15, 2014.
- [107] I. S. Lin, J. D. McKinney y A. M. Weiner, «Photonic synthesis of broadband microwave arbitrary waveforms applicable to ultra-wideband communication,» *IEEE Microwave and Wireless Components Letters*, vol. 15, n° 4, pp. 226-228, 2005.
- [108] M. Burla, Advanced integrated optical beam forming networks for broadband phased array antenna systems, PhD. Thesis, 2013.
- [109] L. Zhuang, C. G. H. Roeloffzen, R. G. Heideman, A. Borreman, A. Meijerink y W. v. Etten, «Single-Chip Ring Resonator-Based  $1 \times 8$  Optical Beam Forming Network in CMOS-Compatible Waveguide Technology,» *IEEE Photonics Technology Letters*, vol. 19, n° 15, pp. 1130-1132, 2007.
- [110] H. Shao, H. Yu, X. Jiang, J. Yang y G. Roelkens, «Large bandwidth and high accuracy photonic-assisted instantaneous microwave frequency estimation system based on an integrated silicon micro-resonator,» de *Group IV Photonics (GFP), 2014 IEEE 11th International Conference on*, Paris, France, 2014.

- 
- [111] W. Wei, L. Yi, Y. Jaouën y W. Hu, «Software-defined microwave photonic filter with high reconfigurable resolution,» *Scientific Reports*, vol. 6, n° 3561, 2016.
- [112] I. G. L. C. D. J. T. A. Z. K. K. L. W. C. G. Z. M. & J. C. D. Pérez, «General-purpose silicon photonic signal processor core,» *to be published in Nature Communications*, 2017.
- [113] J. Carolan, C. Harrold, C. Sparrow, E. Martín-López, N. J. Russell, J. W. Silverstone, P. J. Shadbolt, N. Matsuda, M. Oguma, M. Itoh, G. D. Marshall, M. G. Thompson, J. F. Matthews, T. Hashimoto, J. O'Brien y A. Laing, «Universal linear optics,» *Science*, vol. 349, n° 6249, pp. 711-716, 2015.
- [114] M. A. Nielsen y I. L. Chuang, *Quantum computation and Quantum information*, Cambridge University Press, 2001.
- [115] N. C. Harris, Y. Ma, J. Mower, T. Baehr-Jones, D. Englund, M. Hochberg y C. Galland, «Efficient, compact and low loss thermo-optic phase shifter in silicon,» *Optics Express*, vol. 22, n° 9, pp. 10487-10493, 2014.
- [116] P. Dumais, Y. Wei, M. Li, F. Zhao, X. Tu, J. Jiang, D. Celo, D. J. Goodwill, H. Fu, D. Geng y E. Bernier, «2×2 multimode interference coupler with low loss using 248 nm photolithography,» de *Optical Fiber Communications Conference and Exhibition (OFC)*, Anaheim, CA, USA, 2016.
- [117] Z. Sheng, Z. Wang, C. Qiu, L. Li, A. Pang, A. Wu, X. Wang, S. Zou y F. Gan, «A Compact and Low-Loss MMI Coupler Fabricated With CMOS Technology,» *IEEE Photonics Journal*, vol. 4, n° 6, pp. 2272 - 2277, 2012.
- [118] T. Horikawa, D. Shimura y T. Mogami, «Low-loss silicon wire waveguides for optical integrated circuits,» *Materials Research Society*, vol. 6, n° 1, pp. 9-15, 2016.
- [119] S. Grillanda, M. Carminati, F. Morichetti, A. A. P. Ciccarella, G. Ferrari, M. Strain, M. Sorel, M. Sampietro y A. Melloni, «Non-invasive monitoring and control in silicon photonics using CMOS integrated electronics,» *Optica*, vol. 1, n° 3, pp. 123-136, 2014.

- [120] S. Chen y D. Dai, «Ultra-broadband low-loss  $2\times 2$  MZI (Mach-Zehnder interferometer)-based thermo-optic switch with bent directional couplers on silicon,» de *Optical Fiber Communications Conference and Exhibition (OFC)*, Anaheim, CA, USA, 2016.
- [121] J. Capmany, D. Domenech y P. Muñoz, «Silicon graphene waveguide tunable broadband microwave photonics phase shifter,» *Optics Express*, vol. 22, nº 7, pp. 8094-8100, 2014.